Forschungszentrum Karlsruhe
Technik und Umwelt
Wissenschaftliche Berichte
FZKA 5590

Physics of Intense Light Ion Beams and Production of High Energy Density in Matter

Annual Report 1994

H.-J. Bluhm (Herausgeber)
Institut für Neutronenphysik und Reaktortechnik

Juni 1995

Forschungszentrum Karlsruhe
Technik und Umwelt
Wissenschaftliche Berichte
FZKA 5590

Physics of Intense Light Ion Beams and Production of High Energy Density in Matter

Annual Report 1994

H.-J. Bluhm (Herausgeber)
Institut für Neutronenphysik und Reaktortechnik

Forschungszentrum Karlsruhe GmbH, Karlsruhe
1995

Forschungszentrum Karlsruhe GmbH
Postfach 3640, 76021 Karlsruhe

ISSN 0947-8620

Physik intensiver Strahlen leichter Ionen und Erzeugung hoher Energiedichten in Materie

Jahresbericht 1994

Zusammenfassung:

In dem Bericht werden die in 1994 erzielten Ergebnisse zum Arbeitsthema "Physik intensiver Ionenstrahlen und gepulster Plasmen" dargestellt. Insbesondere werden der Status des neuen 6 MV, 2 TW Impulsgenerators KALIF-HELIA, der Stand der Erzeugung und Fokussierung von Ionenstrahlen hoher Leistung und die numerischen Simulationen und Experimente zur Hydrodynamik der Strahl-Materie-Wechselwirkung beschrieben.

Abstract:

This report presents the results obtained in 1994 within the FZK-program on "Physics of intense ion beams and pulsed plasmas". It describes the present status of the 6 MV, 2 TW pulsed generator KALIF-HELIA, the production and focussing of high power ion beams and numerical simulations and experiments related to the hydrodynamics of beam matter interaction.

Physics of Intense Light Ion Beams and Production of High Energy Density in Matter

Annual Report 1994

Contents

IV. Target physics

I Program goals and summary of results

Program goals and summary of results

H. Bluhm, G. Keßler

I General goals

The main objectives of the intense light ion beam program at the Research Center Karlsruhe are:

1. To investigate and develop the physical and technical foundations for the production and focussing of intense light ion beams with single- or two-stage magnetically insulated vacuum diodes. We are heading for ion beam pulses with pulse durations around 50 ns and power levels around 1 TW which can be focussed to power densities above 1 TW/cm².

2. To produce transient states of high energy densities in matter through the interaction with intense light ion beams and to experimentally diagnose and theoretically model the properties of matter under extreme conditions. Here we strive for specific power depositions above 100 TW/g and for energy densities around 1 MJ/g.
   Besides making accessible a vastly unknown area in the phase diagram of matter the experiments serve to investigate fundamental problems of inertial confinement fusion driven by intense ion beams. Among these are the specific energy deposition of ions in hot dense matter, the stability of ablatively accelerated target layers, and the radiation transport in dense plasmas.

3. Together with these basic research areas we have been looking for industrial applications of the high voltage pulsed power technique which is the fundamental technique of our basic research program.

A brief summary of these applications will be given at the end of this report.

II Machines and pulsed power technique

The basic instrument of our research program is still the high voltage pulsed power generator KALIF which can deliver an electrical impulse of 50 ns duration with an amplitude of 1.7 MV at a power level of 1.0 TW to a matched load.
It has been decided in 1991 to upgrade KALIF with an additional 6 MV pulse line based on a magnetically insulated voltage adder with Metglas filled induction cavities (KALIF-HELIA). The main components of this extension had been completed end of 1993. However, because of delays in the preparation of its site KALIF-HELIA cannot be taken into operation before the end of 1996. *(W. Bauer et al., p. 5)*

Since many years our cooperation with the Institute for Electroenergy Systems and High Voltage Technique (IEH) at the University of Karlsruhe as well as with the Institute for High Voltage Technique (IHT) at the University of Braunschweig has helped to improve our understanding of pulsed power components and to optimize them. Presently the IEH investigates the performance of laser triggered gas switches and of Metglas cores under dynamic conditions, both important components in the new generator KALIF-HELIA.*(H. Frey, p. 15 ; H. König, p. 17)*

III Diode physics

The magnetically insulated proton beam diode in extraction geometry which has been developed for KALIF has produced proton beams with greater than 0.65 TW power which could be focussed to power densities around 1 TW/cm² (200 TW/g in matter). These results were achieved by using an actively generated proton source and by applying rather strong magnetic insulation fields ($V_{crit}/V = 3$).
To further enhance the ion beam power density in the focus we must increase the beam brightness and improve the reproducibility of the beam parameters. The beam brightness is mainly determined by the divergence angle which is imparted to the ions during their acceleration in the diode gap. Among the most important contributors to beam divergence are electromagnetic fluctuations due to instabilities of the electron sheath in the diode gap. A prerequisite for divergence reduction is to understand the nature and the dependability of the diode operating stability. Therefore, we have begun to investigate the dominating frequencies and the phase velocities of the electron sheath instabilities at different times into the pulse. Generally a qualitative agreement with code predictions has been found. It is our goal to measure all relevant fields and beam parameters in the diode gap, both, spatially and time resolved. For that end we have started the development of new spectroscopic and interferometric diagnostics. *(H. Bluhm et al., p. 18)*

To simulate the occurrence of electron sheath instabilities in the diode we are also developing a time dependent initially 2.5-dimensional (and in a later stage 3-dimensional) particle in cell code which solves the complete set of Lorentz-Maxwell-equations for realistic diode geometries. The code uses boundary fitted coordinates and takes advantage of the commercially available CAD-program Autocad to interactively generate the grid for technical geometries. *(E. Halter et al., p. 41)*

Complementary to the diode code development we have initiated the creation of improved analytic models that can describe the observed diode phenomena. This work is done in tight cooperation with the Kurchatov-Institute, Moscow. *(A. Grechikha, A. Gordeev, p. 34)*

Another important limitation of beam quality, diode operational stability and reproducibility can result from the properties of the anode plasma. Therefore, we have continued our effort to build a fast, low impedance high voltage pulse generator to drive the anode plasma discharge in a more controllable way. *(P. Hoppe'et al., p. 27)*

A further possibility to enhance the power density in the beam focus is to add a magnetic lens of short local length to the diode lens whose focal length is restricted to the order of the diode diameter. For that reason we have begun trajectory calculations to investigate and optimize the common action of both lenses taking into account the finite divergence and energy spread of our beams. It has been found that a reduction of the focal spot diameter by up to a factor of two can already be obtained with a simple one turn solenoid. *(W. Bauer et al., p. 58)*

An important application and extension of the experimental techniques and the theoretical tools developed within the intense ion beam program is the simulation of the divertor-plate-erosion during plasma disruptions in a Tokamak magnetic fusion reactor. A mitigating effect is expected from the formation of a vapor shield. Theoretical modeling of this vapor shield has shown that the heat-load of the divertor surface is mainly determined by radiation transport through the vapor cloud. To check the theoretical predictions an ion beam load of more than 10 MW/cm² is needed on the target for a duration of more than 40 μs. The particle energy should be less than 30 keV. *(F. Kappler et al. p. 124)*
PROFA has been built in cooperation with the Efremov Institute in St. Petersburg to explore the feasibility of such a device. In its present configuration with a multispark-anode PROFA produces proton pulses with 30 keV particle energies for pulse durations of 40 μs. The current density in the diode is around 40 mA/cm². Extrapolating the presently achieved data to a larger facility it seems likely that power densities of 10 MW/cm² can be obtained on the target for the required duration. *(V.Engelko et al. p. 64)*

IV Target physics

Important properties of the beam target interaction on KALIF like power density, specific energy deposition, ion-range, ablation pressure etc. can be inferred from the hydrodynamic response of 30 - 50 μm thick foils. The primary measurable quantity in these experiments is the rear surface velocity of the accelerated target. It is derived from the interferometric measurement of the Doppler-shift of laser light reflected from the target surface. *(K. Baumung et al., p. 73)*

In 1994 we have appreciably extended our diagnostic capabilities by developing a new type of laser-Doppler-velocimeter that allows spatially resolved measurements along a line of up to 10 mm length. With this instrument we have been able to measure for the first time the ablation pressure and the target velocity both spatially and time resolved. Thus we could check the planarity of shock waves in our targets, an important condition for the simple interpretation of the target experiments. The new diagnostic also enables us to investigate the growth of instabilities in ablatively accelerated target layers.*(K. Baumung et al., p. 88)*

To measure the central temperature in the targets heated by the intense ion beam from the KALIF-diode we plan to diagnose the K_α emission and absorption spectra which sensitively depend on the electron temperature. To measure these spectra with high resolution a crystal spectrometer has been built. To produce the intense soft x-ray back-lighter source for absorption spectroscopy a 10 J frequency doubled Nd-YAG laser system has been set up.*(G. Meisel et al.,* p. 95)

The interpretation of the measurements will be done with the target-code KATACO which calculates the temperature and density evolution of the ion beam heated target plasma. Atomic

level populations are computed by solving multilevel statistical equations self-consistently with the radiation field and the ion beam properties. To transport the K_α-lines through the target the non-LTE radiative transfer code NLTERT is used. The codes to generate the basic atomic data and to carry out the radiation transport calculations have been developed in tight cooperation with the University of Wisconsin. For the temperature range around 20 eV expected in the KALIF-experiments our calculations have shown that Na and F deliver the most sensitive K_α-spectra. *(B. Goel et al., p. 99)*
Combining the laser-generated backlighter source with the planar ion beam heated target foils also enables us to measure opacities in dense plasmas.

In a very fruitful cooperation with the Institute of Chemical Physics in Chernogolovka we have also performed dynamic tensile strength measurements on single crystals and other solids at hitherto unreached strain rates of up to 10^8/s. *(K. Baumung et al., p. 82)*

V Industrial applications

Until today the most successful industrial application that rose from our program is the use of the pulsed electron beam from a channel spark discharge for the deposition of thin layers of different composition. The unique feature of this deposition technique is that due to the deep penetration of the electron beam into the target material it ablates in very small droplets and largely conserves its stoichiometry. Thus it has been possible to deposit teflon and hydroxil-apatit as well as glass.
In 1994 several contracts have been signed with vendors of deposition techniques as well as with applicants.
Together with Russian Institutes in Tomsk, Jekaterinenburg and St. Petersburg we have initiated the construction of several small pulsed power machines with repetition rate capabilities for large area surface treatment with electron beams, nanopowder production and compression, and fragmentation of solids. Very recently the fragmentation device which runs at 5 Hz has been successfully taken into operation.
A summary of possible industrial applications of pulsed power techniques is given on page . *(H. Bluhm, p. 139)*

II Machines and pulsed power technique

Status of KALIF-HELIA and data acquisition

W. Bauer, H. Bluhm, P. Hoppé, J. Marek, H. Massier, D. Rusch - INR
A. Grünhagen, W. Reeb - HIT
K. Leber, W. Ratajczak - HVT

This report describes the status of design and fabrication of components for the 6 MV, 2.4 TW high energy linear induction accelerator KALIF-HELIA. Especially the physical and mechanical layout of the magnetically insulated vacuum voltage adder is discussed. In addition the main features of the newly developed data acquisition system are presented.

I. Introduction

KALIF-HELIA is a new pulse forming network supplementary to the presently existing coaxial pulse-line of KALIF. It has been designed to deliver a 6 MV, 400 kA electrical impulse of 50 ns duration to a vacuum ion diode. Its main purpose is to produce stiffer ion beams with higher particle energy and larger mass which are less susceptible to deflections by beam selffields and to aberrations of the focussing systems.

KALIF-HELIA uses the same Marx-generator as KALIF to charge 4 intermediate storage water capacitors which are switched out through 4 laser triggered gas switches into a pulse forming and distribution network of 12, nominally 1 MV coaxial lines. Two at a time of the 5.53 Ω pulse forming lines simultaneously drive a toroidal cavity. To symmetrize the current flow in the cavity an azimuthal distribution network is used. Through this distribution network the 1 MV pulses are finally delivered to a 4.45 cm circumferential feed gap. The cavities contain ferromagnetic laminated Vitrovac cores to provide the inductive insulation necessary for voltage addition. Six cavities are connected in series (Fig. 1) to add the voltage pulses on a self-magnetically insulated transmission line (MITL) /1/ to a sum of 6 MV. This pulse is directly applied to the vacuum ion diode.
KALIF-HELIA has been designed by Pulse Science Incorporated (PSI). PSI shall also be responsible for the function of the KALIF-HELIA-system in total. Because of budget constraints we had to split the fabrication of parts between PSI and FZK and to stretch it over several years. The machine was ordered in 1991 and scheduled to start operation in 1994. The intermediate storage capacitors, the pulse forming network and the cavities were built and delivered by PSI before the end of 1993. Also the ferromagnetic cores fabricated by Vakuumschmelze Hanau had been completed before that date. The status of the components to be designed and constructed by FZK is described in section III. However, the date for completion of the machine is determined by the progress in preparing the site.
In 1993 the former TEKO-hall was finally assigned to accommodate KALIF and KALIF-HELIA and applications for the building budget were written. In 1994 the necessary documents have been worked out and sent to the financial authorities for examination. After formal examination which has not yet been completed (March 1995) we need the final approval from the ministry of education and research (BMBF). Despite this tedious procedure we hope to begin with the preparation of the site in the second half of 1995. Operation of KALIF-HELIA is then expected at the beginning of 1997.

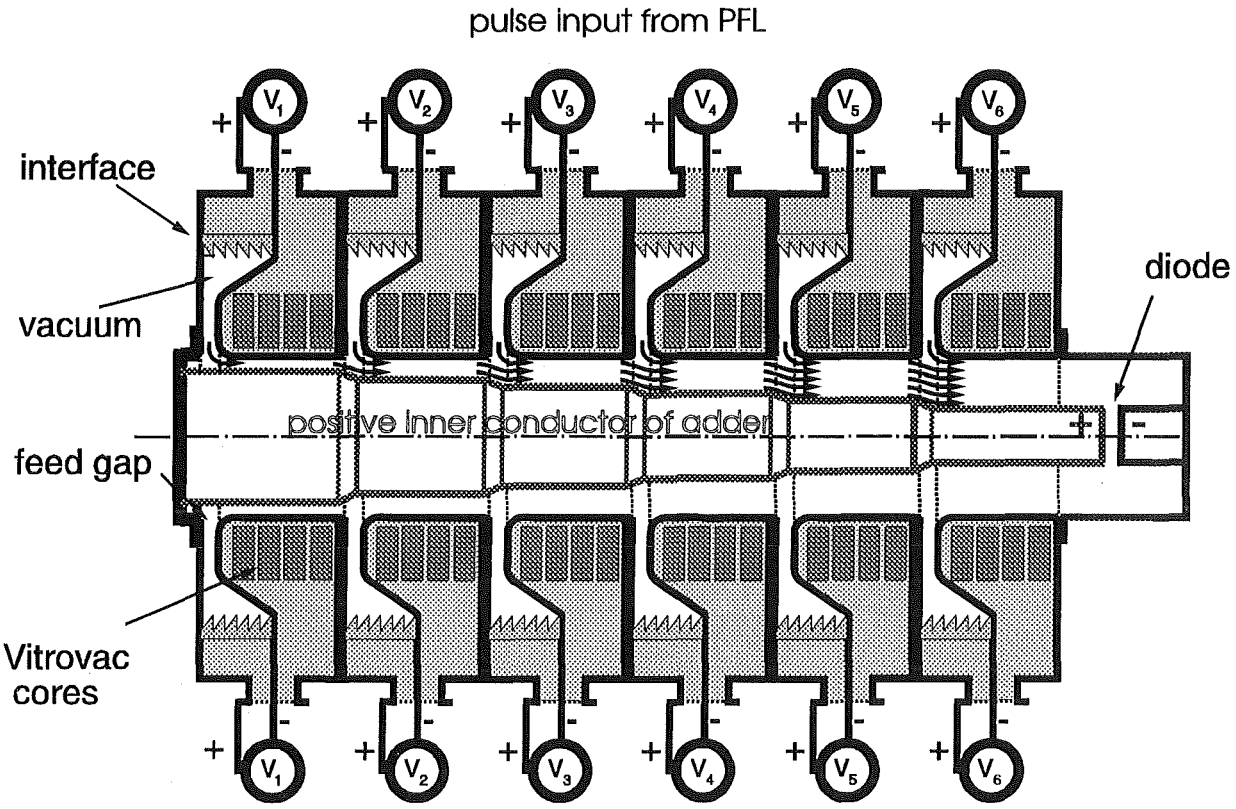

Fig. 1: Schematic of the KALIF-HELIA magnetically insulated voltage adder

II. Summary of component fabrication in 1994

Since it became obvious in 1992 that we would not get the budget and the building permit for preparing the KALIF-hall before 1994 we decided also to stretch the design and fabrication of components in our responsibility over a longer period. At the end of 1994 the status of component construction was as follows:

1.Auxiliary system: The storage and distribution facilities for oil, water and gases are being designed in 1994 and 1995. The distribution of electric power is an integral part of the reconstruction of the building. All new vacuum components have been ordered and delivered according to the specifications of PSI. Fig. 2 gives an impression of the machine and its auxiliary systems.

2.Intermediate store tank: This oil tank with dimensions of 5 x 5 x 5 m^3 is built to house the 4 intermediate store capacitors. It was designed during 1993 and early 1994 and was ordered in July 1994. We expect its delivery in early 1995. There remains little design work to be done for the support of the intermediate water lines and for the high voltage feeds which shall be completed early 1995.

3.Support systems: The proper positioning of the following main components relative to the intermediate store tank must be assured by this support system: the 6 adder cells, the 12 pulse forming lines and the vacuum vessels on both sides of the adder. In addition it has to enable the handling, maintenance and assembly e.g. of the 5.5 m long inner conductor to the cells. Yet, the experimental area needed in front of the diode should not be occupied by support posts. Actually the design of this support system was completed and orders will be placed before the

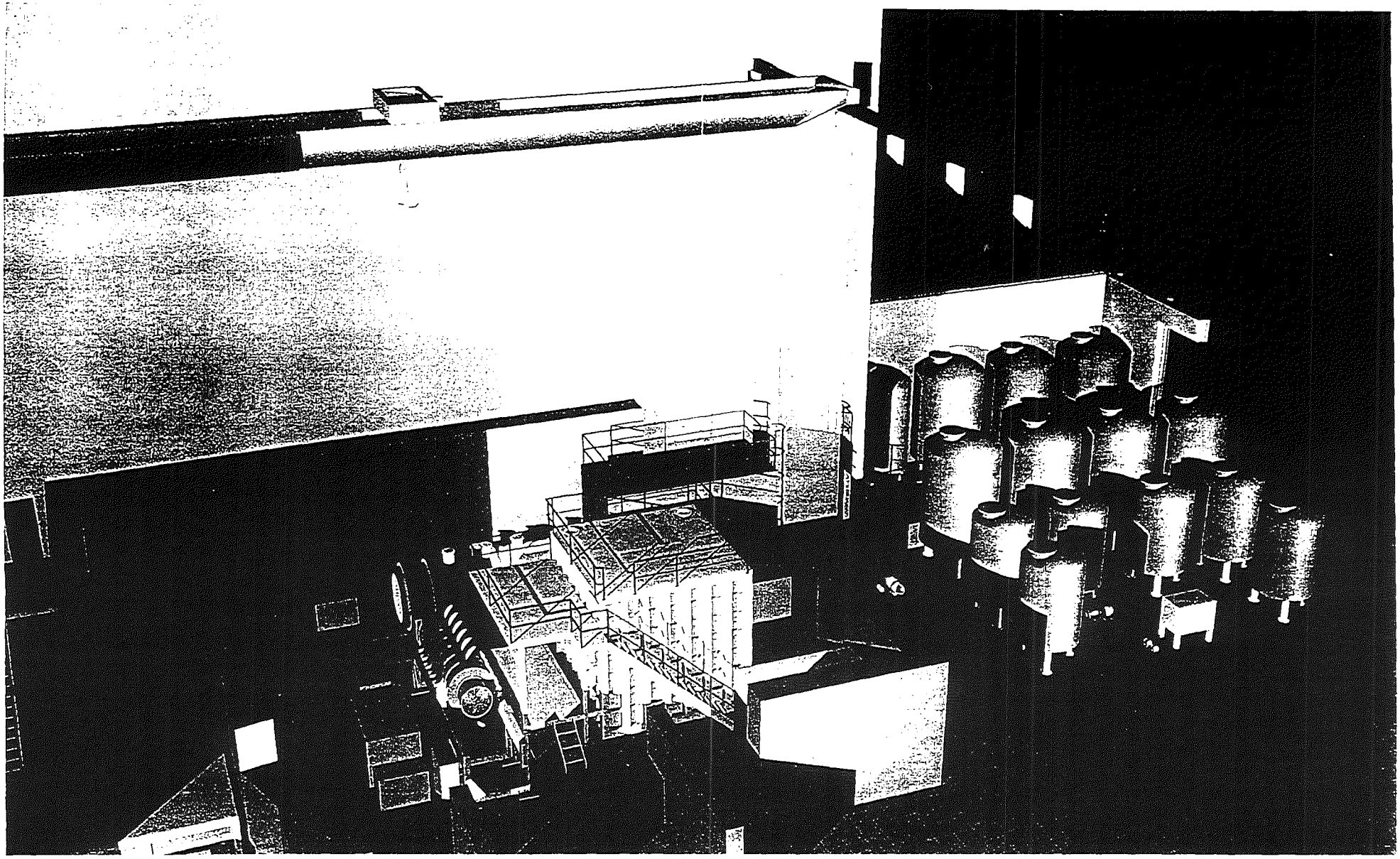

Fig. 2: KALIF and KALIF-HELIA installation at the new site. The cubic tank in the foreground contains the intermediate storage water capacitors of KALIF-HELIA. The voltage adder is located on the left side of that tank. In the background the old KALIF pulse line and the Marx generator are to be seen. The oil/water storage tanks are located on the right hand side of the drawing.

end of March 95. The delivery and the test assembly of the support system is foreseen before end of 1995.

4.Gas-switch laser triggering: The 4 gas switches which deliver the energy from the intermediate store capacitors to the transmission lines will be triggered by a UV laser pulse of about 30 mJ pulse energy each to obtain a low jitter. We chose a KrF-Excimer laser with unstable optics, a pulse energy of 200 mJ, and a pulse duration of 30 ns for this task. The laser and all major components (gas-supply, shielded cabin, optical table) have been delivered; the optical components are ordered and are due early in 1995. In 1995 it is planned to set up the optical path in the laboratory and to test its operation. In addition in 1995 the connection through the tank wall and to the switches as well as the optical path along KALIF-HELIA will be designed and fabricated.

5.Magnetically insulated transmission line and vacuum chamber: The detailed physical and mechanical design is in progress (see section III). Fabrication will take place in 1995 and early 1996.

6.Instrumentation and data acquisition: The required instrumentation for the control of the pulse forming lines and the adder cells was delivered by PSI. The monitors necessary for the measurement of the energy flow in the MITL are under development. More details on the data acquisition systems are described in V.

In summary it can be stated, that all components of KALIF-HELIA will be available before mid of 1996, when the hall is expected to be ready for machine installation.

III. Physical design of the magnetically insulated voltage adder

The series addition of voltage pulses occurs on a self-magnetically insulated vacuum transmission line (MITL) formed by the inner surface of the cavities and a centered anode stalk (Fig. 1). The anode stalk dimensions have to be chosen such that each cavity driver will deliver the same voltage and current to the MITL. This "balanced" system operation is achieved if the anode stalk decreases stepwise in radius toward the end of the adder in such a way that the operating impedance of the k-th segment is equal to $Z_k = k\ Z_1$, where Z_1 is the effective load impedance seen by the first and by all other cavities. The operating voltage on each MITL-segment is then $V_k = k\ V_1$, where V_1 is the output voltage across each cavity feed gap. The main difficulty in designing such a system results from the fact that due to the presence of free electrons streeming in the vacuum-gap between the inner and outer conductor of the MITL the actual operating impedance of each segment depends on the segment voltage and total current.

Maximum power is delivered to the adder if Z_1 becomes equal to the effective generator impedance R_g. Simulating the pulse forming and distribution network of KALIF-HELIA with the transmission line code LEITER /2/ shows that it can be approximated by a Thevenin equivalent source with an open circuit voltage $V_0 = 1.4$ VPFL and an impedance R_g of 5.55 Ω. Charging the PFL to 2.2 MV - which requires a Marx voltage of 90 kV - V_o reaches 3.0 MV and has the shape shown in Fig. 3. The feed gap output voltage is then given by $V_1 = V_o\ Z_1/(Z_1 + R_g)$. Using the equivalent source approximation the adder of KALIF-HELIA

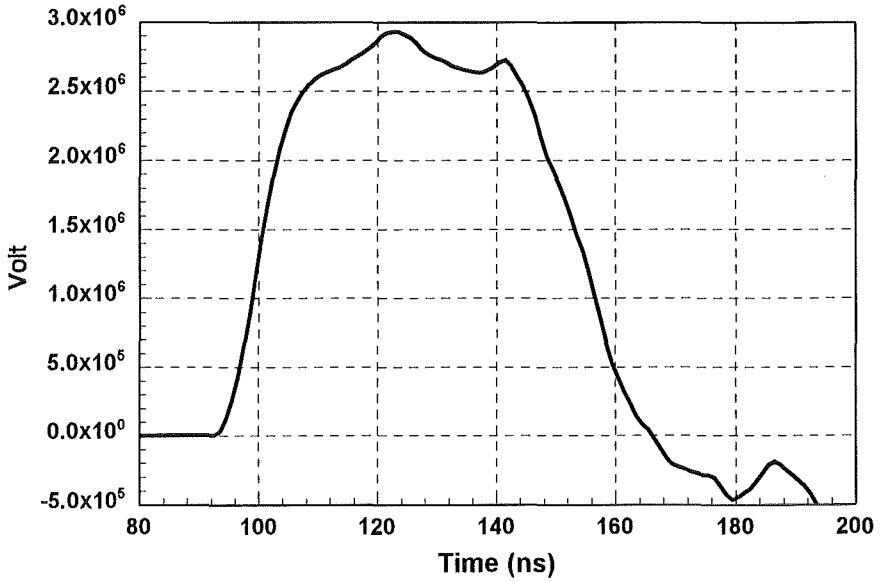

Fig. 3 Open circuit voltage of the KALIF-HELIA pulse forming network at the cavity feed gaps

can be represented by the circuit elements shown in Fig. 4. Here additional delay lines have been introduced between the sources and the feed points to compensate for the wave transit times along the adder. A maximum power of 2.6 TW and a load voltage of 9 MV could be obtained for $Z_1 = R_g$. However, to stay below the safe operating limits of the cavities V_1 should not exceed 1.1 MV, i.e. Z_1 must remain below 3.1 Ω. In this case the line current is 355 kA and the maximum power at the load reaches 2.34 TW. A load connected to the end of the adder should have an effective impedance of 18.6 Ω. Of course, this must also be the

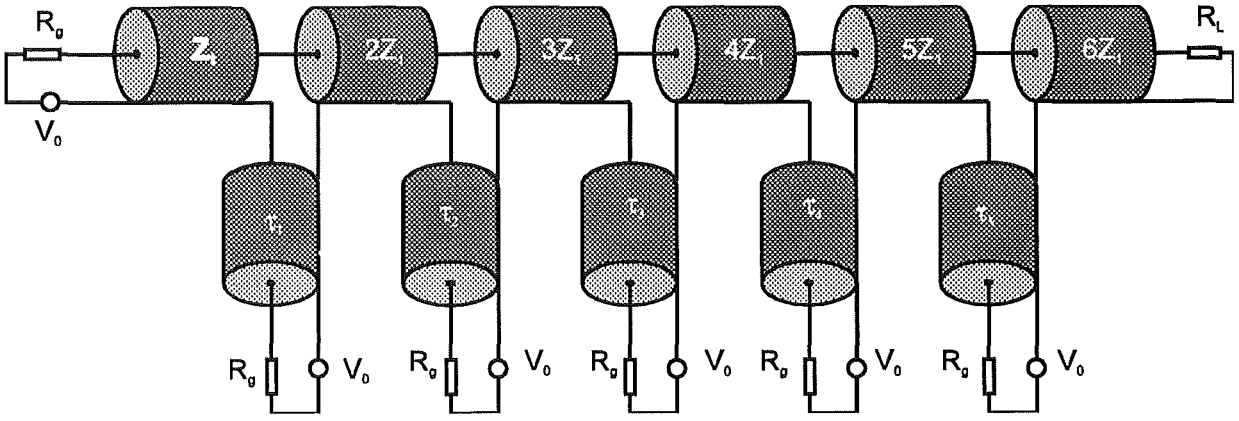

Fig. 4 Circuit configuration used in LEITER to calculate the pulse addition.

operating impedance of the last MITL segment. To calculate the corresponding vacuum impedance we need a suitable physical model of the MITL. For all that we have to consider that the adder of KALIF-HELIA operates in the selflimited mode for less than 24 ns. After that the current in the MITL is determined by the load. A smooth transition from selflimited to load dominated operation is achieved if the load current becomes equal to the selflimited current.

For the positive polarity configuration of the KALIF-HELIA adder, the laminar electron flow model /3/ is only valid for the first MITL segment. Each segment contributes its own electron group to the flow with a particular energy and angular momentum spread. At the end of the adder the different electron groups mix and fill up the entire gap.

A coarse model derived from a simple pressure balance and based on the assumption of constant electron density exists for this so called full gap flow (FGF) /4/. Within this model a simple relationship between the line voltage V_l and the anode - and cathode current I_A and I_C is obtained:

$$V_l = \frac{Z_V}{2}\sqrt{I_A^2 - I_C^2}$$

where Z_V is the vacuum impedance of the line and (I_A - I_C) represents the electron sheath current. For the effective operation of an ion diode the ratio (I_A - I_C)/I_A must be small since only the wall current can be converted into ion current. Accepting a value of 0.5 for this ratio and choosing I_A = 355 kA we calculate for the vacuum impedance of the last adder section Z_V = 42 Ω . From the laminar flow model we obtain Z_V = 6 Ω for the first section. Interpolating between these values we derive the vacuum impedances and the corresponding diameters of the adder stalk listed in the 2nd and 3rd column of Table 1.

Segment	Z_V (1)[Ω]	D_i (1) [mm]	Z_V (2) [Ω]	D_i(2) [mm]
1	6	344	6	344
2	13.2	305	12	311
3	20.4	281	18	281
4	27.6	240	24	255
5	34.8	213	30	230
6	42	189	36	208.5

Table 1 Impedances and inner diameters of the adder segments

Some experiments have shown that a quite effective operation of the positive polarity adder is already obtained for $Z_V = 2\ Z_{operation}$. The segment impedances and diameters corresponding to this observation are listed in columns 4 and 5 of Table 1. Since our main goal with KALIF-HELIA is to achieve a high accelerating voltage we shall construct both adder configurations and investigate their performance as a function of load impedance during the start up experimental program of the machine.

IV. Mechanical design of the voltage adder

Under operating conditions the inner conductor of KALIF-HELIA with its length of about 5.5 m must be cantilevered at the ground side of the first induction cell (see Fig.1 and point A in Fig.5). The opposite free end which carries the anode is at high voltage of up to 6 MV. Bending of the inner conductor will occur due to its own weight (determined essentially by the tube wall thickness required for x-ray shielding) and the weight P of the anode components (up to 200 N). This deformation causes azimuthal impedance variations and anode/cathode miss-alignments. In the design foreseen for KALIF-HELIA the anode/cathode alignment can be adjusted by a counter force applied to the extension tube of the inner conductor (point B in Fig. 5) with point A as the center of rotation. By calculation of the mechanical deformations of the inner conductor the following items were investigated:

- the force necessary for realignment and that effective at the rotation center A,
- the impedance variations,

- the maximum charge allowed by the $\sigma_{0.2}$ = 220 MPa limit of stainless steel.

This deformation calculation was performed with the code ABAQUS [5] resolving the inner conductor by 400 finite elements /5/. To cover the uncertainties in the selection of the adder impedance (see sect. III) two sets of diameters of the inner conductor were considered (Tab. 1). The calculated deformations for the higher impedance version (column 2 in Table 1) are depicted in Fig. 5 for the following 3 cases:

- with the inner conductor cantilevered at point A. In this case the anode center will be 6 mm below the cathode center.
- with a counter-force of 16000 N at point B to align the anode relative to the cathode. Here the maximum azimuthal impedance variation is below 1 %.
- with the inner conductor in its proper mounting position, i.e. supported at its high voltage end. The opposite extension tube end will then be 18 to 19 mm out of axis.

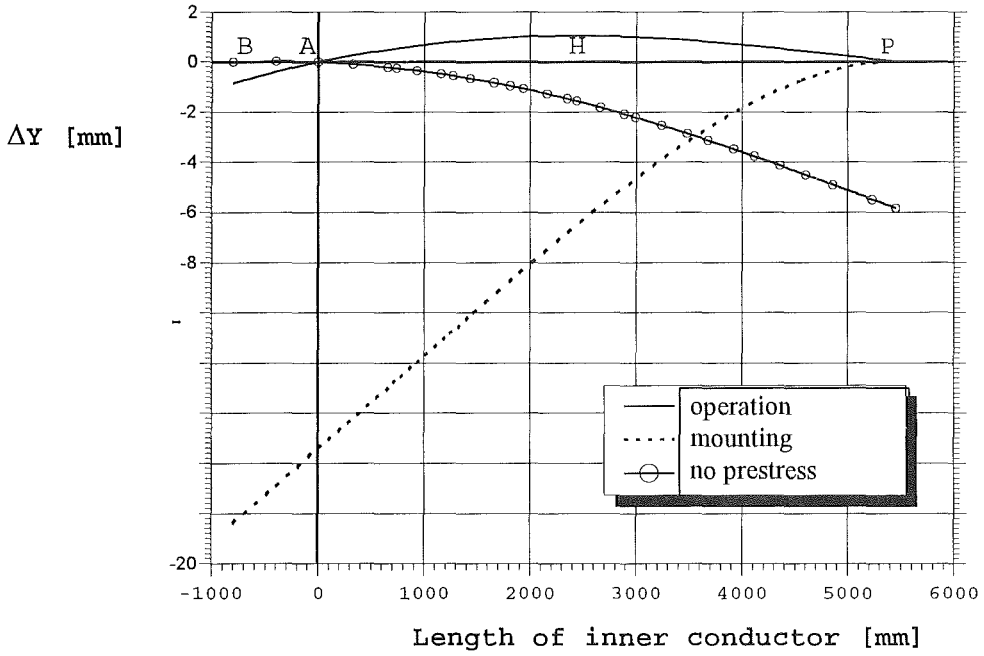

Fig. 5:Deformations of the high impedance version(columns 2, 3 in Tab. 1) of the inner conductor for operating , mounting, and unprestressed conditions.

All calculated mechanical stresses are far below the $\sigma_{0.2}$ limits which might be reached only when the anode weight is increased to about 20 000 N.

For the mechanically stronger low impedance version the calculations gave somewhat smaller deformations. It therefore can be concluded, that the alignment of any inner conductor with dimensions similar to that of that in Tab. 1 version should not disturb the symmetry of the power flow to the diode. The limits for stress/strain in the stainless steel will certainly not be reached by the mechanical load due to the weight of the anode or shielding components.

V. The new data acquisition and evaluation system

A new data acquisition software is under development which shall replace the existing one based on the HP-1000 minicomputer, presumably before installation of KALIF and KALIF-HELIA at the new site. We would like to keep the genuine merits of the old system i.e. its basic concepts for programs and handling of the data acquisition. The following short list describes the presently available programs and their purpose:

ZUSTA	stores the settings of up to 25 digitizers and oscilloscopes of 4 different types and the properties of up to 70 measurement probes
EVA	controls the measurement devices based on the data entered in ZUSTA,and the recording of raw data
ADAM	evaluates the raw data with taylored operators, produces simple graphics and generates evaluated data files for further use, e.g. in reports and publications. Repeated use of the same evaluation procedure is possible through storage of the evaluation file
FOTO	is applied to digitize oscilloscope photographs, but is also used as a means to bring data from other diagrams into the ADAM evaluation
EICHD	is employed to calibrate Tektronix type 7912 AD transient digitizers by interactive adjustment of the grid
LEITER	carries out electrical network calculations based on a transmission line algorithm to interpret measurements, and investigate consistency of data
BUNCH	calculates changes of the ion beam pulse shape along the flight path due to ion velocity variations
IODA	is an image analysis system to automatically count the ion tracks on irradiated ion sensitive films
HOSEA	evaluates image data from the IODA system numerically and generates contour plots

In the final development stage of the old system the HP-1000 computer users could connect personal computers (PCs) with emulated terminals to this host via the local area network (LAN) and evaluate data from any office. Data were acquired on the central computer only. In the new system the central computer ("server") will have two main tasks: the network administation and the main storage for the experimental raw data. The network software allows to link storage locations of the server as "virtual" drives to the individual PCs and evaluation can take place without explicitely transferring files from one computer to the other. Any PC in this system can acquire measurement data and transfer them to the server. Thus data acquisition is not restricted to a single location. At present, in the development phase, two PCs are equipped with interfaces to interact with measurement devices such as transient digitizers.

By choosing PCs as the main devices of the new system a failure in one part of the system is less fatal than before, because any PC can rapidly be exchanged and the LAN may fail without blocking the data acquisition, because the raw data will first be stored on the hard disc of the PC at the measurement place and only subsequently be transferred to the server.

PCs are used because they are cheap and a wide choice of commercially available programs for standard tasks exists, especially for the Windows surface. Only programs for special tasks in the data acquisition need to be self-written. A first version of the new data acquisition program EVA is operating and the necessary complement ADAM for evaluation is being written. Since both programs deal mostly with selection and logical problems they are written in Microsoft Visual Basic 3.0 to render the program with Windows surface properties more suited for intuitive use. The new ZUSTA data base is formatted as a text file with keywords for its main properties and therefore it can be adapted to any new demand.

Visual Basic 3.0 might not be suited for fast numerical work and therefore the network program LEITER was adapted for use on a PC by rewriting it in the new Microsoft 32-bit "Power Fortran", Version 1.0.

With the new generation of transient digitizers the number of measurement channels increased considerably: Tektronix type TDS 640 with 4 channels, and TLS 216 with 16 channels are now available. The number of 11 Tektronix 7912 AD transient digitizers(600 MHz Bandwidth) has been complemented by two of its faster successor, SCD 5000 (5GHz Bandwidth). At present there are about 60 signal channels and more will be needed for KALIF-HELIA. The acquisition and evaluation of the data requires careful administration of signal paths and properties of the measurement channels. The properties of signal probes, cables, passive networks, as well as the informations on the transient digitizer settings must be retrievable. Consequently the format of the new data base is open to expansion.
The problem of combining numerically two ore more signals, e.g. $S_1(t)$, $S_2(t)$, or $V(t)$ and $i(t)$ etc., such as

$$S_{tot}(t) = S_1(t) + S_2(t), \quad \text{or} \quad {}_{diode}(t) = V_{interface}(t) - L \cdot \frac{di}{dt}, \quad \text{or} \quad i(t) = \frac{1}{L} \cdot \int_0^t V(\tau)\, d\tau$$

or $S = S_1(t)$ up to a certain condition and then $S = S_2(t)$

require that the data be on the same discretized time scale. Therefore, operators for selection and interpolation must be available which take into account the various conditions of the time scales.

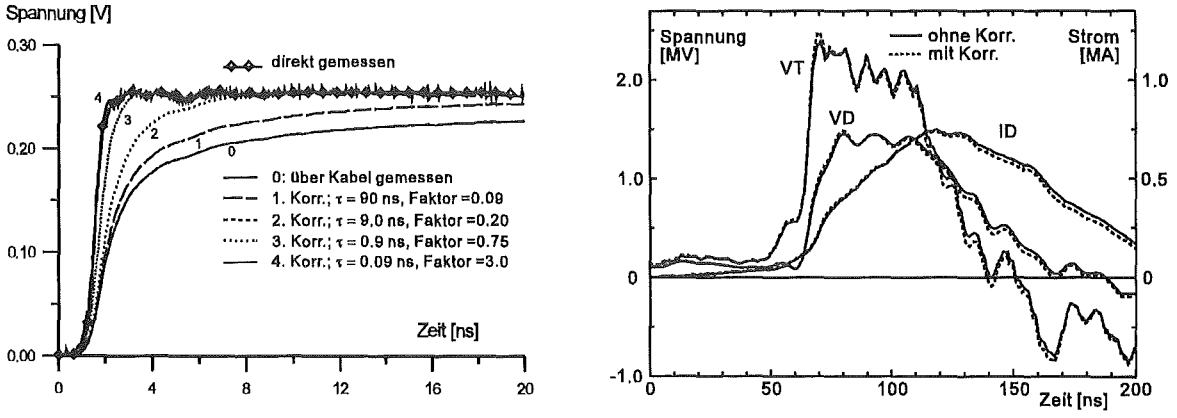

Fig. 6: Correction of signal attenution in cables and effect on the residual error in the voltage and current measurements at the diode.

A new item is the correction of cable attenuation. The operator for this task uses a set of time constants and factors characteristic for the cable. But the operator is not universal: its parameters have to be determined for the time measurement on the real recording settings of the digitizer. Fig. 6 shows an example of such a correction and its effect on evaluated data.

Another effect which has to be cosidered in the measurement of high frequency instabilities in diodes is the nonideal digitization process in transient digitizers of the scan converter type. Even on the newest types neither the claimed channel width can be taken for granted nor is the channel width constant over the measuring interval. Fig. 7 demonstrates the effect on a calibrated new device.

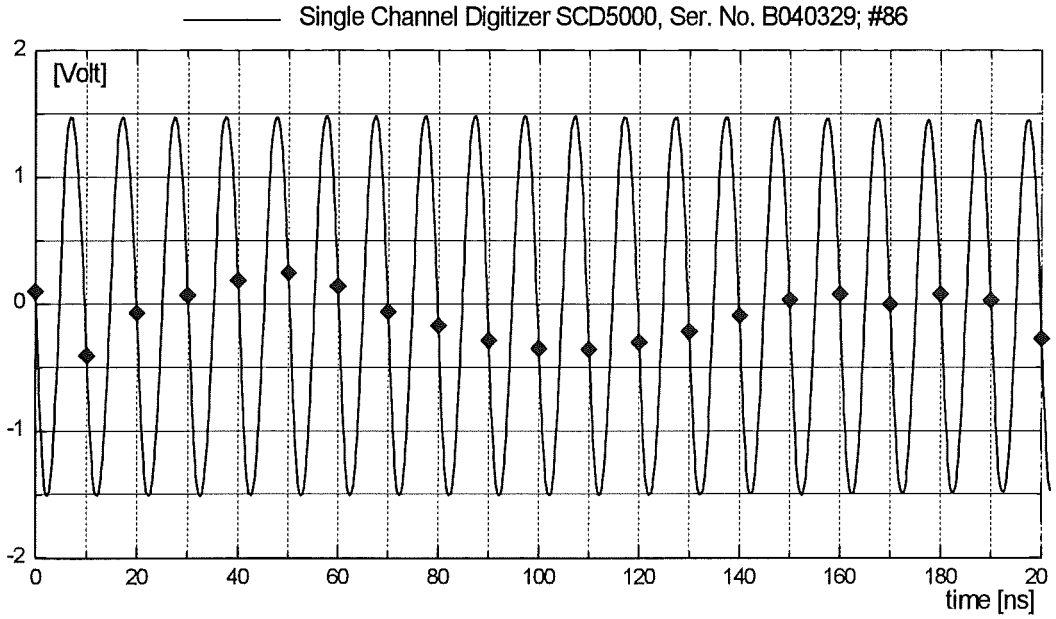

Fig. 7: Residual nonlinearity of the time scale of a scan converter type transient digitizer, demonstrated by marking the grid crossings of a 100 MHz sine wave. The time channel width has been readjusted to yield the correct average. The new channel width is 1.009 times greater than the value given by the calibrated instrument in its output data file. This residual nonlinearity is different for each instrument and has to be eliminated for corellated high resolution measurements.

References

/1/ J.J. Ramirez, K.R. Prestwich, I.D. Smith, Proc. of the IEEE, Vol. 80, 946 (1992)
/27 D. Rusch, interner Bericht (1995), unveröffentlicht
/3/ J.M. Creedon, Journ. of Appl. Phys. Vol. 46, 2946 (1975)
/4/ S.E. Rosenthal, IEEE Trans. on Plasma Science, Vol. 19, 822 (1991)
/5/ A. Grünhagen, P. Hoppé, J. Marek, interner Bericht (1995), unveröffentlicht

The Multichannel Discharge of Laser-Triggered Rail-Gaps

W. Frey, University of Karlsruhe

Because of their low inductance and line-type switching, laser-triggered rail-gap switches can significantly improve the output-pulse fidelity of water-insulated pulsed-power generators, e.g. parallel-plate Blumlein-generators. Operating in the multichannel mode, the low current density on the rail-gap's electrode surface reduces electrode erosion and increases the lifetime. Due to the limited trigger-laser energy in distributed pulsed-power facilities a low intensity triggering with sub-nanosecond jitter is desired.

The rail-gap with its 40 cm brass electrodes uses a mixture of Argon and SF_6 as switching-gas. As a characteristic of the switch inductance, the generator's output-pulse risetime declines with increasing SF_6-concentration, and the rail-gap is triggered at high overvoltages V_T/V_{DC}, Fig. 1. V_{DC} denotes the DC-breakdown voltage of the rail-gap.

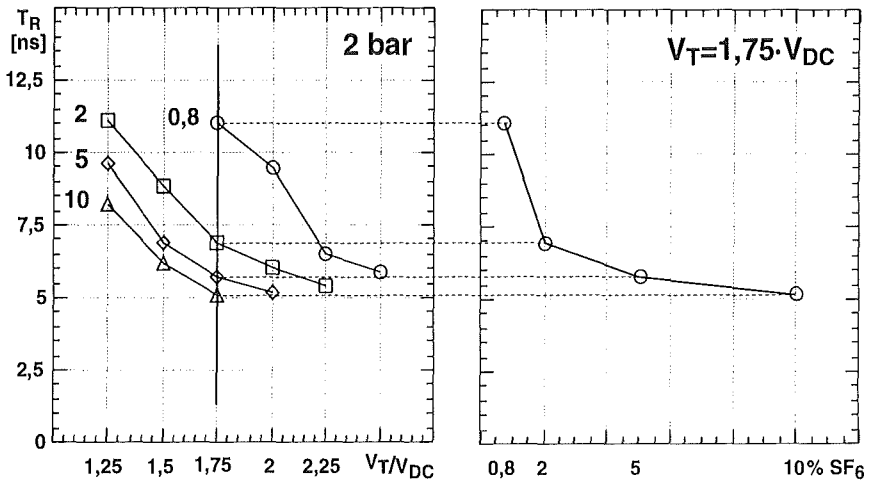

Fig. 1: Impulse risetime of the Blumlein generator versus trigger voltage and SF_6-concentration, right.

Contrary to previous assumptions, the impulse risetime does not depend on the number of spark channels alone. Although the total number of channels decreases, Fig. 2, the impulse risetime improves. The observation of the multichannel discharge by means of a CCD linear image sensor and the classification of the channels by computer image processing into „bright", „medium" and „weak" reveals a correlation between „bright" channels, i.e. the ones initiated first, and risetime.

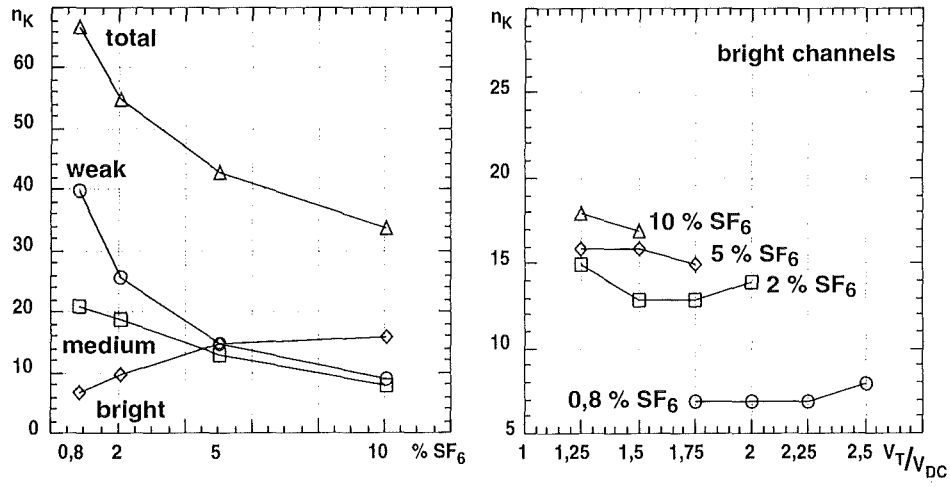

Fig. 2: Spark channels of different luminosity versus standardized trigger voltage V_T/V_{DC}, right.

Due to the constant value of "bright" channels versus trigger voltage, the output-pulse risetime T_R also depends on the closure-time jitter between the channels.

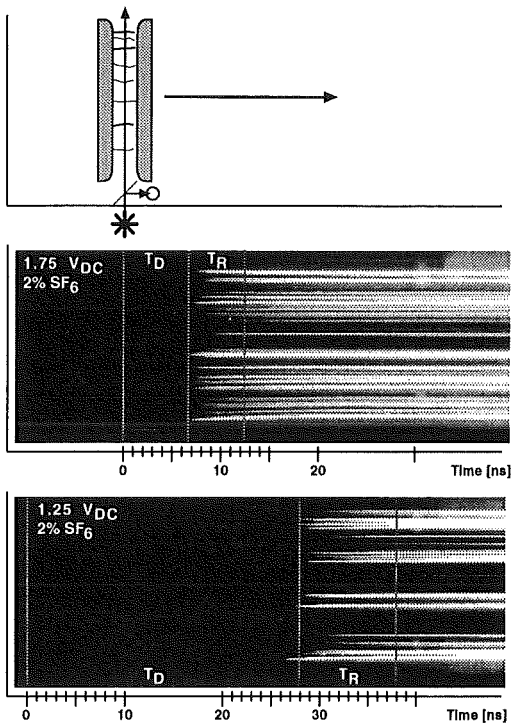

Fig. 3: Streak photographs of the multichannel discharge at different trigger voltages.

Streak photographs, recorded with an IMACON 790, prove that the closure-time jitter reduces when triggering the rail-gap at high overvoltages. "Weak" luminous channels are initiated later than "bright" channels.

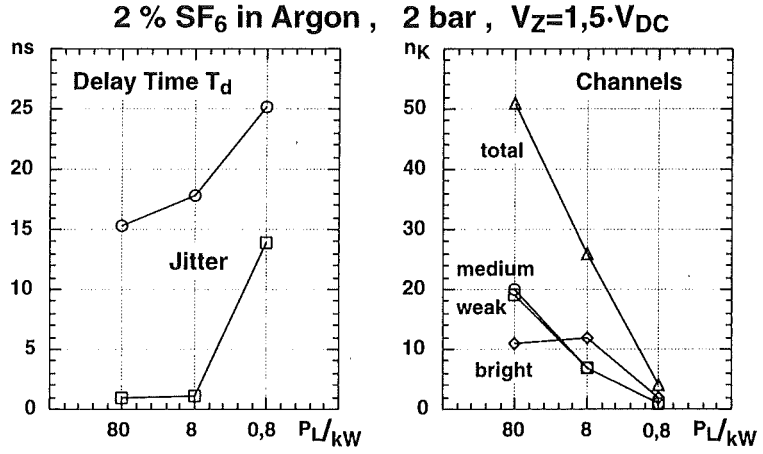

Fig. 4: Laser intensity and rail-gap performance.

At reduced laser-beam intensities a satisfactory multichanneling with bright channels appears at a minimum Nitrogen-laser peak-power of P_L = 8kW, Fig. 4. Due to reduction of laser energy, first the number of "medium" and "weak" channels decreases, indicating that the channels initiated later are generated by laser radiation and not by ionizing radiation from channels already alight.

Using a gas-mix of 2% SF_6 balance Argon the jitter amounts to 1.1 ns. Best jitter results of less than 500 ps are achieved at a 10 % SF_6-concentration and high overvoltages.

For further information contact author by e-mail: frey@ieh.etec.uni-karlsruhe.de

Fast Change of Magnetic Flux in Amorphous Strip-Wound Cores

S . K ö n i g , University of Karlsruhe

Amorphous softmagnetic strip-wound cores are commonly used in pulsed-power applications for ferromagnetic isolation in *Linear Induction Accelerators* and for *magnetic switching* in pulse compression circuits.

Concerning magnetic switching the change of core inductance is used when the magnetization curve changes from the upright to the horizontal part of the hysteresis loop. An impulse-like current in comparison to the small current during the period of core magnetization may flow after saturation of the core. This represents the change-over of a magnetic switch from high impedance to low impedance. The big strip-wound cores used for ferromagnetic isolation must not get to this point of saturation, because they have to ensure isolation of the single stages of Linear Induction Accelerators within the main pulse duration of $t \approx 50\,\mathrm{ns}$.

The cores used for these applications are made of 25µm thick amorphous softmagnetic alloys on Fe-base (e.g. *VITROVAC 7600Z*) with a saturation flux density of $B_S = 1{,}75\,\mathrm{T}$ wound with a 6µm Mylar® interlaminar polyester isolation to reduce eddy-currents.

For exploration duties on small amorphous softmagnetic strip-wound cores with a voltage-time product of about 1,8mVs a complete test circuit is built to drive the core from negative remanence to positive saturation within several 10ns. To receive this high value of $dB/dt \approx 50\,T/\mu\mathrm{s}$ impressed high voltages are necessary. The used test equipment consists of a water-insulated coaxial pulseforming line, a gas-isolated mounting device for the strip-wound core and an electrolytic load to absorb the arriving output-pulse without almost any reflections. All parts except the load circuit have a coaxial geometry and a modular structure to ensure homogenous wave propagation and to have the possibility to use reliable and tested *ns*-measurement techniques for voltage and current.

The pulseforming line with a surge impedance of $Z = 5{,}5\,\Omega$ shapes a rectangle voltage impulse with $U = 70\,\mathrm{kV}$ and $t_{\mathrm{FWHM}} = 42\,\mathrm{ns}$ or 84ns. Capacitive sensors for voltage measurements and *Rogowski*-coils for current measurements used with fast digitizing oszilloscopes (*TDS 640:* 2GS/s and 500MHz) facilitate measurements with true signal courses. Both types of measuring systems are placed in the outerconductor of the pulseforming or transmission line.

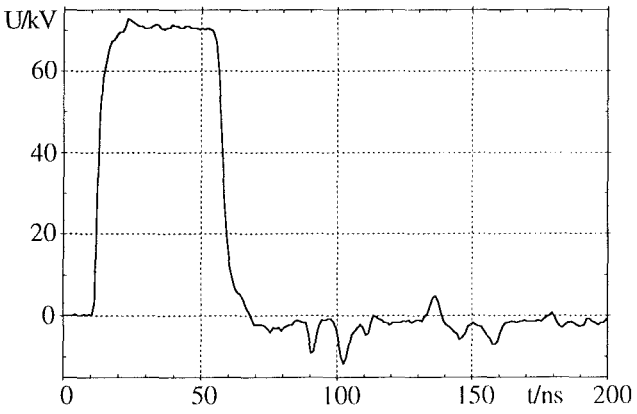

Fig. 1: Voltage output impulse of coaxial pulseforming line

Fig. 1 displays a voltage measurement in the transmission line with connected core mounting device (without a strip-wound core) and electrolytic load. It demonstrates the expected signal course with hardly any reflections of the mounting device and the load.

For further information contact author by e-mail: koenig@ieh.etec.uni-karlsruhe.de

III Production and focussing of high power light ion beams (Diode Physics)

Stability and operating characteristics of the applied B proton extraction diode on KALIF

H. Bluhm, P. Hoppe', H. Bachmann, W. Bauer,
K. Baumung, L. Buth, H. Laqua, A. Ludmirski,
D. Rusch, O. Stoltz, S. Yoo

Abstract

In this contribution we describe detailed investigations of the stability and operating characteristics of a magnetically insulated proton beam diode in extraction geometry developed for the 1 TW, 1.7 MV pulsed power generator KALIF. From an analysis of ion current density fluctuations the frequency spectrum of predominant instabilities has been determined. Although late in the pulse the main frequencies (1.2 GHz) are higher than expected they are compatible with an ion transit time mode. At maximum diode accelerating voltage a parallel load current occurs in the diode which grows at the cost of the useful ion current and absorbs part of the pulse energy. We report on observations that are related to the origin and to the physical nature of the parallel load.

Introduction

The magnetically insulated proton beam diode in extraction geometry developed for the 1 TW, 1.7 MV pulsed power generator KALIF has produced proton beams with greater than 0.65 TW power. The quality of these beams was sufficient to focus them to power densities around 1 TW/cm^2. These results were achieved by using an actively generated proton source and by applying rather strong magnetic insulation fields (Vcrit/V $\geq$ 3). This resulted in a good diode coupling to the generator, a high ion beam production efficiency and a high beam purity. Both, the ion diode and the anode plasma source have been described extensively in the literature /1, 2/. The diode and its main current monitors are presented in Fig. 1. The anode plasma is produced by diverting a small fraction of the generator current early in the pulse through a thin Pd-covered TiH-film deposited on a 0.5 mm thick insulating layer. This is achieved with the help of a plasma opening switch (POS) and a low impedance bypass line. The current heats the film, desorbs the hydrogen from the TiH-reservoir and creates a voltage drop which finally breaks
down the desorbed gas layer and creates a rather uniform hydrogen plasma. The cathode is a thin stainless steel cone with an edge protruding into the acceleration gap. Although it is intended to emit electrons mainly from the cathode tip into the diode gap, it is conceivable that part of the electrons forming the cathode sheath, which strongly influences the diode operation, originate from the POS region in the power feed. The insulating magnetic field of up to 3 T is created with a pair of concentric coils. Inside the cathode cone a current shunt has been integrated into the base plate. Since only a weak electron loss current is flowing from the inner coil to the anode the signal from this current monitor is predominantly due to ion current. It is this signal which plays an important role in the discussion below on the parallel load problem.The total diode current is measured by a similar shunt just outside the diode also integrated into the cathode base plate. Generally this monitor and its counterpart on the anode side read the same current.

Presently, the focusability of our beams is mainly limited by three factors: an ion beam

divergence of about 17 mrad, an ion energy spread of about ± 15 %, and a nonzero canonical angular momentum of the ions due to a 2 mm anode plasma expansion across magnetic field lines. In addition a parasitic load occurring in the diode after peak power has been limiting the beam energy content. These properties are the result of instabilities developing during diode operation. Therefore, to further improve the quality of our beams we must gain a better understanding of the nature and the dependability of the diode operating stability, which is mainly determined by the evolution of the anode plasma and of the electron sheath.

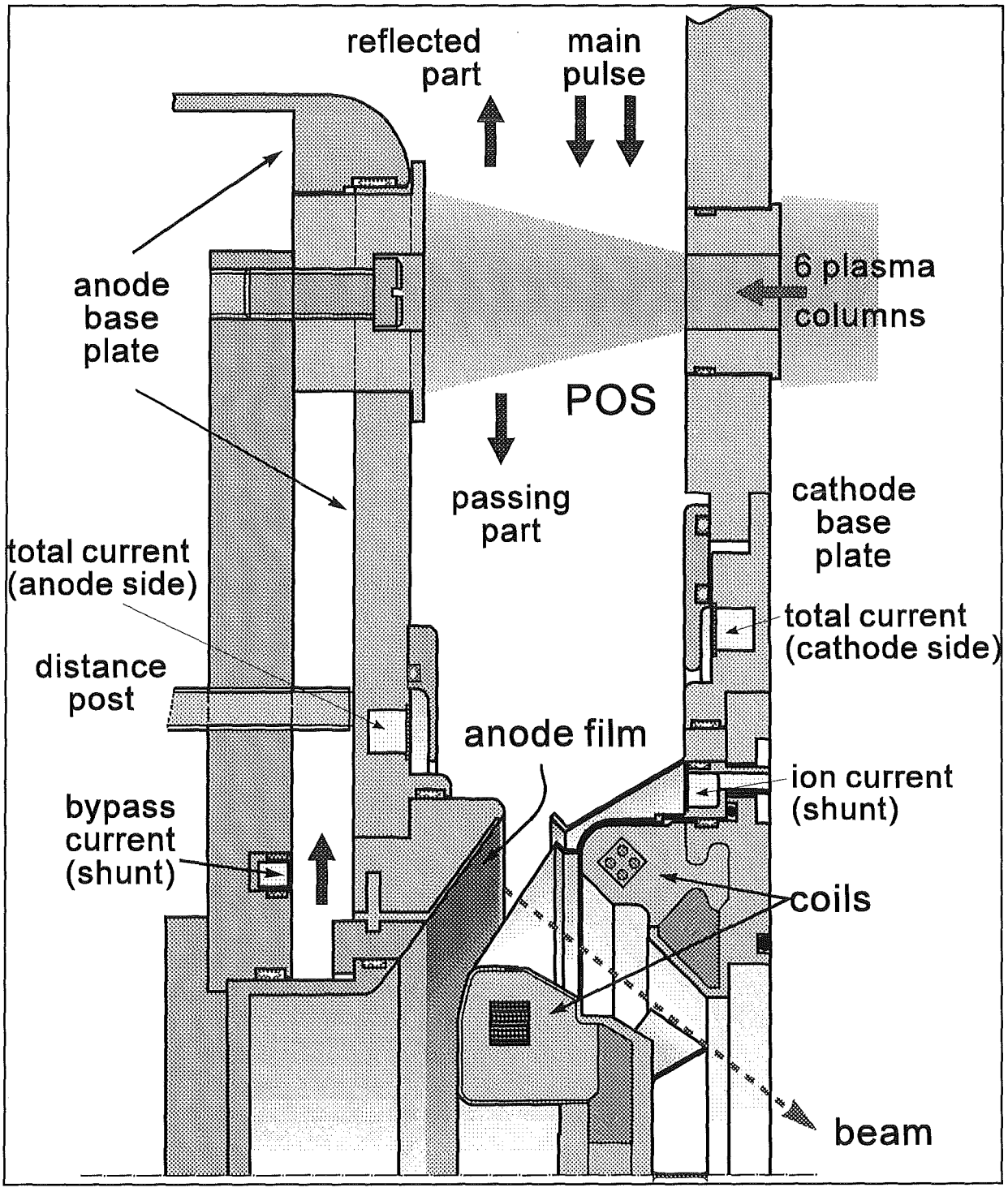

Fig. 1 B_{appl} extraction diode with Pd-covered TiH proton source and current monitors

Our present understanding of electron sheath instabilities and their influence on beam divergence and ion energy spread is largely based on the three-dimensional particle-in-cell code simulations with QUICKSILVER /3/. These calculations require enormous computing resources. Therefore, only very simplified diode models can be treated. Especially, the diode geometry must be idealized and only a limited section along the symmetry coordinate of the diode can be modeled. Also the interactions between the gap instabilities and the expanding electrode plasmas have not been treated.

Therefore, we need some experimental checks of the simulation results to confirm that the features found are the dominating ones. In this contribution we report on measurements that are pertinent to this comparison. In addition we describe recent results on the parallel load problem and on other diode operating features.

Diagnostic tools

Not all quantities which can be obtained from numerical simulations are also easily accessible to measurements. Among those which are both specific and measurable are the frequency spectrum and the phase velocity of the dominating electron sheath instabilities as a function of time. When these instabilities develop the ion current density should be strongly modulated with the electron density fluctuations close to the anode which occur with the frequency of the predominant mode and travel around the azimuthal direction with the phase velocity. Therefore, localized measurements of ion current density fluctuations should give information on the frequency spectrum, and correlating the results from measurements at different azimuthal positions should allow us to determine the phase velocity.

For that purpose we have used a set of six magnetically insulated Faraday cups located in the strong magnetic field (~ 3 T) of our diode coils, about 8 mm behind the initial position of the virtual cathode. They were distributed over three radial and six azimuthal positions covering 180° of the diode circumference. All Faraday cup signals were recorded on a 500 MHz analog bandwidth 16 channel digital scope (Tektronix TLS 216). In addition one signal was recorded in parallel on a 5 GHz transient digitizer (Tektronix SCD 5000). This channel was used to explore the frequency spectrum and it was made sure that the Faraday cup itself and the signal cables did not introduce any further bandwidth limitations. Entrance holes with 0.3 to 1.1 mm diameter drilled into 0.1 mm thick plates of stainless steel or Mo were applied.

Another main diagnostic shown in Fig. 2 consisted of a Rutherford scattering foil placed in the beam focus in combination with a pinhole camera and a cross of 13 Si-pin-diodes. The ions scattered from a 3000 Å Au layer deposited on a 1.5 µm mylar foil were imaged with the help of a pinhole camera onto the pin-diode cross. Each pin diode had a sensitive area of 1 mm^2 and was covered with a 6 µm thick Al foil.

Finally, we used an array of 15 x 40 quartz fibers to locally resolve the light emitted from the diode gap in different spectral regions. Each of the 15 columns collected light from a 0.5 mm thick slice parallel to the anode surface. A fast photomultiplier connected to each of the columns was used to record the light intensity as a function of time. The spectral range was selected with the help of 10 nm wide interference filters.

Results

A typical Faraday cup signal recorded with the 5 GHz transient digitizer is shown in Fig. 3. A period of high frequency oscillations early in the pulse is followed by a period of lower frequency

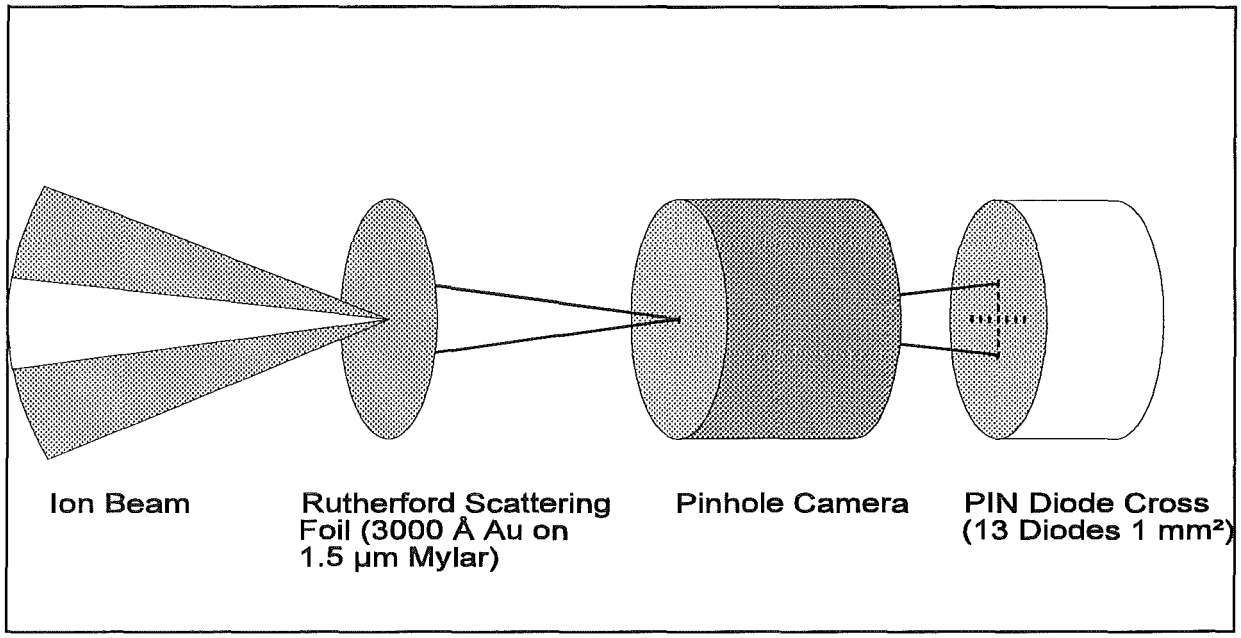

Fig. 2 Focus diagnostic consisting of a 3000Å Au scattering foil, a pinhole camera, and a cross of 13 Si- pin-diodes.

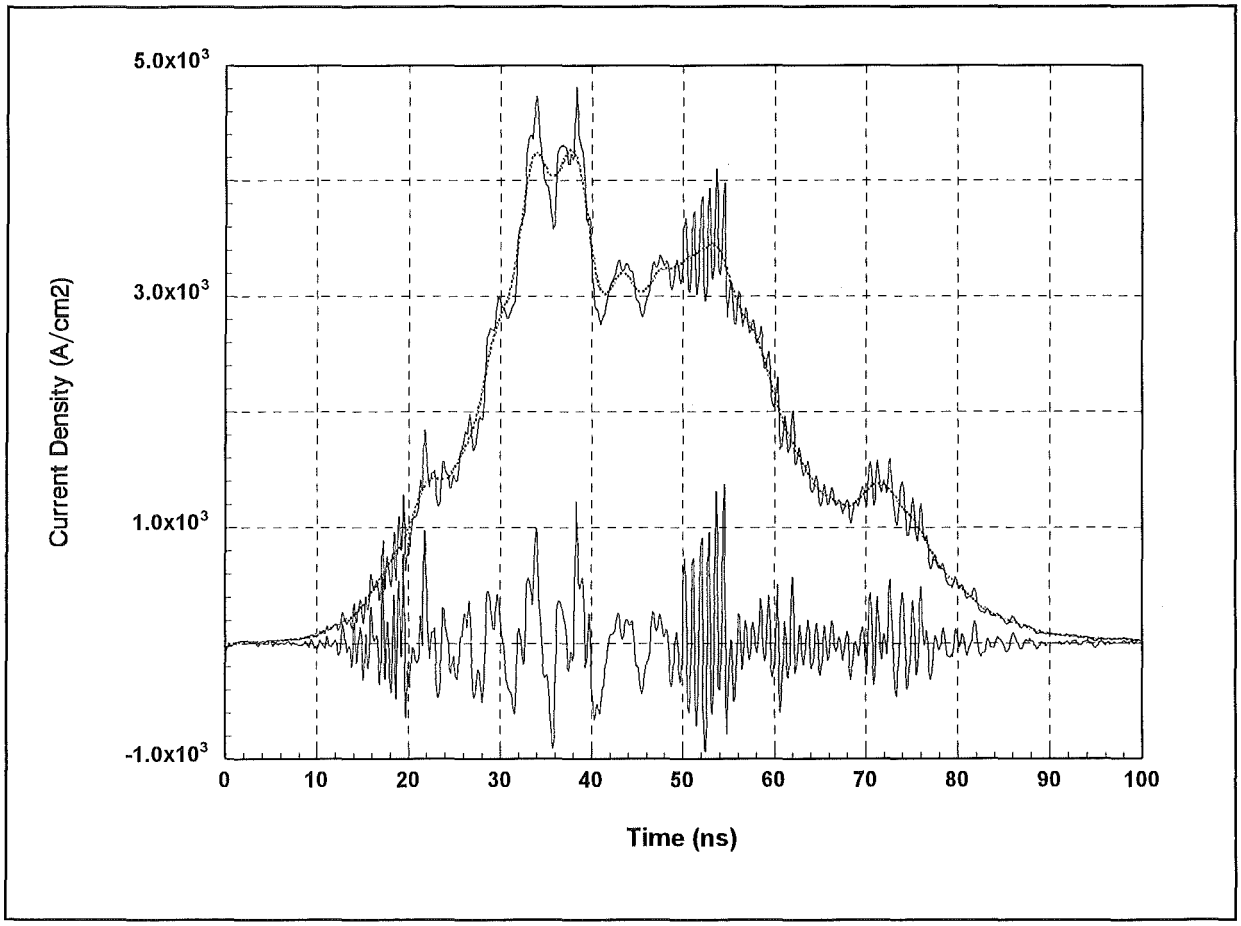

Fig. 3: Faraday cup signal recorded on a 5 GHz transient digitizer, together with smoothed signal and the difference between both (lower trace x 2).

oscillations and another period of high frequency oscillations. Before analyzing the frequency spectrum the signal was smoothed with the help of a Hanning window. Then, the smoothed signal was subtracted from the untreated one and the difference spectrum was subjected to a Fourier transformation. To make the time dependent structure of the spectrum apparent we restricted the analysis to certain time intervals.

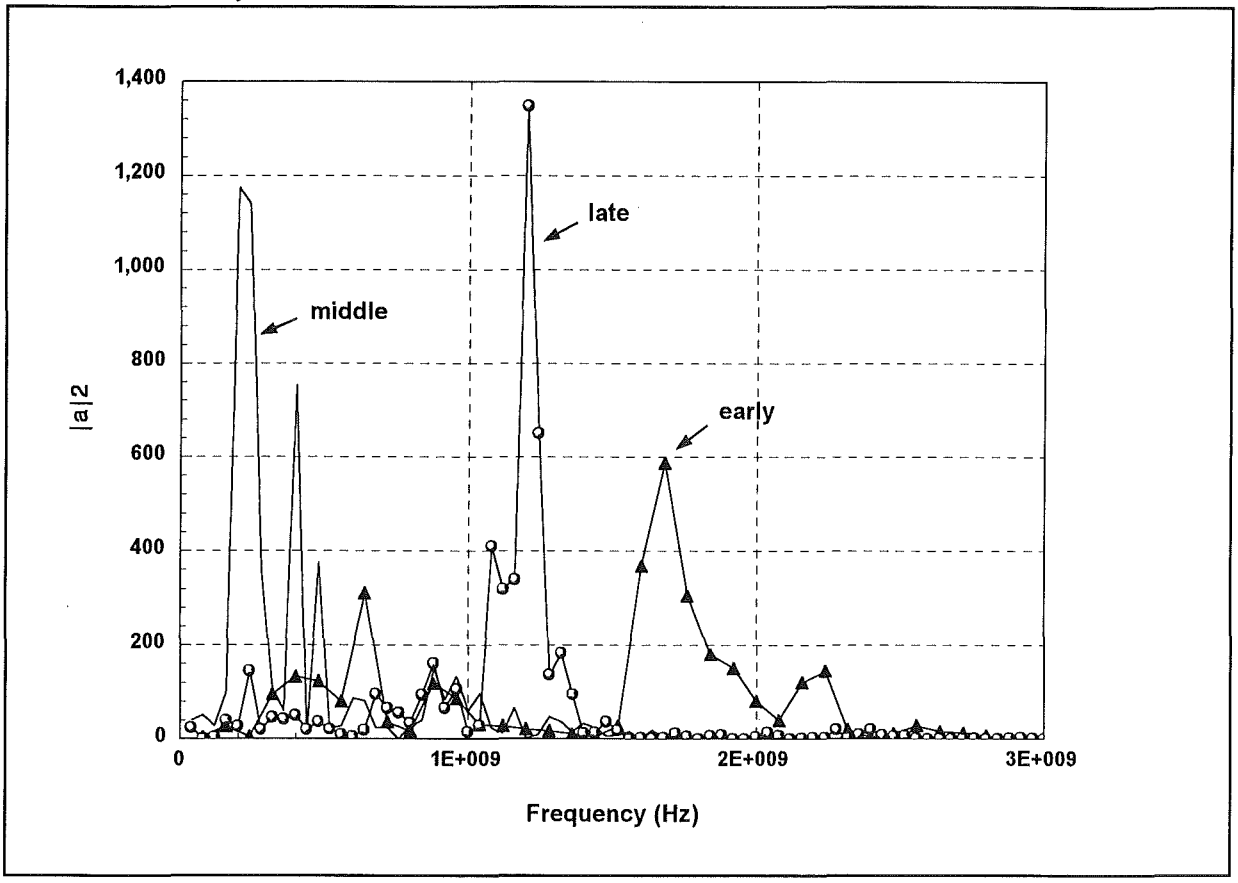

Fig. 4: Current density fluctuation spectrum at different times in the pulse.

As shown in Fig. 4 early in the pulse we observe two dominating frequencies at 1.67 GHz and at 2.20 GHz. This is followed by a lower frequency mode of 0.96 GHz superimposed on a few cycles with 4 - 5 ns period. This phase lasts for about 25 ns. Later in the pulse there is only one frequency at 1.2 GHz left. The general character of this spectrum is quite reproducible. Especially, the frequencies around 1.2 GHz and 1.7 GHz that have strong power appeared regularly with a variability of ± 150 MHz. However, an effective electron limiter distinctly shifts the spectrum to lower frequencies: Early in the pulse two frequencies at 0.5 and 1.0 GHz dominate. Later a frequency distribution centered around 0.86 GHz prevails.

Since we had only 1 channel with 5 GHz bandwidth available and since the predominant frequencies were distinctly above the 500 MHz limit of our other recording channels it was not possible to carry out a real correlation analysis to determine the frequency dependent phase velocities. However, we were able to look for prominent patterns in the Faraday cup signals surviving during the travel around the diode. From the times at which these pattern arrive at different locations it is possible to determine their propagation velocity. It turned out that this was possible only during the second half of the pulse. For Faraday cups aiming at the central part of the emission zone we obtained velocities of between 1/9 and 1/12 c. However these values need further verification using two 5 GHz channels.

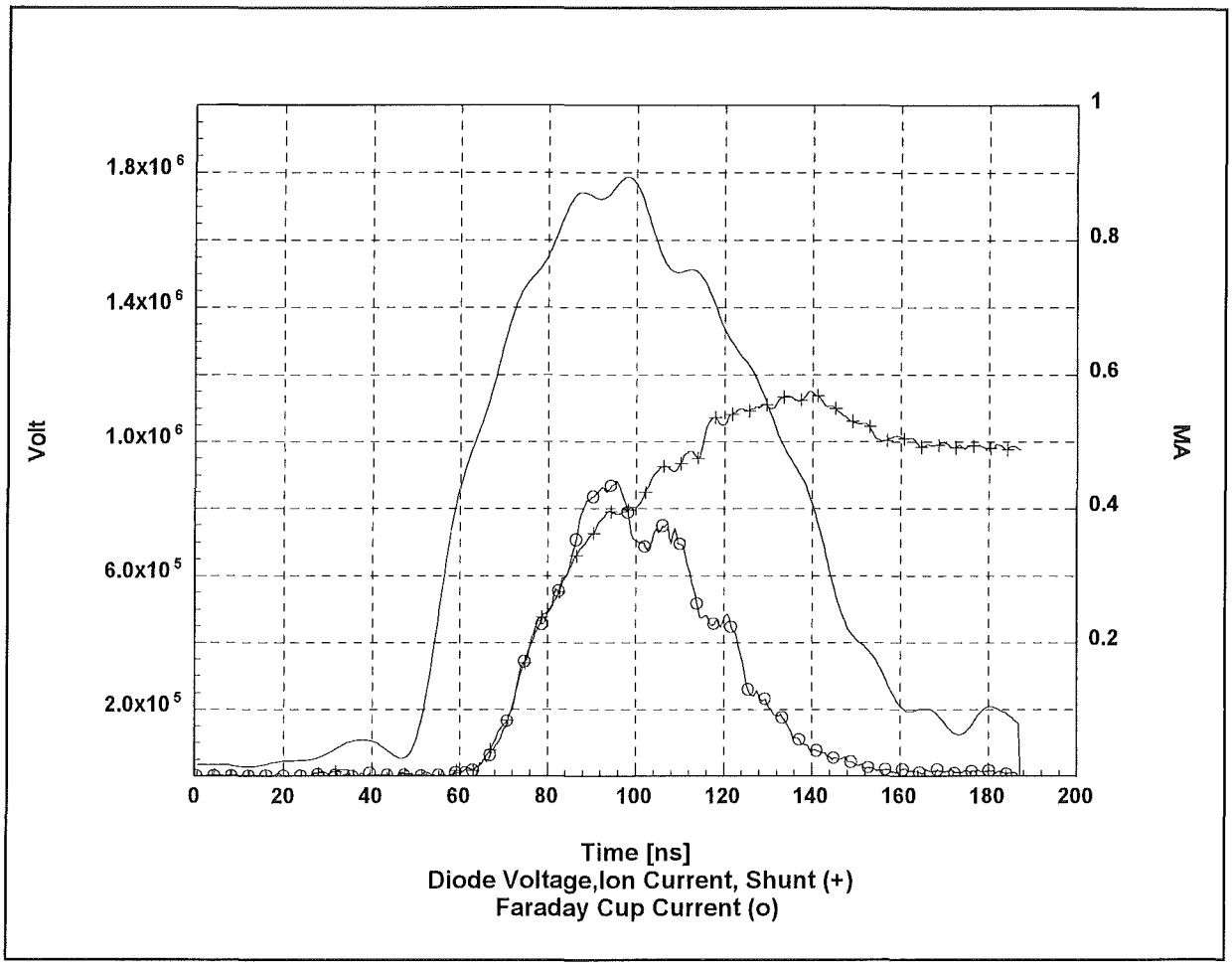

Fig. 5: Comparison of F.C. ion current with shunt ion current. The curve without symbols is the diode voltage.

The effect of a parallel load growing during diode operation becomes evident from a comparison of the ion current measured with electrical monitors with that derived from Faraday cup signals. Such a comparison is shown in Fig. 5. The F.C. ion current has been obtained by averaging the signals from 6 cups and multiplying the result by the anode emission area. While excellent agreement is observed during the rising part of the pulse a rapidly growing discrepancy develops at peak diode voltage. It is remarkable that this coincides with a transition in the frequency spectrum.

If we use the electrical ion current and the diode voltage to predict the shape of a pin-diode signal at the position of the pin-diode cross we find that this shape is much wider than that actually measured. This is shown in Fig. 6. Much better agreement is achieved if a current derived from F.C.s is taken for this comparison. Therefore, we can conclude that as long as the diode voltage remains above 0.6 MV a blockage of protons in the plasma created by ion beam bombardment of the F.C. aperture can be excluded.

The main purpose of the pin-diode cross was to determine the time history of our beam focus which is sensitive to diode stability and operating characteristics. It was found that the duration of the power pulse was 40 ns fwhm. During this period of time the shape of the focus remained nearly unchanged with a diameter of 6.2 mm fwhm.

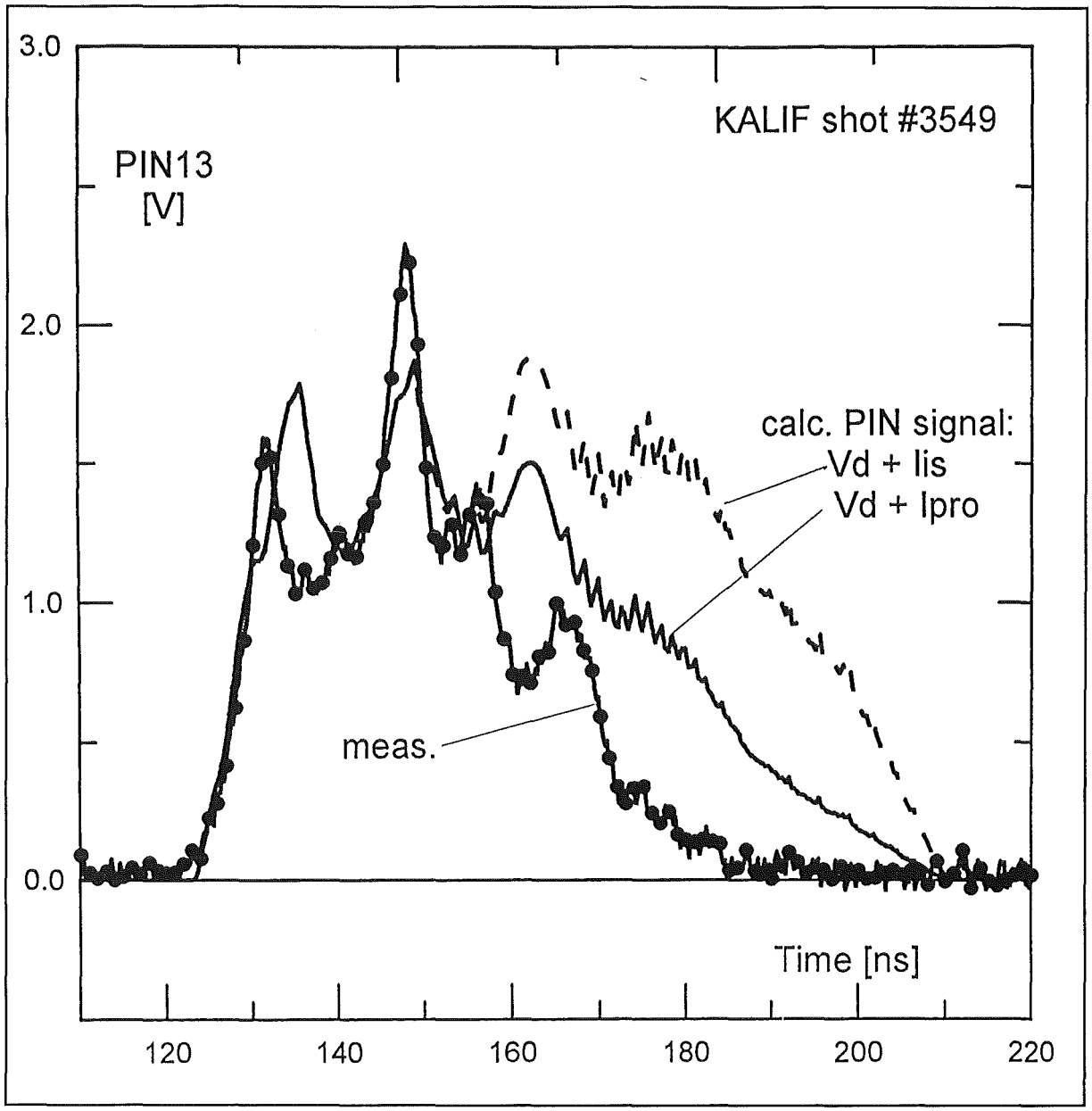

Fig. 6: Signal from the central pin-diode of the focus diagnostic compared to signals predicted from the diode voltage and the shunt or F.C. ion current respectively.

As expected the photomultiplier-fiber array showed that early in the pulse light was only emitted from a small zone in front of the anode and from the cathode tip.This is shown in Fig. 7 About 20 ns after anode plasma formation the light emitting zone had expanded roughly 1.5 mm into the diode gap. However, at the same time a 4 mm wide domain extending from the cathode into the gap began to emit light with growing intensity in a wavelength range around the hydrogen H_α-line. Late in the pulse the luminosity of this zone became even brighter than the anode plasma.

Conclusions

The high frequency fluctuations of the ion current density observed early in the pulse in shots without limiter can probably be identified with the diocotron instability of the electron sheath observed in numerical simulations /3/. At maximum diode operating voltage the current density reaches 4 kA/cm². This suggests that the effective diode gap is probably small at that time. Assuming a "saturated" enhancement of 5.5 an anode cathode gap of about 4 mm is

predicted. This leads to an ion-transit time of about 0.7 ns. Therefore, also the predominant frequency of 1.2 GHz prevailing in the second half of the pulse is compatible with the predicted ion transit time mode. The very low frequency oscillations with periods of 4 - 5 ns occurring before that have also been observed in simulations of diodes with strong magnetic insulation (Vcrit/V > 2) /3/. They have been attributed to cyclic electron losses resulting from an electron density peaked towards the anode.

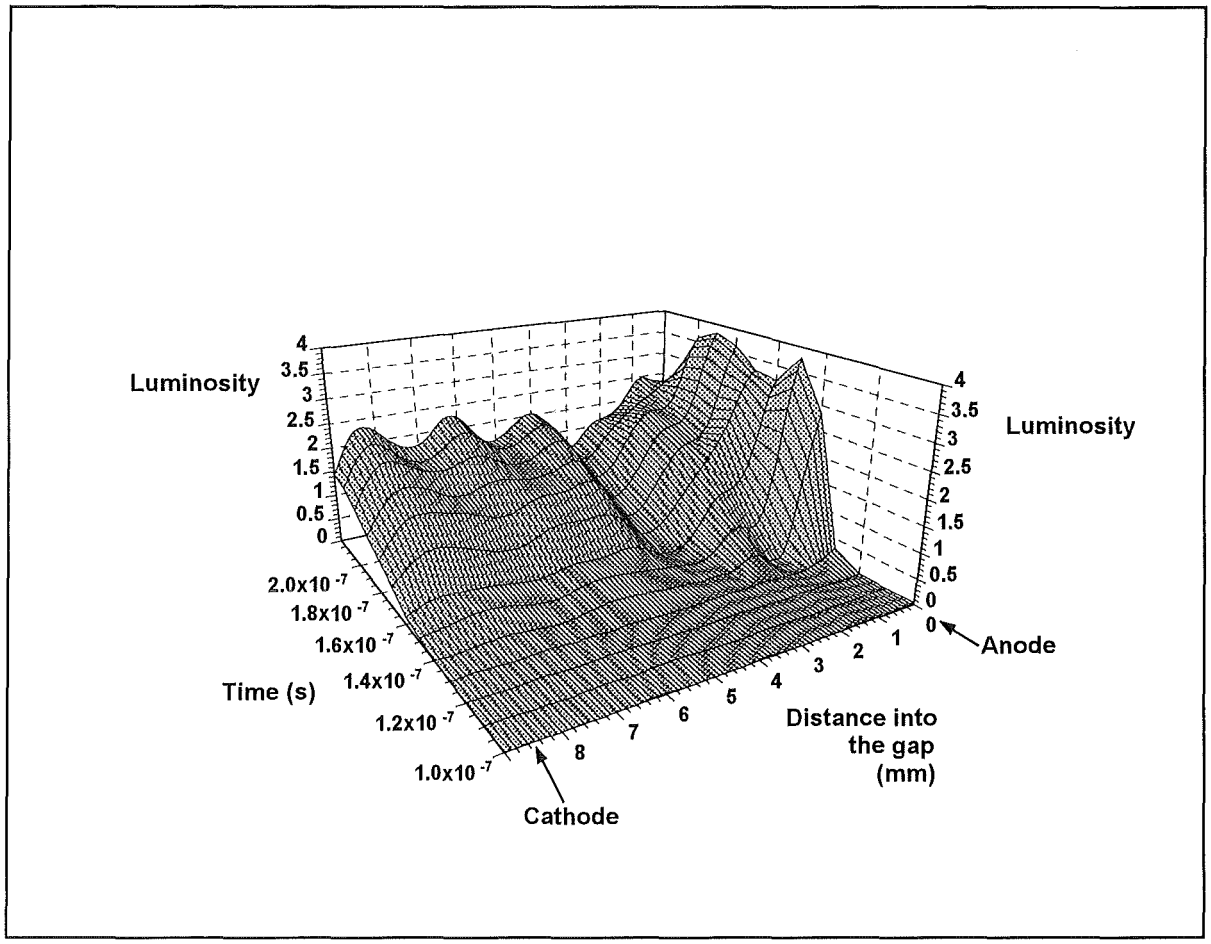

Fig. 7 Luminosity from the diode gap measured with an array of 15 H_α-filtered photomultipliers whose viewfields were evenly distributed over the 8.5 mm wide gap.

Combining the results of F.C. and pin-diode focus measurements demonstrates that the parallel load can at most be partially explained by a plasma blocking effect acting on protons accelerated with the full voltage present in the diode. Also a shortage of protons promoting the acceleration of heavier ion species (which then could be blocked off from the F.C.) is unlikely because this would increase the diode impedance at first. In addition we observe that the F.C. current signal very often follows the same $V^{3/2}$ law during the descending part of the voltage as it was during the rising part. Since both, the ion current monitor and the total current monitor far outside the diode show only very small differences it is also obvious that the parallel load develops inside the diode. It cannot be explained by a plasma closure between the cathode edge and the edge of the ion emitting zone on the anode, because a current connected with it would

not be recorded by the ion current shunt (see Fig. 1). We can also exclude fast electrons because the x-ray signal from the diode is decreasing steadily while the parallel load current is increasing.

There remain three possible explanations: low energy protons or neutrals created by various processes inside the diode or in the non current-neutralized zone, low energy electrons diffusing across the magnetic field lines, and plasma closure at the edges of the ion emitting zone on the anode. Low energy neutrals can only contribute to the current if they spend part of their lifetime in the accelerating gap as ions and then become neutral through a charge exchange collision within a quasistationary neutral layer. Since the charge exchange cross section of H^+ for common gases is rapidly falling at energies above 20 keV these reactions must take place during the initial acceleration phase of the ion. Initially such processes will mainly occur in a region close to the anode where the neutral density is sufficiently high. Only after the diode gap has been filled with a dense neutral background charge exchange collisions will also happen inside the gap. Then, it is conceivable that the electron cloud drifting in the **ExB** direction ionizes part of the neutrals and creates enough low energy electrons to initiate an avalanche breakdown. As ions are extracted from the layer uncompensated magnetized electrons are left behind and it is not yet clear how they can leave the gap. Low energy electrons can only diffuse to the anode if they exchange energy with an electromagnetic wave. Although very efficient microwave production is possible in crossed field devices emissions with the intensities needed to explain the observed phenomena have not been found for ion diodes/4/. In the experiments on KALIF roughly 20 kJ of microwave energy are necessary. Nevertheless, additional measurements of the microwave emission from magnetically insulated ion diodes is desirable. If a plasma closure at the edges of the ion emitting zone shall contribute to the parallel load it must lead to a current path inside the cathode edge, i. e. either to the inner coil structure or to the ring on which the gas cell foil is attached(see Fig. 1).
It is needless to say that late in the pulse a partial blockage of the F.C. aperture or a gap closure disconnecting the ion shunt from the diode current path can also be responsible for part of the parallel load problem.
Further specific diagnostics are necessary to resolve the parallel load problem.

Acknowledgement

The authors thank G. Keßler for his continued support of this work. They also thank the operational staff of KALIF as well as H. Lotz and G. Westenfelder for their technical assistance.

References

/1/ H. Bluhm, P. Hoppe', H. Laqua, D. Rusch; Proc. of the IEEE, Vol. 80, 995 (1992)

/2/ H. Bluhm, H. Laqua, L. Buth, P. Hoppe', D. Rusch; IEEE Trans. of Plasma Science, Vol. 21, 560 (1993).

/3/ T.D. Pointon, M.P. Desjarlais, D.B. Seidel, S.A. Slutz, R.S. Coats, M.L. Kiefer, and J.P. Quintenz; Phys. Plasmas 1, 429 (1994).

/4/ T. J. Renk, D.A. Hammer; Journal of Appl. Phys. Vol. 62, 5, 1655 (1987)

Development of a Low Impedance Pulse Generator for the Anode Plasma Generation in B_{appl} Diodes Used on the KALIF-Accelerator

P. Hoppé, H. Bluhm, H. Laqua, H. Massier, D. Rusch, M. Söhner

The performance of the magnetically insulated ion diode used on the KALIF accelerator depends sensitively on the properties of the anode plasma. This anode plasma should consist of a thin layer of protons only, covering homogeneously and with a sufficiently high areal density the anode surface of 132cm^2. An electrical pulsed generator for the creation of the anode plasma in this diode was designed and tested, which shall replace the present arrangement consisting of a bypass line and the plasma opening switches. This new plasma generator is based on a 0.2Ω impedance Blumlein-generator discharged either through a photoconductive GaAs switch or a dielectric foil switch. The energy supplied by this generator is coupled via 6 parallel striplines to the hydrogen loaded TiPd layer covering the anode surface. Actually the plasma generator can deliver about 20J in a 20ns long pulse with about 5ns rise time to a matched load which is considered to be just sufficient for the production of a suitable anode plasma.

1. Specifications of the Anode Plasma Generator

The performance of light ion beam diodes depends sensitively on the properties of the anode plasma, which delivers the ions to be accelerated by the applied diode voltage. In diodes using a strong externally applied magnetic field for electron insulation, the anode plasma must be produced by an external driver suppling the energy necessary to produce a gas layer and to ionize it. So far in B_{appl} diodes this energy was derived from the accelerator pulse with the help of plasma opening switches (KALIF [1] , LION [2]) or by illumination of the anode surface with laser light (PBFAII [3]). With the POS-system used on KALIF for plasma generation a peak proton power density of up to 1TW/cm^2 has been achieved. However, the time interval of plasma generation cannot be selected independently from the KALIF pulse and the amount of plasma can hardly be controlled. Replacing the present POS-system by an external driver seems to be a suitable method to increase the performance and the reproducibility of our diodes. The anode plasma for the B_{appl} diode operated on KALIF should ideally consist of a thin pure layer of protons with a density of at least $3 \cdot 10^{15}$ protons/cm^2. This layer should uniformly cover the anode surface of 132cm^2 and smoothly conform to the desired anode shape without any protuberances into the acceleration gap. In test-bed experiments performed with hydrogen loaded titanium layers (300Å thick) covered by a palladium layer (200Å thick) to prohibit oxidation, such a plasma has been generated and investigated in detail [4, 5, 6]. The metal films in these test-bed experiments were deposited on a 2x7cm^2, 1mm thick glass substrate and connected to a 1.2Ω, 13ns Blumlein-generator, charged up to 30kV. The electrical current from the generator driven through the metal layers heated them up to their melting point thereby releasing a large fraction of the stored hydrogen. Since the metal resistance increases during the heating phase the voltage drop across the desorbed gas layer increases too and finally creates a multichannel sliding discharge after a critical gas density has been reached. The uniformity of this sliding discharge [6] depends sensitively on the areal capacitance formed between the plasma layer and the metallic bulk substrate (Fig. 1). The displacement current delivered to these capacitors initiates the break-down of the gas layers. If the capacitance is above 2 to 4 pF/cm^2 the discharge channels starting at the HV-electrode tend to develop independently and homogeneously cover the whole anode surface. Extrapolating from previous test-bed results with small samples and from our present experience with the POS-bypass system an energy of about 20J has to be spent within 20ns to produce a suitable plasma layer. Most of this energy has to be deposited in the gas layer during the break-down

phase when the plasma is forming and when the impedance rapidly drops. Therefore, a driver with an impedance as small as 0.2-0.3Ω seems necessary. To rapidly initiate the break-down the current pulse should rise with a rate of at least 2.5kA/ns. Also the open circuit voltage should reach more than 40kV.

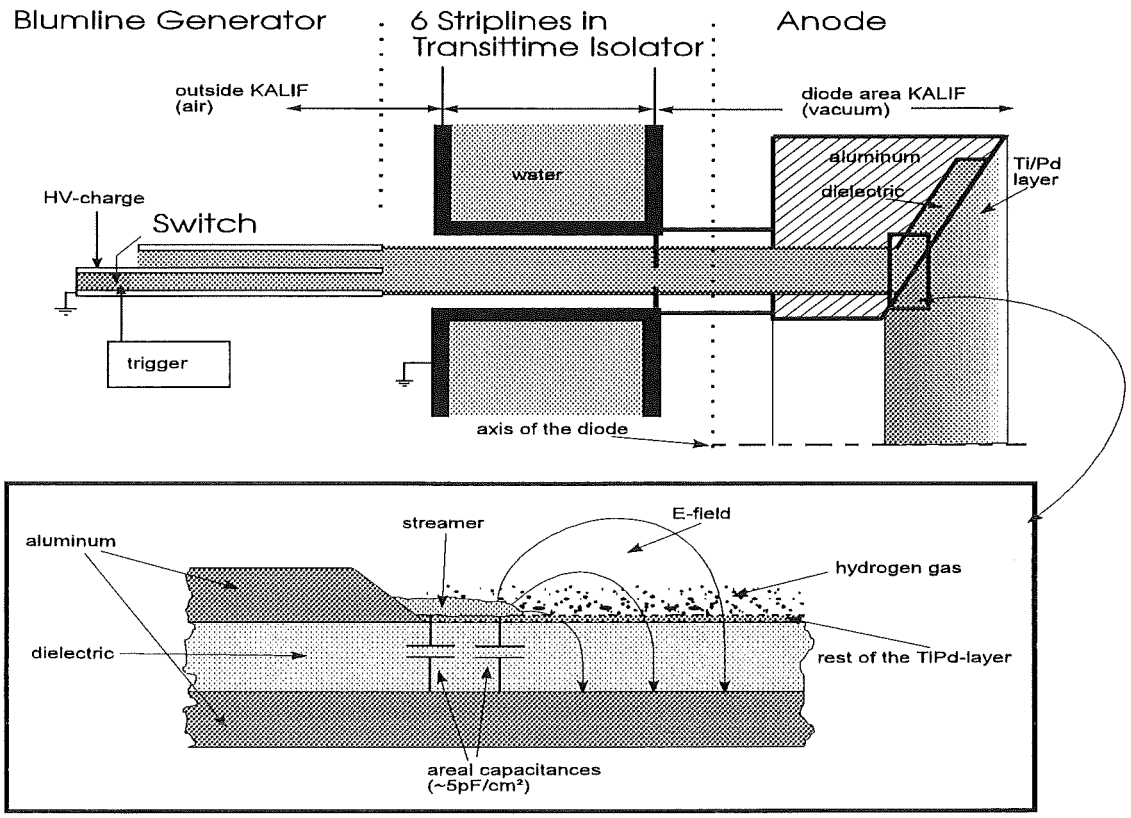

Fig. 1: Schematic of the anode plasma generator foreseen for the B_{appl} diodes used on KALIF

2. Design of the Low Impedance Anode Plasma Generator and the Instrumentation

The main components of the anode plasma generator are (Figs. 1,2):

- A foil insulated Blumlein-generator (60cm x 150cm) with an impedance of 0.2Ω. The discharge of this generator is initiated by either a semiconductor or a foil grounding switch.
- A set of 6 striplines, 8m long, which connect the Blumlein generator to the anode via the transit time isolator. The 2.1Ω striplines (Fig. 3) were individually tested up to 60kV and 40kA for pulse durations of 20ns. The loss of electrical energy was less then 15% for a 8m long stripline [7].
- The trigger and the necessary HV-charging components.

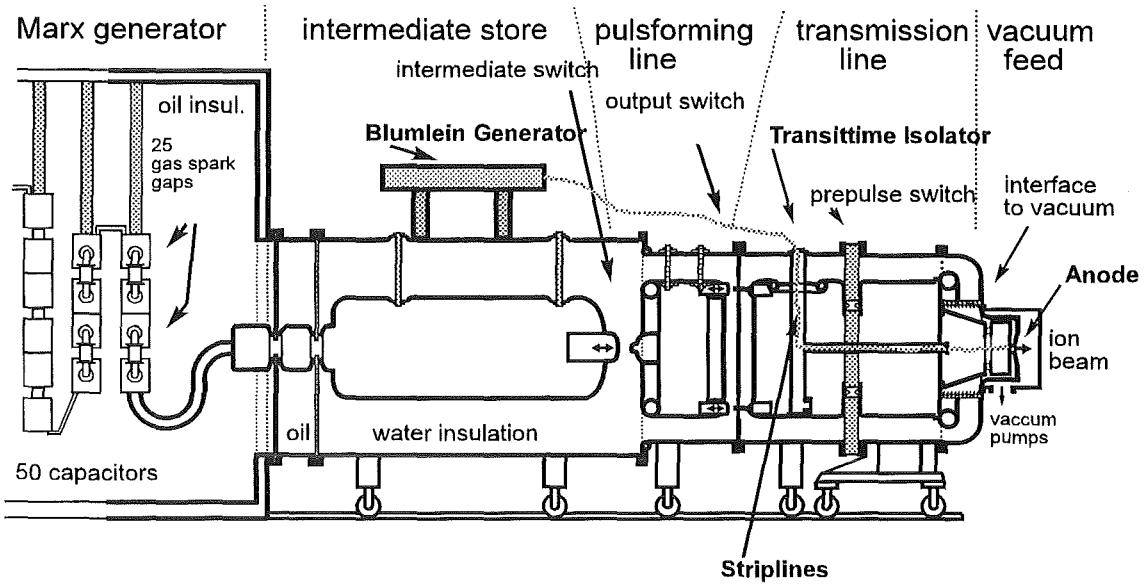

Fig. 2: Arrangement of the anode plasma generator on KALIF

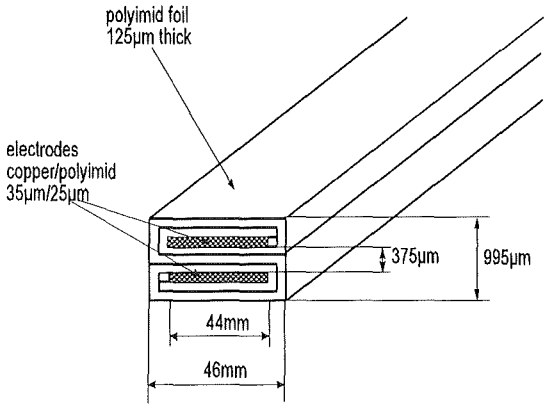

Fig. 3: Cross section through a stripline transmission line

The following general design criteria had to be considered:

- The plasma generator needs only single shot capability, since it is operated less then 5 times per day. All components and connections should be matched as close as possible to the 0.2Ω generator impedance in order to achieve a fast rising pulse at the TiPd-layer.
- The synchronization between plasma generation and KALIF pulse should be better than 10ns. Due to the large jitter of the water intermediate switch this restricts the pretrigger time to less than 250ns.
- Additionally restrictions due to the space available as well as mounting and handling requirements have to be considered.

To measure electrical pulses with rise times in the ns-range sufficiently fast current shunts and capacitive voltage dividers had to be developed. Rise time measurements performed on these transducers with a 2kV pulse generator, having a proven rise time below 200ps, showed a value of 1 to 2ns for both monitor types (Fig. 4) when connected by cables of 15m length to an oscillograph with 500MHz bandwidth. Typical decay time constants of both monitor types to a step input are from 200...300ns. Most of the measurements were performed with the current shunts because - in contrast to the capacitive voltage pick ups - their calibration coefficients do not depend on their specific installation.

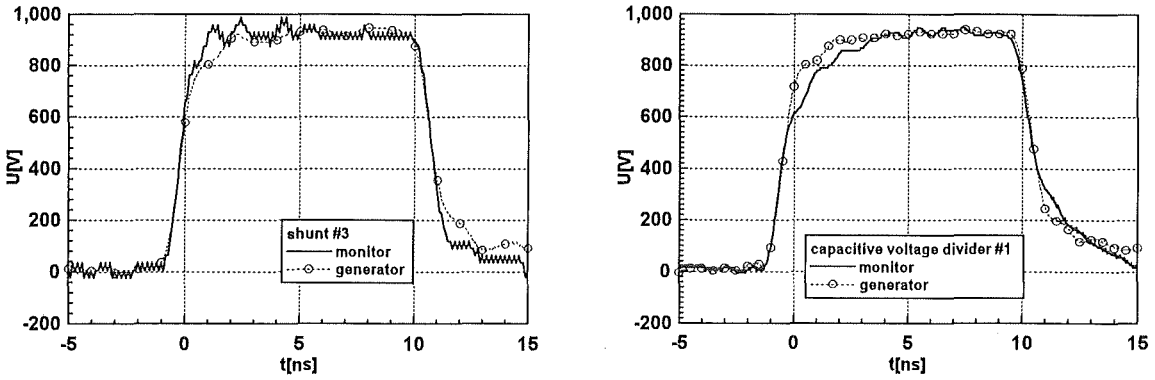

Fig. 4: Measurement of the rise time for current (left) and voltage (right) monitors

3. Investigation of the Fast Grounding Switches

Any fast ns-grounding switch to be used in a 0.2Ω stripline arrangement should be matched to the transmission line impedance, otherwise the pulse rise time would slow down. This restricts the choice to photoconductive switches triggered by a Nd:YAG laser or to dielectric foil switches triggered by electric field distortion. In contrast to photoconductive switches the foil switches cannot operate in a repetitive mode because the foils have to be replaced after each shot. However foil switches are much less expensive than light activated silicon switches developed so far up to a maximum charge voltage of 5 to 10kV [8]. Therefore, it was investigated whether one can reduce the laser pulse energy by using doped GaAs semiconductors not only in the linear-mode (where carriers are produced by the light only) but also in the non-linear mode (where part of the carriers is produced by impact ionization) up to 30...50kV [9, 10, 11]. The experiments were accomplished with up to 40 GaAs-elements activated by a 250mJ Nd:YAG-laser pulse with 6ns pulse width (FWHM). These switches were integrated into the 0.2Ω Blumlein generator charged up to about 20kV. The 6 individual shunt currents measured at the grounded connection points to the striplines (that means at the Blumlein line end opposite to the switch) were nearly identical (Fig. 5). This proves that in principal the GaAs-switch can deliver the same energy to each stripline with a sufficiently fast rise time of about 5ns; the first current maximum is due to the linear conduction mode, the second is related to the non-linear mode (Fig. 6). From the 9kV charge voltage of the Blumlein line only 3kV appeared across a matched load of 0.2Ω i.e. 6kV were lost across the switch. The currents measured for the 9kV charge present the best

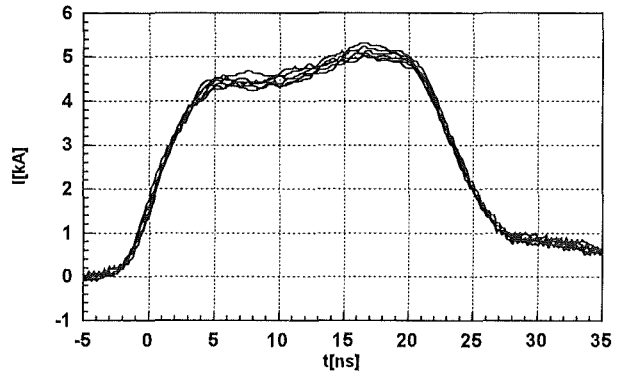

Fig. 5: Currents measured at the end of the Blumlein-line grounded by the photo-conductive switch

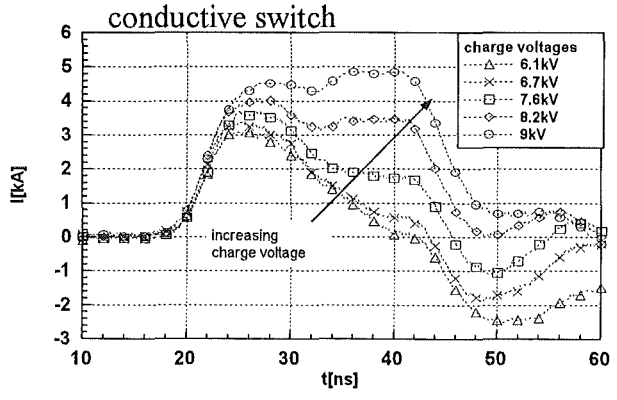

Fig. 6: Influence of the charge voltage of the Blumlein-line grounded by the photo-conductive switches

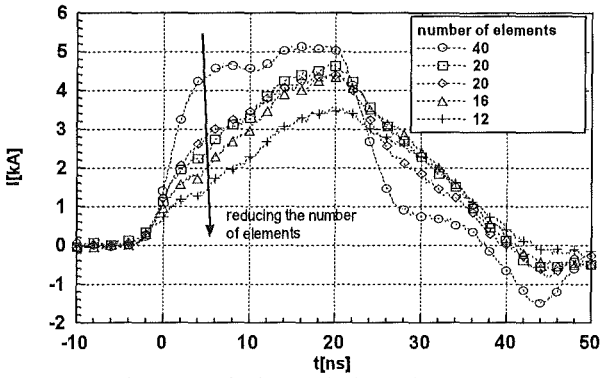

Fig. 7: Characteristics of the photoconductive GaAs switch with increasing current density per switch element

approach to the desired square pulse that can presently be achieved with this photoconductive switch arrangement. Any further increase of the current to be conducted by this switch has to rely on carriers produced by the slow non-linear mode as shown in an experiment using always the same 9kV charge and laser intensity but reducing the number of GaAs-elements carrying the charge (Fig. 7). This test procedure avoids the risk of electrical break-down across the switch elements. The slower current increase is not caused by the reduced switching area (this was much smaller in experiments with break-down foil switches) but is due to a lack of carriers produced in the linear mode. Further limitations to the use of this switch design are related to the break-down risk across the 12mm wide switch elements (around 20kV) and to the damage by thermal heating of the semiconductors at higher currents. Neglecting losses on the transmission lines, an energy of 3J to a matched load of 0.2Ω would be achieved with the GaAs semiconductor switches at a peak voltage of 6kV (open circuit conditions). These values are not sufficient for the anode plasma production in our B_{appl} diode. Further investigations are necessary if the outlined problems should be solved by photoconductive switches. At least an increase of the laser energy by a factor of 10 to 20 and a homogeneous illumination of the photoconducting area seems to be necessary.

The grounding switch used in the test-bed experiments [5] was a foil break-down switch triggered by field distortion by means of a fast rising voltage pulse (30kV/ns) on the metallic foil placed between the upper and the lower insulating foil (Fig. 8). This trigger pulse was provided by a spiral generator with an impedance of 500Ω. The use of the same trigger arrangement on the 60cm wide plasma generator produced current shapes very similar to those measured in experiments where self break-down occurred (Fig. 9). Replacement of the 500 Ω spiral generator by a 50 Ω, 6-stage Marx-generator charged to 35 kV produced the current pulses depicted in Fig. 10 measured at the end of each shorted 8 m long stripline. For a charge voltage of 20 kV the current in each line reached a 15 ns long plateau of about 18 kA within 5 ns. A further increase in charge voltage produced first a 3 ns rise to 19 kA followed by a slower increase to the maximum value of up to 35 kA per line. This change in slope seems to indicate the limit for the current to be conducted by the carriers produced by the trigger generator itself in the insulating plastic foils. Later a part of the carriers are presumably produced by energy from the Blumlein-line generator itself. This would also explain the results achieved with the 500 Ω spiral generator (Fig. 9). The energy released by this trigger generator was too small to produce any charge carriers but was sufficiently high to

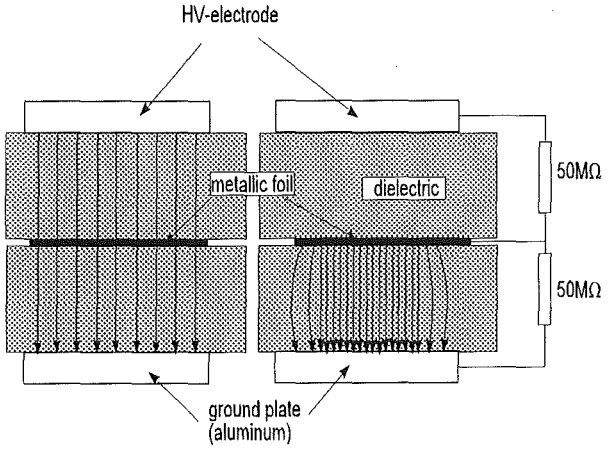

Fig. 8: Operation principle of the dielectric foil switch

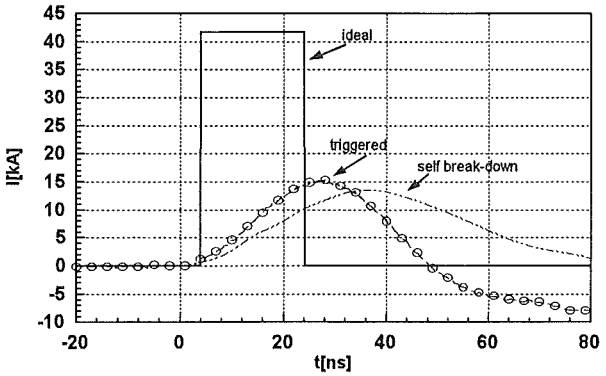

Fig. 9: Switching characteristics achieved with the dielectric foil switch driven by the 500Ω spiral generator

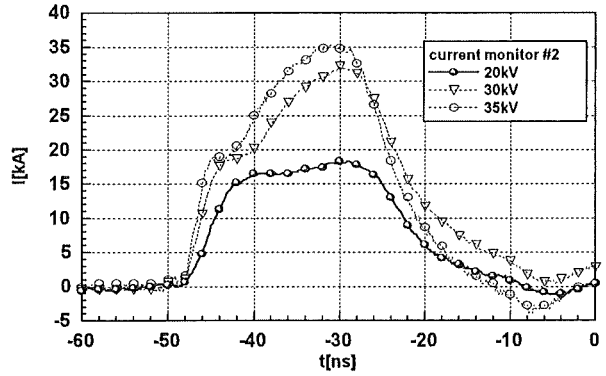

Fig. 10: Switching characteristics achieved with the dielectric foil switch driven by a 6 stage Marx generator

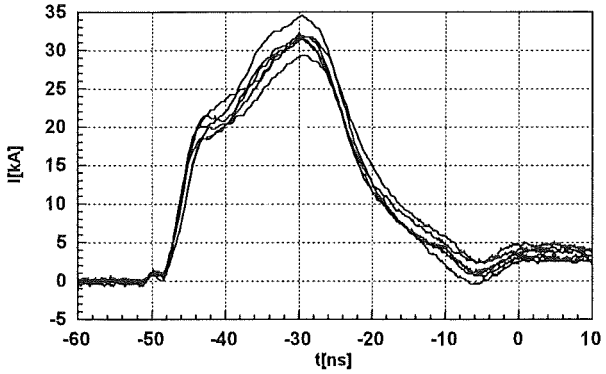

Fig. 11: Symmetry of the currents measured at the shorted ends of the 6 striplines when charging the Blumlein-line to 30kV

predamage the foils thereby initiating a switching with self break-down characteristics. Under this aspect photoconductive and foil grounding switch behave quite similar: A fast current rise is achievable only if the trigger generator delivers enough light or electrical energy to produce a sufficiently high number of carriers for the electrical charge to be switched. With this trigger generator and the foil switch an electrical pulse could be supplied to a matched load with an energy of 19J, a current rise of 15kA/ns and a voltage of up to 50kV under open circuit conditions. The observed symmetry at the end of the 6 striplines was better then ±10% (Fig. 11).

4. Summary and Outlook

The pulse form achieved so far is yet not rectangular but ramping-up. Also problems still exist with the reproducibility of the switch performance, with its reliability and with the trigger delay of roughly 700ns, which is mainly due to the 50Ω Marx trigger generator. These problems might be solved by an arrangement (Fig. 12) similar to that used by Dokopulos [12]: an intermediate 0.6 Ω trigger Blumlein-generator triggered by either a faster Marx trigger generator or a 50kV capacitive pick-up from the KALIF pulse. The required timing conditions when using the capacitive pick-up can be met by delay lines for the 50kV trigger pulse. The energy supplied by this intermediate stage to the foil switch of the main Blumlein-generator should be sufficient to produce enough carriers to avoid the slope change in current rise as observed in Fig. 10. Experiments taking these modifications into account are in progress.

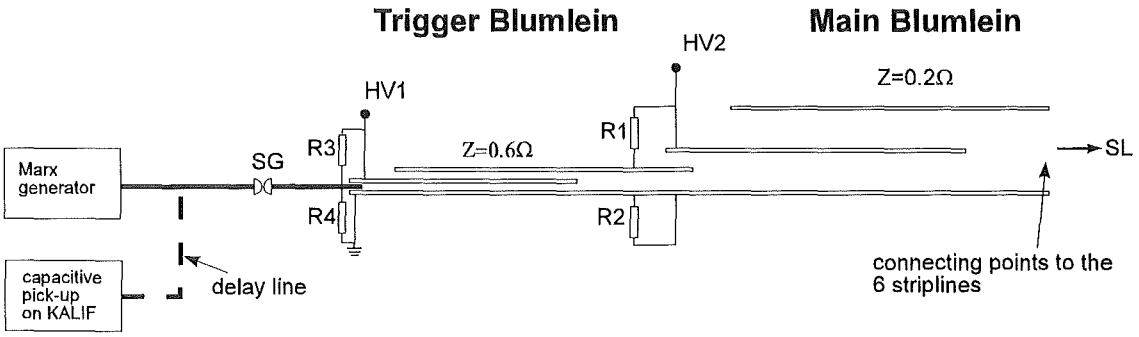

Fig. 12: Schematic of the modified anode plasma generator

References

[1] H. Bluhm, P. Hoppé, H. Laqua, D. Rusch, "Production and Investigation of TW Proton Beams from an Annular Diode Using Strong Radial Magnetic Insulation Fields and a Preformed Anode Plasma Source", Proceedings of the IEEE, Vol. 80, No. 6, June 1992.

[2] G. Rondeau, G Bordonaro, J. Greenly, D. Hammer, "Exploding Metal Film Active Anode Source Experiments on the LION Extractor Diode", in Proc. 8th Int. Conf. High Power Particle Beams (Beams'90), Novosibirsk, USSR, July 2-5, 1990, pp. 499-504.

[3] G. Tisone, T. Renk, D. Johnson, R. Gerber, R. Adams, "Laser Formation of Lithium Plasma Ion Sources for Applied-B Ion Diodes on the PBFA-II Accelerator", in Proc. 9th Int. Conf. High Power Particle Beams, Washington DC, USA, May 25-29, 1992, pp. 800-805.

[4] H. Bluhm, H. Laqua, L. Buth, P. Hoppé, D. Rusch, "Formation of a Homogeneous Hydrogen Plasma Layer for the Production of Terawatt Ion Beams", IEEE Transactions on Plasma Science, Vol. 21, No. 5, October 1993.

[5] H. Laqua, "Das Nicht-Gleichgewichts-Plasma einer Oberflächenentladung auf einem Metallfilm als Ionenquelle", Ph. D. dissertation, Universtiät Karlsruhe (Germany) and Report of the Kernforschungszentrum Karlsruhe KfK 5286, Januar 1994.

[6] H. Laqua, H. Bluhm, L. Buth, P. Hoppé, "Properties of the Nonequilibrium Plasma from a Pulsed Sliding Discharge in a Hydrogen Gas Layer Desorbed from a Metal Hydride Film", accepted for publication in Journal of Applied Physics, Januar 1995.

[7] M. Söhner, "Entwurf und Erprobung eines Pulsgenerators zur Erzeugung des Anodenplasmas in einer magnetisch isolierten Ionendiode", Diplomarbeit,Universtät Karlsruhe (Germany) and Institut für Neutronenphysik und Reaktortechnik Kernforschungszentrum Karlsruhe, December 1993.

[8] D. Giorgi, O. Zucker, A. Wilson, "Light Activated Switched Blumlein-Pulser", paper P1-33 of the 10th Int. Conf. on High Power Particle Beams, June 20-24, 1994, San Diego, USA, to be publ.

[9] U. Katschinski, A. Schütte, J. Salge, "Development of Optically Triggered Semiconductor Switches for the Generation of High Power Pulses", presented at the SPIE's conference on Optically Activated Switching III, Los Angeles, 1993.

[10] U. Katschinski, "Optisch aktivierte Galliumarsenidschalter für die Erzeugung von Hochleistungsimpulsen ", Fortschr.-Ber. VDI Reihe 21 Nr. 157, Düsseldorf (Germany): VDI-Verlag 1994.

[11] H. Meier, U. Katschinski, J. Salge, "Operation of Optically Activated GaAs-Switches in Striplines of low Impedance at Voltages up to 30kV" presented at SPIE's conference on Optically Activated Switching IV, Boston, USA, 1994.

[12] P. Dokopoulos, "Eine folienisolierte Mehrkanal-Funkenstrecke mit Nanosekunden Schaltzeit", ETZ-A Bd. 92 (1971) H.2.

A new electron screening model to describe the impedance evolution in strongly insulated applied-B ion diodes

A. V. Gordeev, A.V. Grechikha**

**permanent address: I.V. Kurchatov Institute of Atomic Energy, Moscow*

1. Introduction

The main reason for the introduction of the new theory presented here is that both the impedance decay observed in most applied-B ion diode experiments /1, 2/ and the transition from a low to a high frequency electron sheath instability in these diodes, found in experiments /3/ and in numerical simulations /4/ as well, cannot be explained in the frame of existing analytic ion diode models /5/.

2. Assumptions

The theory presented is based on the evidence that after onset of the high-frequency diocotron-mode instability electrons begin to fill the diode gap between the virtual cathode and the anode. Due to their chaotic motion they tend to mix. Assuming a drift motion for the electrons diffusing into the gap one arrives at the conservation of the ratio B/n_e along the electron trajectories, i.e. the magnetic field B remains frozen in the electron fluid. Here n_e is the electron density. Consequently B/n_e becomes constant all over the gap. This assumption, supported by plausibility arguments is the main difference compared to the diode model developed by M. Desjarlais /5/. In this model a homogeneous electron density distribution had been assumed within the electron sheath.

3. Results

The ratio B/n_e determines the magnetic Debeye length $r_B = B/4\pi en_e$ at which all electric fields in the gap become screened by the electrons. This scale decreases as the amount of electrons diffused into the gap increases with time.
If the scale length r_B becomes much smaller than the geometric gap the diode impedance is actually defined by small regions of order r_B near the anode and near the virtual cathode where the electric fields remain uncompensated. The exact theory provides $d_{eff} = 9/8\ r_B$ for this limit. This can explain both the experimentally observed impedance decay and the transition from the diocotron to a low frequency instability: The predicted screening reduces the diode impedance due to a reduction of the efficient diode gap and decelerates the electromagnetic waves in the gap by switching off the electrical component. A quantitative comparison of the present theory with experimental results exhibits an exactly constant growth rate of the free parameter N_e in the theory which is proportional to the amount of electrons in the gap. As an example of such a comparison Fig. 1 presents N_e as a function of time for shot No 3558 with the KALIF applied-B ion diode /2/. Also shown in the plot are the diode voltage and the ion current. It is seen that the electron density grows linearly with time. The gradient of this increase determines the rapidity of impedance collaps which in this shot was rather moderate.

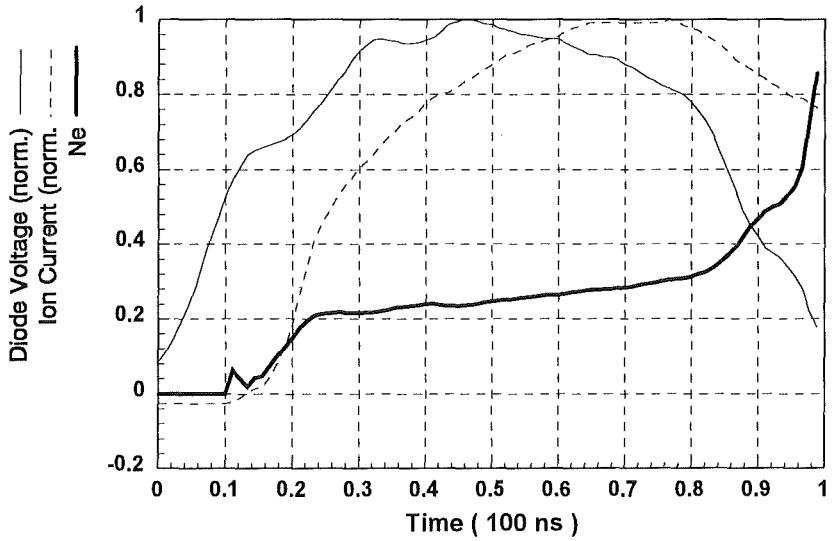

Fig. 1 Diode voltage (normalized: 1= 1.8 MV), ion current (normalized: 1= 480 kA), and parameter N_e which is proportional to the electron density in the diode gap

References

/1/ D.J. Johnson et al.
J. Appl. Phys. 53, 4579 (1982).

/2/ H. Bluhm, P. Hoppé, H. Laqua, D. Rusch
Proc. of the IEEE, Vol. 80, 995 (1992)

/3/ H. Bluhm, P. Hoppé, H. Bachmann, W. Bauer, K. Baumung, L. Buth, H. Laqua, A. Ludmirsky, R. Rusch, O. Stoltz, S. Yoo
"Stability and operating characteristics of the applied-B proton extraction diode on KALIF", Proc. 10th Int. Conf. on High Power Particle Beams, San Diego, Cal. June 20 - 24, 1994 Vol. 1, p. 77 and this report.

/4/ T. D. Pointon, M. P. Desjarlais, D. B. Seidel, S. A. Slutz, R. S. Coats, M.L. Kiefer, J. P. Quintenz,
Phys. Plasmas 1 (2), 429 (1994)

/5/ M.P. Desjarlais,
Phys. Fluids B1, 1709 (1989).

"Catalytic resonance ionization" - a novel, universal technique for the formation of a two-component anode-plasma

B.A. Knyazev, P.I. Melnikov*, H. Bluhm*

**Permanent address: Novosibirsk State University, 630090 Novosibirsk, Russia*

Abstract

In this paper we describe a technique to produce planar and volumetric ion sources of nearly every element. This technique is based on a generalization of the LIBORS-process (Laser Ionization Based On Resonant Saturation) which because of its similarity to chemical catalytic reactions has been called CATRION (CATalytic Resonance IONization). A vapor containing the desired atomic species is doped with a suitable element possessing resonance transitions that can be pumped to saturation with a laser. By superelastic collisions with the excited atoms and by stimulated bremsstrahlung absorption seed electrons are heated and multiplied. It is the heated electron component which then by collisional processes also ionizes the desired atomic species. This technique will work efficiently if both the atom and the ion of the dopant possess resonant transitions that can be pumped by the same laser. Instead of using tunable dye lasers we propose to apply gas lasers which are more robust and appropriate for repetitive long term operation. We present a large number of coincidences between gas laser wavelength and resonant transitions in suitable atoms.

The production of spatially localized plasma layers in contact with surfaces in a vacuum environment is often required in pulsed-power technology. Such plasmas consisting of specific elements are needed for the formation of plasma anodes in high-power accelerators for inertial fusion or industrial applications. In both cases the plasma must be sufficiently uniform and dense.

We propose a novel technique for the production of multicomponent plasmas with high repetition rates and supposedly high efficiencies. This technique also allows to adapt the system to form a plasma with arbitrary elemental composition. Our technique is based on a generalization of the well-known LIBORS-process (Laser Ionization Based On Resonant Saturation) which because of its similarity to chemical catalytic reactions has been called CATRION (CATalytic Resonance IONization).

In both techniques a layer of a gas/vapor with specific elemental composition and sufficiently high density has to be created near a surface in the first stage of the process. It can be produced by means of any suitable technique, e.g. a pulsed injection of gas through special apertures in the surface or a pulsed heating of a surface by an electric current or by laser radiation. The heating leads to emission of a dissolved gas and/or to evaporation of material from the surface. In any case, a transient gaseous layer (further to be referred as "gas") is formed.

In the second stage the gas is exposed to intense laser radiation which provides a saturated population of the resonant atomic level. By superelastic collisions with these excited atoms and

by stimulated bremsstrahlung absorption, seed electrons are heated and multiplied. It is the heated electron component which then by collisional LIBORS-processes also ionizes the gas [1, 2]. The configuration of the CATRION plasma source is schematically shown in Fig. 1.

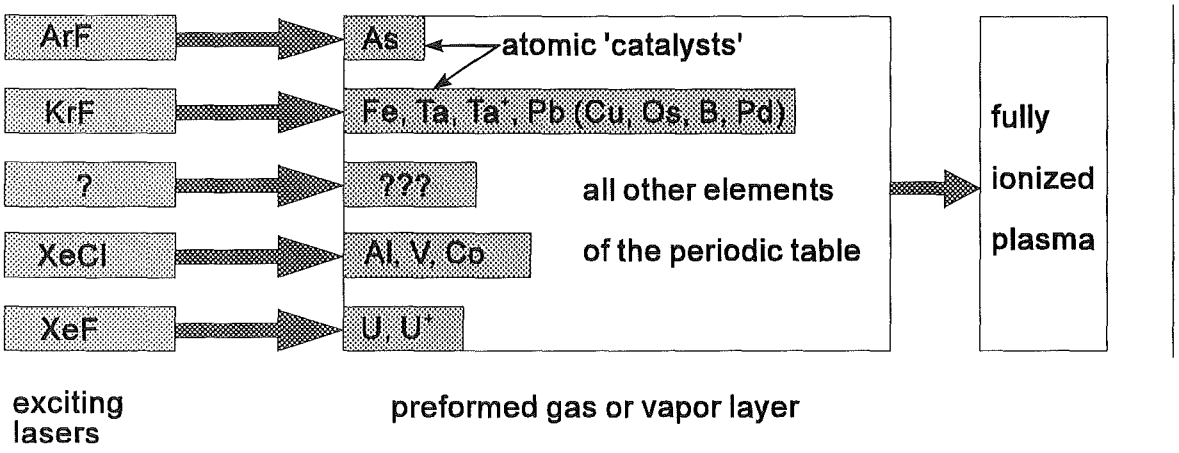

Fig. 1: Anode plasma formation by means of resonant laser radiation in the LIBORS and the CATRION techniques.

The LIBORS-technique has been applied successfully to the formation of a lithium-plasma anode in the PBFA-II diode [3] with the help of the resonant radiation from a dye laser. In principle, any element can be ionized by the LIBORS technique, but to ionize other elements a set of new dye-lasers with wavelength corresponding to a resonance in the level system of these elements should be applied. Unfortunately, flashlamp-pumped dye-lasers are characterized by low efficiency and by low operational life. Their wavelengths do not cover the UV spectral range, whereas resonance transitions of many elements are just occurring in that range. These disadvantages can be overcome by use of the CATRION technique if the application allows the admixture of a specific element in the plasma.

To ionize a gas by means of this technique one has to add to the gas a certain amount of atoms with resonance transitions coinciding with the lasing wavelength of any robust pulsed laser. We have identified seventeen elements of the periodic table, whose resonance transitions overlap with or are close to the lasing spectra of eximer lasers. Fig. 2 demonstrates the shapes of lasing spectra of the most effective eximer lasers (as well as of nitrogen lasers) and the resonance transitions of the above mentioned elements. The upper curves are the fluorescence spectra of corresponding laser transitions. The lasing spectra can be tuned, in principle, inside these ranges by the use of selective laser cavities.

This special element, which we will call further a "catalyst", absorbs the intense laser radiation in the saturation regime and provides a high non-equilibrium population of the upper level of the "catalyst"-atom. Because of the high density in the layer and the saturation of the transition, the probability for electron and photon-electron collisions with the excited atom exceeds the probability of radiative transitions and quenching collisions. As a result, the temperature of the seed electrons in the layer sharply grows and the electrons finally ionize all components of the gas.

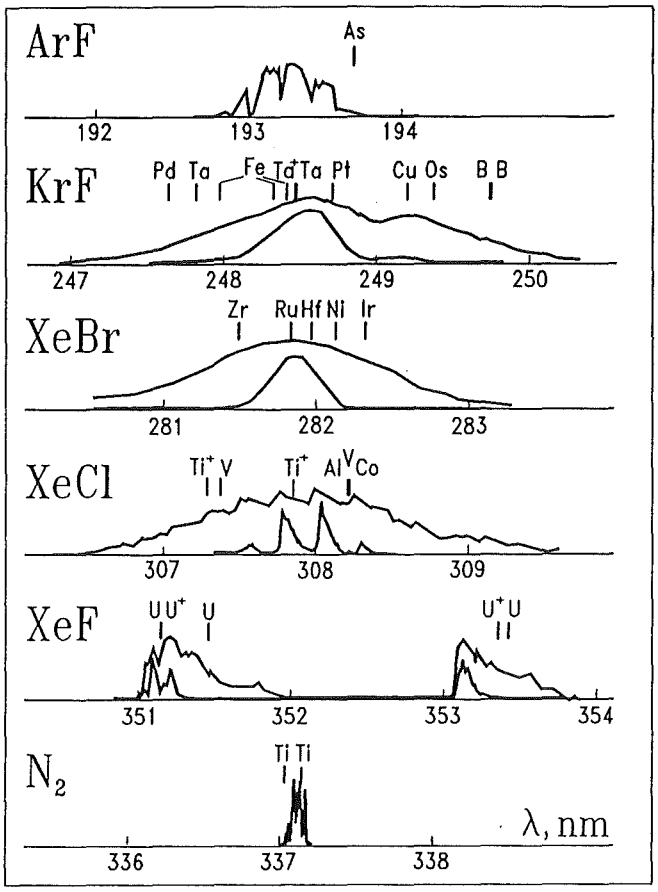

Fig. 2 The lasing spectra of certain robast gas lasers and the nearby resonance spectral lines of several elements.

It should be pointed out, however, that the rate of ionization of excited catalyst atoms is higher then of other non-excited components of the gas mixture. This can lead to only partial ionization of the atoms of interest o us. This difficulty can be overcome if a catalyst ion has the resonance transition at the same wavelength. We have found two "catalysts" (Ta and U) for which both the atom and the single charged ion have resonance transitions at the same wavelength. This allows to continuously pump laser energy into the layer even after complete ionization of the "catalyst"-atoms has occurred.

To estimate the laser intensity required to achieve saturation we have derived the balance equation for the population of a resonance level under steady-state conditions. Let A_{21} and A_{2k} be the Einstein coefficients for the resonance and for the cascade transitions respectively and j_ω be the spectral power density of the laser radiation. The cross-sections for the stimulated transitions σ_{12} and σ_{21} are equal to

$$\sigma_{21}(\omega) = \frac{\lambda^2}{4} a_{21}(\omega) A_{21}, \quad \sigma_{12} = \frac{g_2}{g_1}, \quad \int a_{21}(\omega)\, d\omega = 1$$

Under steady state conditions a balance equation for the population of a resonance level can be derived.

$$n_1 \int j_\omega(\omega)\sigma_{12}(\omega)\, d\omega - n_2 \left[\int j_\omega(\omega)\sigma_{21}(\omega)\, d\omega + A_{21} + \sum_k A_{2k} \right] = 0 \qquad (1)$$

By definition, the saturation parameter is equal to unity, when the rates of spontaneous and stimulated transitions from the upper level (the terms in the square brackets of eq. (1)) are equal. If the laser line is sufficiently broad as compared to the atomic line-width, the saturated radiation intensity j^s_ω is given by the following relation:

$$j^s_\omega = \frac{4}{\lambda^2}\left(1 + \frac{\sum_k A_{2k}}{A_{21}}\right)$$

Let us denote the expression in the brackets by ξ. In the case of a two-level system $\xi = 1$, and $j^s_\omega = 4/\lambda^2_{21}$ [cm^{-2}]. Multiplying j^s_ω by the photon energy $\hbar\omega_{21}$ and transforming from frequency to wavelength, we obtain for J^s_λ :

$$J^s_\lambda = \frac{1.4\,10^{14}\,\xi}{\lambda^5[nm]}\left(\frac{kW}{cm^2\,nm}\right)$$

The quantity J^s_λ/ξ depends only on the laser wavelength and is presented for several gas lasers in Table 1. If cascade transitions from the resonance level are possible these intensity values can be much higher.

laser	ArF	KrF	XeBr	XeCl	N_2	XeF
λ	193	248	282	308	337	351
J^s_λ/ξ	530	150	80	50	33	27

Table 1: Laser wavelength (nm) and saturated intensities (kW/cm²nm)

It should be noted that, on the one hand, the specific value of saturation must be sufficiently low, to produce the most effective absorption of the laser light in the vapor cloud, and on the other hand, it should be sufficiently high to provide an adequate rate of energy transfer to the electrons. To reach a saturation parameter close to unity and to deposit the laser radiation with high efficiency, the lasing spectrum and the atomic absorption line must overlap at least partially.

From Fig. 1 one can see that for certain atoms the overlapping is not too good, and very high laser intensities may be required to saturate these transitions. However, one important point to remember is that the absorption line can be significantly broadened in the resonant light field [4] or due to collisions among gas particles ("pressure broadening"). Overlapping may also be improved by tuning of the laser spectra with a selective resonator within the spectral ranges shown in Fig. 1. An ultimate solution to the problem of optimizing both the vapor density and the radiation intensity is beyond the scope of this work and needs experimental investigations.

Finally, we can list the advantages of the technique of Catalytic Resonance Ionization (see Fig. 3):

(i) For the ionization of gaseous layers which can consist of very different chemical elements including the "catalyst", one needs a single non-tunable pulsed laser only. To prepare the system for the formation of a plasma with other elemental composition only the initial gas mixture must be changed. In this case, the only necessary restriction is to include in the new gas composition the same "catalyst". If it is more convenient, a new laser and a corresponding "catalyst" can be used. A sufficiently large number of "catalysts" simplifies the problem of fabrication of suitable surfaces and allows to obtain very complex gas mixtures.

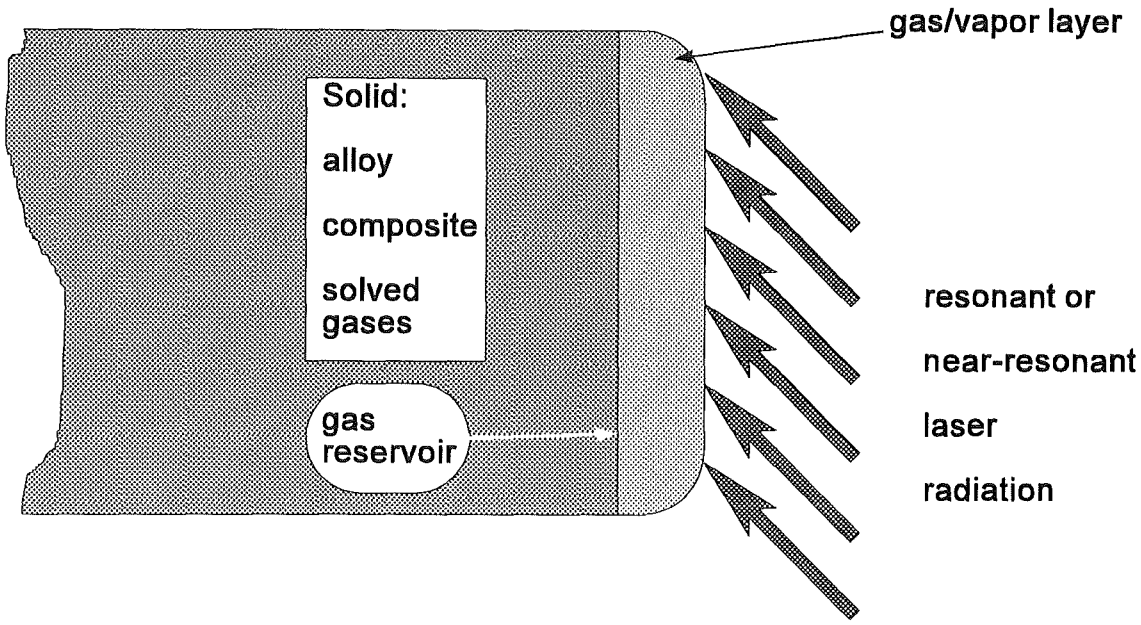

Fig. 3 Schematic of the CATRION plasma source.

(ii) When a short-wavelength laser is applied for the irradiation a copious amount of seed electrons will naturally occur. They will be produced automatically by means of photoionization of excited atoms. This cannot be obtained with the longer wavelength dye lasers.

(iii) The coincidence of wavelengths of resonance transitions in both the atom and the ion, identified for at least two "catalysists" gives us the possibility to pump laser energy into the gas even after complete ionization of the "catalyst" atoms. The possibility does not exist in the usual LIBORS process.

(iv) For the case of a multicomponent plasma there is in addition the possibility to vary the densities of the components independently. This allows to change the absorption coefficient of resonance radiation and to control the rate and the volumetric characteristics of the gas ionization.

References

[1] R.M. Measures, P.G. Cardinal, Phys. Rev. A, 23, 804 (1981).
[2] V.a. Kas'yanov, A.N. Starostin, Plasma Chemistry, issue 16. Moscow: Energoatomizdat, 1990 (in Russian).
[3] G.C. Tisone, T.J. Renk, D.J. Johnson, R.A. Gerber, R.G. Adams, Proc. BEAMS-92, V. 2, 800, 1992.
[4] A. Maitland, M.H. Dunn, Laser Physics, North-Holland, 1969.

The Karlsruhe Diode Simulation Code - Status of the Development

E. Halter[1], M. Krauß[2], C.-D. Munz,
R. Schneider, E. Stein, U. Voß, T. Westermann[3]

Institut für Neutronenphysik und Reaktortechnik, Forschungszentrum Karlsruhe / Technik und Umwelt, Postfach 3640, D-76021 Karlsruhe

A brief conceptual overview and the actual status of the Karlsruhe Diode code development is given in this paper. Two new important attainments are presented in more details: A new interactive grid generation modul to generate complex computational grids in a comfortable way is now available, and furthermore, a new field solver for the instationary Maxwell equations based on high resolution finite-volume methods is proposed.

1. Introduction

To get a deeper insight into the physical phenomena playing an important role in the ion diodes, and hence a better interpretation of the experimental results, extensive numerical simulations have to be performed. From experimental investigations it is obvious [2,3], that the non-neutral plasmas inside the ion diodes can be described mathematically by the fundamental Maxwell-Vlasov equations. In view of numerical modelling, it is more convenient to replace Vlasov equation by its characteristic equations resulting in the so-called Maxwell-Lorentz system.

A simulation program, based on the numerical solution of the Lorentz and stationary Maxwell equations has been developed at the Forschungszentrum Karlsruhe [21] in the last years. This BFCPIC program is an extension of a $2\frac{1}{2}$-dimensional PIC-code [1,8] to boundary-fitted coordinates [15]. This code is an excellent tool for the optimization of the design of the technical relevant diodes [19] and their resulting focusing properties. However, important questions concerning the origin and consequences of electromagnetic instabilities inside the anode-cathode gap which lead to the observed microscopic divergence cannot be answered by this stationary code. For that purpose, the full instationary Maxwell equations have to be considered. In order to remove this lack, the goal of the Karlsruhe Diode (KADI) code initiative is to develope a program system solving numerically the instationary 3-dimensional Maxwell-Lorentz equations for technically relevant geometries. Because of the complexity of this goal it is convenient to pass several intermediate stages: First of all, a $2\frac{1}{2}$-dimensional time-dependent version of the program system should be developed for cartesian grids. Afterwards, an extension of this code to boundary-fitted coordinates should be performed. Finally, the acquired knowledge and experience should be combined, resulting in a 3-dimensional time-dependent production code for boundary-fitted coordinates.

[1]Fachbereich Feinwerktechnik, Fachhochschule Karlsruhe, Postfach 2440, D-76012 Karlsruhe
[2]Hauptabteilung für Datenverarbeitung und Instrumentierung, Forschungszentrum Karlsruhe / Technik und Umwelt, Postfach 3640, D-76021 Karlsruhe
[3]Fachbereich Naturwissenschaften, Fachhochschule Karlsruhe, Postfach 2440, D-76012 Karlsruhe

The organization of this report is as follows. In Section 2 the Maxwell-Vlasov equations are listed and the realization of the numerical model as the whole is briefly sketched out. Numerical realization and algorithmical transposition requires a computational grid. A new way of grid generation [6] for complex geometries, developed in close collaboration with the Fachhochschule Karlsruhe is presented in Section 3. One of the most important parts of a Maxwell-Lorentz code is the field solver for the full instationary system of Maxwell equations. Therefore, a main point of our work was to find out appropriate strategies and to show realizable solutions how to solve the Maxwell equations numerically [7]. A brief overview of the resulting construction methods of the field solver for arbitrary structured grids is given in Section 4. Depending on the method under consideration, different algorithms solving numerically the Maxwell equations for cartesian and cylindrical coordinates are implemented. Finally, in Section 5 some results for test problems are presented and a short outlook of the further activities is given.

2. Mathematical and Numerical Model

An important sub-class of phenomena of a real plasma is obtained, if only the interaction of the charged plasma particles with the electromagnetic field is considered. This idealized theoretical model seems to be sufficient for most physical phenomena observed in ion diodes and is descriped mathematically by the Maxwell-Vlasov equations. Because strong electromagnetic fields occur we have to use the relativistic Vlasov equation (see, e.g., [5])

$$\partial_t f_\alpha + \mathbf{v} \cdot \nabla_x f_\alpha + \mathbf{F}_L \cdot \nabla_p f_\alpha = 0 \qquad (1a)$$
$$\mathbf{F}_L = q_\alpha(\mathbf{E} + \mathbf{v} \times \mathbf{B}) \qquad (1b)$$

for the theoretical treatment. Here, $f_\alpha = f_\alpha(\mathbf{x}, \mathbf{p}, t)$ denotes the distribution function in phase space of each plasma component $\alpha = e, i$ for electrons and ions, respectively, and $\mathbf{F}_L$ is the Lorentz force. In the language of partial differential equations, the general solution of (1) is given by its characteristic equations, the so-called Lorentz equations,

$$\frac{d\mathbf{x}(t)}{dt} = \mathbf{v}(t) \quad (2a) \qquad \frac{d\mathbf{p}(t)}{dt} = \mathbf{F}_L\,, \quad (2b)$$

where the relativistic momentum is determined according to $\mathbf{p} = m\gamma\mathbf{v}$ with $\gamma^2 = 1 + \frac{\mathbf{p}^2}{m^2c^2}$. The difficulty in solving (2) arise from the fact that the fields are not given explicitly. Rather they have to be calculated in a self-consistent manner from the Maxwell equations

$$\nabla \times \mathbf{B} - \partial_t \mathbf{E} = \mu_0 \sum_\alpha q_\alpha \int d^3p \mathbf{v} f_\alpha \quad (3a) \qquad \nabla \times \mathbf{E} + \partial_t \mathbf{B} = 0 \quad (3b)$$
$$\nabla \cdot \mathbf{B} = 0 \quad (3c) \qquad \nabla \cdot \mathbf{E} = \frac{1}{\epsilon_0} \sum_\alpha q_\alpha \int d^3p f_\alpha \quad (3d)$$

Obviously from (1) and (3), the Maxwell-Vlasov and consequently the Maxwell-Lorentz system (2), (3) form a non-linear model system described by an integro-differential equation.

For the numerical realization of the Maxwell-Lorentz system (2), (3) well-known techniques called particle methods [8] are applied. The new phase space coordinates for an ensemble of particles for a new time level $t = t_{n+1}$ is obtained by the numerical solution of (2). The assignment of the charge and velocity of the particles to the nodes of the computational grid with special techniques [8] - often called Particle-in-Cell (PIC) methods - leads to an approximation of the source terms of equations (3a) and (3d). The new electromagnetic fields are then obtained

by the field solver of the full set of Maxwell equations. The last step within the iteration circle is to interpolate these new fields with a consistent method to the actual position of the macro particles at $t = t_{n+1}$ and to calculate the Lorentz force according to (1b).

Most steps of the particle treatment are already realized in the stationary Maxwell-Lorentz solver [21] for boundary-fitted coordinates. Therefore, we can refer to methods such as the particle pushing [18], localization [20] and interpolation [14], well established in the BFCPIC code. However, these subroutines require a careful adaptation to the new data structure fixed by the solution method of the instationary Maxwell equations. A modified and tested version of these particle treatment routines should be available at the beginning of this year.

3. Grid Generation

Numerical solution of concrete field problems such as the instationary Maxwell equations require an appropriate discretization of the underlying computational domain. Well established grid generation procedures for complex geometries are based on methods using boundary-fitted coordinates [15]. A brief overview, especially of the derivatives of these methods used in our context is given in [6]. From the practical point of view, grid generation for technical field calculations is often cumbersome and connected with great efforts. The aspired accuracy in mapping the geometry demands for the acceptable representation of the boundary of the considered geometry, the controlling of the grid fineness and the avoidance of strong distortions of the grid. A suitable way to record the geometry of a technical device is to use one of the widespreaded CAD-systems. A new strategy combining this powerful construction tool (with all its auxillaries like ZOOM-functions, etc.) directly with grid generation was recently proposed in [6] and enables us now to generate a computational grid in two dimensions in an effective and comfortable manner. An appropriate CAD-system which satisfies our requirements is AutoCAD (version 12). This is a so-called open system which allows us to refer to self-written routines [6], necessary for the grid generation and optimization. Without going into the details, we summerize here the essential advantages of this new grid generation modul called InGrid (**In**teravtive **Grid** generation). In general, it turns out that the time spent on generating a computational grid becomes reasonably small. Since the grid generation is performed interactively, each intermediate step can be evaluated on the screen and suitable actions for a further optimization of the grid can be done directly. Therefore, it is planned for the future that this interactive method is put into action to generate the computational grid in a standardized way for all ion diodes under consideration. A modified version of InGrid which considers the special data structure of the BFCPIC code is in preparation and should be available in February 1995.

The general operation method of the InGrid modul is illustrated in Figure 1, where several grid generation steps for a special device are shown. For that purpose, a simple rectangular grid is posed optionally within the computational domain (Fig. 1a). After pulling the four corners of this grid to appropriate positions (Fig. 1a), the outer boundary of the grid and some inner grid lines have successively to be brought to coincidence with the border of the computational domain. Smoothing of the grid edges and the subsequent smoothing of the grid as the whole is shown in Figure 1b and 1c. Often numerical methods require that inner structures of the computational domain coincide with grid lines. This implies that single grid points, or sometimes, whole grid lines have be to projected onto these structures as it is depicted in Figure 1d. Undesired distortions of the grid can influence effectively the accuracy and robustness of the applied numerical schemes. The disadvantageous run of the grid lines in Figure 1e can be

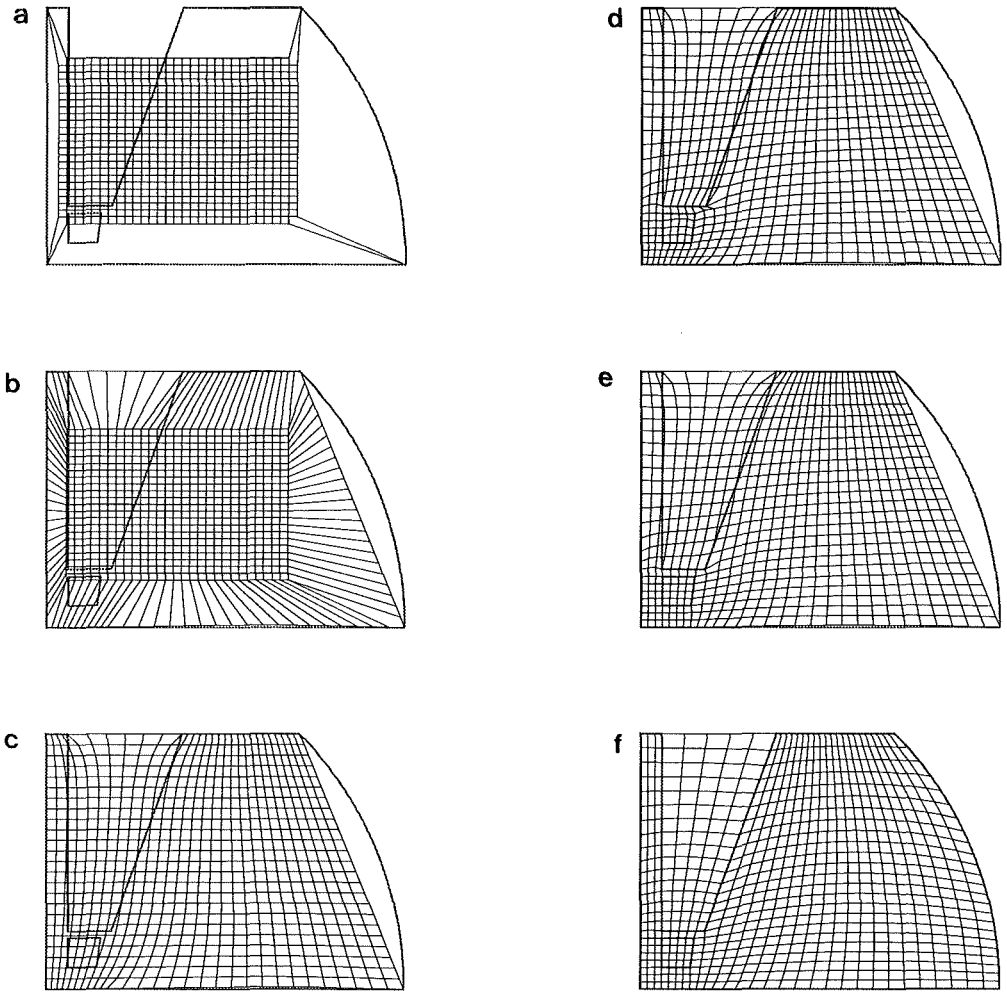

Figure 1: Interactive grid generation performed with the program InGrid. The sequence of intermediate steps usually seen on the screen, gives information about the numerous optional function keys available in and the advance of InGrid to generate a boundary-fitted grid.

removed if one grid line is pulled out of the right border of the distinct upper inner structure. After repeated relaxation and appropriate mapping of the grid lines onto the border of the computational domain the boundary-fitted grid generation is finished (Fig. 1f).

4. Numerical Treatment of the Maxwell equations

Well established concepts solving numerically the field equations (3) in the context of plasma simulation [4] are based on finite-differce (FD) methods on staggered grids [22]. A very clear presentation of these methods which are second order accurate in space and time, is given in [16,17]. Integrating the instationary field equations (3) by using Stokes's theorem, staggered grids are introduced in a natural way: electric and magnetic quantities are calculated on the so-called "electric" and "dual" or "magnetic" grid, respectively. Such kind of cartesian FD methods are successfully applied in the Quicksilver code (see e.g. [13]). However, it has been found out that an implicit discretization of Maxwell's equations is necessary in order to stabilize the field solver. An extention of the FD methods from equidistant to irregular square grids can be done applying transformation methods dicussed for example in [9].

An alternative approach solving Maxwell's equations numerically is obtained using high resolution finite-volume (FV) methods [10]. This proceeding seems to be interesting, because these methods are very evident and robust, and beyond that, a lot of experience is available [11,12] in the INR. As it is shown in [7], Maxwell's equations can be written as a conservation law, that means in the form

$$\partial_t u + \sum_{i=1}^{3} \mathcal{K}_i \frac{\partial u}{\partial x_i} = q(u) \; . \qquad (4)$$

Here, $u = (E_1, E_2, E_3, B_1, B_2, B_3)^T$ denotes the vector of the conserved quantities, the $\mathcal{K}_i \in R^{6\times 6}$ are constant matrices and the right-hand side (rhs) $q(u)$ contains the current density (cf eq.(3)). In this paper, we restrict ourselves to the cartesian 2-dimensional and the rotationally symmetric case, where x_1, x_2 stands now for x and y or z and r, respectively. In the latter case the rhs depends on the geometry, whereas the matrices remain the same (for more details see [7]). For conservation laws such like (4), there exists a large class of methods in conservation form, also called FV methods. These methods are also well-known as high resolution schemes for hyperbolic conservation laws and have been developed originally for the equation of gas dynamics [10]. The FV methods are obtained by approximating the conservation laws (4) integrated over an arbitraryly shaped cell V_{ij} of the grid and the time interval $[t_n, t_{n+1}]$. With $u_{ij}^n = \frac{1}{|V_{ij}|} \int u(t_n)\, dV$, the mean value of u over the grid cell with the volume $|V_{ij}|$, one gets using the Gaussian law

$$u_{ij}^{n+1} = u_{ij}^n - \frac{\Delta t}{|V_{ij}|} \sum_{\beta} g_{ij,\beta} + \Delta t\, q_{ij} \qquad (5a)$$

$$g_{ij,\beta} \approx \frac{1}{\Delta t} \int_{t_n}^{t_{n+1}} \int_{S_{ij,\beta}} (n_{ij,\beta}^{(1)} \mathcal{K}_1 + n_{ij,\beta}^{(2)} \mathcal{K}_2)\, u\, dS\, dt \; , \qquad (5b)$$

where again q_{ij} denotes the source term averaged over V_{ij} and $[t_n, t_{n+1}]$. The sum in (5a) runs over all sides of the cell V_{ij} and the so-called numerical fluxes $g_{ij,\beta}$ have to be approximated from (5b) (see [7]), where $n_{ij,\beta}^{(1)}$ and $n_{ij,\beta}^{(2)}$ denote the cartesian components of the outer normal. The numerical fluxes have to be estimated from the knowledge of the u_{ij}^n. This is done by solving the so-called Riemann problem [10,11]. In the present linear case it can be solved exactly. In this way one takes into account the wave structure of solutions of hyperbolic conservation

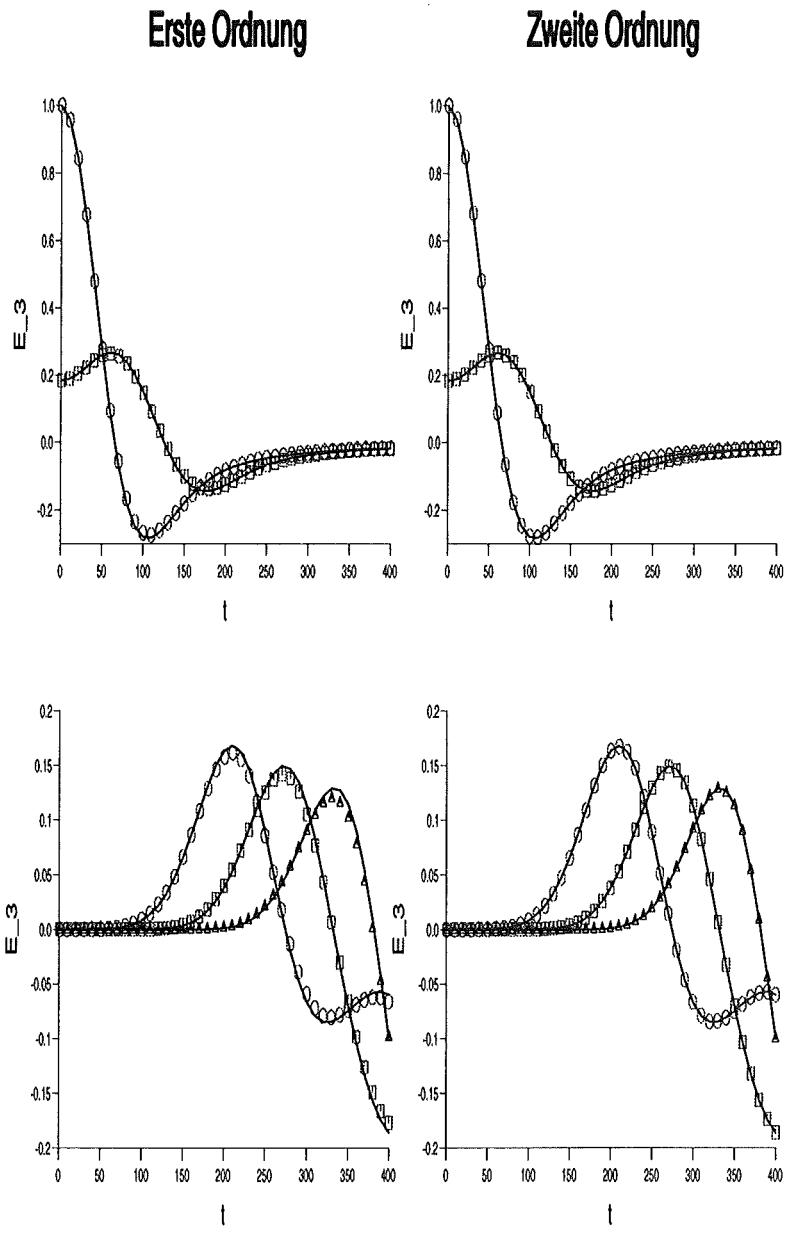

Figure 2: Temporal evolution of the third component of the electric field E_3 on the nano-second time scale for five different but fixed points in space. The numerical results obtained from a first (left) and second (right) order FV scheme are compared with the exact solutions (solid lines).

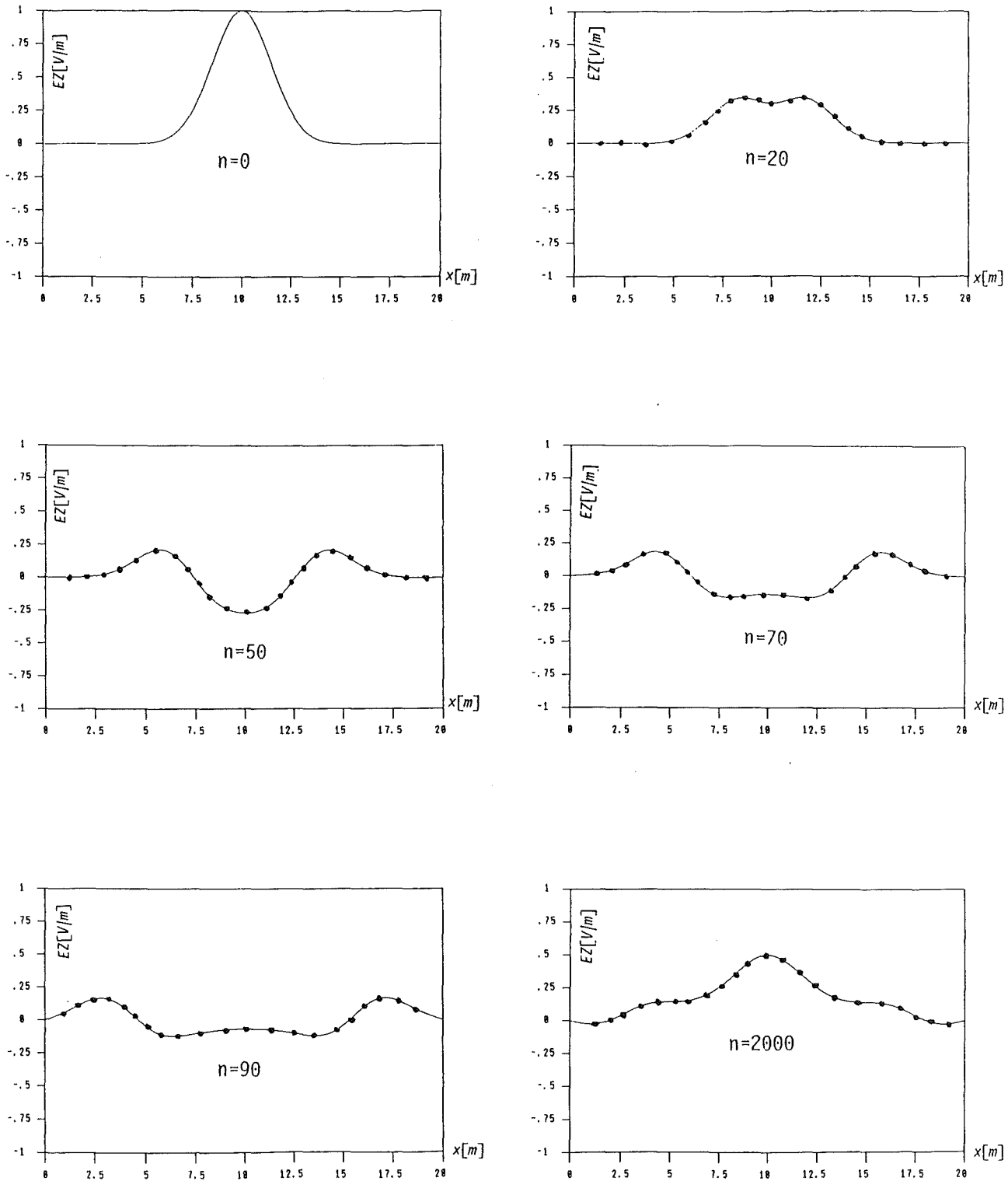

Figure 3: Comparison between the exact ("—") and numerically ("• • •") calculated third component of the electric field using a FD scheme. With constant $\Delta t = 0.235ns$ and according to $t = n\Delta t$, the snapshots are recorded at t = 4.70, 11.75, 16.45, 21.15, 470.00 ns.

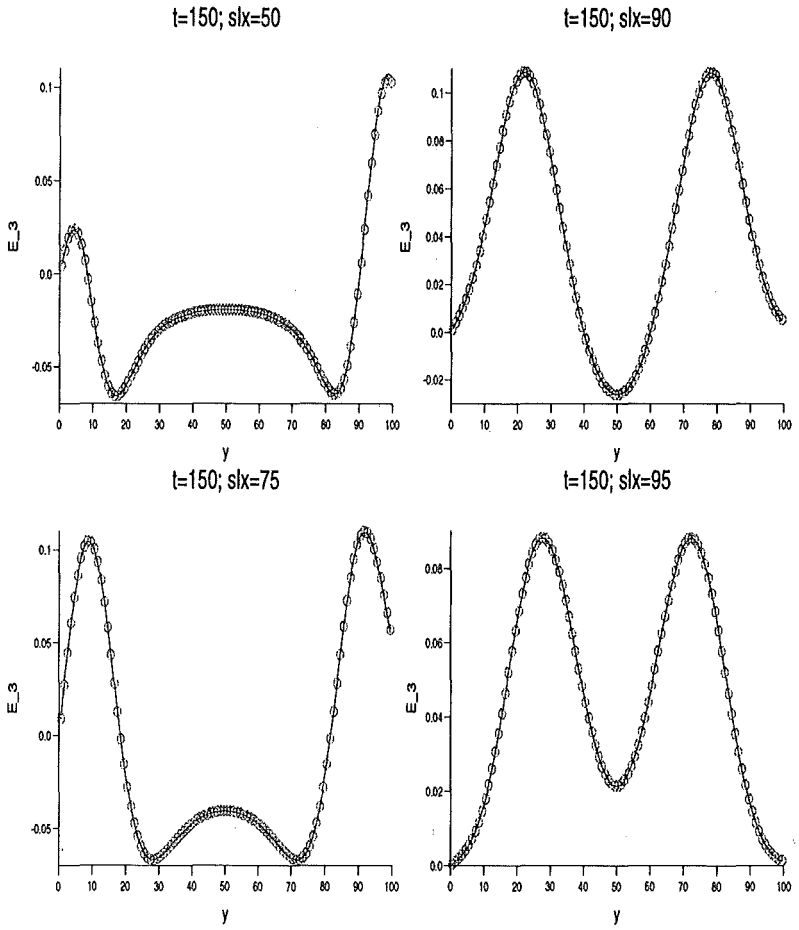

Figure 4: Comparison of the numerically obtained reference solution ("—") with this one calculated for the "open border" condition ("ooo") at t = 150ns for four x-slices ($x = 50$, $x = 75$, $x = 90$, $x = 95$) using a second order FV scheme.

laws, responsible for the robustness of these schemes. We want to emphasize, that FV methods describe the time evolution of the mean value of u over a grid cell. The numerical fluxes depend on the values of u_{ij}^n for in general, different i, j but the same n. Therefore, FV methods are explicit methods. The order of the schemes depends on the numerical flux calculation and can be easily extended to two or even higher order [11,12]. Another advantage of the FV approach is, that there are no additional assumptions needed about the grid. In fact, FV methods can be constructed for arbitrary irregular grids [7]. As it is shown furthermore in [7], the treatment of both physical and open boundary conditions can be realized numerically in a very easy way.

Program versions for cartesian and cylindrical coordinates using FD and FV methods are finished for testing. In the course of this year, it should be found out by means of concrete test problems which scheme is the most suitable fot the application to ion diode simulations.

5. Results

On the basis of typical initial-boundary-value (IBV) problems [7], the $2\frac{1}{2}$-dimensional field solvers based on FD and FV methods, respectively, are tested for cartesian and cylindrical coordinates. For that purpose, different possible boundary conditions like "perfect conductor", "open border", "periodic border", etc., have to be formulated clearly and realized numerically [7]. The results shown in Figures 2 to 4 are obtained for a special IBV problem which could be treated analytically. The third component of the electric field E_3 is excited initially according to a sharp Gaussian in the center of the computational domain which is surrounded by a perfect conductor. The exact and numerically obtained temporal evolution of E_3 at five different but fixed points in space is depicted in Figure 2. The results of the first order upwind scheme (left) are in an acceptable and those of the second order extension (right) are nearly in a perfect agreement with the exact solution. A further comparison between the exact and numerically calculated electric field E_3 using a FD scheme is presented in Figure 3. Obviously, the agreement between the exact and the numerical results are pretty well. Results testing the "open border" condition are shown in Figure 4. Obviously, this numerical motivated condition [7] influence insignificantly the wave propagation.

Acknowledgements

It is a pleasure to thank S. Illy and E. Borie for numerous stimulating and helpful discussions and for the advices concerning technical details in testing the field solver.

References

1. Birdsall, C.K. and Langdon, A.B.; *Plasma Physics via Computer Simulation*, McGraw-Hill, New York, 1985.
2. Bluhm, H., Hoppé, P., Laqua, H., and Rusch, D.; *' Production and investigation of TW proton beams for an annular diode using strong radial magnetic insulation fields and a preformed anode plasma source '*, Proc. IEEE **80**, 995 (1992).
3. Bluhm, H.J., Laqua, H.P., Buth, L., Hoppé, P.J.W., and Rusch, D.; *' Formation of a homogeneous hydrogen plasma layer for the production of Terawatt ion beams '*, IEEE Trans. Plasma Sci. **21**, 560 (1993).

4. Boris, J.P.; *' Relativistic Plasma Simulation - Optimization of a Hybrid Code '*, Proc. 4th Conf. on Num. Sim. of Plasmas, NRL Washington DC, 1970.
5. Davidson, R.C.; *Theory of Nonneutral Plasmas*, Benjamin, Reading, 1974.
6. Halter, E., Kündahl, J., Krauß, M., Munz, C.-D., Schneider, R., Stein, E., Voß, U., and Westermann, T.; *' Interaktive Gittererzeugung im Rahmen eines offenen CAD-Systems '* , 9. DGLR/AG STAB-Symposium 1994, Erlangen, 1994.
7. Halter, E., Krauß, M., Munz, C.-D., Schneider, R., Stein, E., Voß, U., and Westermann, T.; *' Conceptual Studies to solve the instationary Maxwell-Vlasov Model System numerically '*, Forschungszentrum Karlsruhe - Technik und Umwelt GmbH, in preparation.
8. Hockney, R.W., Eastwood, J.W.; *Computer Simulation using Particles*, McGraw-Hill, New York, 1981.
9. Holland R.; *' Finite-Difference Solution of Maxwell's Equations in generalized non-orthogonal Coordinates '*, IEEE Trans. Nucl. Sci., **30**, 4589(1983).
10. LeVeque, R.J.; *Numerical Methods for Conservation Laws*, Birkhäuser, Basel, 1990.
11. Munz, C.-D.; *' Theorie und Numerik nichtlinearer hyperbolischer Differentialgleichungen '*, Kernforschungszentrum Karlsruhe GmbH, **KfK 4805**, Karlsruhe, 1990.
12. Munz, C.-D.; *' Godunov-Typ Verfahren für die Gleichungen der kompressiblen Strömungsmechanik '*, Kernforschungszentrum Karlsruhe GmbH, **KfK 5058**, Karlsruhe, 1992.
13. Pointon, T.D. et al.; *' Three-dimensional particle-in-cell simulation of applied-B ion diodes '*, Phys. Plasmas, **1**, 429, (1994).
14. Seldner, D., Westermann, T.; *' Algorithms for Interpolation and Localization in Irregular 2D Meshes '*, J. Comput. Phys., **79**, 1 (1988).
15. Thompson, J.F., Warsi, Z.U.A. and Mastin, C.W.; *' Boundary-fitted coordinate systems for numerical solution of partial differtial equations - A review '*, J. Comput. Phys. **47**, 1 (1982).
16. Weiland, T.; *' Eine Methode zur Lösung der Maxwellgleichungen für sechskomponentige Felder auf diskreter Basis '*, AEÜ, Band 31, Heft 3, 116 (1977).
17. Weiland, T.; *' On the Numerical Solution of Maxwell's Equations and Applications in the Field of Accelerator Physics '*, Deutsches Elektronen-Synchrotron, DESY 84-006, Hamburg, 1984.
18. Westermann, T.; *' Teilchenfortbewegung in elektro-magnetischen Feldern '*, Kernforschungszentrum Karlsruhe GmbH, **KfK 4325**, Karlsruhe, 1988.
19. Westermann, T.; *' Optimization by numerical simulation of the focusing properties of self-magnetically insulated ion diodes '*, Appl. Phys. Lett. **58**, 696 (1991).
20. Westermann, T.; *' Localization Schemes in 2D Boundary-Fitted Grids '*, J. Comput. Phys., **101**, 307 (1992).
21. Westermann, T.; *' Numerical modelling of the stationary Maxwell-Lorentz System in technical devices '*, IJNM **7**, 43 (1994).
22. Yee, K.S.; *'Numerical Solution of Initial Boundary Value Problems Involving Maxwell's Equations in Isotropic Media '*, IEEE Trans. Ant.& Prop., **14**, 302(1966).

Characteristics of the Ion Beam Produced by the B_Θ Diode

P. Hoppé, H. Bachmann, W. Bauer, H. Bluhm, L. Buth,
H. Massier, D. Rusch, O. Stoltz, W.Väth

The comparison of measured to calculated data of foil acceleration experiments showed considerable discrepencies which partly might be due to experimental uncertainties. Therefore the characteristics of the beam produced by the B_Θ diode -routinely used for this type of experiments- were reinvestigated with respect to the maximum of the proton power density and to its pulse width. A most likely time history of the proton power density achieved in the focus is suggested. Furthermore the reproducibility of beam generation and possible measures to reduce the uncertainty in the achieved proton power density were considered. Finally estimates are given concerning the non-protonic components in the ion beam.

1. Introduction

In foil acceleration experiments performed at the high power pulse generator KALIF [1] the light ion beam produced in an ion diode [2] impacts on a thin foil target placed in the focal plane of the diode. As a consequence the foil is accelerated to velocities up to 12 km/s measured by the ORVIS system [3]. For the interpretation of this type of experiments theoretical models are under development which need the ion beam characteristics as input data. Due to unexpected large differences between calculated and measured acceleration data [4] also the beam characteristics were considered as a possible error source. These differences were found especially pronounced in acceleration experiments carried out with the B_Θ diode: the maximum of the measured proton power density as well as the pulse duration should be reduced by a factor of about 2 in order to match the calculations. Therefore the characteristics of the beam produced by this diode type [5] were reinvestigated in a set of new experiments.

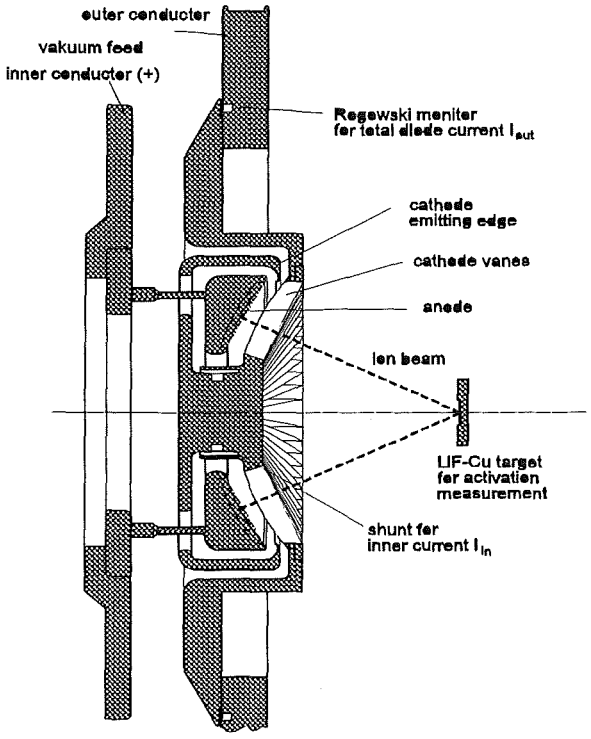

Fig.1: Cross section of the B_Θ diode

The basic and most reliable diagnostic tool for the ion beam delivered by any focussing diode consists of an appropriate nuclear activation target placed in its focal plane, hence the use of an acceleration foil in the same shot is not possible. This means one has to rely either on the reproducibility of the beam parameters produced in subsequent KALIF pulses or one can try to relate the beam parameters for a particular shot to some other diagnostics compatible with the acceleration experiment. An ion diode should convert the electrical energy provided by the pulsed power generator with high efficiency into kinetic energy of an ion beam. Therefore it was tried first to relate the measured electrical quantities like voltage at the diode V_d and/or the currents outside I_{out} and inside I_{in} of the diode to the parameters of the ion beam (Fig.1). Later also the signals of other monitors were investigated whether they can be used for beam characterization.

2. Measurement of the maximum value of the proton power density

For the numerical simulation of the foil acceleration experiments it is normally assumed that the ion beam impinging on the foil consists of protons only. In acceleration experiments the foil was placed in the focal plane, determined by shadow box diagnostics (Fig. 1). Neglecting time-of-flight effects the maximum of the proton power density is expected at this position and at the time the electrical power transferred to the diode reaches its maximum. Therefore the most interesting quantity to be verified is the 'peak' proton power density. This value also characterizes the performance of a focussing diode and is therefore necessary for its optimal design. This peak proton power density $p_{p,p}$ was determined by the following expression:

$$p_{p,p} = \frac{1}{A_t} \cdot \langle I_p \rangle \cdot f_r \cdot f_t \cdot V_{d,p} \qquad (1)$$

In this equation $\langle I_p \rangle$ is the mean proton current calculated from the count rates of an appropriate activation target placed in the focal plane. Appropriate activation materials for the ion energy range achieved at the KALIF generator are lithiumfluorid on copper or carbon [6]. In contrast to C targets the activation results from LiF/Cu targets are not sensitive to ablation. Therefore LiF/Cu targets can be placed directly in the focus whereas C targets should be used at positions where the beam current density is below some 100 A/cm^2. The mean proton current $\langle I_p \rangle$ determined with such activation targets is an average over both, the area A_t of the target as well as over all time intervals during which the activation conditions are fulfilled. Assuming that during the pulse: a) the space distribution of the beam is constant and independant from its time history and b) the ratio between diode and proton current also remains constant, one can relate the mean proton current $\langle I_p \rangle$ to its value in the center of the focus at the time the electrical power in the diode reaches its maximum by two separable and constant coefficients f_r and f_t. The coefficient f_r than accounts for the radial distribution of the proton density (measured in nuclear reaction experiments on boron foils [7]) while the coefficient f_t describes the time evolution of the current in the diode, i.e. the ratio of the current in the diode at peak power to the mean diode current. This mean diode current is calculated with the same weighting function as used for the determination of the mean proton current. The radial distribution coefficient f_r found in 3 experiments with boron foils varied from 2.75 and 3.25 for a target diameter of 20 mm [8]. This coefficient cannot be determined for a particular acceleration experiment: the use of a boron foil is not compatibel with an acceleration foil. In contrast to f_r the coefficient f_t can be determined for each experiment, typical values are from 1.1 to 1.3. Finally, the diode voltage V_d (i.e. the voltage at the mid radius of the diode) was determined by applying inductive correction terms to the voltage measured at the water/vacuum interface or to the voltage measured closer to the diode by the vacuum voltage monitor. The maximum error in the measured diode voltage is below 10%. The diode voltage $V_{d,p}$ to be used for the determination of the peak proton power density in eq.1 is the voltage which occurrs at the moment the electrical power in the diode reaches its maximum.

The peak proton power density estimated in that way in earlier experiments was always based on the calibration data measured on a Van de Graaff generator for LiF/Cu activation targets with a 1 mm thick LiF layer sintered on a 5 mm thick copper substrate of 50 mm diameter. This calibration was checked in a set of new experiments where carbon and LiF/Cu targets were mounted together far downstream of the focus where possible azimuthal asymmetries in the ion beam should smooth out and the current densities were sufficiently low to avoid

ablation of the carbon target surface. The activation of a carbon and a LiF/Cu target in the same pulse showed about 10 % difference only for LiF/Cu targets fabricated in batch1. For two targets fabricated later (batch 2) a difference of 23% and 36 % was found compared to the carbon targets as well as to the Van de Graaff calibration. These observed sensitivity changes of the sintered LiF/Cu activation targets might be caused by impurities introduced to the LiF layers by the sintering process. Contaminants like carbon or metals may absorb or slow down protons which hence contribute less to the activation. Therefore the sintered targets were replaced by 1 mm thick LiF glass discs - which cannot have this type of contamination - fixed on a copper substrate of the same dimensions as already used before (batch 3). The peak proton power densities measured with these targets were found in agreement with the results from the sintered batch 1 targets.

The calculation of the peak proton power density evaluated with eq.1 for 16 activation experiments using LiF/Cu targets from different batches and in different experimental campaigns gave peak proton power densities in the focus from 0.1 to 0.19 TW/cm^2. In these experiments no anomalies in the electrical signals were observed and the diode was always used in its standard geometry (Fig.1). The most probable value of the peak proton power density is 0.15 TW/cm^2 only instead of 0.25 TW/cm^2 quoted earlier [5]. The reduction is mainly caused by the sensitivity problems of the LiF/Cu targets described before. This difference as well as the large experimental uncertainty of ±0.05 TW/cm^2 - just covering the results of these 16 activation experiments - explains at least a part of the discrepencies between the calculations and the experimental data [10].

3. Investigation of the reproducibility of ion beam generation

In order to reduce the experimental uncertainty of the peak proton power density achieved in a particular foil acceleration experiment attempts were made to relate the LiF/Cu activation results to expressions calculated on basis of the measured voltage or currents at the diode. Since the novel monitor for the measurement of the current I_{in} was operational only in the last experimental campaign, this comparison had to be limited to 12 activation experiments. Neither mean values like the mean ion current I_p' calculated from the difference of the measured currents I_{out} and I_{in} (Fig.2) nor peak values of e.g. the diode power $P_d = V_d I_{out}$, the ion power $P_{ion} = V_d$ (I_{out} -I_{in}) or the time-of-flight corrected ion power to the focal plane (Fig. 3) could be correlated to the activation results. Also relations to the peak value of the x-rays produced by the electron losses and measured with PIN diodes were not found.

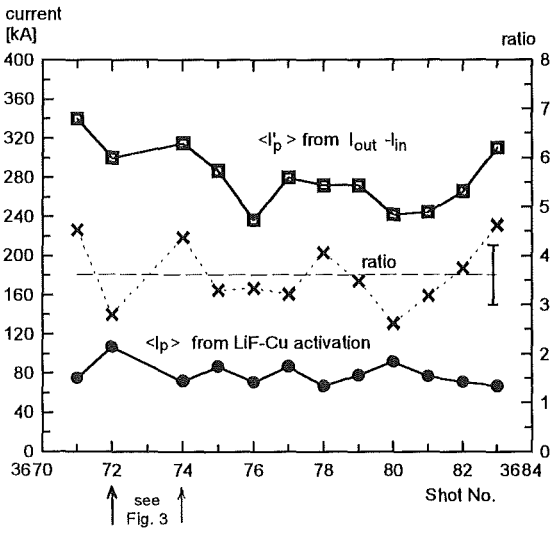

Fig.2: Comparison of the mean currents from activation and electrical measurements

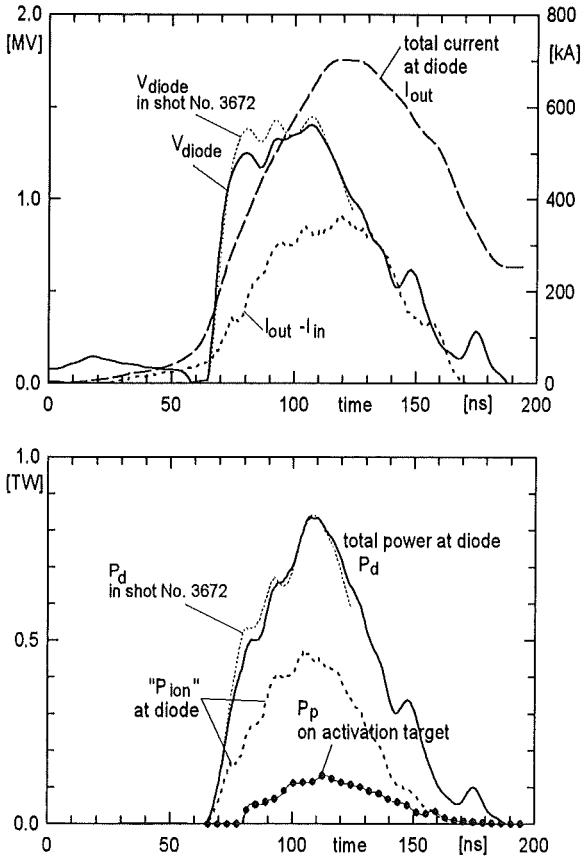

Fig. 3: Electrical data for the shots No. 3672 and No. 3674. Differences between the signals - as far as noticable - are marked.

The electrical signals measured near the diode are consistent with all other diagnostics of the KALIF generator and are also in agreement with transmission line calculations. Therefore they are considered as reliable. Variations of the sensitivity of the LiF glass activation targets are unlikely since this LiF glass is fabricated in large quantities and was from the same batch. A reduction in the sensitivity of the LiF/Cu targets due to proton range shortening in the hot surface plasma produced by the ion beam in principle is possible but this effect is expected to occur for proton power densities above 0.3 to 0.4 TW/cm^2 [9]. However, the fraction of the mean proton current collected in the focus plane (i.e. including fractions of the beam outside of the surface of the activation target) was only between 22% and 33% of the mean diode current $\langle I_{out} \rangle$ and from 36% to 63% of the mean ion current $\langle I_{out} - I_{in} \rangle$. This means that only a small part of the total electrical energy flowing into the diode is transferred to protons with energies above the 500 keV activation threshold of LiF and that most of the diode current I_{out} is due to either protons of lower energies or heavier ion species or to electron losses. The even larger spread in the fraction of the mean ion current mentioned before might indicate that in addition also the focussing properties - described by the coefficient f_r - of this diode do not remain constant. This is clearly demonstrated by quite different peak proton power densities (0.18 TW/cm^2 for No. 3672 and 0.12 TW/cm^2 for No. 3674) measured in two experiments with very similar electrical characteristics (Figs. 2,3). The contrary was also observed: experiments showing quite different electrical data produced similar activation results. These observations help to understand the ±0.05 TW/cm^2 spread of the peak proton power density around the most probable value of 0.15 TW/cm^2 delivered to a target in the focal plane. They also explain the lack of a clear relation between the peak proton power density found in activation experiments and all other diagnostics. This also means that for a shot showing normal electrical signals no possibility exists to reduce the experimental uncertainty of the peak proton power density achieved in the focus of the B_Θ diode.

4. Time history and composition of the ion beam

With the problems described above a precise and reliable time history of the proton power density in the focus cannot be established on basis of the measured currents and the voltage at the diode. Therefore the curve achieved by scaling the peak proton power density from activation measurements of 0.15 TW/cm^2 to the peak of the ion power in the focal plane P_{foc} should be considered as a best estimate only (Fig. 4).The fast rising leading edge is due to 'bunching' of the protons: protons of lower energies which started earlier in time at the anode may reach the target together with protons born later but accelerated to higher energies. Thereby the leading edge of the power in the focus steepens up during voltage rise and

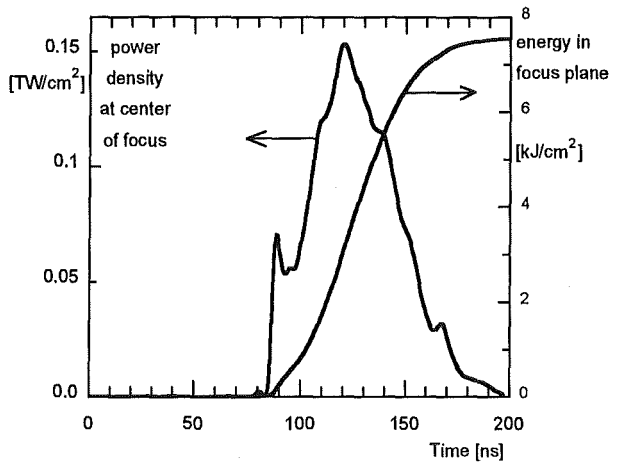

Fig. 4: Proton power density in the focus estimated on basis of the electrical signals

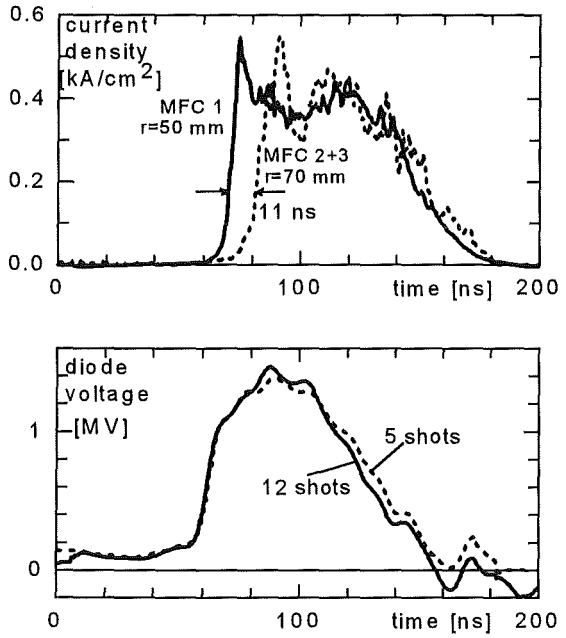

Fig. 5: Averaged signals of magnetically insulated Faraday cups placed on different radial positions (above) and averaged diode voltage (below)

stretches out during voltage decay. This sharp rise was found in all experiments and was also observed by the ORVIS system [3]. Details of the first peak occurring in the power density in the focus are of course not very reliable. However, at least the steep increase also seems to be observable by magnetically insulated Faraday cups used on different radial positions behind the cathode grid (Fig. 5). The delay of 11 ns in the cup signals from different radii is connected to the turn on characteristics of this diode. Due to the rather small insulating magnetic field of these cups of 0.1 T only their sensitivity throughout the pulse may not remain constant. However, such sensitivity changes should have only a minor influence on the measured time duration of the ion beam from 60 to 80 ns (Fig. 5).

Indications on the composition of the ion beam were achieved from experiments where 6 μm thick aluminum foils were placed some millimeters in front of the aperture of the Faraday cups. The signals of unfiltered and filtered Faraday cups (Fig. 6) show no significant difference for most of the time. This would indicate that the ion beam does not contain a significant fraction of carbon C^+ ions because they could only penetrate the aluminum foil if their energy is above 9 MeV. This would require an acceleration voltage which cannot be supplied by the KALIF generator. The trailing edge of the filtered Faraday cup signals might show the absorption of low energy protons by the 6μm aluminum foil when compared to the unfiltered signal. This result would indicate that most of the beam observed on the position of these Faraday cups i.e. just behind the cathode is due to protons. However, because of their aperture of 1 mm diameter, these cups sample only a very small part of the beam (0.1%). A further indication on the beam composition comes from the time lag measured between the onset of Faraday cup signals mounted behind the cathode and far behind the focal plane (Fig. 7). This time lag corresponds to the time of flight of protons with a maximum energy of 1.4 MeV as measured by the peak of the diode voltage. No distinct patterns in the Faraday cup signals related to ions with different charge to mass ratios could be identified. This supports the results of the filtering experiments.

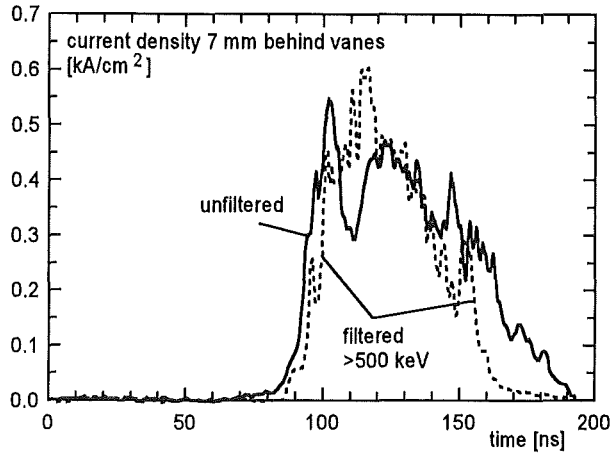

Fig. 6: Averaged current densities measured by unfiltered and filtered Faraday cups 7 mm behind the cathode grid

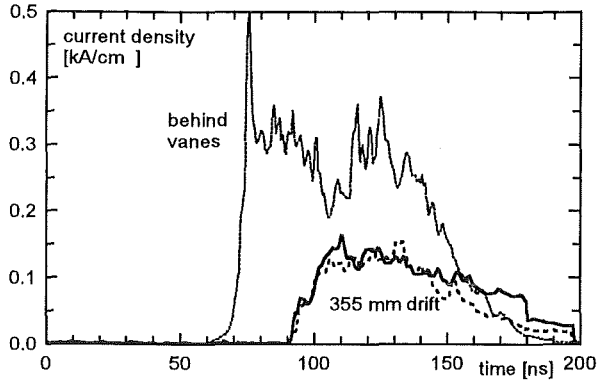

Fig.7: Current density at two locations in 355 mm distance from the diode to produce time-of-flight separation of the ion species

The following rough current balance can also give some information on the beam composition. In some experiments the measured current in the focal plane due to protons with energies above 500 keV was around 60% of the ion current calculated from the difference between the outer and inner current I_{out} and I_{in} respectively. The I_{out} measurement does not take into account electron losses in the magnetically insulated vacuum transmission line between the diode and the place of the current monitors. The monitor for the current I_{in} cannot measure - by principle - vacuum electron flow. Therefore this current will be underestimated. The transparency of the cathode grid will become certainly smaller due to plasma formation on the grids and finally the protons with energies below 500 keV will not contribute to the activation of the LiF/Cu target. All of these phenomena are time dependent and cannot be estimated reliably. However all of them tend to enhance the discrepency between the current delivered to the LiF/Cu target and the measured ion current. If each of them contribute with 5 to 10 % only, this rough balance supports the measurements of the magnetically insulated Faraday cups: the non-protonic ion fraction of the beam monitored downstreams of the cathode grid of the B_Θ diode is surprisingly low. However, whether this is related to the absorbtion of the carbon ions in the cathode plasmas or to the insulating magnetic field of 0.1 T only of the Faraday cups remains an open question.

5. Conclusions and outlook

In summary it can be stated that part of the discrepencies among the calculations and the ORVIS results might indeed be related to the beam characteristics which had to be reduced from 0.25 TW/cm^2 to 0.15 TW/cm^2 for the peak proton power density. However the length of the pulse is certainly not below 60 ns and could not be reduced to half as suggested by the calculations. With these beam parameters and the spread of $\pm$ 0.05 TW/cm^2 for the peak proton power density a much better agreement was achieved between calculated and measured foil acceleration data [10]. However, the rather large experimental uncertainty in the determination of the peak proton power density - which could not be reduced by other measurements - is limiting the verification of impact target codes as well as the determination of e.g. equation of state data used in these codes. It seems to be not possible to generate ion beams with better reproducibility with this B_Θ diode. The diode therefore should be redesigned. Finally it should be pointed out that the evaluation of the peak proton power density by eq.1 is based on shot to shot reproducibility as well as a relation between electrical signals and

activation results. Due to the very high x-ray background produced by this diode these assumptions so far could not be verified by applying time resolved focus measurements by e.g. a PIN diode array in a shielded pin hole camera looking onto a gold scattering foil in the focal plane. A better shielding of this diagnostics is in preparation.

References

[1] D. Rusch, W. Ratajczak:
Die Erzeugung hoher elekrischer Energiedichten mit dem Impulsgenerater KALIF
KfK - Nachrichten, 24, 1/92, S. 13-18

[2] W. Bauer, H. Bluhm, P. Hoppé, H. Karow, D. Rusch, H. Laqua:
Erzeugung und Fokussierung von Leichtionenstrahlen mit Impulsenergien von 50 kJ und Leistungsdichten um 1 TW/cm^2
KFK - Nachrichten, 24, 1/92, S. 3-12

[3] K. Baumung, D. Rusch, J. Singer, S. Razorenov, A. Utkin, G. Kanel:
Hydrodynamic Beam-Target Experiments on KALIF
this report.

[4] O. Vorobjev, A. Ni, B. Goel:
Numerical Simulation of Foil Experiments with Light Ion Beams
KfK - Bericht Nr. 5299, April 1994

[5] W. Bauer, H. Bachmann, H. Bluhm, L. Buth, P. Hoppé, H. Karow, H. Lotz, D. Rusch, C. Schultheiss, E. Stein, O. Stoltz, T. Westermann:
New Results from Experimental and Numerical Investigations of the Selfmagnetically B_Θ-insulated Ion Diode
Proc. of the 9 th Int. Conf. on High Power Particle Beams, Eds. D. Mosher, G. Cooperstein, Wash. DC. 1992, Vol.2, 735

[6] R. Leeper, J. Chang, D. Hebron:
Bull. Am. Phys. Soc. 27, 984 (1982)

[7] A. Klumpp, H. Bluhm:
Untersuchungen zur Diagnostik von intensiven gepulsten Protonenstrahlen mit Hilfe der B,α Reaktion
KfK - Bericht Nr. 4130, Sept. 1986

[8] W. Bauer, H. Bachmann, H. Bluhm, P. Hoppé, H. Karow, D. Rusch, C. Schultheiss, O. Stoltz:
The Small B_Θ-Diode, First Experimental Results
Primärbericht 3.90, unpublished

[9] B. Goel, priv. communication

[10] B. Goel, O. Vorobjev:
Reinvestigation of Foil Acceleration Experiments
this report.

A CONTRIBUTION TO THE MAGNETIC FOCUSING IN AN APPLIED-B-EXTRACTOR ION DIODE

W. Bauer, W. Höbel, A. Ludmirsky*, E. Stein, T. Westermann**

Forschungszentrum Karlsruhe mbH, Postfach 3640, 76021 Karlsruhe, Germany

*Permanent address: SOREQ NRC, Yavne 7600, Israel
**Permanent address: Fachhochschule, Moltkestraße 4, 76133 Karlsruhe, Germany

Abstract

To obtain well focused beams is one of the key problems in light ion beam driven inertial confinement fusion. Extractor diodes with externally applied magnetic field show at present divergences of about 17 mrad. This work investigates the possibility of improving the focusing by applying a magnetic field in the vicinity of the focus: It can be generated by a solenoidal lens at the focal plane. The focusing properties of the diode are simulated using a quasi-stationary 2.5-dimensional particle-in-cell code. The applied magnetic field which is needed as input to the PIC-code is computed by PROFI. The simulations show that the effect of the suggested solenoid is indeed an improvement of the focusing both for beams with a Gaussian distribution of divergence angles and for beams with an energy distribution taken from an actual experiment.

I. Introduction.

Ideally the ion beam generated in an applied B extractor ion diode is focused by proper shaping the geometry and the fields in the diode. For many reasons this ideal cannot be fully accomplished. Influences which are difficult to control are for instance the effect of non ideal shapes of the anode and cathode plasmas or the applied magnetic field, and the unknown self-fields generated by beam instabilities. It is, of course, due to Liouville's theorem not possible to reduce the 6 dimensional phase space in order to obtain a smaller focus spot size, but it is indeed possible to reduce the beam radius while locally increasing the angle, under which the particles reach the focus. Since the power density P at the focus depends on the brightness B of the ion source and on the incident angle α according to

$$P = \pi \cdot B \cdot \sin^2\alpha$$

an increase of α might result in a higher focused power density. There are many schemes described in the literature, see for instance [1], where the final focusing of an ion beam is accomplished by a solenoidal lens situated a few meters in front of the focus, some way downstream from the diode. In the present work we investigate the application of such a focusing magnet in close vicinity of the focus of the applied B proton extraction diode presently under investigation at KALIF [2]. Particle-in-cell - calculations using the 2.5-dimensional quasi stationary code "BFCPIC2H" [3] suggest a positive effect of such a magnetic field on the focus size.

The magnetic field is generated by a coil similar to the small coil used for generating the applied B-field of the diode or by a one-turn coil that is sacrificed at each pulse. The use of a laser-driven coil as suggested in [4] and [5] seems technically difficult.

II. Codes used for Particle-in-Cell Simulations.

We use a combination of codes to simulate the particle motion in and outside our diodes. They are based on the quasistationary Particle-in-Cell-Code "BFCPIC2H" that, using a boundary-fitted grid, calculates the electric fields of the empty diode, emits particles at the surfaces, follows them on their way through the diode and calculates self-consistently electric and magnetic fields generated by the particle flux. The code uses as input the static external magnetic field computed by the program "PROFI" [6]. Since PROFI uses its own (rectangular) grid, the magnetic field inside the diode is interpolated to the boundary-fitted grid inside the diode.

To follow the particles through the driftspace outside the diode up to the focus, the program "DRIFTPIC" [7] is applied. It self-consistently computes the magnetic fields in the drift-space. Again the magnetic field calculated by "PROFI" is used. DRIFTPIC assumes total space charge neutralization and current neutralization with a percentage that can be specified. Moreover, it takes into account that the neutralization is reduced in the vicinity of strong transverse magnetic fields.

III. Results.

The following figures show the main contours of the diode together with trajectories outside the diode in the drift-space, using either some of the particles generated by the PIC-code or particles with special hand-selected starting conditions at the entrance of the drift-space. The figures have to be considered as rotationally symmetric around the Z-axis.

In fig. 1, ions as they are generated by the PIC-code in the diode are shown. They produce a rather broad focus around Z = 150 mm. Switching on the one-turn coil situated at Z = 140 mm as shown in fig. 2. the focusing behaviour is considerably improved. In fig. 3. three of the previous trajectories are given an artificially introduced divergence of ± 1°. The additional magnetic field apparently results in an improved focus also in this case.

The results discussed so far suggest, that in the case of a *non ideally focusing* diode the additional magnetic field indeed improves the focus. In fig. 4 the initial conditions have been changed in such a way, that all beamlets leaving the diode arrive at exactly one focus point, if the additional magnet is switched off. This perfect focus is made *worse* by the additional magnet, as fig. 5 shows.

To study more thoroughly the influence of the additional magnet in the presence of a beam divergence and for different beam energies, the following procedure was chosen: The beams leaving the diode and entering the drift region were given a Gaussian distribution of divergence angles with a half angle of 1°. For each of these beamlets the radius R was recorded, at which they arrive at the distance Z of the smallest beam radius. This count was plotted versus the radius in fig. 6 for both cases when the additional magnet is switched on and off. The corresponding curves demonstrate clearly an improvement of the focus by the magnet.

In a similar way the influence of different beam energies was investigated in fig. 7. Here the particle distribution measured by a Thomson-parabola-spectrometer [8] was considered *in addition* to the Gaussian distribution of divergence. The improvement by the additional magnet can still be recognized, but is less pronounced than in fig. 6.

Instead of the one-turn solenoid also a coil of type that is used as the inner coil of the Applied-B-Diode could be chosen. It is, however, necessary to increase the current in this coil by at least a factor of 1.5 compared to usual values necessary for the operation of the diode to obtain noticeable results.

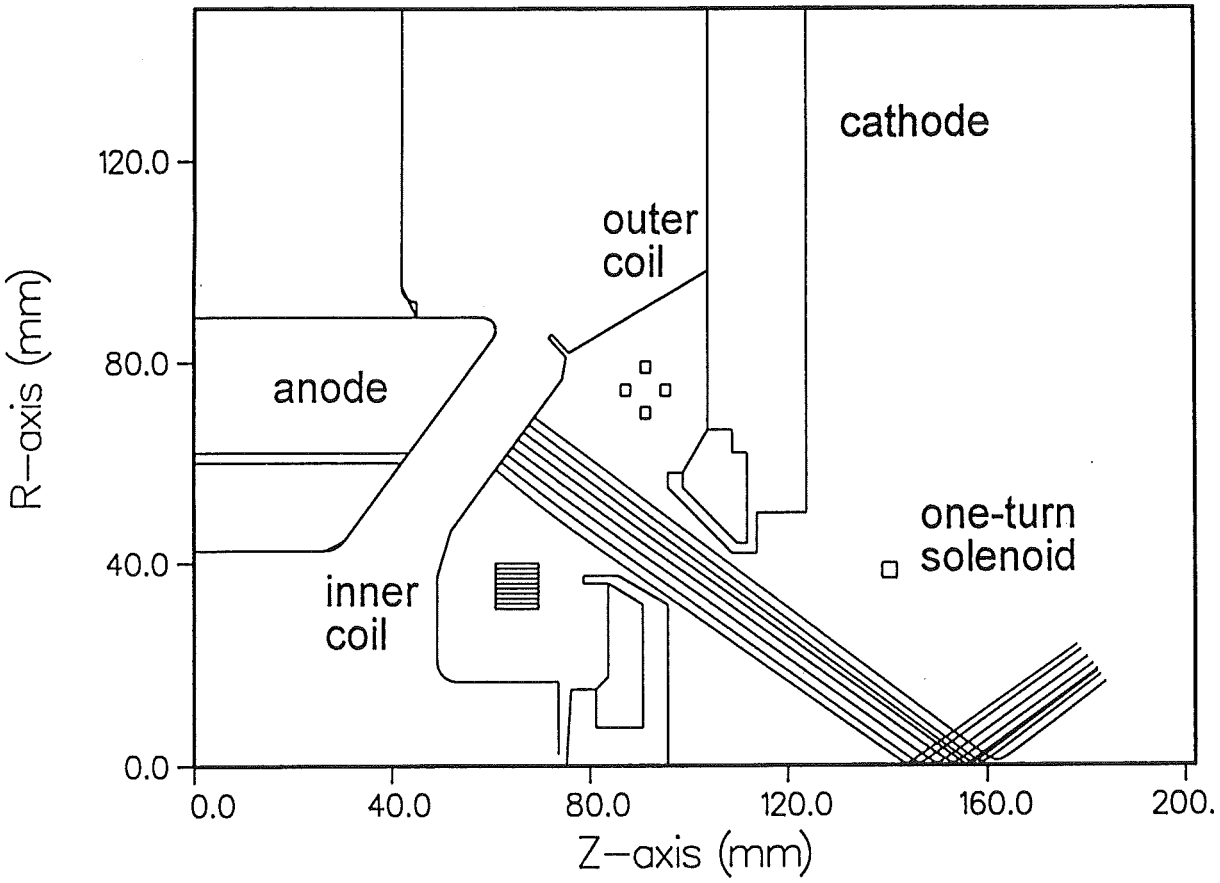

Fig. 1: 8 typical proton beams in the applied B proton diode [2] simulated by BFCPIC2H [3] showing a rather broad focus at about 150 mm.

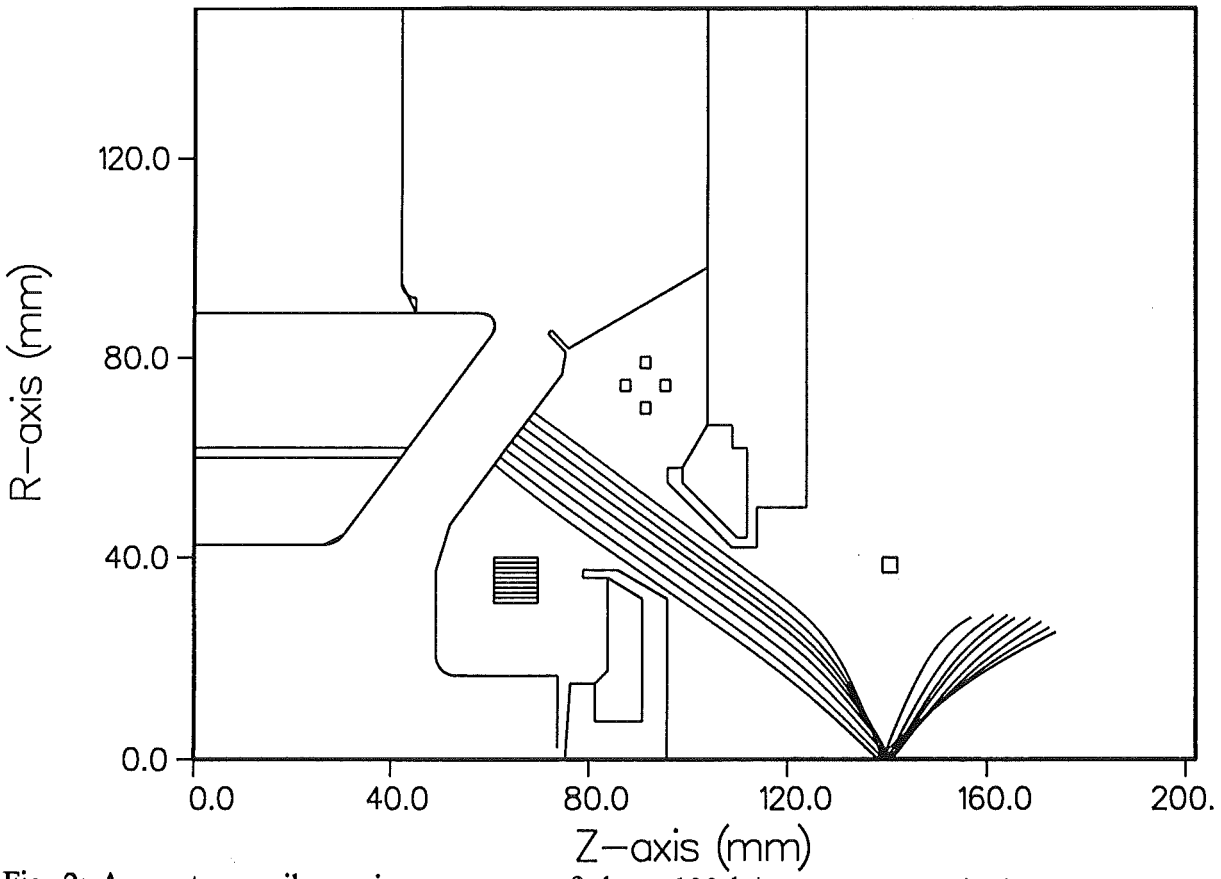

Fig. 2: A one-turn coil carrying a current of about 100 kA concentrates the beams at a somewhat smaller focus length of 140 mm with a considerably reduced focus diameter.

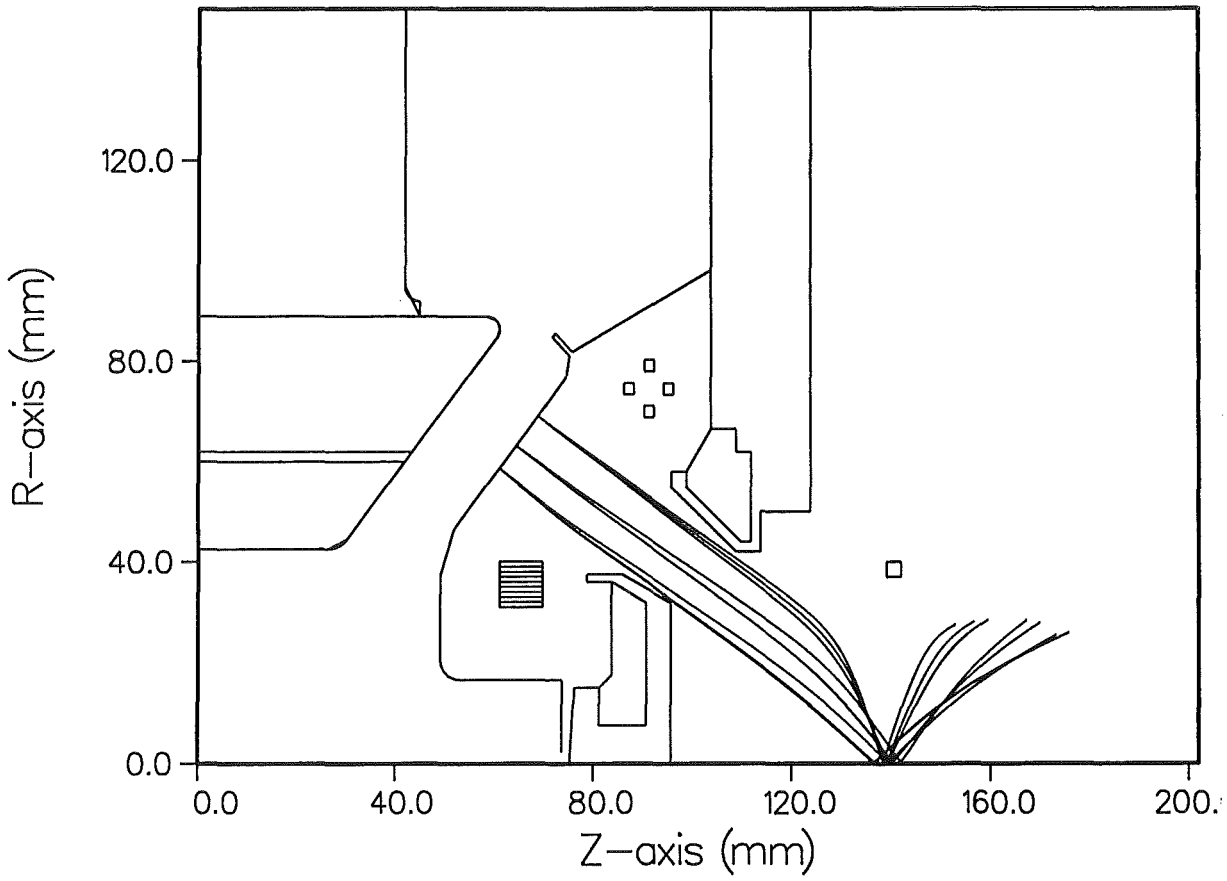

Fig. 3: Three of the above beams are shown with a 1° initial divergence at the diode exit, showing that the improvement of the focus by the magnet is maintained.

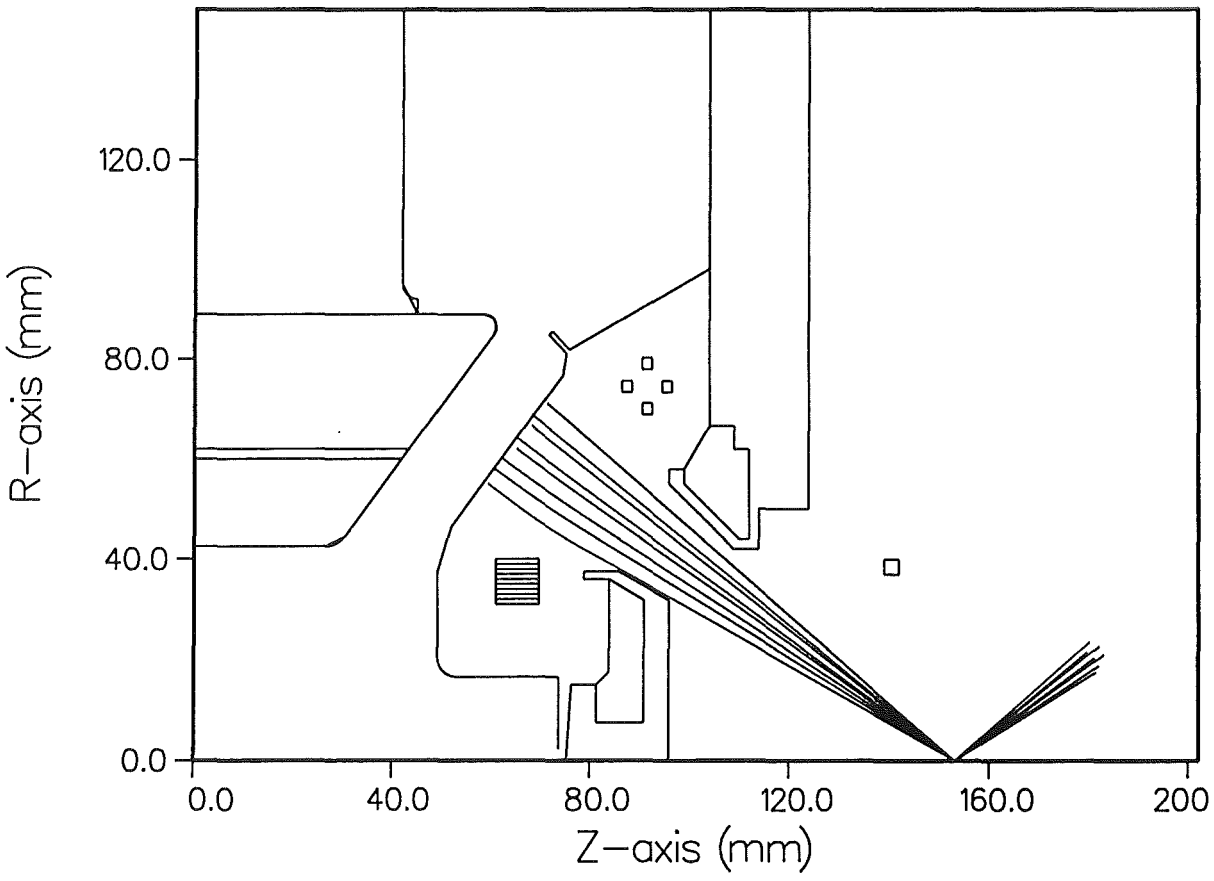

Fig. 4: Artificially changed initial conditions leading to an ideal focus.

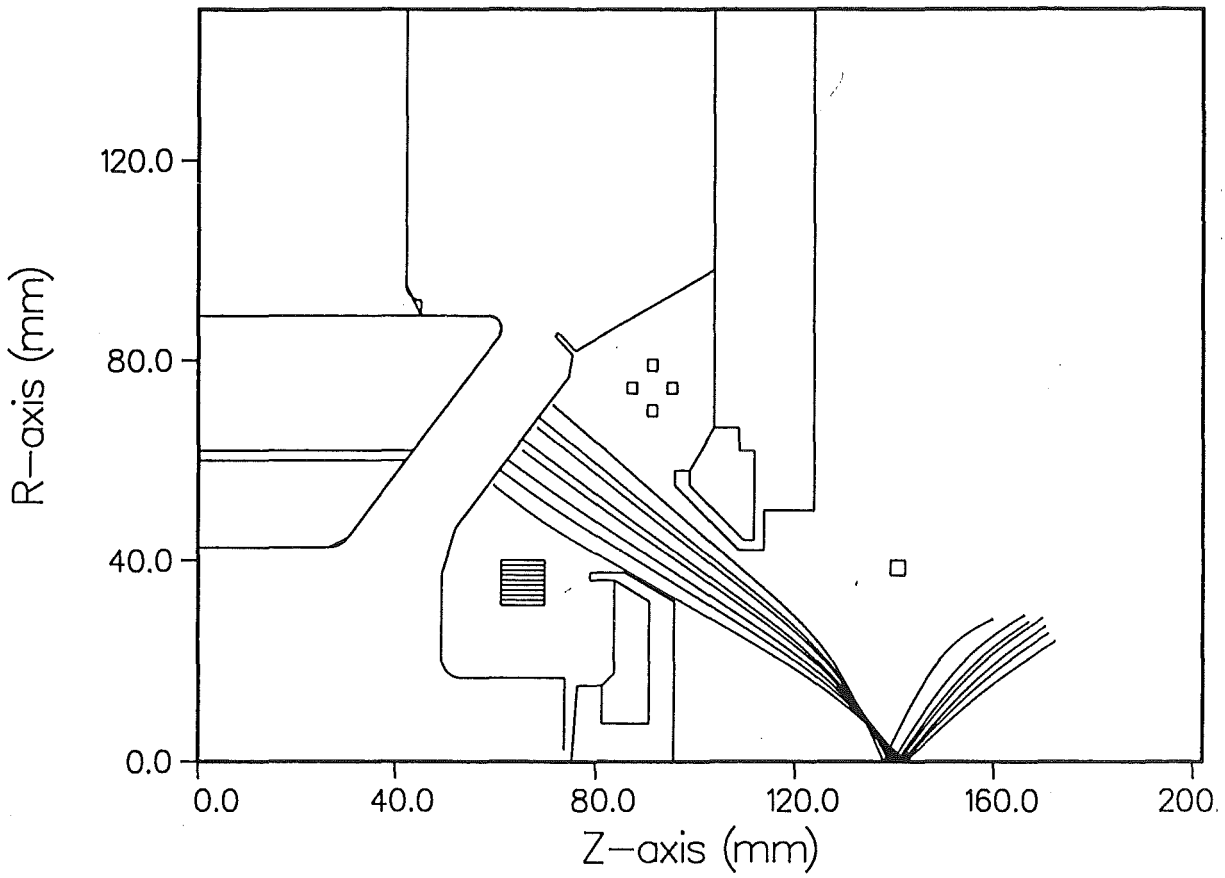

Fig. 5: The additional magnet disturbs the ideal focus of fig. 4.

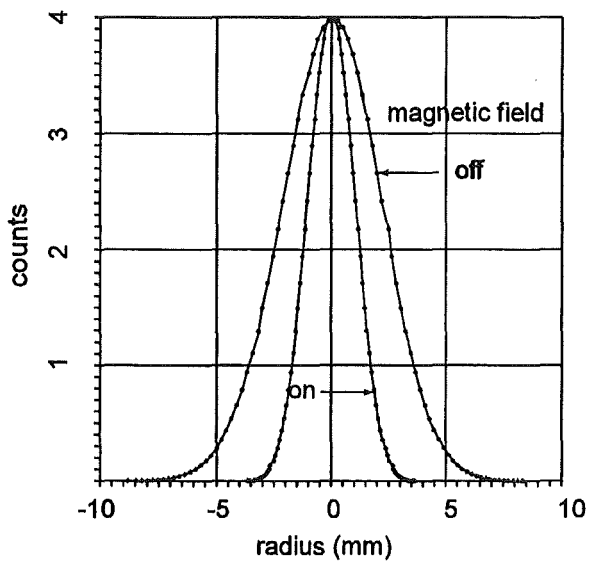

Fig. 6: Beam profile at the focus for a Gaussian-shaped divergence distribution. FWHM = 2.5 and 5.2 mm for magnetic field switched on and off, respectively.

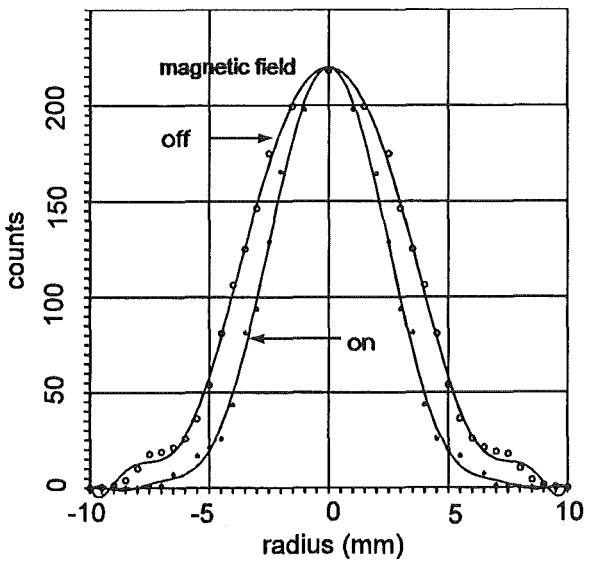

Fig. 7. Beam profile at the focus for a Gaussian-shaped divergence distribution and for an experimental energy distribution of the protons. FWHM = 5.6 mm with magnetic field and 7.7 mm without it.

IV. Conclusion.

The simulations have shown, that in the case of a non-ideally focusing diode an additional magnet in the vicinity of the focus can improve the focus considerably. The influence of beam divergence on the focal size can be reduced by a factor of about two for mono-energetic beams and by about 30 % for beams with a realistic energy distribution. For a first experiment to investigate this scheme we think of using a coil similar to the inner coil of our Applied-B-Diode driven from a separate condenser bank. Another possibility would be a one-turn solenoid wound from a wire that is sacrificed for each shot. Simulations to investigate the possibility of using a plasma-channel in the drift space or a longitudinal magnetic field generated by a wire on axis are under way. Apart from the question of a possible realization the investigation can be considered as an interesting example for the application of our PIC-code.

References:

[1] F. Ottinger, D. Mosher, J.M. Neri, D. V. Rose, C. L. Olson, "Transport and Focusing Considerations for Light Ion ICF Systems", 9th International Conf. on High-Power Particle Beams, Wahington, DC, 1992, p. 60

[2] H. Bluhm, P. Hoppé, H. Bachmann, W. Bauer, K. Baumung, L. Buth, H. Laqua, A. Ludmirski, D. Rusch, O. Stoltz, "Stability and operating characteristics of the applied B proton extraction diode on KALIF", 10th International Conf. on High-Power Particle Beams, San Diego, 1994

[3] T. Westermann, "A Particle-in-Cell Method as a Tool for Diode Simulations", Nucl. Instr. Meth. **A 263**, (1988), p. 271, or more recently: "Numerical Modelling of the Stationary Maxwell-Lorentz System in Technical Devices, Int. J. Num. Modelling: Electronic Networks, Devices and Fields 7, (1994), p. 43 - 67

[4] J. L. Borowitz, S. Eliezer, Y. Gazit, M Givon, S. Jackel, A. Ludmirski, D. Salzmann, E. Yarkoni, A. Zigler, B. Arad, "Temporally Resolved Target Potential Measurements in Laser-Target-Interactions", Journal of Applied Physics **20**, 1987, p. 210

[5] H. Daido, F. Miki, K. Mima, M. Fujita, K. Sawai, H. Fujita, Y. Kitagawa, S. Nakai, C. Yamanaka, "Generation of a Strong Magnetic Field by an Intense CO_2 Laser Pulse", Phys. Rev. Lett. **56 (8)** (1986) p. 846-849

[6] PROFI, Program Documentation Version 7.4, PROFI-Engineering, Otto-Röhm-Straße 26, 64293 Darmstadt, Germany

[7] L. Feher, W. Schmidt, T. Westermann, "DRIFTPIC, a Computer Program for the Calculation of Ion Trajectories in the Drift Section of Externally Applied-B Diodes",
KfK-report 5207 (July 1993)

[8] H. Bluhm, P. Hoppé, H. Laqua, D. Rusch, "Production and Investigation of TW Proton Beams from an Annular Diode Using Strong Radial Magnetic Insulation Fields and a preformed Anode Plasma Source", Proc. IEEE, **80, NO. 6** (1992), p. 995 - 1009

DEVELOPMENT OF A LONG PULSE PROTON BEAM GENERATOR FOR ITER DISRUPTION SIMULATION EXPERIMENTS

V. Engelko, H. Giese, S. Schalk, Ch. Schultheiß, H. Würz

ABSTRACT

One of the subjects of major concern in present divertor tokamak research is the substantial heat load to which divertors are exposed during operational instabilities like plasma disruptions and to lesser extent during ELMs (Edge Localized Modes). Although numerical simulations predict that the plasma impact on the divertor surface is mitigated by the formation of a plasma shield, the efficiency of this autoprotective action remains questionable as long as the numerical models have not been validated by adequate experiments, in which divertor candidate materials are subjected to comparable load conditions. In this context, investigations using proton beams are considered to form a valuable complement to the presently performed experiments using electron beams and plasma guns. A proton beam facility (KANDIS) has therefore been designed, which can deliver a power density of $10\,MW/cm^2$ with pulse durations up to 40 μs and which consists of basically two sections: A vacuum diode of $10^4\,cm^2$ surface area for the production and ballistic focusing of the proton beam and a magnetic compression unit, in which the beam is focused to a target spot about 1 cm radius. To check the validity of its design and to test its components, a replica of this facility is presently being investigated, in which the diode surface was scaled down by a factor of 6. While mesurements of the anode current density, of the pulse duration and of the beam divergence gave satisfactory results, the beam transport is still problematic due to insufficient space charge neutralization.

1. INTRODUCTION

Plasma disruptions and ELMs (Edge Localized Modes) in tokamak fusion reactors lead to substantial energy deposition on the surface of divertor plates, causing evaporation of divertor material and hence shortening of divertor lifetime. Estimations of divertor heat load in ITER disruptions predict power densities of the order of $10\,MW/cm^2$. Of particular interest in the context of divertor heat load assessment is the formation of a plasma shield at the divertor surface. For more details see the accompanying paper of F. Kappler et.al. [1]. The protective action of the plasma shield is of prime importance in divertor erosion and numerous experiments in which divertor candidate materials are exposed to electron or plasma beams are carried out to validate the presently used numerical methods [2-5]. Although these experiments deliver valuable information, complementary investigations using proton beams are considered useful, since they could avoid some of the difficulties encountered in electron beam and plasma experiments. Proton energy deposition in matter occurs over a smaller, more realistic range than for an electron beam of equal energy. For plasma beams it is difficult to assess the actual power deposition (current measurements fail for reasons of electrical neutrality), and to distinguish between incoming and condensed plasma and plasma belonging to the shield.

A proton beam facility (KANDIS) was therefore suggested for disruption simulation experiments and a conceptual design was worked out in cooperation between the Forschungszentrum Karlsruhe and the Efremov Institut in St. Petersburg / Russia [6]. KANDIS has to reach a target power density of $10\,MW/cm^2$ with proton energies of up to 50 keV and pulse

lengths of more than 10 μs. As the proton source, a large spherical vacuum diode with 10000 cm^2 surface area is proposed with ballistic focusing of the emerging proton beam. After passing through the focal point of the diode at a distance of 1 m, the beam is further compressed to a cross section of 1 cm^2 by a strongly inhomogeneous magnetic field. The magnetic induction at the target position would reach 5T, close to the value observed at the ITER divertor position. The available pulse length of this facility would obviously be much shorter than the duration expected for ITER disruptions but would fit the duration of ELMs. However, in any case the proton beam pulse duration of KANDIS would be long enough to establish the key phenomenon of plasma shielding. To check the validity of the conceptual design of KANDIS and to test the feasibility of its different components, the test facility PROFA was built and taken into operation in 1993. The key issues presently investigated in PROFA are the maximum achievable anode current density (the required value is 0.1 A/cm^2), the maximum attainable pulse length (presently 40μs), the beam divergence (30mrad were assumed in the KANDIS design, based on experimental results in a small test facility [7, 8]), and optimization of proton beam transport and focusing.

The following contribution presents a concise description of the PROFA facility and discusses the present state of the experiments and their interpretation.

2. GENERAL DESCRIPTION OF PROFA

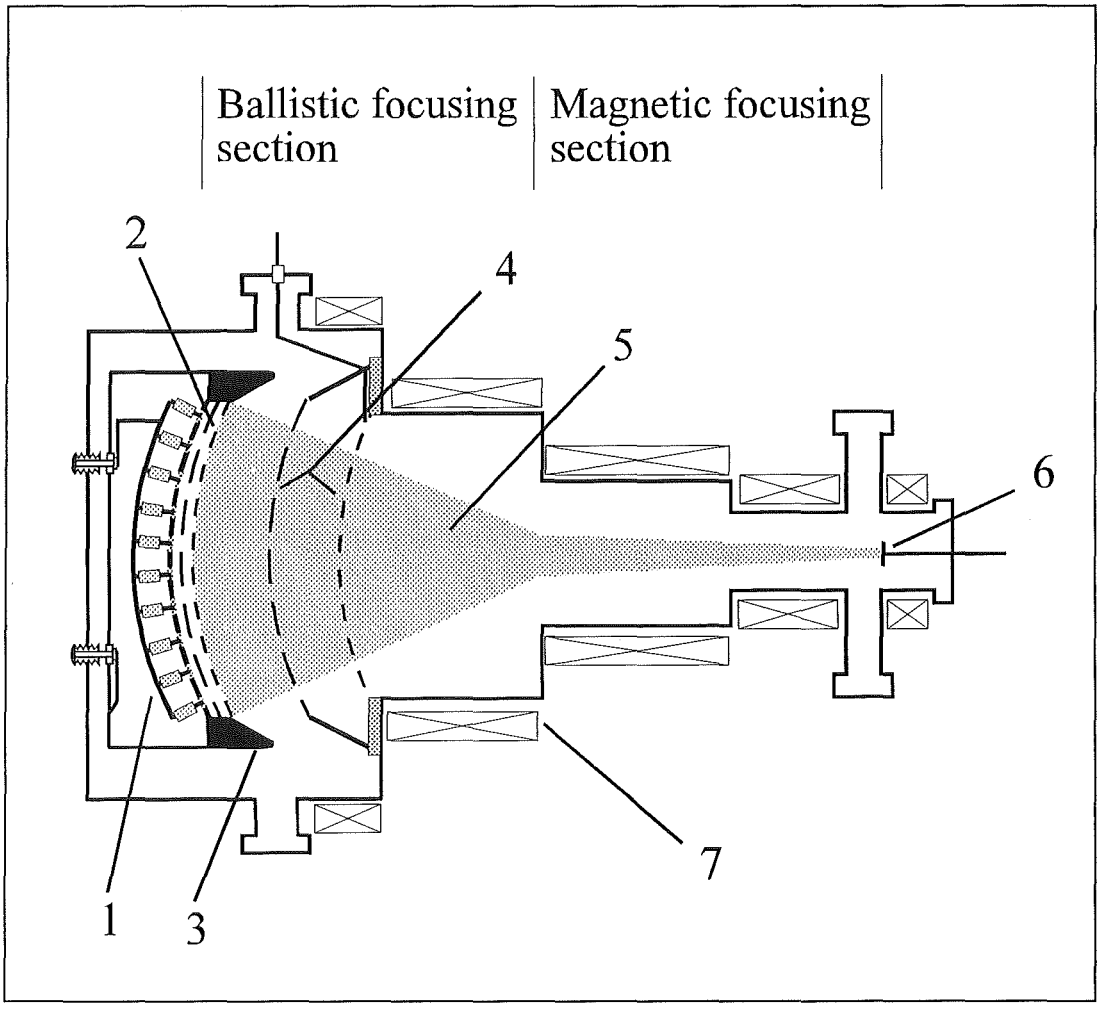

Fig. 1: Scheme of the long pulse proton beam facilty PROFA
1 Multispark-anode; 2 Shield plates; 3 Pierce electrode; 4 Cathode grids; 5 Proton beam; 6 Target; 7 Magnetic field coils

Representing a scaled down replica of the projected KANDIS facility, PROFA also comprises a vacuum diode of spherical shape and concave surface, serving for the production and ballistic focusing of the proton beam, and a drift section in which this proton beam is compressed by interaction with a strongly inhomogeneous magnetic field (Fig.1). The surface area of the diode electrodes is of the order of 1500 cm^2 and thus smaller by a factor of 6 than that of the KANDIS diode.The diode focal distance was 60 cm, its inter-electrode gap ranged from 3-5 cm and the length of the magnetic focusing channel was about 1 m, depending on the particular experimental setup. The vacuum diode is driven by a 50 kJ high voltage pulse generator presently set up for operating voltages of up to 50 kV and for pulse durations of up to 40 μs.

Special care was taken in the design of the magnetic coil system to optimize compression characteristics and to minimize deterioration of the ballistic focusing performance of the diode by the superimposed presence of the magnetic field. Calculations showed that this task is best solved by using two separately driven coil systems of very different induction, the one with high induction being located towards the far end of the focusing channel. The resulting magnetic induction ranges from about 1 mT in the diode area to 4 T at the target position at the end of the focusing channel. The two coil systems are driven by capacitor banks loaded to 3-4 kV. The total energy stored in the capacitor bank is 60 kJ.

Apart from the simplicity of its overall construction, the PROFA facility has the additional merit of offering a substantial degree of experimental flexibility: components of the vacuum diode can easily be modified to investigate different cathode and anode geometries, axial parts of the vacuum vessel can be demounted to insert diagnostic equipment, and some of the magnetic coils can be optionally deactivated or shifted axially to optimize beam compression.

3. THE PRESENTLY INVESTIGATED DIODE

3.1. Multispark-anode (MA)

Since initial experiments using an adsorbate anode did not allow the production of sufficiently intense proton pulses over more than 10μs [8], a pulse duration which was considered insufficient for the intended application, an alternative anode type was investigated in PROFA that uses an active mechanism for proton production, i.e. it does not rely on the assistance of cathode electrons. This anode consists of a spherical concave stainless steel shell containing a rectangular matrix of 1500 holes with an average distance of 1cm. Presently only half of these holes are filled with polyethylene plugs of 8.5mm diameter each containing a central wire electrode. All 750 electrodes are connected with each other via current limiting resistors and their common node point is connected to ground through a current controlling RC-network. With the appearance of the high voltage pulse in the diode, a discharge is initiated across the surface of each polyethylene plug leading to the build-up of a thin plasma layer from which protons can be extracted by the inter-electrode field. Perforated shield plates in front of the anode protect the polyethylene plugs from direct electron bombardment and act as a plasma reservoir.

The most significant advantages of this anode type over the initially investigated adsorbate anode are:

(i) The time-dependence of the plasma production can be easily controlled by modification of the external RC-network and it is independent of the development of the diode discharge current.

(ii) The total proton current can be controlled by the number of active polyethylene plugs.

(iii) The active ignition procedure produces a more homogeneous plasma cover over the anode surface than was the case with the adsorbate anode where local variations of field strength, hydrogen desorption rate etc. disturb the homogeneity.

(iv) The maximum pulse length obtained with this anode type was 40 μs, limited by the capability of the pulse generator.

It was for these advantages that the majority of the experiments in 1994 were performed using the Multispark-anode.

3.2. Cathode

For the operation of diodes employing an anode with active plasma production, like the MA described above, it is not necessary for the cathode to emit electrons, since the liberation of hydrogen from the anode surface does not depend on this process. Therefore the diode would in principle work with a simple wire grid cathode. The vital demand of space charge neutralization, however, without which the proton beam would rapidly expand instead of being focused as soon as it enters the drift space behind the cathode, cannot be satisfied by this simple cathode construction.

Possible solutions to the problem of space charge neutralization will be discussed in a later section.

4. THE PRESENT STATE OF THE INVESTIGATIONS

4.1. Pulse length

As mentioned above, the maximum pulse length of the proton beam obtained up to now in PROFA was 40 μs, limited by the capability of the high voltage pulse generator. The typical shape of the diode high voltage pulse and the corresponding signal recorded using a Faraday-cup positioned in the drift space are shown in Fig.2. A recently installed crow-bar device allows to short-circuit the diode at a given instant, and to suppress oscillations between pulse generator and diode in the case of mismatched load operating conditions.

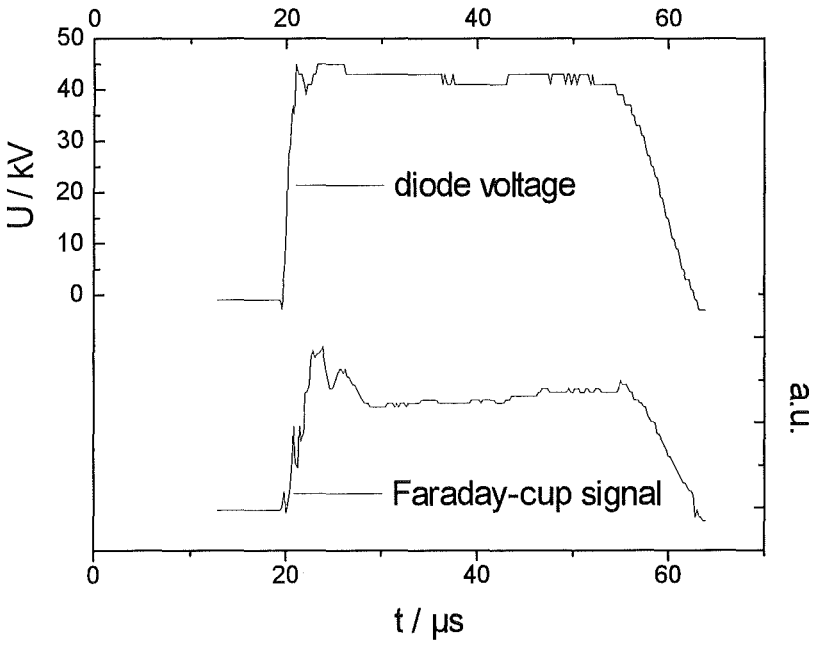

Fig. 2: Example of the long pulse proton beam capability of the PROFA diode.
Upper trace: diode voltage pulse. Lower trace: signal from a non biased, open Faraday-cup with a diameter of 3 cm, located 1.5 cm behind the cathode grid.

In this context it is interesting to consider mechanisms that could limit the diode pulse length even if the pulse generator's capability was extended. Conceivable mechanisms that could cut off the normal operation regime of the diode could e.g. be a vacuum breakdown or a discharge in gas, desorbed from the surface of the diode electrodes. Since the average electric field strength in PROFA is relatively low, ($5-10\,kV/cm$), the gas discharge is the more likely mechanism. With a gas expansion velocity into vacuum of $\leq 10^5$ cm/s and a diode gap distance of 2-5 cm, a gas desorption from the cathode grid could limit the pulselength to 20-50 μs, a desorption from the anode surface to 50-80 μs.(Gas released from the anode has to pass the 2 perforated shields in front of the anode, the outer one being located 3cm from the anode surface.)

4.2. Diode current density

The diode current density is governed by the Child-Langmuir law.
For unipolar mode:

$$j_{CL}^{+} = \frac{4\varepsilon_0}{9}\sqrt{\frac{2e}{m}}\frac{U^{3/2}}{d^2} = \frac{4\varepsilon_0}{9}\sqrt{\frac{2e}{m}}\frac{E^{3/2}}{\sqrt{d}}$$

For bipolar mode:

$$j_{CL}^{\pm} = 1.8 \cdot j_{CL}^{+}$$

To reach the anode current density of $0.1\,A/cm^2$ foreseen for KANDIS, the electric field strength has to be $20\,kV/cm$ in unipolar operation but only $5\,kV/cm$ in bipolar operation. It would therefore obviously be more attractive to use a bipolar operation regime and a first series of experiments was run using a multipoint cathode [10]. However, difficulties in the interpretation of the measurements could presently not be overcome and it was decided to continue the experiments with unipolar operation using a cathode grid.

The current density was measured in three different ways:

- measurements of the total diode current;
- biased collector with a diameter of 3 cm;
- electrically shielded and magnetically insulated collectors with a diameter of 10 mm and 19 mm respectively and diaphragm apertures of 3 mm.

It is important to note that none of these methods can yield an absolutely correct result:

- A measurement of the total diode current is impeded by the existence of many currents flowing in the system, namely: ion currents to the focusing channel wall and to the cathode grid, ion current due to ionization of residual gas, electron currents from the cathode grid to the anode and into the focusing channel, electron currents of secondary emission from the chamber wall and due to ionization of residual gas.
- A biased collector changes the potential distribution in the focusing channel and therefore the distribution of the electron space charge. The latter leads to a change of ion trajectories and ion current density.
- A shielded collector with a diaphragm must be oriented precisely along the ion trajectory, otherwise the current density will be measured too low.

Despite these problems, the results of the measurements allowed to conclude that in long pulse unipolar mode of the diode operation the anode current density was more than $40\,mA/cm^2$.

It should be pointed out that the current density decreases after several hundreds of shots. This can be ascribed to a hydrogen depletion of the surface of the anode polyethylene plugs. To ensure a constant level of ion current density, these plugs should therefore be replaced after a certain number of shots. It proved also beneficial to expose the polyethylene plugs in the MA anode from time to time to a hydrogen atmosphere.

4.3. Beam composition

The beam composition was investigated using a time-of-flight method. For this analysis and also for the study of the ion beam divergence an additional small test facility was built at the St. Petersburg State University, scaling down the PROFA dimensions by approx. a factor of 15. The results obtained are:

The mass spectrum of the ion beam depends on the anode discharge current, on the number of pulses, on the vacuum conditions and on the angle of observation. After conditioning of new polyethylene units by several shots under residual gas pressure, the ion beam consists mainly of protons (>90%). Measurements of the beam composition after several hundreds of shots showed the appearance of heavier components with atomic masses of 6, 8, 12, 18, 22, 24, 30, 44. The change of the ion beam mass spectrum can be attributed to the already mentioned hydrogen depletion of the polyethylene surface layer and to the formation of metal films, provoked by evaporation of the anode spark electrodes. The lifetime of the polyethylene units can be prolonged if the anode discharge current is increased, enhancing self-cleaning mechanisms.

4.4. Efficiency of beam transport and focusing

Numerical simulations for the KANDIS facility have shown [9] that apart from other obvious factors like the adequacy of the magnetic field distribution, which will not be discussed in the present context, the efficiency of beam transport and focusing depends strongly on the microdivergence of the beam, and on the level and detail of ion beam space charge neutralization. Special attention was therefore given to the assessment of these parameters in the PROFA experiments.

Divergence: Two diagnostic methods were applied in the PROFA experiments:1) shadowbox measurements with an ion sensitive film as the detector; 2) investigations with a movable collector sampling a small part of the beam, which is propagating in a certain angular direction. In both cases the divergence exceeded 30 mrad, i.e. the limit for which the magnetic compression system had been designed. One reason for such a big divergence is that in PROFA the space charge of the beam is not fully neutralized (see below). Complementary measurements run at the small test facility in St. Petersburg, in which the experimental setup provided a better space charge neutralisation, indicate that the divergence of the proton part of the beam is less than 30 mrad.

Neutralization of beam space charge: Calculations for KANDIS indicated that the beam transport efficiency changes drastically with the spatial distribution of neutralizing electrons [9]. Two cases were considered:

i) the beam space charge is neutralized by electrons provided by a plasma filling of the whole focusing channel, and

ii) the space charge is neutralized by electrons filling only the volume, which is defined by the magnetic force lines going through the edge of the anode.

In both cases the microdivergence of the beam had been assumed to be 30 mrad in accordance with the preliminary experimental data [8]. The results of the calculations showed that in the first case the efficiency of beam transport to the target is 50% and in the second case 100%. Although the reason for this behaviour has not yet been finally clarified, the important conclusion of these numerical studies is, that it is not only important to provide a sufficient number of electrons to achieve space charge neutralization, but also to confine these within the beam volume to optimize beam transport!

To study the different possibilities of space charge neutralization in PROFA, the following sources of electrons have been investigated :

1. Secondary emission electrons from the metal grid cathode or from the wall of the focusing channel: The cathode grid as a source for neutralizing electrons has the major disadvantage that the diode electric field hinders the secondary electrons from penetrating into the focusing channel. Hence the main electron source, while using the cathode grid, is the wall of the focusing channel. This mechanism does not work any longer if the magnetic field is applied, because the electrons can not cross the magnetic field lines.

The situation is significantly improved if an additional metal grid is introduced behind the cathode grid. Now secondary emission electrons from this grid can contribute to the neutralization and the ion beam is transported to the target. Determination of the transportation efficiency, which is synonymous with measuring the ion current at the target, is complicated, since the beam is current neutralized and stripping the electrons from the beam is made difficult by their high kinetic energy and by the high induction of the external magnetic field at the target. Therefore the ion current at the target was obtained by comparing the current to the focusing channel wall with and without magnetic field and from the measurement of the current density in the central part of the target. Furthermore the beam cross section on the target was determined from traces on an ion sensitive film in the target plane. From these measurements it can be concluded that the efficiency of beam transport is better than 50%.

In order to provide an appropriate number of secondary emission electrons the transparency of the second grid has to be rather low which reduces the total ion beam current significantly. Thus the possibility to accomplish neutralization of the space charge of the beam with a high vacuum gas discharge in the focusing channel was considered. The discharge has to be a high vacuum type, since the commonly applied technique of using a separation foil between diode and focusing channel is precluded by the low kinetic energy of the ions.

2. Plasma of a gas discharge in the focusing channel: Since a strong magnetic field is used in the focusing channel of PROFA, it seems reasonable to employ a Penning discharge (PD). The feasibility of such adischarge is not straight forward since there was no experience with the ignition of a PD in such rather big volume with strongly inhomogeneous magnetic fields and with a rather low residual gas pressure. In addition it was not clear whether the discharge would influence the diode operation, and what electric field distribution would be established in the discharge volume etc..

To explore the practical potential of a PD under such conditions, a first series of experiments was performed recently using a proton pulse length of 10 μs and a residual gas pressure of $\leq 2 \cdot 10^{-4}$ mbar. The target and the cathode grid were electrically connected with each other and biased to a negative potential of several kV with respect to the wall of the focusing channel. It has been found that a PD ignition was possible, that it did not affect the diode operation, and that the electric field was mainly oriented radially. Supplementary tests showed that PD ignition was even possible with a grounded target, a consequence of the 'magnetic mirror' effect in the strongly inhomogeneous field present in the focusing channel.

Although difficulties do still exist with the timing of the PD ignition and with the discrimination between contributions of the PD and of the diode to the current on the target, it is presently believed that the PD has the biggest potential for high efficiency beam transport.

A comparison between the required parameters and the presently achieved values is given in the table below:

	Required	Present achievements on PROFA
Proton energy (keV)	30	30
Anode proton current density (mA/cm^2)	100	> 40
Pulse length (μs)	10	40
Efficiency of beam transport	> 0.9	> 0.5 (with 2 cath. grids)
Degree of space charge neutralization	1	0.99
Proton fraction in beam	100%	> 90%
Beam divergence (mrad)	30	20-40

5. CONCLUSIONS

The experiments performed at the PROFA facility in 1994 demonstrated the applicability of a vacuum diode as a long pulse proton beam source in unipolar mode. The design of the multispark anode allows to produce a homogeneous plasma cover over a large surface area and a sufficient density to reach values close to the required proton current density of $0.1 A/cm^2$. Repetitive replacement and/or cleaning of the polyethylene units in the multispark anode guarantees a high percentage of hydrogen in the anode plasma.

Investigations on proton beam behaviour in the focusing channel showed agreement with the results of numerical simulations. The proton beam is efficiently transported and focused to the target, if the neutralization of the ion beam space charge is provided. A new method for space charge neutralization of low kinetic energy proton beams has been demonstrated. It is based on a low density gas discharge inside the focusing channel.

Future activities will concentrate on the determination of the limiting parameters for diode operation (pulse duration, current density, electric field strength), on the improvement of the diagnostics for the beam parameters at the target, on the study of the physics processes in the focusing channel and on the optimization of the space charge neutralization method.

LITERATURE

1. F. Kappler et.al. — The numerical modeling of plasma shield formation and divertor plate erosion during ITER tokamak plasma disruptions. This report
2. M. Febvre, E.V. van Osch, H. Viallet — Disruption-like heat load tests with EB200 test facility. to be published in Proc. 18th Symp. On Fusion Tech., Karlsruhe, August 1994
3. V.N. Litunovski et.al. — Experimental complex for high heat flux. Materials interaction research. to be published in Proc. 18th Symp. On Fusion Tech., Karlsruhe, August 1994
4. V. Engelko et.al. — Test of divertor materials under simulated ITER plasma disruption conditions at the SOM electron beam facility. to be published in Proc. 18th Symp. On Fusion Tech., Karlsruhe, August 1994

5.	V.S. Koidan et.al.	Electron and hot plasma stream target interaction experiments under simulated ITER plasma disruption conditions at the GOL-3 facility. to be published in Proc. 18th Symp. On Fusion Tech., Karlsruhe, August 1994
6.	V.Engelko, et. al.	Pulse intense proton beam facility for ITER disruptions simulation to be published in Proc. Beams '94, San Diego 1994
7.	V.Engelko et.al.	A new vacuum diode with adsorbate anode and multipoint explosive emission cathode for production of intense long pulse proton beams. 15th Int. Symp. on discharges and electrical insulation in vacuum, Darmstadt 1992
8.	V.Engelko, Ch. Schultheiß	Model of the vacuum diode with adsorbate anode operation. to be published in Proc. Beams '94, San Diego 1994
9.	V.Engelko, et. al.	Compression of intense proton beams to be published in Proc. Beams '94, San Diego 1994
10.	M.A.Vasilevskii, I.M.Roife, V.I.Engelko	Operating characteristics of explosive-emission multipoint cathodes with microseconds pulse length. Sov.Phys.Techn.Phys.,Vol.26.No.6,pp.671-688,1981

IV Target Physics

Hydrodynamic Beam-Target Experiments on KALIF

K. Baumung, D. Rusch, J. Singer, S.V. Razorenov*, A.V. Utkin*, G.I. Kanel*

From the hydrodynamic response of 10- to 100-μm-thick targets ion beam parameters like proton range, power density, and ablation pressure can be determined as a function of time. For the first time, using 1-dim spatially resolving laser-Doppler velocimetry, the ablative acceleration and the ablation pressure history could be measured across the ion beam focus. First experiments on the development of Rayleigh-Taylor instabilities during the ablative acceleration of thin, structured foils were performed at a ~10-μm-resolution.

1. Introduction

The B_Θ-diode, which was used for the experiments presented here, provides a peak power density of ~0.15 TW/cm^2 and specific energy depositions up to10 MJ/g. The hydrodynamic response of thin target foils can be utilized as a complementary diagnostic tool to provide information on properties of the ion beam, the beam-target interaction, and on the behaviour of matter at high energy densities [1,2]. In our experiments, metal foils of 10 to 100 μm thickness are placed in the ion beam focus, and the rear surface motion is measured by laser-Doppler velocimetry at a sub-nanosecond time resolution (cf. ref. [3] in this report). The primary measuring quantity is the velocity of the rear free surface from which the pressure p and the density ρ can be deduced by applying the hydrodynamic relations used in shock-wave physics. Recently, we have investigated in more detail the the beam-target interaction up to the KALIF peak voltage, and the propagation of the ablation plasma beyond the maximum proton range. For the first time, using 1-dim spatially resolving velocimetry, we have measured the ablation pressure history, and the ablative acceleration across the beam focus. The same technique was applied to investigate the growth of Rayleigh-Taylor instabilities during the ablative acceleration of targets furnished with periodical 2-dim structure.

2. Experimental

2.1. Measuring principle

The hydrodynamic phenomena during the early phase of the interaction are shown in fig.1 in a h,t-digram where h is the Lagrangian space coordinate. Due to time-of-flight compression of the beam front on the 15-cm-trajectory from the anode plasma to the target the first protons to reach the target have intermediate energies of 0.5-1 MeV and thus a certain initial range ρ which increases later as the voltage rises. The bulk energy deposition in the dense, cold, and thus little compressible material leads to a rapid pressure increase. The pressure is unloaded into one direction by material ablation, and into the other direction by transmitting a pressure wave into the adjacent cold material. This pressure wave is connected with a mass flow away from the ablation zone. The compression wave (solid line) reaches the rear surface at t_1. Pressure waves are reflected from free surfaces as rarefaction waves running back into the target.

(*) *Russian Academy of Science, Inst. of Chemical Physics, Chernogolovka*

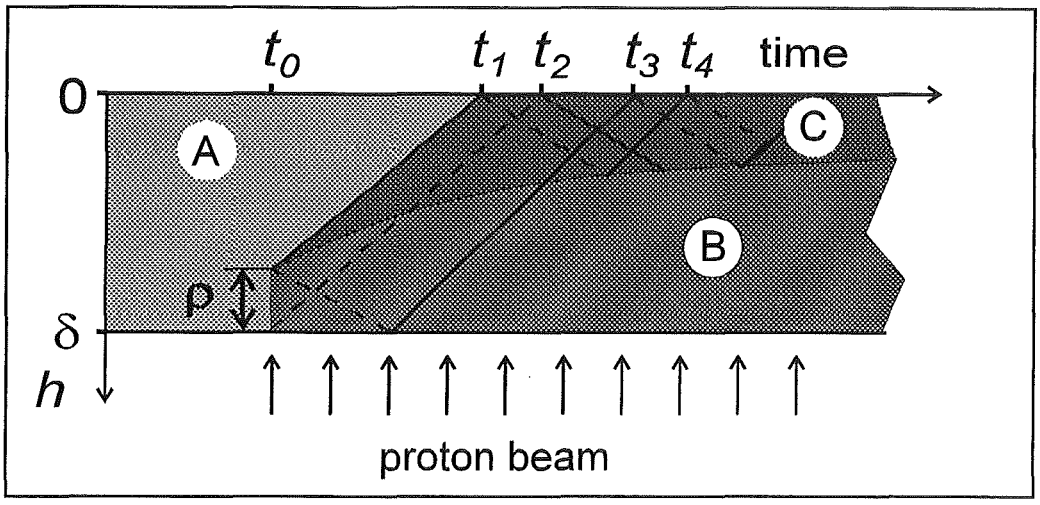

Fig. 1.: Schematic h,t-diagram (h: Lagrange coordinate) of the hydrodynamic phenomena in a the target in the early phase of energy deposition. At t_0, the proton beam of initial range R hits the target of thickness d. Pressure waves (solid lines) and release waves (dashed) reverberate in the target and gradually accelerate the rear target surface (A: undisturbed material; B: energy deposition zone; C: solid, compressed material.).

Rarefaction waves (dashed lines) are reflected from both, free surfaces and the ablation plasma boundary as pressure waves. Until t_3, the response of the rear surface contains information only on the ablation zone. Later on ($t>t_4$), wave reverberations in the condensed part superimpose to the effects originating in the energy deposition zone. They can be used to estimate the residual thickness of the target, which is proportional to t_4-t_1 , but blur the information on the ablation pressure.

The disturbances due to the reflections may be suppressed in the time interval of interest (~100 ns) by bringing the rear surface in close contact with a thick, optically transparent window having the same dynamic properties as the target. We use aluminum as target material, and LiF-single-crystal as a window. In this case, no reflection occurs at the interface between the two materials, and the velocity of the Al-LiF-interface recorded by the velocimeter is identical with the mass velocity $u_p(t)$. The transit time trough the window is much longer than the duration of the phenomena to be observed. Because of the increase of the propagation velocity u_s with pressure any finite pressure gradient would steepen and end up as shock front discontinuity after several nanoseconds, or several 10 µm distance covered. So, if we want to determine the pressure which is induced from the ablation zone in the adjacent condensed matter as a function of time, the particle velocity has to be measured very close (< 10 µm) to this zone. With proton ranges of ~25 µm this leads to total target thicknesses of ~30 µm.

The ablation pressure is calculated from the measured velocity u_p by applying the mass conservation (1), the momentum conservation (2) and the Hugoniot equation of state (3), the initial conditions being p_0=0, and $\rho=\rho_0$.

$$u_s \rho_0 = \rho_1 (u_s - u_p) \qquad (1)$$

$$p_1 = \rho_0 u_s u_p \qquad (2)$$

$$H(p, u_p, \rho) = 0 \qquad (3)$$

The velocity measurements were performed with the experimental setup described in detail in ref. [3] in this report.

2.2. Measurements and results

2.2.1. Ablative acceleration of thin targets

The first acceleration of the rear target surface is due to the decompression of the material as the first pressure wave reaches this free surface (t_1 in fig. 1). The reverberation of pressure waves from the ablation zone to the rear surface and decompression waves running in the opposite direction successively increase the velocity: the non-ablated part of the target is "ablatively accelerated". Fig. 2 shows, for the first time, the velocity history of a 50-µm-thick aluminum foil placed in the focal plane of the B_Θ-diode as a function of the distance to the KALIF axis. The initial jump to ~3 km/s is caused by the relatively high power density of the beam front, which may amount to >50% of the peak value, and which is due to the time of flight compression of the beam. The acceleration is maximum in a central region of 2 mm diameter where the velocity reduces slightly until the arrival of the reflected pressure wave (at t_3 in fig. 1) at ~ 6 ns. Two millimeters out of the beam axis, the velocity only stagnates during this period. This is probably due to a change in the focusing properties of the diode since this time period coincides with a strong increase of the bremsstrahlung signal and thus the electron loss current providing the self-insulating magnetic field. So far, spatially resolved measure-

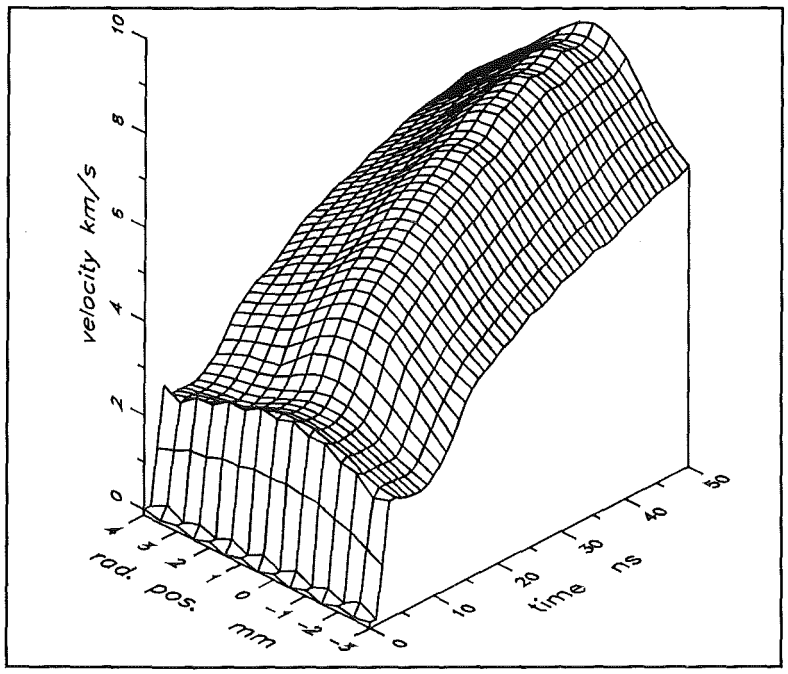

Fig. 2:
Ablative acceleration of an initially 50-µm-thick aluminum foil as a function of the radial position and time

ments could be performed with the B_Θ-diode only. The results confirm that, within a central area of ~2 mm diameter, the assumption of plane waves, which is a basic requirement for the spall strength measurements, is fulfilled for both direct drive and impact experiments using ablatively accelerated flyer plates (for details see ref. [3] in this report). From the spatially resolved measurements also follows that the power maximum scatters within a couple of millimeters around the diode axis. This is probably due to the relatively simple diode design with its fairly inhomogeneous flash-board ion source.

Both, the rise time of the initial velocity jump (t_1-t_0 in fig. 1) for different KALIF voltage histories, and the loss of reflectivity of the rear surface of sub-range targets of different thicknesses yield the evolution of the ion range in time. From the periods of the wave reverberations (t_4-t_1) for different target thicknesses, the thickness of the residual condensed layer, and thus the position the boundary of the ablation plasma can be deduced as a function of time [2].

At 30 ns after the energy deposition onset, i.e. after the energy maximum of protons on target, the thickness of the ablation zone exceeds the maximum proton range in cold matter. Since range shortening was observed in the ablation plasma due to the additional slowing down effect of free electrons [4] we made a series of experiments using two target foils separated by a 2-mm-gap. The large distance was necessary to decouple the hydrodynamic effects

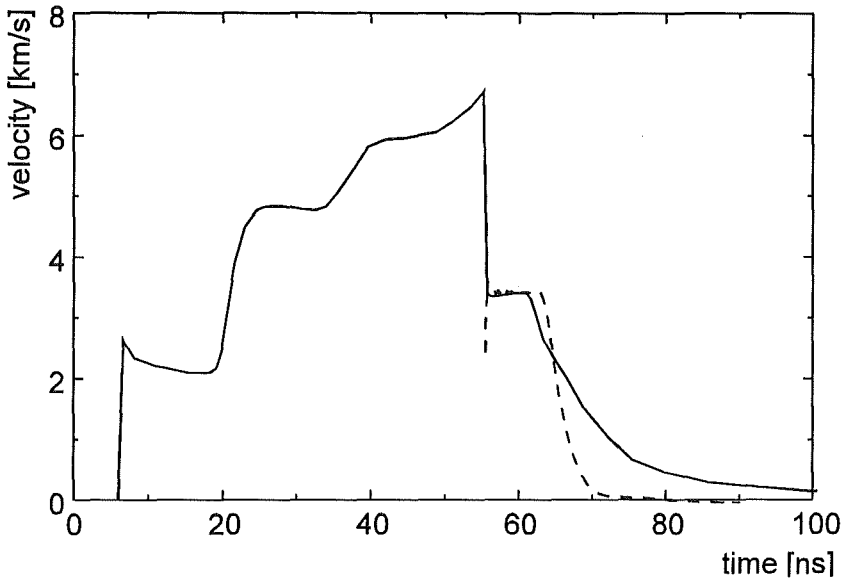

Fig. 3:
Impact of an ablatively accelerated aluminum foil of 71 μm initial thickness on a LiF-window (solid line). The dashed curve was calculated for a cold 48.5-μm- thick impactor. The difference is due to material ablation beyond the proton range of 22.5 μm and the momentum of the plasma plume.

of the two foils. The thickness of the foil facing the beam was increased stepwise until there was no more acceleration of the second foil detectable. This allowed to fix the maximum range of 1.53-MeV-protons to 22.5 μm. This is 4 μm less than the value for condensed aluminum.

The further progression of the ablation zone into the condensed part was demonstrated by impacting an ablatively accelerated aluminum foil ("flier") of 71 μm initial thickness on a LiF-window. In this experiment, the laser-Doppler velocimeter records the velocity of the rear flier surface through the window during the acceleration, and the velocity of the interface after impact (see fig. 3). Because of the nearly identical dynamic properties of the two materials, the particle velocity at the interface drops to exactly one half of the flier velocity at impact. The impact generates a compression wave propagating into both materials. The velocity remains constant until the arrival, at the interface, of the unloading wave generated in the flier by the reflection of the pressure wave at the ablation plasma boundary. The pressure plateau which would be caused by the impact of a 48.5-μm-thick flier (initial thickness minus maximum proton range) is displayed in fig. 3 by the dashed line. The measured plateau is significantly

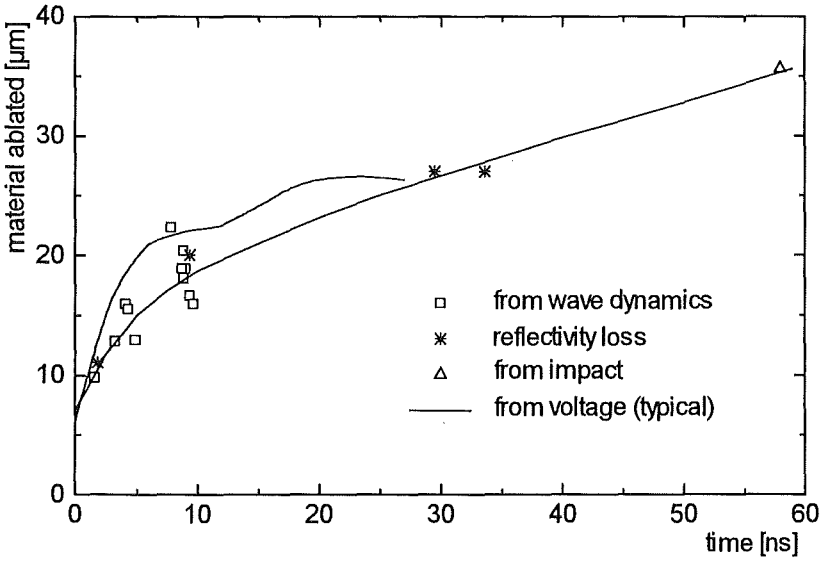

Fig. 4:
Thickness of the ablated material layer as determined by different methods in different shots (dashed), and proton range in cold matter for a typical KALIF voltage trace (solid) as a function of time.

shorter because of the progression of the ablation zone due to heat transport by ~13 μm, the "tail" being longer because of the momentum of the plasma plume. Fig. 4 shows the penetration of the ablation plasma into the target together with the "cold" proton range for a typical KALIF pulse.

Consitent 1-dim simulations of the ablative accelerations of foils of different thicknesses suggests that both EOS-data sets used considerably underestimate the pressure in the ablation plasma for $\rho \leq 0.01\ \rho_0$ at intermediate (~50 kJ/g) specific energy densities (see ref. [4] in this report and ref. [5]). This illustrates that even simple acceleration experiments may provide useful contributions to EOS data for the cold, dense plasma encountered in our experiments.

In direct drive acceleration experiments we have launched homogeneous target foils of ~10 to 25 μm residual thickness to velocities beyond 13 km/s. The potential of multilayer targets is being investigated by code simulation and experimentally, with the goal to reach hypervelocities. Simulations suggest that, using an optimized triple layer target consisting of a thin high-Z tamper (Au, Pb), a low-Z ablator with a high sound velocity like Be or diamond, and the actual flyer, hypervelocities exceeding 20 km/s could be obtained. This would open the possibility to investigate, by impact experiments, the state of matter in the 100- to 1000-GPa-range. Applications could range from EOS and phase transition measurements up to micrometeorite simulations.

2.2.2. Ablation pressure measurements

The quantitative and time-resolved measurement of the ablation pressure is the first step in determining the thermodynamical state of the relatively cold (~10 eV), dense (10^{20}-10^{22} cm^{-3}) plasma created by the interaction of the ion beam with condensed matter. With the two diodes used on KALIF we measured peak amplitudes of ~25 GPa (B_Θ-diode) and ~65 GPa (applied-B diode), respectively. These values approximately correspond to code predictions.

Fig. 5 shows for the first time the evolution of the ablation pressure as a function of the radial distance from the KALIF axis. With the B_Θ-diode, the bunching of the beam front results in an initial jump of the power density which leads to a fast pressure increase. Like in fig. 3 with the ablative acceleration the pressure varies by a few percent only in a 1- to

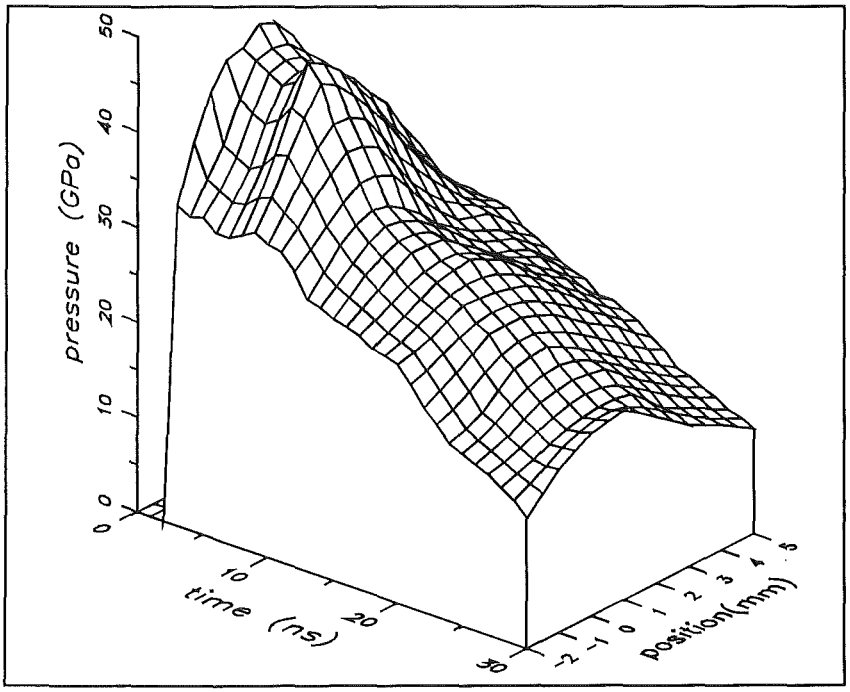

Fig. 5:
Ablative pressure obtained with the B_θ-diode in aluminum as a function of the radial postion and time

2-mm-diameter area around the axis. The temporary increase of the pressure after ~5 ns is due to a steeper voltage rise and thus a proton range increase. This results in the progression of the Bragg peak into cold material , and hence in a stabilization of the pressure for a few nanoseconds. Then, the compressibility of the ablation zone increases due to material expansion, and the pressure starts dropping despite further energy input. Although material ablates into 2π the radial pressure profile flattens by ~10 % only in the 30-ns-period displayed in fig 5.

2.2.3. Dynamic strength measurements

As shown above, KALIF is well suited to generate short, intensive pressure pulses in condensed matter. When reflected on a free surface, such pulses generate backward running tensile stress waves whose amplitude increases with the distance to the surface until the material fractures or "spalls". Both, tensile strain and strain rate, at which the rupture occurs, are deduced from a single velocity history measurement. The dynamic tensile strength increases with the strain rate. At KALIF, strain rates up to $10^8 s^{-1}$ can be realized which exceeds by two orders of magnitude the range of conventional methods. This is why spall experiments are performed during each target campaign. The recent state, in particular the spatially resolving measurements, is discussed in ref. [7] in this report..

2.2.4. Investigations on the hydrodynamic stability of ablatively accelerated foils

In some of our acceleration experiments using 33-µm-thick aluminum foils which were performed with the standard, not spatially resolving velocimeter we lost the laser light signal 10-20 ns after motion onset. Break-through of a heat wave front due to suspected beam filamentation leading to melting or evaporation of the rear target surface, tilt of the surface so that the sensing lightbeam is deflected beyond the acceptance angle of the velocimeter, or the formation of hydrodynamic instabilities were taken into consideration as possible explanations.

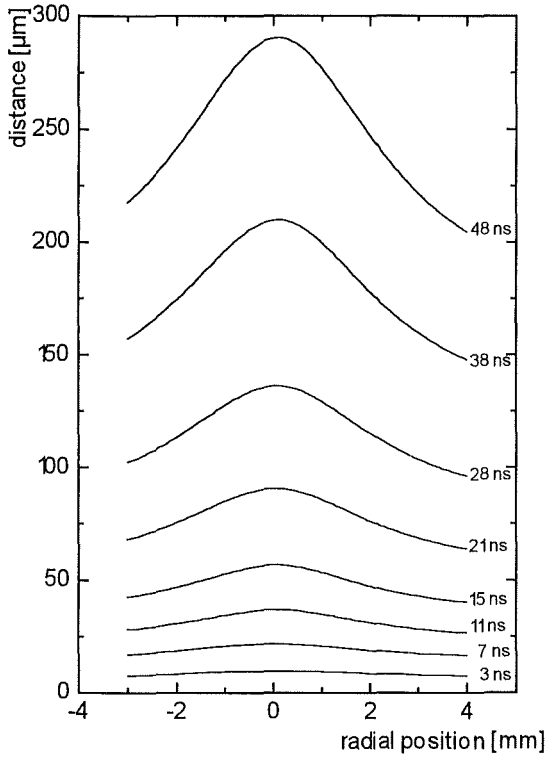

Fig. 6: Deformation of a planar 50-µm-thick foil during acceleration

If submitted to a constant acceleration a - normal to the interface between two inviscid fluids, and directed from medium 1 to medium 2 - the initial amplitude η_0 of a disturbance in the shape of the interface will vary as

$$\eta(t) = \eta_0 \frac{e^{\sigma t} + e^{-\sigma t}}{2} \quad , \quad \text{where}$$

$$\sigma = \sqrt{\frac{2\pi}{\lambda} \frac{\rho_2 - \rho_1}{\rho_2 + \rho_1} a} \, ,$$

ρ_1 and ρ_2 are the densities, and λ is the wavelength of the disturbance [8]. If $\rho_1 > \rho_2$, the amplitude η will show only oscillatory variations in time, in the other case the initial disturbance will grow exceedingly .

This latter phenomenon is known in literature as Rayleigh-Taylor instability. As early as

1974, the issue of instability growth on laser-driven ablatively compressed d-t-fusion pellets was investigated by computer simulations and analytical approaches (see e.g. [9]).

So far, this problem was studied experimentally only in laser- but not in ion beam-driven experiments (cf. e.g. [10]). One motivation for setting up a spatially resolving velocimeter was to find out whether this technique can be applied to the investigation of the growth of Rayleigh-Taylor instabilities of ablatively accelerated layers of condensed matter. The idea was that the penetration of the lighter medium into the denser should be detectable in the velocity distribution at its rear surface provided the target thickness is comparable with the wavelength of the the perturbation.

Concerning the loss of signal in acceleration experiments, spatially resolved measurements reveal a considerable deformation of the target foil as shown in fig. 6. As a result, light from points outside the optical axis is reflected under increasing angles and is vignetted by the aperture of the final imaging lens. Thus, if in normal ORVIS experiments the sensing area is not located in the beam axis - which is quite probable since the beam position scatters - the reflected cone of light can be vignetted very soon, especially in experiments with thin foils which accelerate and deform faster.

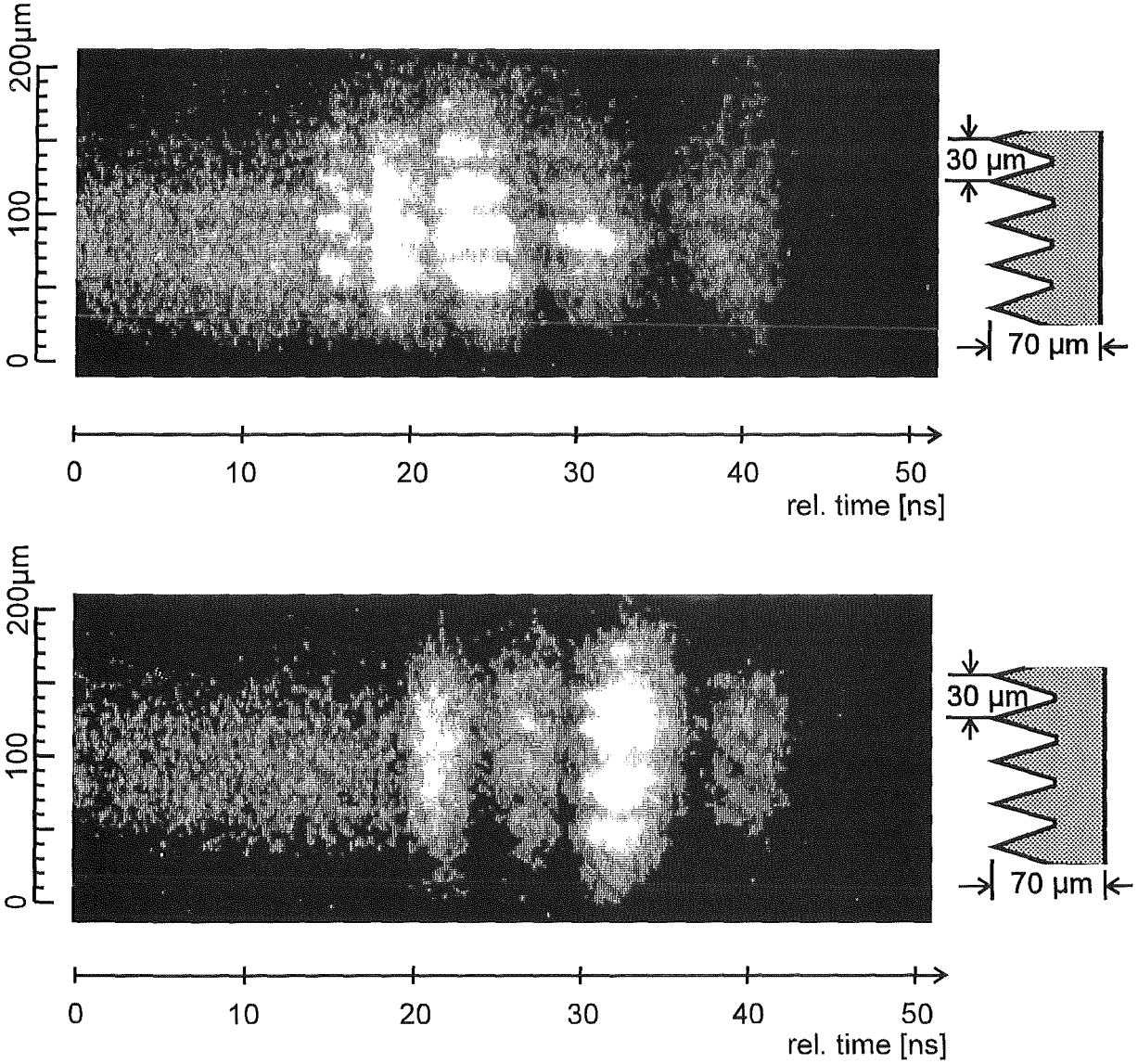

Fig. 7: Raw data (velocity interferograms) of experiments using structured targets. The velocity of the rear surface increases (bright-dark modualtion) acording to the structure from the beginning (upper) , or later into the acceleration process (lower). Cf. text.

In experiments on Rayleigh-Taylor instabilities, usually layers with a small pre-formed periodical perturbation are used. For first experiments, we had aluminum targets prepared in the micro-machining workshop oft the HVT-EA department at FZK. With the diamond tools available the structure shown in fig. 7 could be manufactured whose aspect ratio is rather high. So far, in two experiments two very contradictory results were obtained which are displayed as raw data in fig. 7. One cycle of the intensity variation in time indicates a velocity increase by 1.55 km/s in these expriments.

In the upper interferogram the mechanical structure of the surface exposed to the proton beam is visible in the velocity distribution on the rear surface from the beginning (start at 15 ns). The first jump in brightness occurs at the positions of the "bottoms", i.e. the smallest thickness of the target. About 2 ns later, the velocity increase occurs in the intermediate positions of the "ridges". Lateron, this time difference can not be discerned any longer. The vertical intensity modulation within the bright fringes is presumably due to the different light reflection properties of convex and concave parts of the rear surface corresponding to the locations of the bottoms and the ridges of the front side, respectively .

In the lower interferogram, the acceleration of the rear surface is homogeneous in the beginning (start at ~17.5 ns). Only ~15 ns later, an intensity modulation of the fringes appears as above. The reason for the very different behaviour is not understood yet. It could be due to different local power histories caused by the spatial scatter of the beam focus.

At the moment, the only the following conclusions can be drawn:

- We have found the spatial structure of the front side of the target in the velocity profile of the rear surface.
- The velocity history could be measured with a ≤10-μm-spatial resolution.
- For further experiments, several details should be modified.

A much smaller aspect ratio of the perturbations and different wavelengths should be used. Reference experiments with very smooth targets should be performed. Since aluminum is to soft to give a smooth, optical mirror like finish by micro-machining we should probably use an other material like e.g. bras. To reduce the brightness modulation within the fringes caused by the deformation of the specularly reflecting surface, the surface should reflect more diffusely. However, because of increased light losses in this case, an improved illumination system should focus the laser light exactly to the target surface of interest (~ 20×200 μm) instead to the actual 250-μm-diameter spot.

3. Conclusions

Our experiments on KALIF have demonstrated that a comparatively simple method like the investigation of the hydrodynamic response of planar targets by sub-nanosecond resolution velocimetry is a useful tool for high-power ion beam and beam-target interaction diagnostics. The extension of the velocimeter to 1-dim spatial resolution opens up new diagnostic possibilities for the examination of beam properties and probably for the investigation of hydrodynamic instabilities. The potential of KALIF as a generator of intense pressure pulses for matter and materials research has been verified in various experiments. The development of optimized triple layer target consisting of a thin high-Z tamper, a low-Z ablator, and the actual flyer, hypervelocities exceeding 20 km/s could be obtained. This would open the possibility to investigate, by impact experiments, the state of matter in the 100- to 1000-GPa-range.

Acknowledgment

This work was supported by the German-Russian Scientific and Technological Cooperation Treaty and The NATO Science Programme. The authors would like to thank O. Stoltz for his continuous technical support with the B_{Θ}-diode, and the KALIF operators for conducting the shots.

References

[1] K. Baumung, H.U. Karow, H.J. Bluhm, P. Hoppé, D. Rusch, G.I. Kanel, A.V. Utkin, S.V. Razorenov, and V. Licht: Light-Ion Beam-Target Interaction Experiments on KALIF, *Nuovo Cimento*, **106 A** (12), 1771 (1993).

[2] K. Baumung, H.U. Karow, D. Rusch, G.I. Kanel, A.V. Utkin, V. Licht: High-Power Proton Beam-Matter Interaction Diagnostics by Analysis of the Hydrodynamic Response of Solid Targets, *J. Appl. Phys.*, **75**(12), 7633 (1994).

[3] K. Baumung and J. Singer: A Novel High-Resolution Line-Imaging Laser-Doppler Velocimeter, this report.

[4] B. Goel and H. Bluhm, *Journ. de Physique - Coll. C7,* **49,** C7-169 (1988).

[5] B. Goel and O.Yu. Vorobjev: Reinvestigation Foil Acceleration Experiments, this report.

[6] O.Yu. Vorobjev and B. Goel: Reinvestigation of Aluminum Foil Acceleration Experiments, KfK Internal Report 51.03.02/03A, October 1994.

[7] K. Baumung, D. Rusch, J. Singer, S.V. Razorenov, A.V. Utkin, G.I. Kanel: Measurement of the Tensile Strength of Solids at Very High Strain Rates, this report.

[8] G. Taylor: The instability of liquid surfaces when accelerated in a direction perpendicular to their planes, *Proc. R. Soc. Lond.*, **A201**, 192 (1950).

[9] S.E. Bodner: Rayleigh-Taylor Instability and Laser-Pellet Fusion, *Phys. Rev. Lett.*, **33**, 761 (1974).

[10] E.M. Campbell: Recent results from the Nova program at LLNL, *Laser. Part. Beams*, **9**, 209 (1991).

Measurement of the Tensile Strength of Solids at Very High Strain Rates

K. Baumung, D. Rusch, J. Singer, S. V. Razorenov*, A. V. Utkin*, G. I. Kanel*

Short, intense pressure pulses generated by the interaction of the KALIF beam with solid matter are used to perform dynamic tensile strength measurements at strain rates of ~10^6 s^{-1} -$10^8 s^{-1}$. The shock wave phenomena involved and the the experimental technique are reviewed. The basis of the data evaluation, and some recent results are discussed. The problem of the planeness of the pressure wave front is addressed and new possibilities of spatially resolving spall strength measurements are presented.

1. Introduction

The theoretical ultimate tensile strength of solids σ_u can be estimated from the lattice constant a, the surface energy γ, and the bulk modulus E as

$$\sigma_u = 1/2 (4\gamma E / a) \approx E/10 - E/5 .$$

However, quasi-stationary experiments (at strain rates $(\delta x/x)/\delta t \approx 10^{-2} s^{-1}$) always yield values which are by more than two orders of magnitude lower. This is due to the fact that the mechanical and plastic properties of solids are usually controlled by lattice imperfections. Fracture under tensile stress is due to the generation and growth, respectively, of different kinds of distortions like second-phase particles, grain boundaries, lattice defects, dislocations, etc. .

Single crystals are largely free of various stress concentrators that will act as damage nucleation sites in polycrystalline materials, and show dynamic strengths 2-4 times higher than the latter. They are supposed to fail under stress essentially due to the growth of lattice dislocations generated during the plastic deformation prior to rupture.

If the stress is applied at increasing strain rates the finite growth rate of defects becomes noticeable and the resistance to fracture increases. It is also believed that the mechanisms leading to fracture change with the strain rate applied. That is why experiments on both, poly- and single crystals at high strain rates are of high interest for physics of strength. With experiments using explosive drivers strain rates up to ~10^6 s^{-1} can be realized. Using the proton beam of the KALIF B_Θ-diode as an ablative driver we have reached strain rates up to ~$10^8 s^{-1}$.

2. Experimental method

The measurement of the resistance of solids to dynamic fracture is based on the detection of so-called "spall phenomena". This failure mode is typical of shock-wave loading. It occurs when short shock waves, after reflection at a free surface, generate tensile stresses inside the bulk material which finally lead to rupture or spalling [1,2].

Shock-waves build up when a strong pressure wave is propagating into a compressible medium in which the sound velocity increases with pressure. In this case, the peak pressure part of the wave will overtake the preceding zones of lower pressure, and result in a shock front,

(*) *Russian Academy of Science, Inst. of Chemical Physics, Chernogolovka*

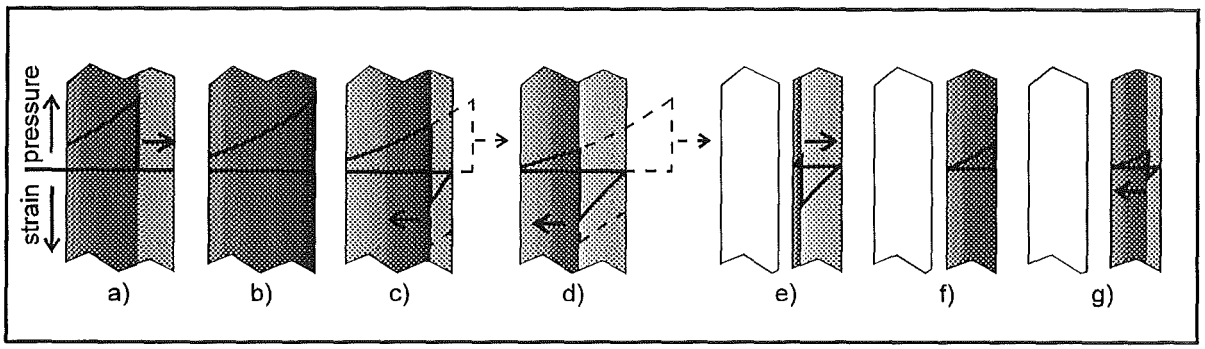

Fig.1: Schematic presentation of dynamic loading and fracturing (spalling) of a solid by reflection of a short shock wave at a free surface.

i.e. a sharp jump - within ≤1 ns and across a few micrometers in space - in pressure p, density ρ, and mass flow velocity u_p . On the other hand, the rear slope of the pressure wave " fans out " since lower pressure states increasingly lag behind. As a consequence, any finite pressure pulse, disregarding its initial distribution, will result in an approximately triangular shape consisting of a steep increase followed by smooth decay (cf. Fig. 1a) . As the shock wave propagates, the peak pressure reduces due to dissipation losses and the rear slope decreases. At peak pressures of 30 to 100 GPa and rise times <10 ns encountered in KALIF experiments a shock front forms after a transit time of a few nanoseconds, and a distance covered of a few 10 µm, respectively.

The process of tensile stress generation by the reflection of plane, triangular shaped shock wave and subsequent fracturing is schematically displayed in figs.1a - 1f together with the wave phenomena in the material layer detached from the bulk material, the so-called "spall plate". Fig. 2 shows the corresponding measured velocity history of the free surface of the spall plate.

The triangular-shaped pressure wave propagates from left to right (fig.1a). When it reaches the free surface at the left the compressed material expands freely thereby accelerating the

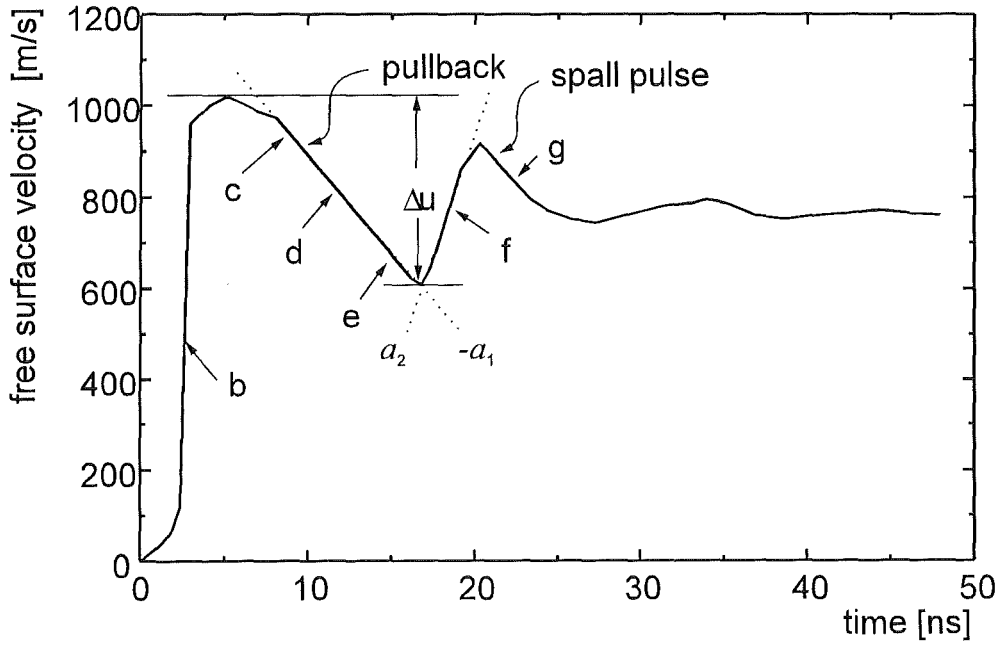

Fig.2: Free surface velocity of a 280 µm thick molybdenum single crystal. a_1 and a_2 are the slopes of the velocity profile. Other labels correspond to the sequence of fig.1.

surface to the velocity $u_{fs}= 2\times u_p$ (detail b in fig. 2). The expansion leads to material straining and thus to a deceleration of the surface (detail c). In terms of shock wave physics, the wave is reflected at the free surface as at an "open end", the boundary conditions being: inversion of amplitude and direction of propagation, and $p = 0$ at the surface. The superposition of two plane, oppositely running rarefaction waves, the trailing edge of the initial pressure wave moving to the right, and the tensile stress wave moving to the left, yields a residual stress whose amplitude increases with the distance to the free surface (figs 1c, 1d). When the stress exceeds the material strength rupture or spalling occurs in a plane parallel to the wave fronts and the expanded material of the spall plate bounces back from the spall surface thereby generating another pressure wave moving to the right again (fig1e). The information about spalling arrives at the rear surface with this pressure wave (fig. 1f) which is again reflected as a stress wave (fig. 1g). The wave reverberations in the spall plate are superposed to the surface velocity at the moment of rupture and are damped down due to dissipative losses (cf. fig. 2).

2.2. Experiments

The experimental setup for the spall experiments is similar to that one shown in the article on laser Doppler velocimetry in this report. The target is positioned in the focal plane of the B_Θ-diode. It consists either of just the sample whose dynamic tensile strength is to be measured, or of a sandwich consisting of an aluminum foil separated from the sample by a small gap [3]. The velocity history of the free surface opposite to the pressure source is measured by an ORVIS-type laser-Doppler interferometer inside a 200-µm-diameter sensing spot with a nanosecond time resolution (figs 2 and 3). Recently, we have used, for the first time, a spatially resolving interferometer allowing the measurement of the velocity along a 0.2 to 8 mm long line. The objective was to investigate the spatial dependence of the spall strength over distances of ~1 mm , and to check the planeness of pressure waves generated by both, the direct drive and the impactor method . Fig. 4 displays the spall profile of a molybdenum single crystal which was deformed by rolling. The spatial resolution was normal to the rolling direction. The material seems very viscous since the spall pulse is little pronounced.

Specimen thicknesses are in the range of 30-800 µm with diameters of 10-25 mm. As will be shown in the next chapter the strain rate depends on the slope of the release wave - the "tail"- following the initial shock front. Since this slope reduces as the wave propagates into the material the strain rate can be adjusted approximately by varying the thickness of the sample. On the other hand, the peak load pressure also affects the failure threshold through the generation of dislocations. In order to obtain comparable spall strengths, the peak load should be approximately constant in one test series. For strain rates of $\sim 10^6$ s^{-1} the ablation pressure

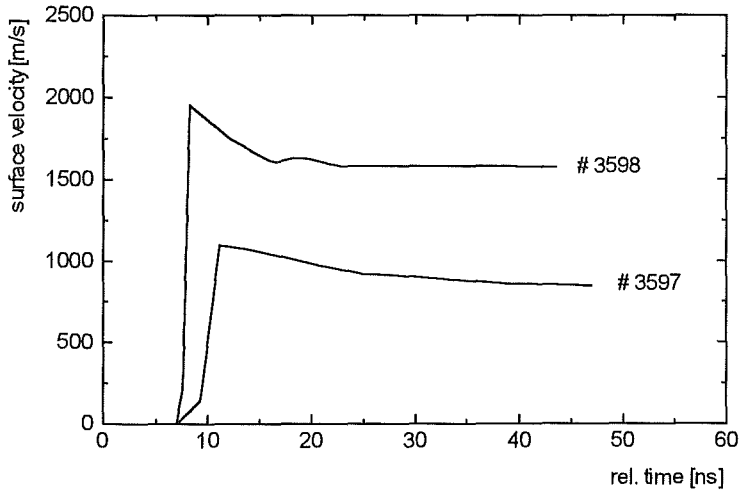

Fig. 3:
Surface velocity profiles measured with 304-type stainless steel of 300 µm thickness. The load in the 300-µm-thick specimens was generated by material ablation (#3597), and by impact of an ablatively accelerated aluminum foil of 50 µm thickness (#3598). Due to the viscosity of the material the spall pulse is damped out.

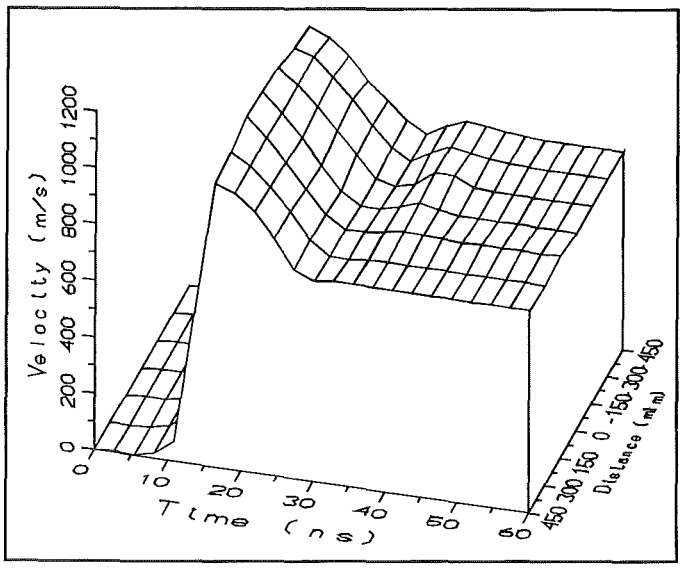

Fig. 4:
Spatially resolved surface velocity profile of a deformed molybdenum single crystal. The crystal was rolled to 1/10 of its initial thickness, the rolling direction being normal to viewing direction of the velocimeter. Due to the high viscosity of the sample the wave reverberations after rupture are strongly damped.

pulse generated by the direct beam interaction (see ref. [4] in this report) is used with specimen thicknesses of 300-800 μm. For higher strain rates the impactor method is applied: an initially 33 to 75 μm thick aluminum foil is ablatively accelerated by the ion beam and strikes the specimen. Due to the impact in both, the impactor and the specimen, a compression wave is generated whose amplitude is given by the impactor velocity and the hydrodynamic properties of the materials. The pressure remains approximately constant during a period Δt which is determined by the thickness of the impactor d and the propagation velocity u_s of the pressure wave : $\Delta t = 2d/u_s$. Since u_s varies weakly with the impact velocity, Δt is adjusted by the flyer thickness. With aluminum impactors the initial thickness is reduced by ~25 μm due to material ablation so that in our experiments the effective thicknesses at impact were ~10-50 μm. The impact velocity was adjusted to ~ 4-5 km/s by selecting appropriate distances (~100-500 μ) between impactor and specimen. The resulting peak pressure was 60-100 GPa. Using specimen thicknesses between 30 and 400 μm allowed to realize strain rates from 2.8×10^6 to 2.8×10^7 s^{-1}.

2.3 Data evaluation and results

There exist different approaches to infer the tensile stress in the spall plane from the wave phenomena observable at the surface [4,5]. We use an acoustic approximation in which the spall strength σ^* is calculated from the pullback amplitude Δu, the material density at zero pressure ρ_0, and the bulk sound velocity c_b as

$$\sigma^* = \tfrac{1}{2}\, \rho_0\, c_b\, \Delta u.$$

The bulk sound velocity is the propagation velocity of the initial compression wave and is determined from the peak surface velocity using the Hugoniot equation of state. The strain rate in the spall plane is directly determined from the deceleration of the pullback a_1 in the free surface velocity profiles (cf. fig.2)

$$\dot{\varepsilon} = a_1 / 2c_b.$$

Results of spall strength experiments obtained by the Russian colleagues using explosively accelerated impactors (O) and results obtained at KALIF (+) on a 304-type stainless steel are shown in fig. 5 as a function of the strain rate.

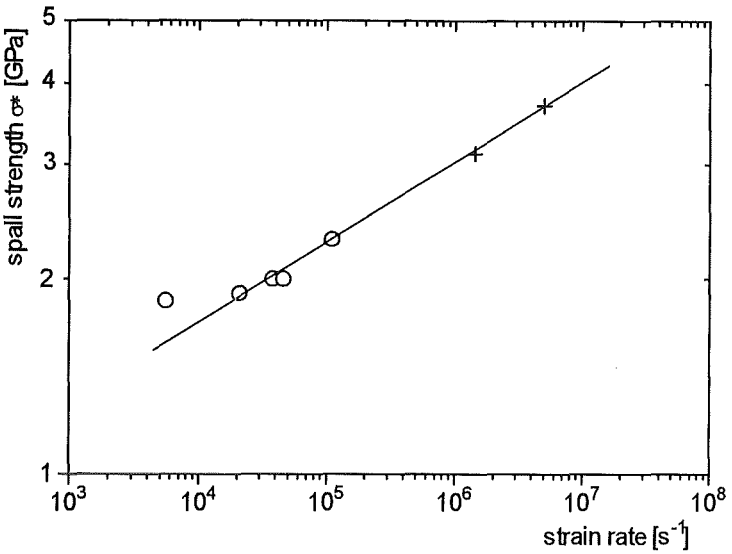

Fig. 5:
Spall strength of 304-type stainless steel as a function of the strain rate. Results from experiments using explosives (O) and KALIF (+) as a pressure generator (direct drive lower, ablatively driven impact loading upper value).

The spatially resolving experiments have shown that the initial pressure pulse generated by the beam front has a diameter comparable to the nominal focus fwhm of ~8 mm. Due to the time-of-flight compression of the beam front in the B_Θ-diode the initial specific energy deposition may reach that one at peak voltage. Since the compressibility of the target material increases as temperature rises, the peak pressure is generated at the beginning of the pulse. Hence, spalling is induced by this first pressure wave of large diameter and the plane geometry is ensured although the beam axis can move by ~1 mm from shot to shot. The planeness of the pressure wave generated by an impactor was investigated by impacting a foil on the aluminized surface of a thick, optically transparent window (LiF which has hydrodynamic properties nearly identical to those of aluminum; this avoids partial wave reflections at the interface). Under typical conditions - aluminum foil of 50 µm initial thickness, 135 µm gap - the impact is plane within a ~2-mm-diameter as can be inferred from the interferogram displayed in fig. 6. The deformation of the foil within this area is ±2 µm, the tilt at the edge being <10 mrad. Nevertheless, since the reproducibility of the position of the beam axis is comparable several experiments should be performed and checked for consistency.

Fig. 7 shows the variation of the spall strength of a deformed molybdenum single crystal over a distance of ~1 mm normal to the rolling direction of the specimen. First experiments

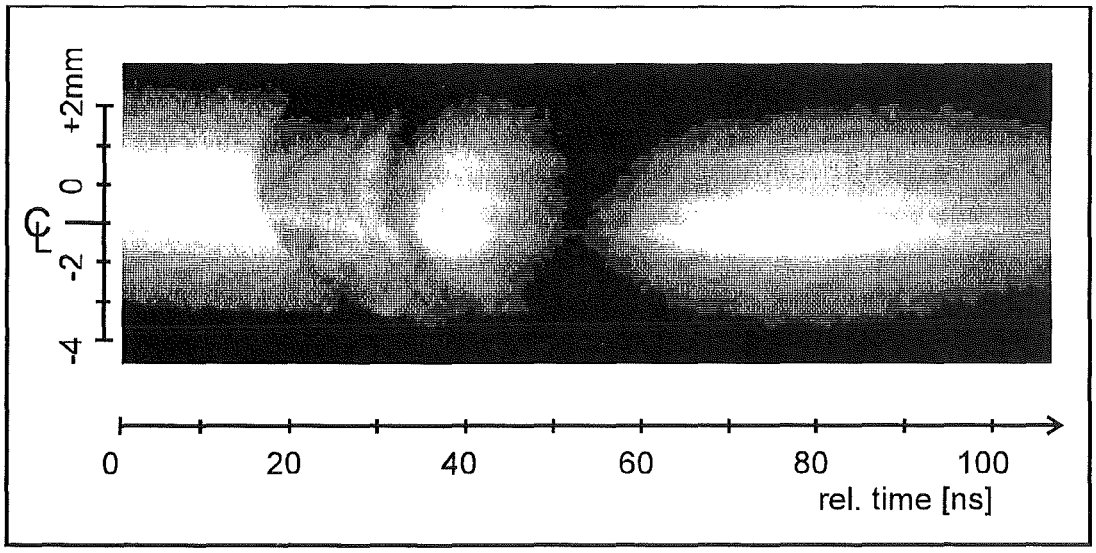

Fig. 6: Velocimeter interferogram of the impact of a ~25-µm-thick aluminum foil on a plane surface. The impact velocity is ~5.3 km/s.

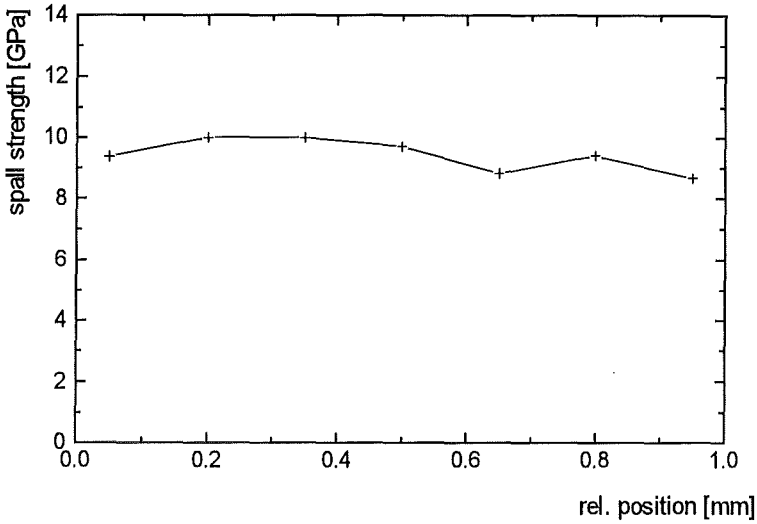

Fig. 7:
Spatial variation of the spall strength of a molybdenum single crystal deformed by rolling. The "micro spall strength" was measured in the direction normal to the rolling direction.

with high purity copper foils annealed at 800 K under cover gas to obtain coarse crystalline structure (~50-μm grain size) indicate considerable spatial variations of the spall strength. In the next campaigns we intend to investigate other materials, and in particular the spall behaviour across grain boundaries. Maybe, a the spatially resolved "micro spall strength" can achieve an importance comparable to e.g. the micro hardness.

3. Conclusions

KALIF as an ablative generator of very short, intense compression pulses in solid samples and the laser Doppler velocimeter, including the spatially resolving version, provide unique possibilities for studying the strength of materials under nanosecond load durations. We plan to continue this work on various materials, and to explore the potential of the spatially resolved measurements.

Acknowledgement

This work was supported by the German-Russian Scientific and Technological Cooperation Treaty and The NATO Science Programme. The authors would like to thank Otto Stoltz for his continuous technical assistance, and the KALIF operators for conducting the shots.

References

[1] J.A. Zukas, T. Nicholas, H.F. Swift, L.B. Greszcuk, and D.R. Curran, *Impact Dynamics* (Wiley, New York, 1982).
[2] A.V. Bushman, G.I. Kanel', A.L. Ni, and V.E. Fortov, *Intense Dynamic Loading of Condensed Matter* (Taylor and Francis, London, Washington, 1993).
[3] G.I. Kanel, S.V. Razorenov, A.V. Utkin, V.E. Fortov, K. Baumung, H.U. Karow, D. Rusch, V. Licht, *J. Appl. Phys.* **74**(12), 7162 (1993).
[4] K. Baumung, D. Rusch, J. Singer, S.V. Razorenov, A.V. Utkin, G. I. Kanel: Hydrodynamic beam-target experiments on KALIF, this report.
[5] S.A. Novikov and A.V. Chernov, *J. Mech. Tech. Phys.* **23**, 703 (1982).
[6] G.R. Gathers, *J. Appl. Phys.* **67**(9), 4090 (1990).

A Novel High-Resolution Line-Imaging Laser-Doppler Velocimeter

K. Baumung and J. Singer

This article gives an outline of the principle of laser Doppler interferometers of the VISAR- and ORVIS-type in general, and a description of the setup realized at KALIF. Then our novel line-imaging version is presented which takes care of the localization of the interference fringes and applies an intermediate imaging. Using a low f-number lens allows to realize a spatial resolution <10 μm, to vary the field of view between 200 μm and 8 mm, and to manage that at a laser power of ≤1 W. Two interferograms illustrate the operation of this interferometer as a line-imaging VISAR or ORVIS, respectively.

1. Introduction

Laser-Doppler velocimeters of the VISAR [1] and ORVIS [2] type are widely used in shock wave physics. They are based on the measurement of the Doppler shift $\Delta\lambda_D=\lambda_D-\lambda_0$ of laser light (wavelength λ_0) reflected by a moving surface, and allow to record velocity histories in the range of ~100 m/s to >10 km/s at a sub-nanosecond temporal resolution. These instruments have a ~200-μm-diameter sensing area corresponding to the size of the focal spot of the laser beam. Uniform velocity representative of the surface motion is assumed for this area and spatial resolution is not of interest.

In many shock wave experiments, plane geometry is aimed at in order to obtain clear test conditions, and to facilitate data evaluation. To check the planeness of impactors, a line-imaging VISAR was set up by Hemsing at LANL [3] allowing to measure the velocity along a distance of a couple of centimeters. In hydrodynamic target experiments going on at KALIF the proton beam of ~5-8 mm fwhm focus diameter is used to generate pressure pulses or ablatively accelerate thin targets. Although target thicknesses are <<1 mm in most cases, it is important to know over which diameters planar geometry may be assumed. Since, in addition, the hydrodynamic response of thin targets turned out to be a simple, complementary means for the diagnostics of beam parameters [4] an upgrade of our velocimeter to one-dimensional spatial resolution seemed desirable. In the following, a line-imaging velocimeter is described including a new feature which allows to obtain high (≤10 μm) spatial resolution, and operates at laser powers of ≤ 1W typical of normal ORVIS or VISAR-type velocimeters.

2. Experimental setup

2.1. Measuring principle

The design principle of the velocimeter results from the following conditions:

- The Doppler shift being small - $\Delta\lambda_D/\lambda \approx 6\times10^{-6}$ for a surface velocity of 1 km/s - a high-resolution spectrometer has to be used.
- The reflecting surface can not be expected to maintain mirror-like optical finishing throughout the experiment. Surface distortions will cause diffuse, or divergent, reflection. This requires a certain minimum acceptance angle of the spectrometer.

High spectral resolution can be obtained either by low-order interference ($\Delta\varphi/2\pi$ = 1...4) of a large number of partial beamlets ($N \sim 10^5$ with a grating spectrometer) or by high-order interference ($\Delta\varphi/2\pi \sim 10^5$) of a few partial beams ($N \approx 10$ with the Perot-Fabry or Lummer-Gehrcke interferometer). The "**V**elocity **I**nterferometer **S**ystem for **A**ny **R**eflecting surface" or VISAR is a two-beam interference spectrometer (see fig.1) achieving high resolution by a large ($\Delta x \approx 10^5\ \lambda$) path difference of the two beams. The light pattern at the output of the interferometer represents successive high-order interference fringes of the laser line λ_0. If the wavelength changes due to Doppler shift the phase difference between the two beams leaving the spectrometer changes by

$$\Delta\varphi = 2\pi \cdot \frac{\Delta x}{\lambda_D} \cdot \frac{\Delta\lambda_D}{\lambda_0} \qquad (1)$$

A change of the phase causes the intensity at a fixed point of the interference pattern to vary as $I \sim [1+\cos(\Delta\varphi+\varphi_0)]$, where φ_0 is the initial phase at zero velocity, or, if a fixed intensity is considered, a displacement of the locus of this intensity in the direction perpendicular to the fringe orientation by a distance $\delta = d \times (\Delta\varphi/2\pi)$ where d is the spacing between two successive fringes. For velocities $v << c_0$ of the reflecting surface (c_0 is the vacuum speed of light) the Doppler shift is given by $\Delta\lambda_D/\lambda_0 = -2v/c_0$. Thus, recording either the intensity variation, or the displacement of the fringes directly yields the surface velocity. In both cases, clear interference fringes of good contrast are needed. That requires the two partial beams at the interferometer output to be collinear, i.e. to superpose point by point over the whole cross-section.

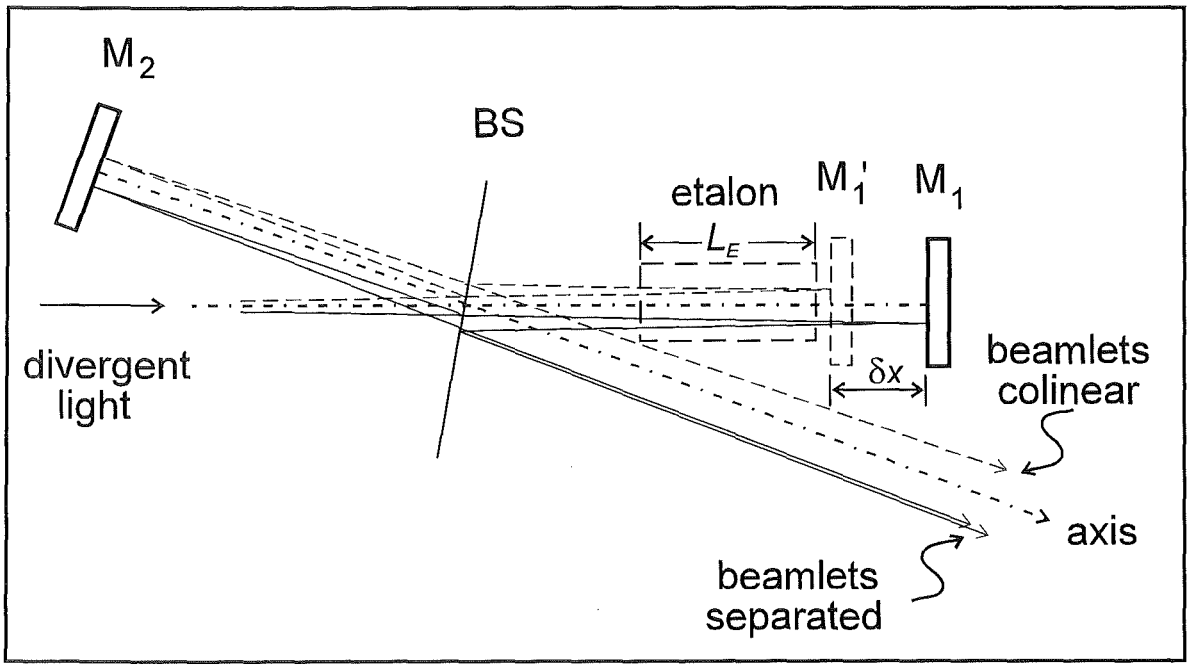

Fig.1: Scheme of the oblique Michelson-type interferometer used in VISAR instruments

How both, collinearity and a large path difference, can be realized simultaneously with divergent light follows from fig.1. A beam splitter BS divides the incoming beam to the two legs of different length. The two partial beams are reflected by mirrors M_1 and M_2 and recombine at the output. Due to the divergence of the input beam the cross-sections of the two partial beams at the output will be different (beamlets traced as solid lines), i.e. they are not collinear. Inserting a glass etalon of length L_E and refractive index at the laser wave length n_0 into the longer leg makes mirror M_1 appear at a position M'_1 which is by $\delta x = L_E(1-1/n_0)$ closer to the beam splitter. Adjusting the interferometer so that the distances to the beam splitter of M'_1 and

M_2 are the same provides the collinearity of the two partial beams (beamlets traced as dashed lines) while the geometrical path difference δx is increased by the additional optical path length of the etalon $\delta x_{opt}=L_E(n_0-1)$ so that the total path difference becomes $\Delta x=L_E(n_0-1/n_0)$. The velocity change causing a phase shift of 2π, i.e. one full cycle in the intensity variation or the displacement of the interference pattern by one fringe spacing d is called the fringe constant v_0 and indicates the instrument sensitivity. It depends on the etalon properties only, and is set by the etalon length. A ~3% correction δ_n allows for the dispersion $dn_0/d\lambda$ of the etalon.

$$v_0 = \frac{\lambda_D c_0}{L_E (n_0 - 1/n_0)(1+\delta_n)} \qquad (2)$$

The interferometer can be adjusted in in two different ways according to the two methods of measuring the phase shift mentioned above. If the axes of the partial beams are aligned parallel the interference fringes represent a circle surrounded by a series of bright and dark circular, so-called Haidinger rings whose radii increase proportional to $\sqrt{n}$, the order of the n-th ring from the center being $N+n$. Depending on the sign of the phase shift, rings disappear into or emerge from the center. The interferometer is adjusted so that the diameter of the central circle and contrast is maximum. A photomultiplier of corresponding diameter placed in the center then measures intensity variations as indicated above. The drawback of this simple arrangement is that the sign of a velocity change is uncertain so that additional effort is needed (for details see ref. [1]). This technique is applied with the VISAR.

If the the axes of the partial beams intersect at a small angle, the interference pattern forms a series of straight fringes which displace in a direction perpendicular to their orientation if the velocity changes, the direction depending on the sign of the velocity change. An electrooptical streak camera with the input slit set parallel to the fringe displacement allows to record both, amount and direction of a velocity change at a sub-nanosecond resolution. This is the technique applied with the "Optically Recording VISar", the ORVIS. Since the KALIF group disposes of streak cameras we have chosen this variant.

2.2. The KALIF ORVIS

Figure 2 gives an overview of the ORVIS used with the KALIF accelerator. The target, whose velocity history is to be measured, is located in the focal plane of the ion diode inside the vacuum chamber at ~10 cm from a 80-mm-diameter window. Lens L_1 (f= 300 mm, d=80 mm) is used to focus the 2-mm-diameter beam of a single mode Argon ion laser (λ_0=514.5 nm) to the target surface. It collects a considerable part of the diffusely reflected light and collimates it to an approximately parallel beam. A telescope is used to reduce the beam diameter from 80 mm to ~15 mm to adapt it to the 28 mm aperture of the etalon. The interferometer is set up at a 4-m-distance behind a concrete shielding wall. Initially, we chose the conventional Michelson configuration with the rectangular arrangement of the two legs. This setup is convenient for realignment after changing the etalons. The astigmatism introduced by the 8-mm-thick beam splitter under 45° does not affect the quality if the interference fringes. Lens L_2 is used to adjust the cross section of the beam to the 5-mm-diameter of the image guide. We use this light guide despite the 50% transmission loss. It is replaced by a reticle eyepiece which facilitates much the readjustment of fringe position and contrast after a modification.

The cylindrical lens images the straight line interference pattern to a series of bright spots to improve the intensity transmitted to slit of the IMACON 675 streak camera. To protect the camera from excessive dc light both, an electromechanical and an electrooptical shutter (Pockels cell) are provided. Since the mechanical shutter is by far the slowest component of

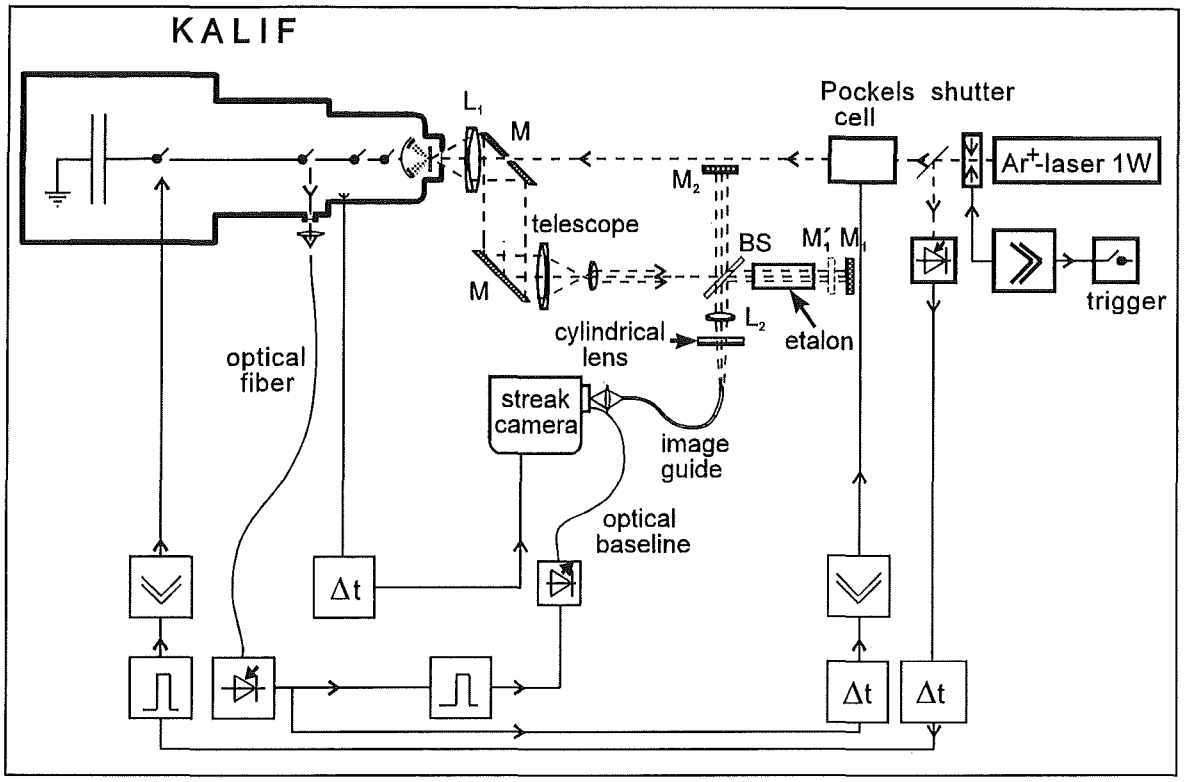

Fig.2: Scheme of the ORVIS setup at KALIF

the system (7±1 ms response time) the signal of a photo diode behind the shutter is used to trigger KALIF. The ion pulse is delivered to the target ~3.5 μs later. A Pockels cell with an extinction ratio of ~500 is used to reduce the light intensity until about 100 ns prior to the shot. The trigger signal for the Pockels cell is derived from the light flash emitted by the switch between the intermediate store and the pulse forming line. The streak camera is triggered like most of the other signal acquisition by an electrical pulse picked up from the pulse forming line. This trigger shows a ±7 ns jitter with regard to the ion pulse on target. This allowed us to realize total streak lengths down to ~20 ns providing a 250-ps-time resolution. A light pulse from a laser diode ($\lambda \approx 630$ nm) can be fed by an optical fiber to the lower edge of the camera slit to trace a baseline on the streak records. This improves the reading precision of slow, small fringe displacements.

2.3. The line-imaging variant

The coherence length of a single frequency line of Argon ion lasers is many meters. Thus, collinear alignment of the instrument gives concentric interference fringes which are visible on a screen put into the output beam, disregarding the distance to the beam splitter. For the ORVIS straight fringes are used. In this case, a special adjustment called "defocusing" is described in ref. [3] to obtain fringes of good contrast at the camera slit.

Spatiallly resolving velocimetry requires imaging of the moving surface onto the camera slit. This in general affects the condition for good contrast. If, like in Helmsing's instrument, a big f-number is used, i.e. the beam divergence is small, no special care is necessary to obtain reasonable contrast. At smaller f-numbers, the depth of field becomes smaller and the fringes become "localized" [5]. With the Michelson interferometer, they are localized in the virtual air wedge between mirror M_2 and the image M_1" seen in the beam splitter of the apparent image

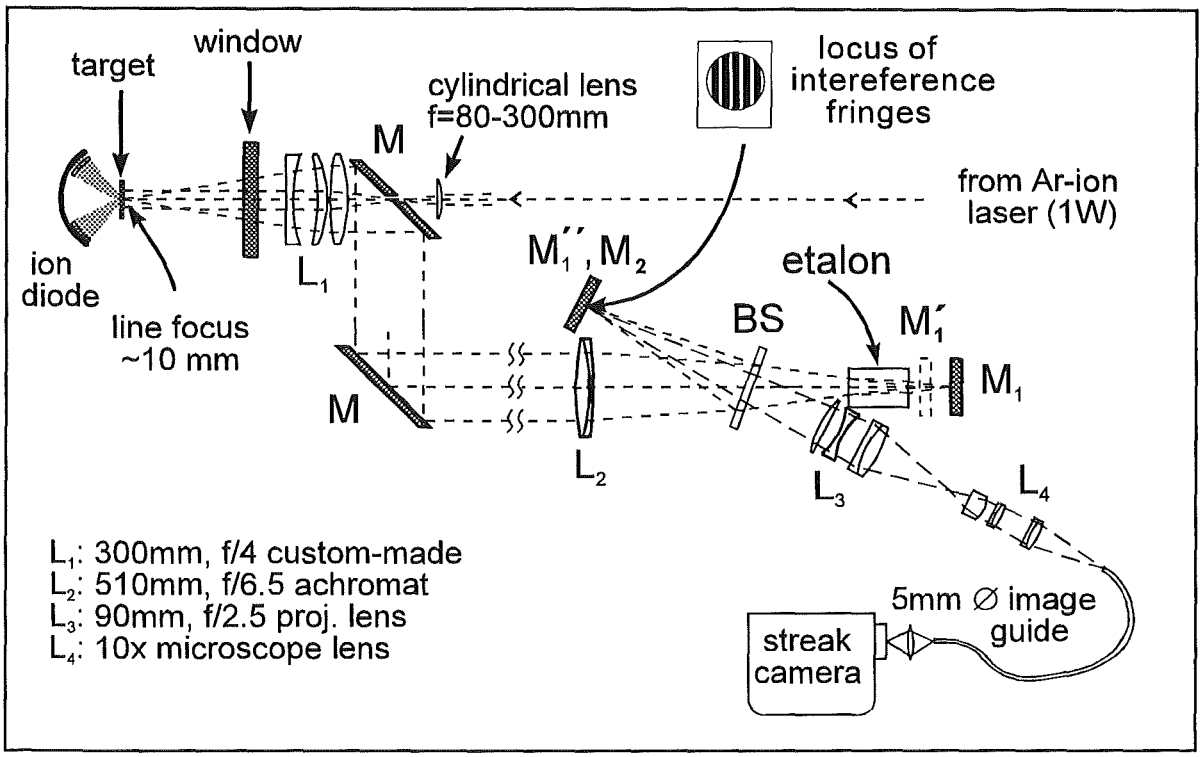

Fig. 3: The high-resolution line-imaging velocimeter used at KALIF

M_1' of mirror M_1. In the aligned interferometer, the mirror planes M_2 and M_1'' virtually coincide (cf. fig. 3). We therefore decided to perform the imaging of the object by an intermediate picture located in this mirror plane as shown in fig. 3.

The line to be imaged is illuminated by a cylindrical lens in front if L_1. which fans out the focus to a line. To get a more uniform intensity distribution, the beam expander at the laser output (not shown in the figures) is slightly detuned to provide a 4-mm-diameter "hollow" beam profile at L_1 rather than a Gaussian distribution. Using a cylindrical lens of 80 mm focal length illuminates a line ~10 mm long and ~150 µm wide rather uniformly. For smaller fields of view, cylindrical lenses with focal lengths of 200 and 300 mm are used. For spatial resolutions in the 10-µm-range the field of view is ~200 µm so that the circular focus of the laser beam can be used.

The intermediate imaging offers the possibility to adapt the magnification to the experimental requirements. The measurements of the radial dependence of ablative pressure and acceleration needs a maximum field of view of ~8 mm. In this case, L_3 provides a suitable image size of ~5 mm on the image guide input. First investigations on the spatial dependence of the dynamic tensile strength of solids (see ref. [6] in this report) was performed over 1-2 mm distances. In this case, the second imaging was provided by the telescope L_3, L_4 . First experiments on the development of Rayleigh-Taylor instabilities during the ablative acceleration of thin, structured foils were performed at a ~10-µm-resolution (cf. article on hydrodynamic experiments in this report). In this experiment, L_2 was removed and the intermediate image was directly generated by L_1. That is a high-precision, custom-made lens designed to furnish optimum resolution close to the diffraction limit at the laser wavelength taking into account the refractive properties of the 10-mm-thick window of the KALIF vacuum vessel. The further magnification was achieved by the telescope. High spatial resolution requires the astigmatism of the beam splitter positioned obliquely in the beams to be small. This is why we set up the line-imaging velocimeter with an angle of ~25° between the input beam and the normal of the beam splitter plane. The interferometer can be adjusted to operate in the VISAR or ORVIS mode, respectively. In the first variant, the camera slit is either located in the center of the

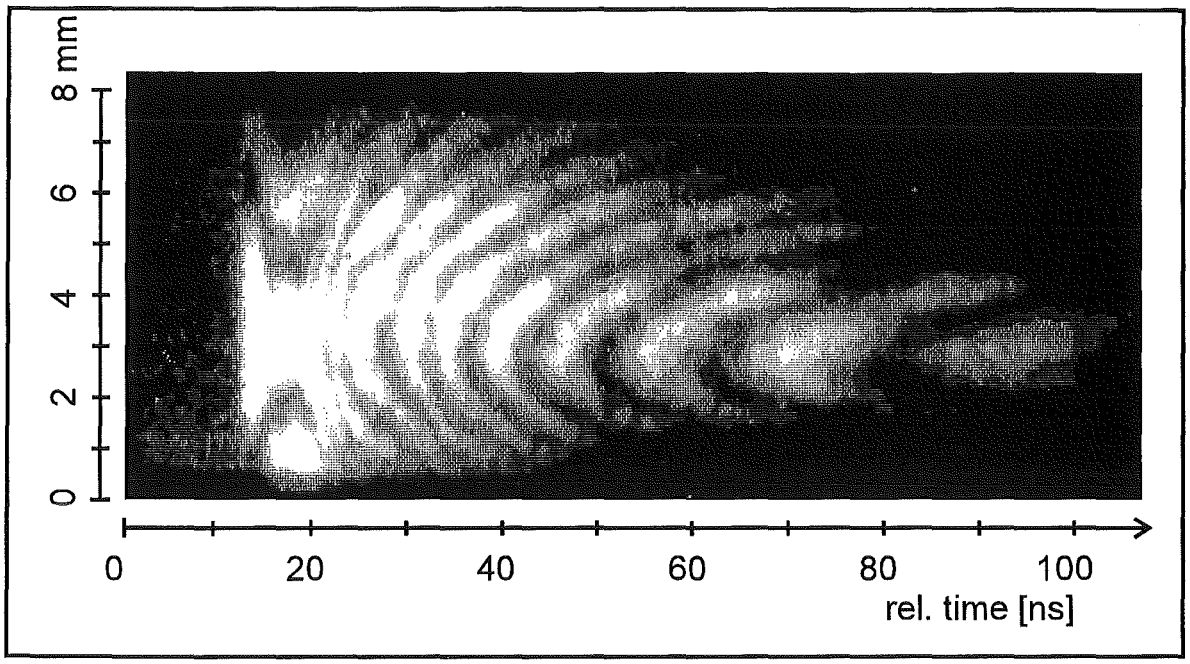

Fig.4: The interferogram obtained with the line-imaging VISAR shows the acceleration of a 50-µm-thick aluminum foil. Fringes indicate lines of constant velocity. The velocity increase between two fringes is v_0= 610 m/s. The initial jump to ~2000 m/s is not resolved on this time scale.

central Haidinger circle or it is aligned parallel to the straight interference fringes. In both cases, if the velocity change is the same over the whole surface viewed, the light intensity varies the same way along the whole slit. Thus, a constant acceleration results in a series of bright and dark fringes perpendicular to the streak direction, the time between to bright fringes indicating a velocity change by one fringe constant v_0. If the velocity is spatially dependent, the straight fringes deform to curves connecting points of equal velocity in the x,t-plane as displayed in fig.4. Such single VISAR interferograms are very illustrative and provide optimum

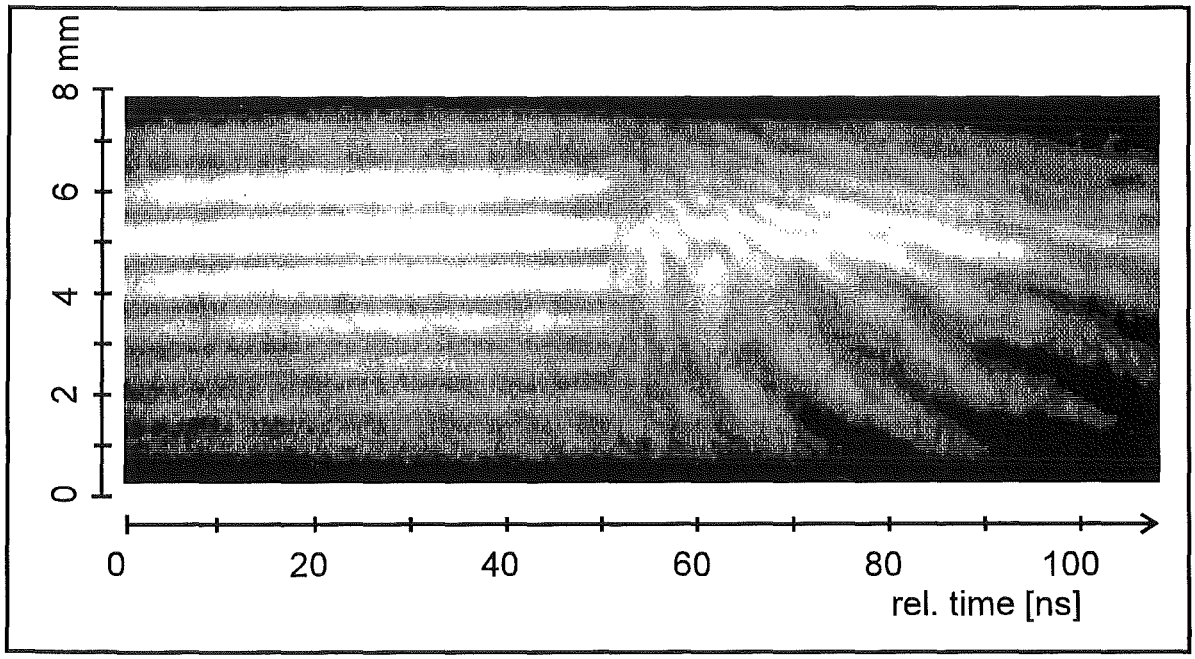

Fig. 5: Interferogram recorded with the line-imaging ORVIS using a 33-µm-thick aluminum foil backed by a LiF-window. In this case, the mass velocity inside a dynamically homogeneous target is measured without wave reflections from the free surface. Fringe constant v_0=268 m/s.

spatial resolution. However, as already mentioned, the sign of the velocity change is not known. A second or, like in Helmsing's experiments three additional interferograms are recorded simultaneously in order to obtain quadrature phase components [3] and thus the sign of the velocity changes. For simple cases like the investigation of the planeness of the ablation pressure pulse or of an accelerated impactor a single interferogram is sufficient as fig. 4 illustrates. Another disadvantage of this configuration is that the size of the central interference ring reduces if the etalon thickness, or the sensitivity, respectively, is increased. This is due to the spherical aberration of thick plane parallel plates. Straight fringes get curved outside an circular region corresponding to the central circle. This reduces the useful field of view with increasing sensitivity.

If the camera slit is oriented perpendicular to the fringe direction like in the simple ORVIS the interferogram consists of fringes parallel to the streak direction as long as the velocity is zero. As the velocity changes, they are deflected in the direction perpendicular to the streak, the amount and direction depending on both, the amount and sign of the velocity change of the given spatial position as illustrated in fig. 5. To determine the velocity history at a given place the intensity variation at the corresponding ordinate has to be read from the interferogram as a function of time.

First results obtained with the KALIF line-imaging velocimeter are presented in two preceding articles of this report on hydrodynamic experiments, and dynamic tensile strength measurements.

3. Conclusions

We have presented a novel line-imaging laser Doppler velocimeter which uses low f-number optics and takes advantage of the spatial localization of the interference fringes in the mirror planes for an intermediate imaging. This allows to obtain optimum contrast, and to vary the magnification in a wide range. Our custom-made lens especially designed for imaging through the window of the vacuum vessel not only provides a high spatial resolution of ~5μm but, due to the low f-number of 4 allows to operate the instrument at laser powers < 1W common for usual velocimeters.

Acknowledgement

The authors would like to thank D. Rusch for the screen room work, Otto Stoltz for his technical assistance, and the KALIF operators for conducting the facility.

References

[1] L.M. Barker and R.E. Hollenbach, *J. Appl. Phys.*, **43**, 4669 (1972).
[2] D.D. Bloomquist, S.A. Sheffield, *J. Appl. Phys.*, **54**(4), 1717 (1983).
[3] W. F. Hemsing et al. : VISAR: Line-imaging interferometer, *Ultrahigh- and High-Speed Photography, Videography, Photonics, and Velocimetry,* L. L. Shaw et al. (ed.), Proc... SPIE 1346, pp. 133-140 (1990).
[4] K. Baumung, H.U. Karow, D. Rusch, G.I. Kanel, A.V. Utkin, V. Licht: High-Power Proton Beam-Matter Interaction Diagnostics by Analysis of the Hydrodynamic Response of Solid Targets, *J. Appl. Phys.*, **75**(12), 7633 (1994).
[5] M. Born and E. Wolf, Principles of Optics, 6th ed.(Pergamon Press, Oxford, 1980) p.301.
[6] K. Baumung, D. Rusch, J. Singer, S.V. Razorenov, A.V. Utkin, G.I. Kanel: Measurement of the Tensile Strength of Solids at Very High Strain Rates, this report .

Development of a K_α Temperature Diagnostic for Light Ion Beam Target Experiments

G. Meisel, A. Ljudmirsky, J. Singer, H. Bluhm, and T. Schön

The temperature of dense plasmas produced by the KALIF ion beam shall be determined from the satellite structure of fluorine K_α x-ray lines measured both by emission- and absorption- spectroscopy. The applied crystal spectrometer must be protected against the intense background light and the debris generated during a KALIF shot. A frequency doubled Nd:YAG laser/amplifier system is being set up to generate the backlighter x-rays for the absorption measurements; its design parameters are discussed.

KALIF with its self-magnetically insulated B_Θ diode enables us to produce an intense proton beam that can be focused to a power density of 0.15 TW/cm^2 with 20 nsec duration [1]. If solid matter is bombarded with this beam, power densities of 20 TW/g are obtained, resulting in a dense plasma with kT $\approx$ 10 ... 20 eV. It is the goal of the present development to determine the temperature T of this plasma experimentally by analyzing its soft x-ray emission and absorption [2]. For this purpose thin CH target foils are doped with small amounts of fluorine and sodium, the K_α satellite structure of which is to be recorded during a KALIF pulse.

In an accompanying paper by Goel et al. [3] the calculations are described that were performed to predict the fluorine K_α spectra as a function of the plasma density and its temperature. Fig. 1 shows an emission spectrum for kT = 10 eV in more detail [4], demonstrating that a spectrometer resolution of about 1000 is required.

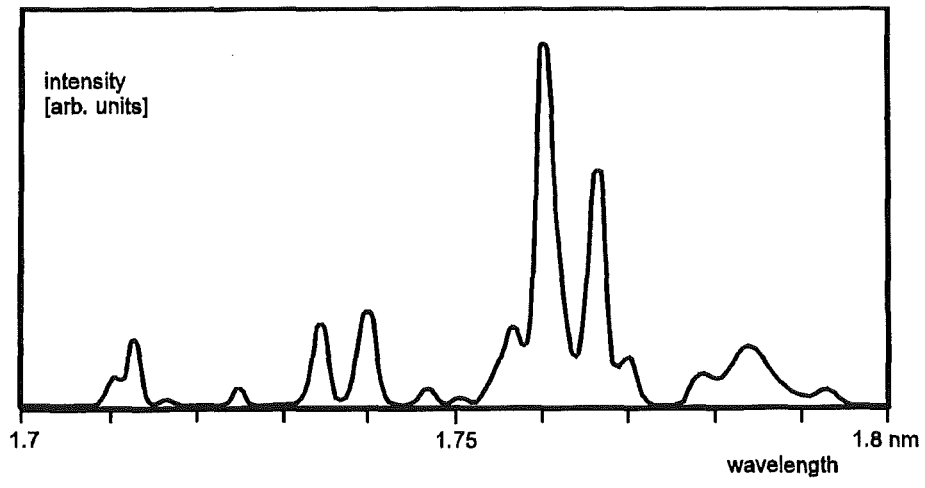

Fig.1: *Fluorine K_α emission spectrum as calculated for kT = 10 eV. A resolution of 1000 was assumed. (Taken from [4].)*

Figs. 2 and 3 are schematic diagrams of the experimental setup for emission and absorption, respectively.

Fig. 2 applies to emission of fluorine K_α radiation around $\lambda = 1.75$ nm. According to Bragg's law these soft x rays are energy selectively reflected by a RAP or KAP crystal. These crystals

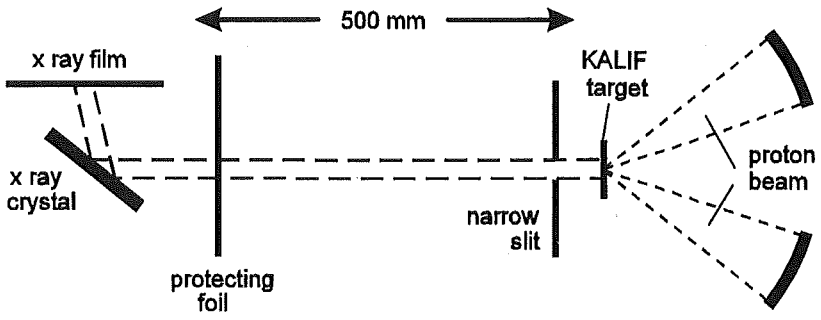

Fig.2: *Schematic diagram of the setup for K_α emission spectroscopy.*

have the required resolution of 1000 [5]. The spectra are to be recorded on x ray film [6]. The slit in front of the target defines a narrow secondary x ray source; its width sets a lower limit to the width of a spectral line as observed on the film. Thus it is one of several parameters determining the resolution of the spectrometer. A resolution of 1000 as required here calls for a slit width ≤ 0.5 mm. A thin aluminized foil is mounted in front of the crystal to make sure that the film is not exposed to visible and ultraviolet light.

Fig. 3 gives the setup to be used for absorption spectroscopy. A laser induced plasma behind the target serves as a broadband narrow source of soft x rays ("backlighter") [8]. As its emission traverses the target, its spectrum is modified by absorption. The absorption spectrum is dispersed by the crystal and recorded on film as before.

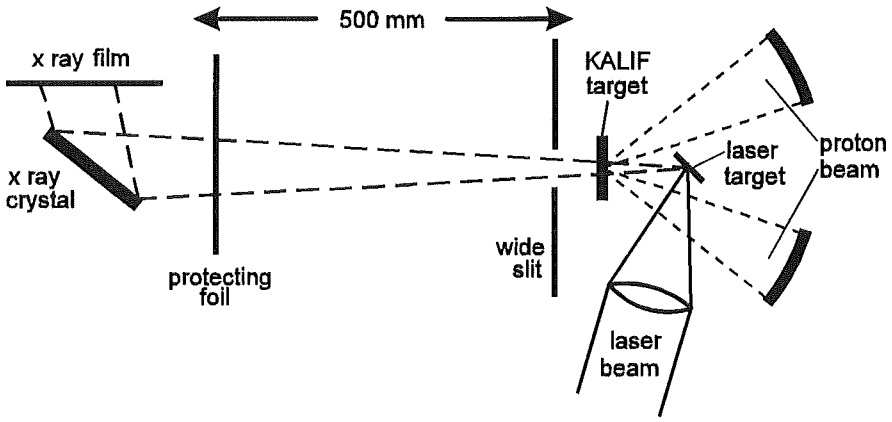

Fig. 3: *Experimental setup for "backlighter" absorption spectroscopy.*

We have studied the blow off accompanying a KALIF shot since this blast easily destroys the foil protecting the film against undesired exposure. Furthermore, this debris also would ruin the crystal if it were allowed to deposit onto it.

First, we have determined the time of flight which the debris needs to arrive at the spectrometer position in order to define the speed required for a fast shutter to block the debris. For this purpose a rotating disk was mounted behind a fixed slit at the spectrometer position to record the temporal structure of the arriving debris material. The result of this investigation showed that the debris had two well distinguished components. There was one

fast component arriving 50 μsec after the KALIF shot and lasting for about 50 to 100 μsec. It caused a dark grey deposit on the rotating disk. About 5 msec later a "slow" component arrived at the shutter, corresponding to a speed of 100 m/sec. This "late" material formed a mat black deposit. An energy dispersive analysis of x-rays (EDAX) showed that the deposit mainly consisted of various metals (Cu, Cr, Fe, Ni, Sn, Zn, Pb, Al) occuring in the diode. The "early" component most likely is carbon.

From these results it is concluded that a mechanical shutter has to travel a distance of 10 mm (which is the width of the spectrometer crystal) within about 50 μsec. If the shutter is made of a rotating disc with a 10 mm wide hole, a circumferential speed of 200 m/sec is required, which is well within reach of existing technology.

Secondly, we have investigated the paths the debris material takes on its way to the spectrometer. We found that the fast component passes through the central target area, whereas the late part almost exclusively flows radially behind the target (fig. 4). Thus the latter part was completely removed by inserting a tube blocking this path. The early direct component was reduced by mounting a slit as required for emission (see fig. 2). We found that the attenuation is sufficient for the thin foil to withstand safely the remaining blast for a slit length of 10 mm and a slit width of 0.5 mm

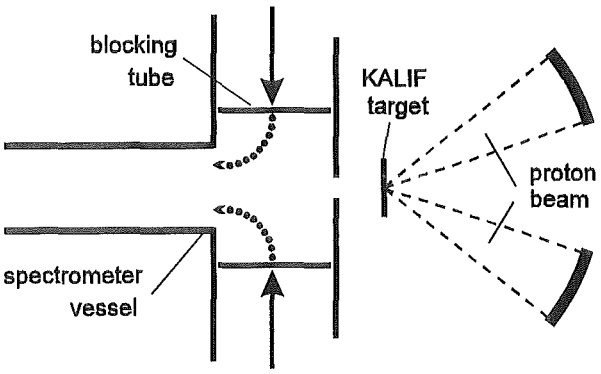

Fig. 4: The "late" debris component takes a path that can be blocked without detrimental effects to the x rays.

In backlighting measurements the resolution limiting role of the slit width is played by the size of the laser focus. No limiting apertures are allowed along the path from the backlighter to the crystal. Therefore, only an aperture at least several millimeters wide and a few millimeters long is acceptable. It is supposed (but not known for sure) that the attenuation of the blast thus obtained will be sufficient.

The laser system to be used to generate x rays for tests of spectrometer crystals and to produce the backlighter plasma has a Nd:YAG oscillator with a 3 stage Nd:Glas amplifier. Its design goals are as follows: Pulse energy 20 J for a pulse duration of 5 nsec at λ = 1064 nm. Its frequency doubled pulse energy shall be 7 J. The Nd:YAG oscillator is fed from an injection seeder for single mode operation so that the output beam has a well defined temporal structure. The output beam is expected to have 28 mm diameter with 0.3 mrad full angle divergence. This will allow us to focus the beam to a spot of 150 μm diameter by a lens of 0.5 m focal length. The approximate average power density for the frequency doubled output will be 8 TW/cm^2 as required [8]. The pointing stability of 0.025 mrad ensures that the focus does

not move by more than 10 % of its diameter. The system has been ordered and built, but does not yet meet the specifications.

Acknowledgment. The EDAX measurements were kindly performed by Dr. G. Schumacher.

References

[1] P. Hoppé et al., this report

[2] E. Nardi and Z. Zinamon: J. Appl. Phys. **53** (1981) 7075

[3] B. Goel et al., this report

[4] J.J. MacFarlane, and P. Wang: Report FPA-94-1 (January 1994)

[5] B.L. Henke, P. Lee, T.J. Tanaka, R.L. Shimabukuro, and B.K. Fujikawa: Atomic Data and Nuclear Data Tables **27** (1982) 1

[6] B.L. Henke, F.G. Fujiwara, M.A. Tester, C.H. Dittmore, and M.A. Palmer: J. Opt. Soc. Am. B **1** (1984) 828

[7] P.D. Rockett, C.R. Bird, C.J. Hailey, D. Sullivan, D.B. Brown, and P.G. Burkhalter: Applied Optics **24** (1985) 2536

[8] K. Eidmann and W. Schwanda: Laser and Particle Beams **9** (1991) 551

K_α -SPECTRA FROM HOT DENSE PLASMAS PRODUCED BY LIGHT ION BEAMS

B. Goel,W. Höbel, A. Ludmirsky [1], J.J. Mac Farlane [2], P. Wang [2],

[1] Permanent address: Plasma Physics Dpt., SOREQ NRC, Israel

[2] Permanent address: Fusion Technology Institute, University of Wisconsin, Madison, USA

Abstract

The K_α-spectrum is a sensitive indicator of the state of a plasma created by the interaction of an ion beam with matter. K_α satellite lines are generated due to the change in charge screening when electrons are removed from the L-shell. Fluorine having electrons only in K and L shells is an obvious choice to produce K_α-satellite lines even at moderate temperatures. However, Fluorine K_α-radiation has large attenuation coefficients in the detector windows. An alternative substance for the temperatures expected in the plasma produced by the KALIF beam is Sodium. In this paper we present calculations for K_α-spectroscopy on Fluorine and Sodium samples and show that at temperatures expected in the plasma produced by the KALIF beam these elements can successfully be used as temperature diagnostic materials. To qualify our method we present a comparison of our calculations with a recently measured X-ray transmission through an Aluminum sample.

I. Introduction

The KALIF (**K**arlsruhe **L**ight **I**on **F**acility) proton beam has been focussed to 0.15 TW/cm^2 with the selfmagnetically insulated B_θ-diode and more recently to about 1 TW/cm^2 with the applied B diode [1]. The interaction of the above beams with matter produces a hot dense plasma at temperatures of a few tens of eV. To experimentally characterize the state of matter produced by such beams parameters like temperature and density have to be measured. In the KALIF experiments K_α-satellite spectroscopy will be used to determine the temperature in the plasma created by the interaction with the proton beam. K_α satellite lines are generated due to the change in the screening of the nuclear charge when electrons are removed from the L-shell through thermal electron collisions. Holes in the K-shell are produced by direct interaction will the beam protons. The satellites are blue shifted with respect to the K_α-lines originating from the fully occupied L-shell. Thus K_α-spectroscopy is a readily available tool to determine the degree of ionisation in the plasma. This can then be used to determine temperature and density of the plasma. To use this method effectively for temperature measurements the diagnostic-ions present in the plasma should have holes in the L-shell created by electron collisions. Depending on the expected beam parameters, this determines the choice of materials that can be used for K_α-satellite spectroscopy.

For the KALIF beam the obvious choice is fluorine. Fluorine having electrons only in the K and L shell would show a blue shift of K_α-lines for any degree of ionisation. The wavelength of the Fluorine K_α-line is 18.3 Å and shifted satellites lie between 17 and 18 Å. In this region the transparency of windows is low and the reflectivity of the analyzing crystals is low too. Moreover, at higher beam powers all L-shell electrons may be removed and F can no longer serve as the diagnostic element. The next suitable substance for our conditions is Sodium. The L-shell in Sodium is filled and it requires at least 2 electrons to be removed to obtain a K_α-satellite. Therefore, in our experiments on KALIF we will use both F and Na in the form of NaF as a diagnostic material. The purpose of this paper is to show that K_α-satellite spectroscopy on F and Na can be used to diagnose conditions in plasmas at low to moderate temperatures ($2\text{eV} \leq T \leq 30$ eV). Both emission and absorption spectroscopy will be carried out. Emission spectroscopy requires sufficiently intense lines. The intensity of emitted lines depending on the particle beam power. In most cases this intensity does not allow a time and space-resolved measurement due to the limited detector efficiency. Absorption spectroscopy has the advantage that with a short pulse back lighter source time resolved measurements can be performed. The procedure for the calculation of K_α-line spectra is as

follows. First a multigroup radiation hydrodynamic calculation is carried out to obtain the temperature and density profiles of the tracer layer as a function of time. In a second step the K_α-spectra are determined using a collissional radiative equilibrium model.

II. Theoretical Models

The temperature and density evolution of the target plasma created by the interaction with the KALIF beam is calculated with the Karlsruhe Target Code (KATACO). It is a 2 temperature single fluid 1 D radiation hydrodynamic code (Fig.1) and includes among other processes realistic ion beam energy deposition, multigroup radiative energy transport. In addition it has provisions to include any set of equation of state and opacity data.

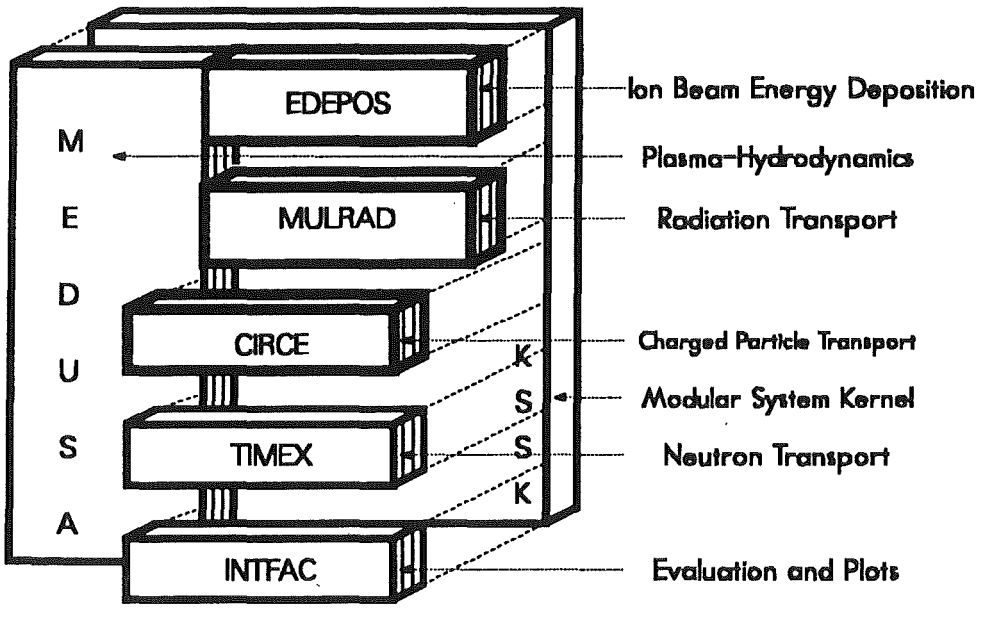

Figure 1. KATACO Program Structure: The Karlsruhe Target Code KATACO is a multilevel modular program system.

The K_α-spectrum is calculated using the non-LTE radiative transfer code NLTERT. Atomic level populations are computed by solving multilevel statistical equations self-consistently with the radiation field and the ion beam properties. Radiation transfer effects are calculated using an escape probability model. Proton impact ionization cross sections were computed using a CPSSR model [2-5]. In our calculations we consider atomic energy levels distributed over all 10 ionization stages of Fluorine and all 12 ionization stages for Sodium.

III. Results

Calculations have been performed for a bare diagnostic layer equivalent to 1 μm of solid thickness. The beam parameters used are those for the KALIF beam from a B_θ-diode with a peak power density of 0.2 TW/cm^2 and from an applied B-diode with a of peak power density of 1 TW/cm^2. The tracer thickness has been optimized for emission spectroscopy. It is sufficiently thin to mitigate any opacity effects yet sufficiently thick to produce an adequate photon flux at the detector. For thin tracers the emitted flux is nearly proportional to the tracer thickness because the plasma is optically thin. For $L_0 > 0.1$ μm the K_α lines become optically thick and the flux increases slower than linearly. When the tracer thickness is > 10 μm the flux becomes constant. This occurs because the plasma becomes optically thick for all wavelength in this spectral region. Therefore, increasing the tracer thickness beyond 10 μm will not significantly increase the number of K_α photons reaching the detector. Instead the effect is to skew the satellite spectrum toward an apparently higher ionization stage, making it more difficult to determine plasma conditions from emission spectra. Thus the optimum tracer thickness for experiments utilizing emission spectroscopy is ~ 0.1 - 1 μm. If absorption spectra are to be measured the tracer thickness should be at the lower end of this range. In Fig. 2 we show the temperature and density evolution of a 1 μm thick bare NaF target irradiated by a proton beam of 0.2 TW/cm^2 from the B_θ-diode. It is seen that both the temperature and density profiles are generally flat. Only at the outer edge the gradient is large. This gradient can be drastically reduced by tamping the target.

The Fluorine K_α-spectra from these simulations are shown in Fig. 3. Early in time (10 ns) a temperature of ~ 2 eV is achieved and only O and N-like lines are visible in the emission and absorption spectra. As the temperature rises with time higher ionization stages appear. The absorption spectra also contain some K_β lines. In case of a time integrated emission spectrum measurement all these K_α-lines occur

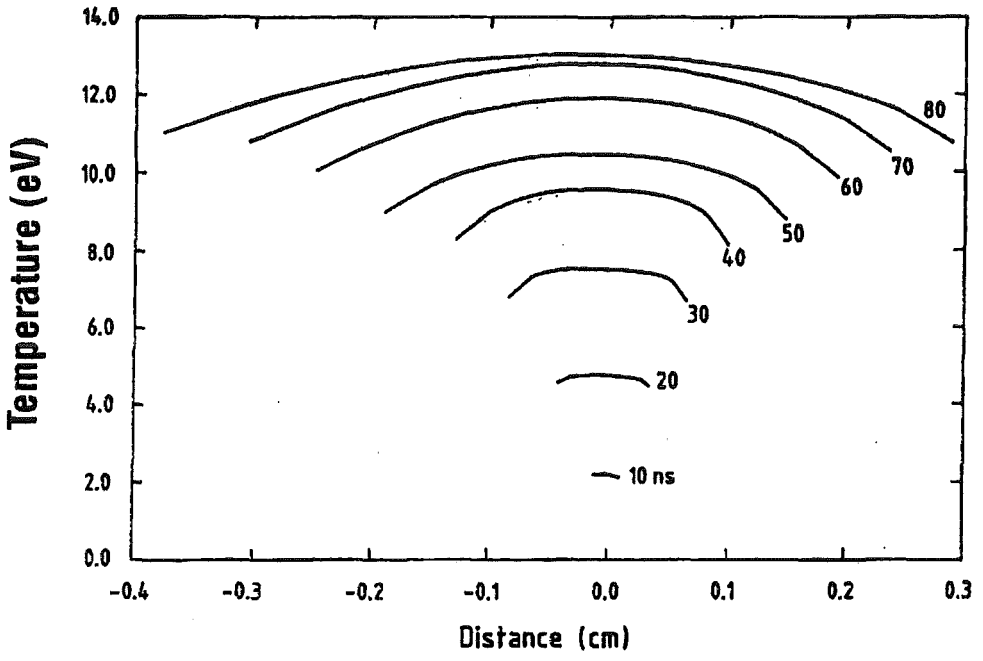

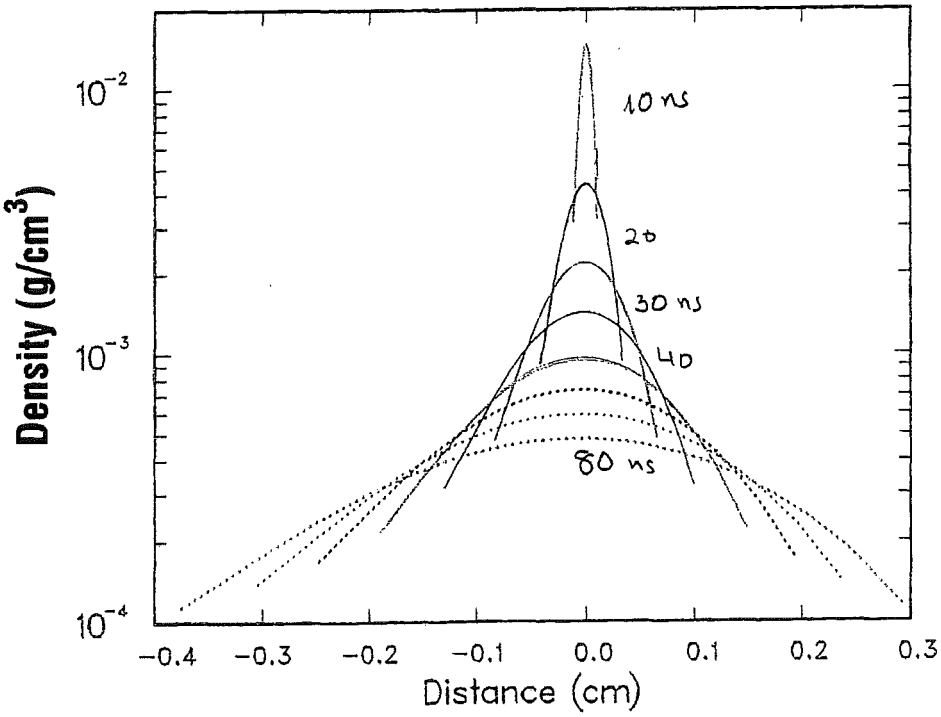

Fig.2 The evolution of the temperature and density profiles in a 1 μm thick F-target irradiated with the 0.2 TW/cm2 proton beam from a B_θ-diode.

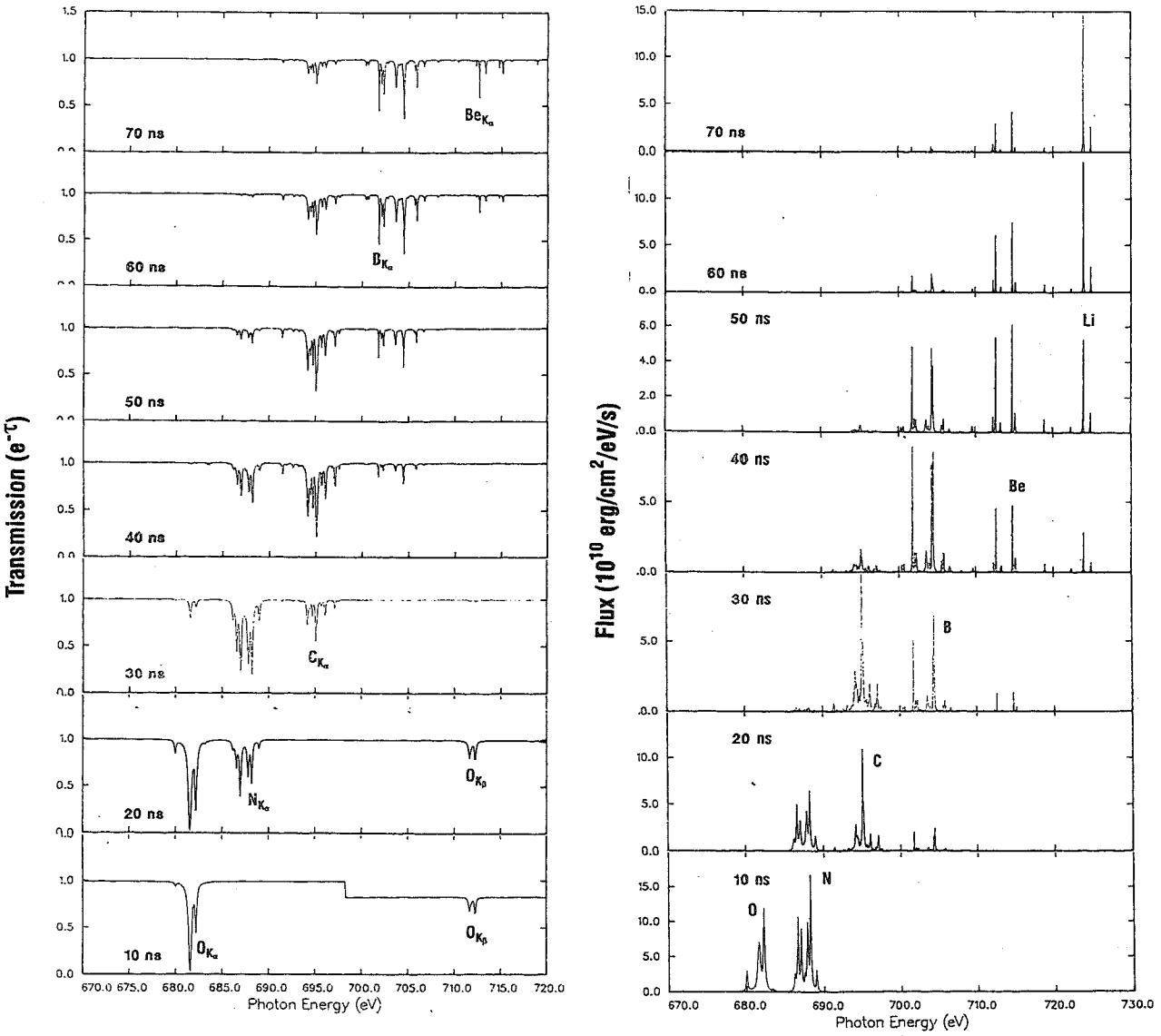

Fig.3 Evolution of absorption and emission spectra from a 1 μm thick F-target during irradiation with the 0.2 TW/cm^2 proton beam from a Bθ-diode.

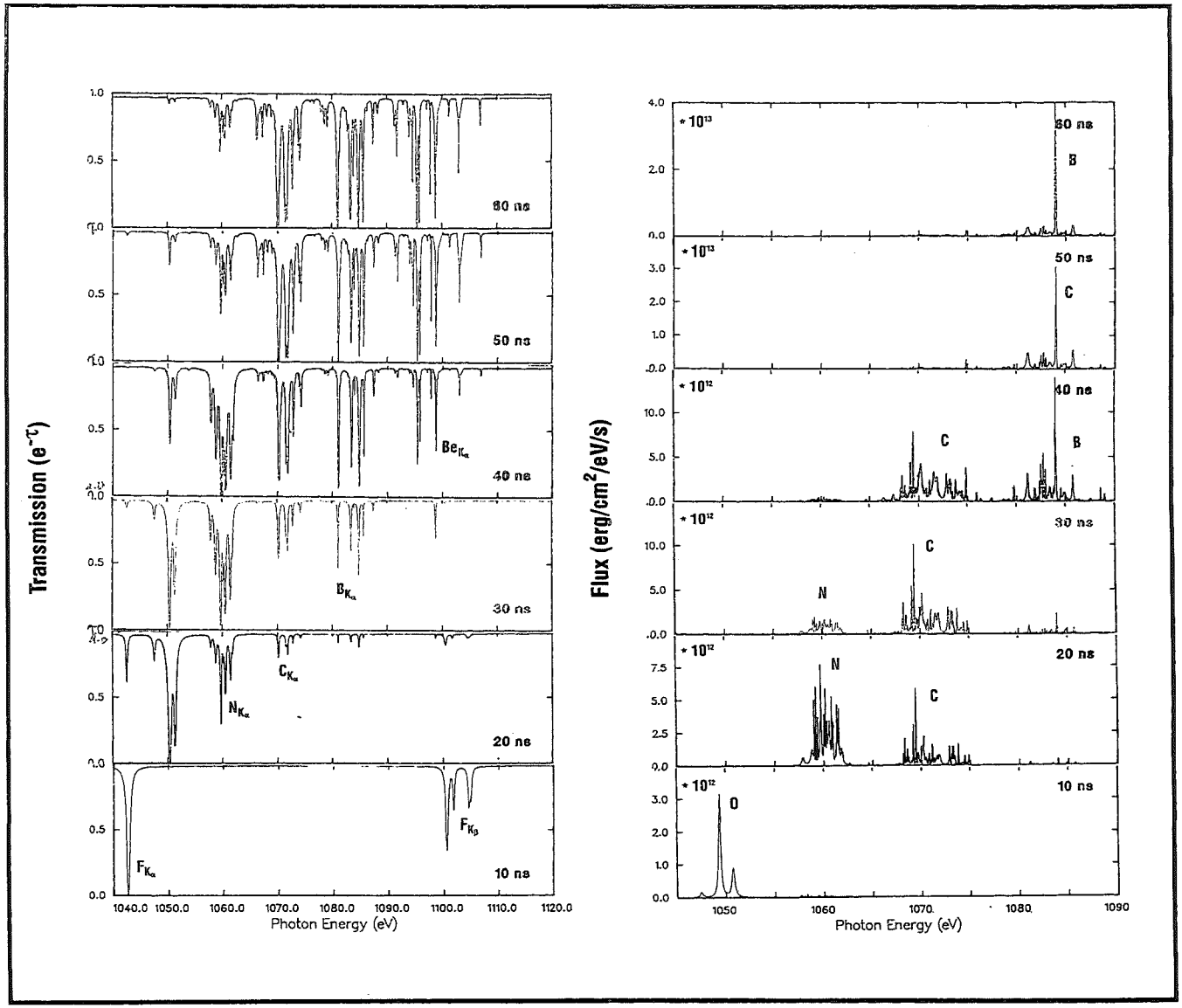

Fig.4 Evolution of absorption and emission spectra from a 0.1 μm Na target irradiated with a ~1 TW/cm^2 proton beam from an applied B diode.

on the record. However, at higher beam power only He an Li like lines will be observed.

Fig. 4 shows the K_α-spectra from a 0.1 µm Na-layer irradiated with a 1 TW/cm^2 beam. The overall behaviour of the spectrum is similar to that from the F target at 0.2 TW/cm^2. Of course, the temperatures become higher due to the higher beam power density. The line groups do not purely originate from a single ionization state as indicated in the plot. Sometimes the next lower ionization state has a spectator electron in the M-shell and does not contribute effectively to the shift in energy. E.g. at 20 ns the lines emitted from N-like ions are in the energy range of 1057 eV to 1061 eV, while lines from O like ions with 1 electron in the 3d shell correspond to energies of about 1060 eV. As the temperature rises further to about 20 eV (50 ns), the emission spectrum becomes dominated by the 2S-2P transition (1084 eV) from B-like ions. Contributions from other ionisation states become very small after this time.

Finally we check our model by comparing with results from the transmission experiment performed recently [6] at MPQ, Garching. In this experiment the iodine laser ASTRIX IV (200 J /0.4 ns at 440 nm) has been focussed into a spherical hohlraum of 3 mm diameter. The absorber foil was glued to one of the two diagnostic holes with 1 mm diameter. To reduce the axial density gradient due to expansion of the heated Al-absorber sample 560 Å thick carbon layers on either side of the sample were used to tamp the expansion. The thickness of the Aluminum foil was 1075 Å (30 µg/cm^2). In Fig. 5 we compare our calculated result with the experiment. The agreement with the experimental data is satisfactory for an assumed plasma temperature of 20 eV and a density of 0.02 g/cm^2. The calculated spectrum is sensitive to both temperature and density and thus plasma temperature and density can be determined from such a comparison.

IV. Summary and Conclusions

We have curried out spectral line calculations for the development of the K_α-diagnostic as a suitable tool for temperature measurements in ion beam experiments on KALIF. It has been shown that it is possible to extract temperature information from a spectroscopy of K_α-lines emitted from the tracer elements F and Na. For a beam power density of the order of 0.2 TW/cm^2 the plasma temperature in Fluorine rises up to 15 eV. As the plasma temperature increases the K_α-lines are shifted to shorter wavelength. In the time integrated Fluorine K_α-spectrum

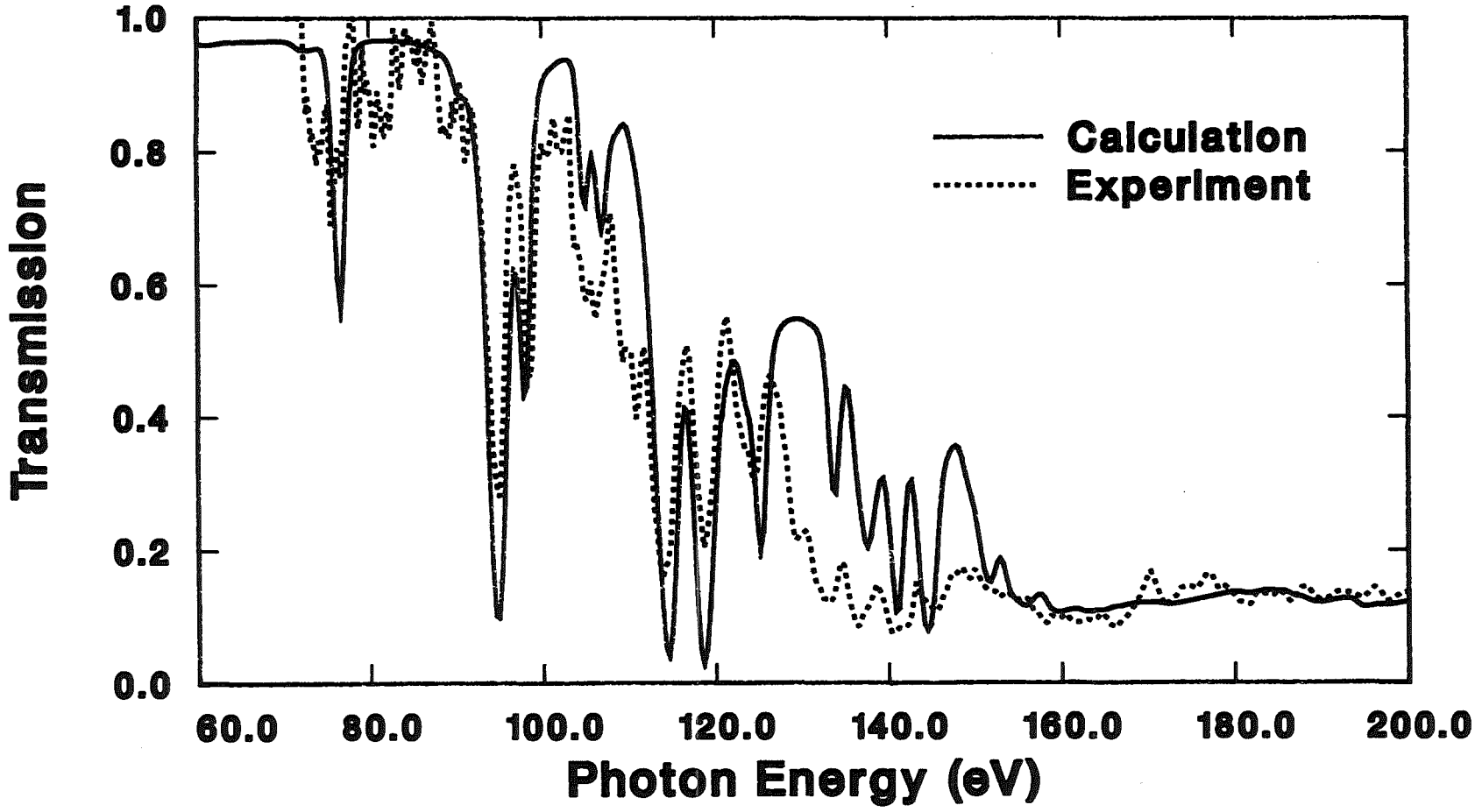

Fig.5 Comparison of the measured X-ray spectrum transmitted through an Al plasma heated by an intense laser beam with a computer simulation. The areal density of the Al layer was 30 μg/cm^2. The numerical results are in best agreement with the experiment for a target temperature of 20 eV and a density of 0.02 g/cm^3.

lines from all ionization states ranging from O-to Li-like ions are observed. With an experimental resolution of 1000 some lines of the same ionization state may even be resolved. However, at higher plasma temperatures the time integrated spectrum from Fluorine ions becomes dominated by lines from Li and He like ions. Therefore, at higher power densities another element like Na has to be used. Using a composition like NaF as the tracer material and applying emission and absorption spectroscopy simultaneously a very good temperature sensitivity can be obtained.

In this paper we have presented calculations for emission and absorption spectroscopy on bare tracer layers only. In a real experiment, however, the diagnostic layer will be sandwiched or embedded in the target. Depending on the optical properties of the material the temperature and density profiles will be different from those reported here. While calculating the spectrum we have also to account for the attenuation of the radiation in the ambient materials. Further detailed calculations are required for actual experimental conditions.

V. References

[1] H. Bluhm et al., Proc. of the IEEE '80 (1992) 995

[2] J. J. MacFarlane and Ping Wang et al., Phys Rev. E47 (1993) 2748

[3] Ping Wang, J. J. MacFarlane, G.A. Moses, Phys. Rev. E48 (1993) 3934

[4] J. J. MacFarlane and Ping Wang et al., Laser & Particle Beams (1995) in press

[5] Ping Wang, J. J. MacFarlane, G.A. Moses, Laser & Particle Beams (1995) in press

[6] G. Winhart, K. Eidmann, et al., XUV opacity measurements and comparison with models, presented at "Radiative Properties of Hot Dense Matter", Sarasota, Oct. 1994

Reinvestigation of Foil Acceleration Experiments

B. Goel and O. Yu Vorobjev[1]

Forschungszentrum Karlsruhe
Institut für Neutronenphysik und Reaktortechnik
Postfach 3640
D-76021 Karlsruhe, Fed. Rep. Germany

1) Permanent address: Institute of Chemical Physics, Chernogolovka, Russia

Abstract

The dynamics of foil acceleration experiments performed on KALIF has been reexamined. New numerical simulations have been carried out using the recently determined beam parameters. These calculations include realistic physical parameters, e.g. realistic equations of state, the effects of range shortening in the hot plasma, electron and radiative heat conduction, etc. Calculated values are compared with experimental values of the free surface velocity. The newly determined beam profile leads to reasonable agreement. We have used in our calculations a simple analytic equation of state and studied the effect of parameter variations. The results of this work can be used to check equation of state data in the region of strongly coupled plasmas.

1. Introduction

Intense ion beams can be used to generate ultrahigh pressures in condensed matter [1], [2]. Light-ion beams generated at the Karlsruhe Light Ion Facilitiy (KALIF) typically have a focus of less than 1 cm diameter. The maximum power density at KALIF achieved to date is of the order of 1 TW/cm^2 [3]. The 1.5 MeV protons of the KALIF beam from a B_θ-diode can deposit up to 50 TW/g or (2.5 MJ/g) in the ablation zone of the target. A strongly coupled, hot and dense plasma is thus created. The states of matter produced by the KALIF beam are depicted in Fig. 1. Experimental regimes accessible in traditional explosion experiments are shown along the Hugoniot curve. Release isentrops for shock

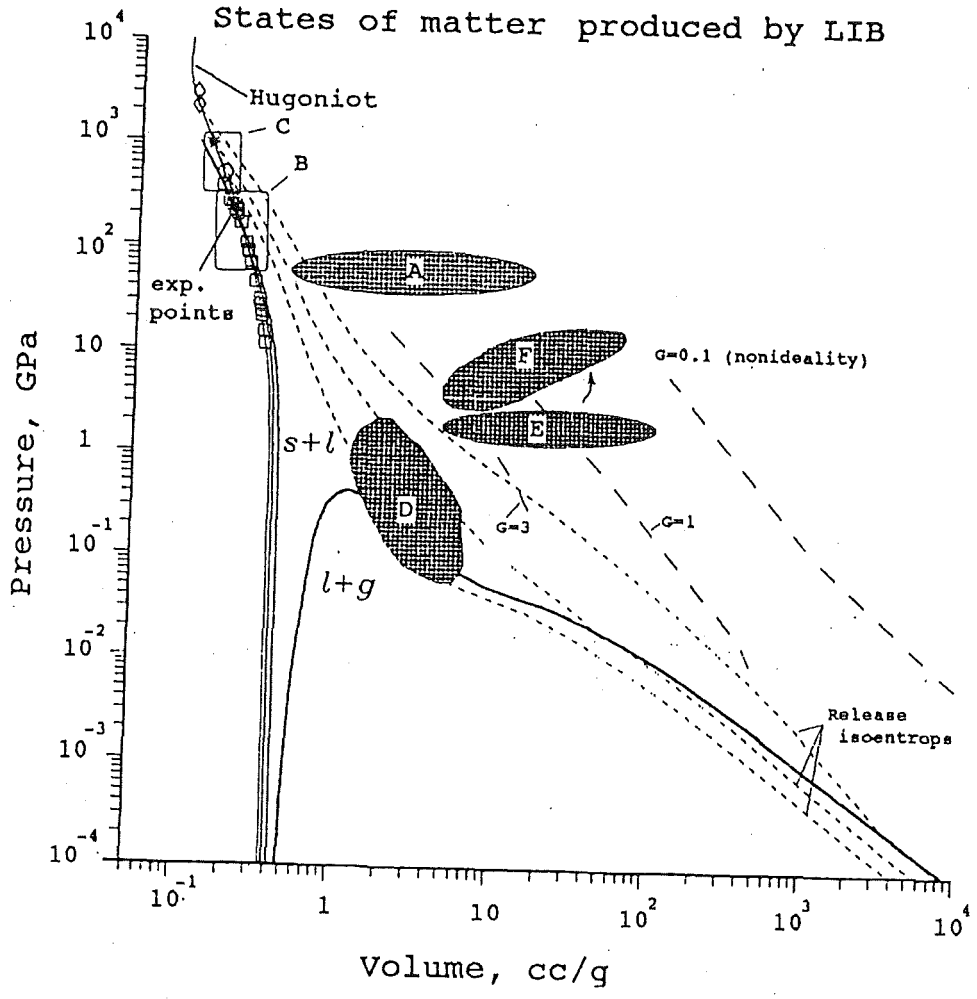

Fig.1 **States of matter produced by the interaction of a light ion beam with solid Al. For details see text**

pressures of 6, 10 and 20 Mbar are shown by dotted lines. Dashed curves represent plasma states with different degrees of nonideality. Region **A** corresponds to the states of matter produced in the energy deposition zone of a super-range Al foil. Pressures generated in condensed targets with light ion beams can be increased by using flyer plate impact technique (region **C**). A plasma near the critical point (**D**) is produced during the unloading of these highly compressed states. Region **E** corresponds to the plasma states of a subrange foil

heated by a beam with 0.1 TW/cm^2 power density. The collision of such a plasma with a hard wall will produce a hotter plasma (region F). To describe the plasma state obtained in experiments on KALIF sophisticated theoretical tools are required. Experimental information is scarce in this region of strongly coupled plasmas. A successful interpretation of beam-target interaction experiments, in the long run, can serve as a check of theoretical models and of the equation of state data base. Due to the large focus size shocks generated in the light-ion beam experiments are basically planar, and also the classical mechanism of ion energy deposition makes the analysis of these experiments less ambiguous.

Intense ion beams generated with pulsed power machines, such as KALIF, show a change in the beam particle energy and in the focussed power density on the target as a function of time. For the theoretical analysis of these experiments it is vital to know the exact shape, magnitude and time dependence of the particle beam. Intensive work has been done during the last year to redetermine the parameters of the proton beam from the B_θ-diode [4]. Those parts of the target which receive energy from the beam change with the energy of the impinging ions. These changes are amplified by the evolution of the target properties (i.e. temperature and density).

In this paper we present an investigation of the dynamics of thin-foil acceleration by light-ion beams and an analysis of various experiments performed at KALIF [5]. The peak beam power is estimated to be 0.15 $\pm$0.05TW/cm^2. The results of simulations depend mainly on two factors: the power density profile and the equation of state in the region of strongly coupled dense and hot plasma. In our calculations a simple analytical form has been used for the equation of state. The parameters of the equation of state have been adjusted to fit the available experimental data adequately. An analytical equation of state has been chosen to facilitate numerical stability of the code and to provide handy parameters for variations.

The experiments analyzed in this paper have been extensively described elsewhere [5]. In our analysis we assume that the beam characteristics do not change appreciably from shot to shot. The electrical signals on the diodes were measured regularly and showed no major differences for successful shots. The total beam intensity was measured by nuclear diagnostics in separate shots. Because of experimental constraints these beam diagnostics cannot be performed together with foil acceleartion experiments.

In the following sections we briefly present our numerical method, the equation of state model, the analysis of experiments, and some conclusions.

2. Mathematical Model

The Euler equations of motion are used to describe the dynamics of matter under the impact of a beam. They express conservation laws for mass, momentum, and energy

$$\frac{\partial \rho}{\partial t} + \frac{\partial \rho u}{\partial x} = 0 \qquad (1)$$

$$\frac{\partial \rho u}{\partial t} + \frac{\partial (\rho u^2 + p)}{\partial x} = 0 \qquad (2)$$

$$\frac{\partial}{\partial t}\left[\rho \left(e + \frac{u^2}{2}\right)\right] + \frac{\partial}{\partial x}\left[\rho u \left(e + \frac{u^2}{2}\right) + pu - \lambda_e \frac{\partial T}{\partial x} + S_r\right] = Q(x,t) \qquad (3)$$

where ρ is the density; p is the pressure; T is the temperature; u is the mass velocity; e is the specific internal energy; and Q(x,t) is the power density deposited in the target by the beam. The following caloric equation of state is used to close the set equations of the system (1-3):

$$p = p(e, \rho^x), \quad \rho^x = \frac{\rho}{1 - \rho V_p} \qquad (4)$$

The radiative energy transfer is treated in the radiation heat conduction approximation. In this case, the energy flow is proportional to the temperature gradient, the proportionality coefficient being expressed by the Rosseland mean free path, ℓ

$$S_r = - \frac{16\sigma T^3}{3} \ell \frac{\partial T}{\partial x} \qquad (5)$$

where σ is the Stefan-Boltzmann constant. Thus the conductive energy flow consists of two terms: electron and radiative conductivity. The electron conductivity coefficient, λe, and the Rosseland mean free path, ℓ , are functions of density and temperature [7]. The maximum target temperature reached in KALIF experiments with the B_θ-diode does not exceed a few 10's of eV. Therefore, the energy of the radiation field is not very important in our calculations and the simple approximation of radiation heat conduction is deemed adequate to calculate the radiative heat transfer. The absorption of the beam energy in the target is calculated in a single-particle approximation. The stopping power is calculated by semi-empirical formulas developed in [8]. The hydrodynamical calculations are performed using the Godunov method on the moving grid [9]. The nodes of the grid move with contact velocities calculated by solving the Riemann problems between neighbouring cells [10].

3. Wide-Range Semiempirical Equation of State

For our numerical simulations we require an equation of state (EOS) that adequately describes the shock compression of cold matter as well as the plasma thermodynamics in the energy deposition region. In the following a semi-empirical equation of state is developed which adequately describes the experimental data of shock wave compression in solid samples in the pressure range of up to several Mbar. Following the usual procedure, the internal energy is divided into two parts: The cold energy, E_c, is only a function of both the temperature and the density. As our simple equation of state model does not contain the temperature we shall use (p,ρ) as variables.

$$E(p,\rho) = E_c(\rho) + E_t(p,\rho) \qquad (6)$$

For the calculations we need the functions $P(\rho,E)$ and $C_s(\rho,E)$. To describe Hugoniot data for solid matter we choose the cold pressure in the traditional form

$$P_c\ (\rho) = \sum_{i=1}^{5} a_i \delta^{(i/3+1)},\ \delta > 1 \qquad (7)$$

$$P_c\ (\rho) = \frac{\rho_0 C_{s0}^2}{(N\text{-}M)} (\delta^N - \delta^M),\ \delta < 1 \qquad (8)$$

where $\delta = \rho/\rho_0$ and ρ_0 and C_{s0} are normal density and sound velocity respectively. The coefficients a_i are found by solving the system of linear equations which results from matching the properties of matter at normal conditions (normal sound velocity, Grüneisen coefficient, zero pressure) and at high compressions where the Thomas-Fermi-Dirac model is applicable. The cold pressure term dominates strongly over the thermal term in shocked states of solid matter at pressures up to several Mbars. The thermal pressure is related to the thermal energy through the Grüneisen parameter γ, which is represented as a function of energy and density

$$P_t = \gamma\,(E, \rho) E_t \rho \qquad (9)$$

We use the following dependence of the Grüneisen parameter on the internal energy

$$\gamma = \gamma\,(\rho)_\infty + \frac{\gamma\,(\rho)_0 - \gamma\,(\rho)_\infty}{1 + \left(\frac{E}{E_0}\right)^{\alpha}}, \qquad (10)$$

where E_0 and α are fitting parameters. According to eq. (10) $\gamma\,(\rho)$ tends to $\gamma\,(\rho)_\infty$ for hot matter.

To describe the asymptotic behaviour of γ in the limits of high compression (Fermi gas) and expansion (ideal gas) we give both functions γ_0 and γ_∞ the asymptotic vlaue 2/3 for $\rho \to \infty$ and $\rho \to 0$ respectively.

$$\gamma\,(\rho)_0 = \frac{2}{3} + \left(\gamma_s - \frac{2}{3}\right) \frac{2}{\frac{\rho_0}{\rho} + \frac{\rho}{\rho_0}}, \qquad (11)$$

$$\gamma(\rho)_\infty = \frac{2}{3} + (\gamma_{min} - \frac{2}{3}) \frac{2}{(x+1/x)^\beta}, x = \frac{\rho_0}{\rho} \xi, \qquad (12)$$

where γ_s is the Grüneisen coefficient at normal conditions, ρ_0 is the normal density, γ_{min} is some minimum value of γ in dense plasmas and ß and ξ are fitting parameter. The parameter ξ is the plasma density where γ_∞ reaches its minimum value. This density approximately corresponds to the critical point and is about an order of magnitude smaller than the normal density. The parameter ß determines the rate of increase of γ from its plasma value to the asymptotic value of 2/3 for an ideal gas. These parameters together with α are the most important parameters. As to the parameter E_0, it can be matched by fitting data from shock-wave experiments with porous samples. To describe the compression of porous samples the thermal component of the pressure in the EOS must be corrected for densities close to normal density. The results from Hugoniot adiabate calculations for solid and porous samples (E_0=30 kJ/g) show good agreement with the experimental data. We also find that our simple analytical EOS describes available experiments on isentropic expansion of shocked material. The analytical form of the equation of state is convenient for numerical calculations. It saves simulation time and assures the continuity of pressure and sound velocity over the entire range of the simulation. The temperature is calculated by using the tabulated SESAME equation of state.

4. Qualitative Analysis

To develop an understanding of the importance of various phenomena we start with a qualitative analysis of the pressure generated in the target by an ion beam in the simple situation of constant proton energy and a constant rise in beam power. Let us consider a power density growth rate of 0.005 TW/ns/cm^2 typical for KALIF. If the ion range is equal to 20 µm a specific energy of about 50 kJ/g is deposited in the first 10 ns. If the material heated by the beam remained at normal density the pressure would rise to about 3 Mbar in the energy deposition zone. Actually, the pressure level stays one or two orders of magnitude below. This is due to two reasons. The first reason is the expansion of matter and as a consequence, a density drop. The second one is the decrease of the pressure generating parameter γ (=P/(ρE)) from its initial value of about 2 (solid state) to 0.3 (plasma). If at the beginning of energy deposition all energy is transformed into kinetic energy we have an expansion velocity of about 7 km/s for a deposited energy of 50 kJ/g. This means that after 10 ns the size of the energy deposition zone will be 10 times larger (and correspondingly the density 10 times smaller)

than its original value. For such an expanded material the parameter γ reaches the minimum value for a strongly coupled plasma namely 0.3 ± 0.05 [11].

If we assume a constant Grüneisen parameter and uniform density in the energy deposition zone the pressure will remain constant as long as the power growth is linear, since both the specific volume and the specific energy of heated matter grow approximately quadratic with time [10].

When the energy deposition zone becomes so large that the wave transit time is much larger than the characteristic time of pressure growth due to energy deposition, the assumption of uniform distribution of parameters throughout the plasma zone is no longer valid. For our considerations the first 10-20 ns is the most interesting and also most difficult stage for the theoretical analysis is of the beam-target-interaction.

5. Numerical Simulations

In contrast to what has been assumed in the previous section the beam power profiles and the particle energy evolve in a complicated and, often, non-monotonic way. To take these changes of the beam parameters into account detailed numerical simulations have been made using the formalism described in sections 2 and 3. The real experimentally determined time evolution of the power density [4] was used in our numerical simulations. This profile has the temporal behaviour given in Fig. 2a with a maximum around 30 ns. The corresponding proton energy evolution is presented in Fig. 2b. Both of these profiles have been corrected for the transit time from the diode to the target. To begin with our analysis SESAME [12] and Bushman [6] tables for the equation of state were used to do calculations with the experimentally observed time evolution of KALIF beam (Fig.2) assuming a peak power density of 0.15 TW/cm^2. Results of these calculations (Fig.3) show that both of these EOS lead to inadequate results in the time interval between 10 and 20 ns. At this stage the density of the ablation zone is an order of magnitude less than the initial density and the temperature has risen to about 10 eV. These states of matter correspond to the region of strongly coupled plasmas. Note that in this region the uncertainty in the equation of state models is large and experimental information is lacking. To improve this situation we used our semiempirical EOS mode. After adjusting some parameters in that EOS model we could describe the foil acceleration experiments reasonably well.

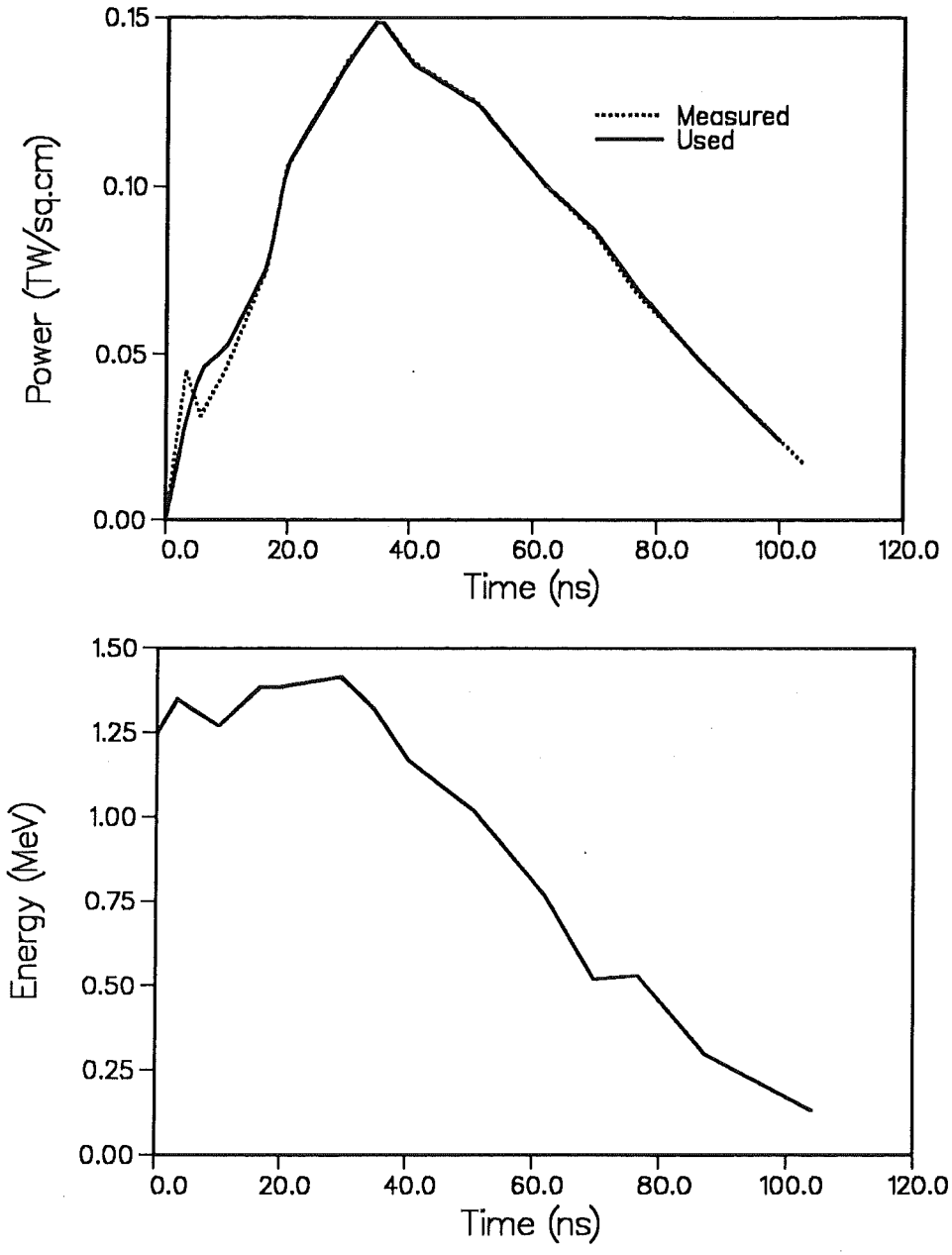

Fig. 2 **Measured and applied time evolution of the power density and the proton energy in the beam focus.**

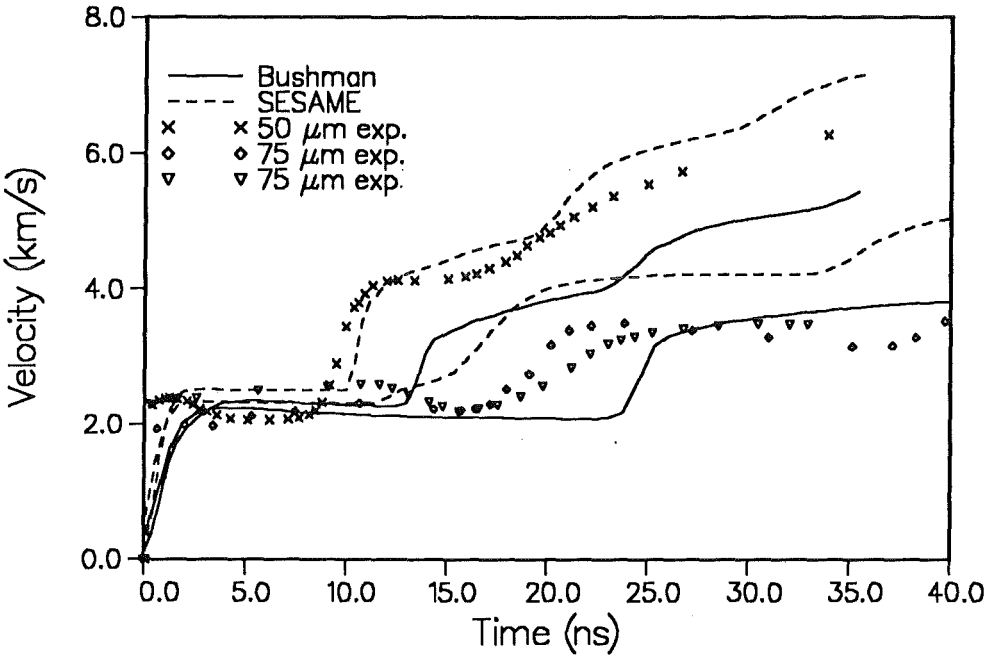

Fig. 3 **Comparison of experimental and calculated velocities of 50 and 75 μm thick Al-foils ablatively accelerated by the proton beam with the beam characteristics of Fig.2. The simulations have been carried out using tabulated SESAME and Bushman eos data.**

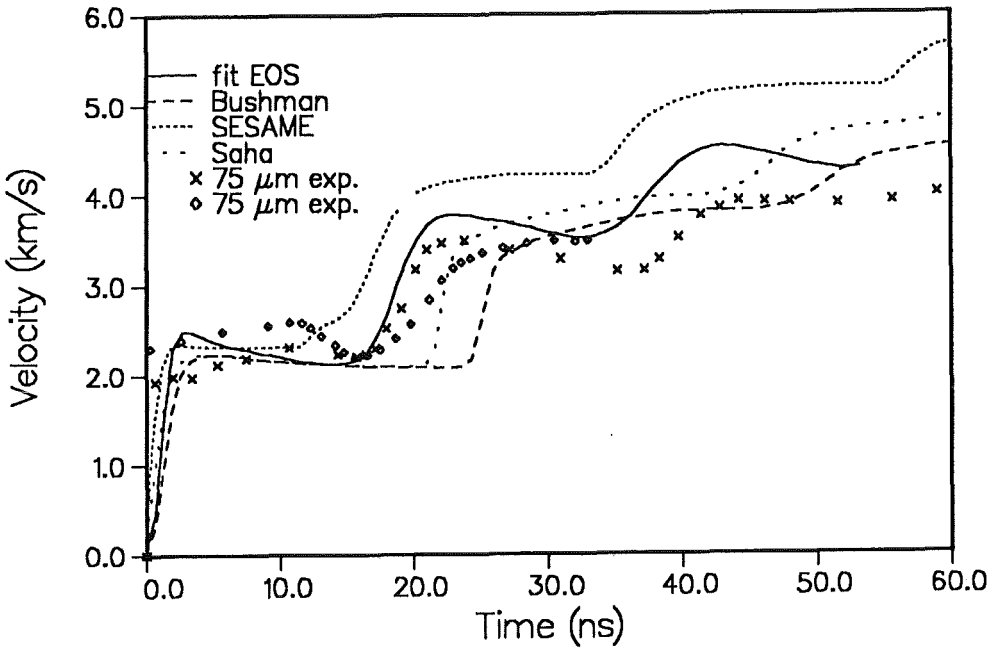

Fig. 4 Comparison of experimental and calculated velocities for a 75 μm thick Al-foil. Here, in addition to the numerical results presented in Fig. 3, the improvement achieved by the fitted analytical form of the eos is shown.

The results of the numerical simulations for a 75 μm Al foil performed with different equation of states are shown in Fig.4. It is evident that our EOS considerably improves the agreement with the experimental data. In Fig. 5 the simulation results with our equation of state have been plotted for all analyzed experiments together with the original experimental data. Considering the fact that we are using the same beam parameters for different experiments the agreement is rather good. As seen from Fig. 2b the proton beam energy starts

dropping after about 30 ns. The energy deposition zone then moves away from the solid part which is accelerated. The detachment of the energy deposition zone is further enhanced by the range shortening effect in the heated medium. For KALIF conditions a range shortening by a factor of 2 has been observed [14]. Finally, after about 60 ns the pressure waves from the deposition zone can no longer reach the accelerated foil, because its velocity becomes larger than the characteristic velocity of the ablation zone boundary. From this time on the energy deposition does no longer influence the acceleration of the foil. Thus after this time the power does no longer effect the analysis. In fact the decoupling of the energy deposition zone occurs much earlier. We may conclude that after about 45-50 ns the temporal evolution of the beam profile is no longer important for the foil acceleration.

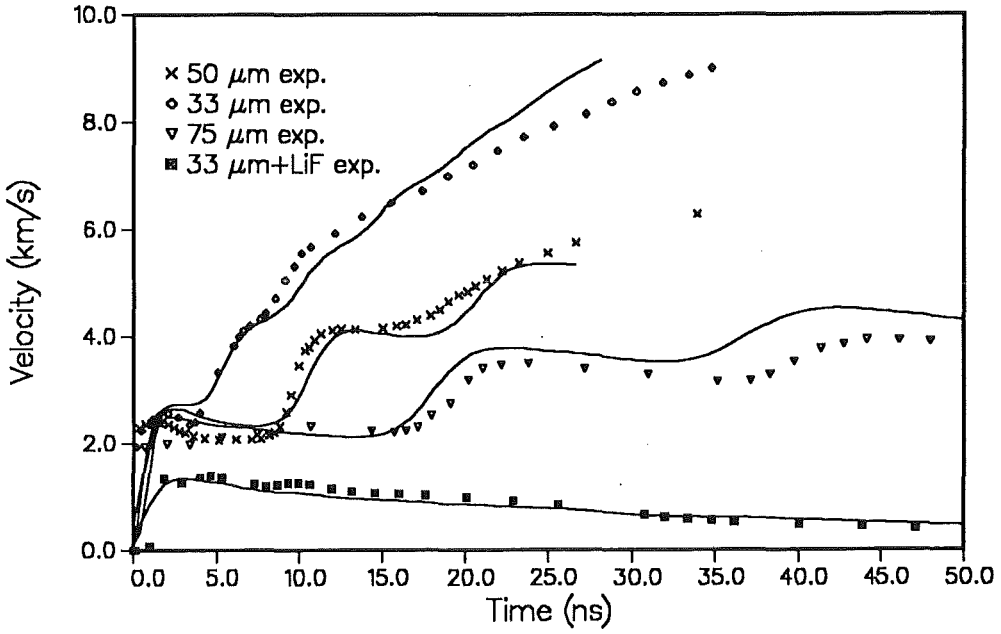

Fig. 5 Simulation results for a large variety of different foil thicknesses using the adjusted analytical form for the eos. Satisfactory agreement is demonstrated with all experimental data.

All considerations mentioned above are valid only if the calculated energy deposition is correct. To check this we have compared in Fig.6 the proton range calculated during the present computations with that in cold and hot matter obtained with the stopping power model described in [14]. Assuming that the temporal profile of the beam evolution is that shown in Fig.2, we can, within certain limits determine the equation of state parameters. Presently the accuracy of this procedure is limited by the reproducibility of the beam parameters.

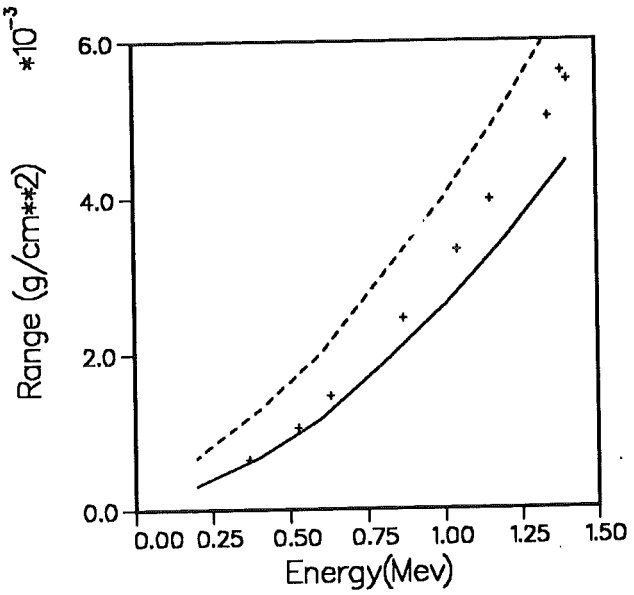

Fig. 6 **Evolution of the proton range (crosses) versus particle energy together with the range in cold (dashed line) and hot (solid line) (T=25 eV, ρ=0.1 g/cm³) aluminum targets. Since the ion energy is falling over most of the beam pulse the plot also demonstrates the increasing range shortening with time.**

6. Conclusions

We have recalculated the foil acceleration experiments using the recently determined temporal evolution of power and particle energy for the B_θ-diode of KALIF. After removing the peak in the beam power at 5 ns into the pulse the beam characteristics can be used to reproduce the experimental data of the foil acceleration experiments. This analysis provides information on the equation of state in the region of strongly coupled non ideal plasmas. In this region experimental informations are scarce. Thus the present data can aid theoreticans to check EOS models. In a subsequent paper we shall discuss the implications of differences in EOS data.

7. References

[1] K. Baumung et al., Hydrodynamic Target Experiments with Proton Beams at KALIF, Proc. Ninth International Conference on High-Power Particle Beams, (ed. D.Mosher, G. Cooperstein), May 25-30, 1992, Washington DC, USA, Vol. I. p.68.

[2] B. Goel, O. Yu. Vorobjev, A.L. Ni, Generation of Ultra High Pressure with Light Ion Beams, Proc. Ninth International conference on High-Power Particle Beams, (ed. D.Mosher, G.Cooperstein), May 25-30, 1992, Washington DC, USA, Vol.II, p.957.

[3] H. Bluhm et al., Focussing Properties of a Strongly Insulated of a Applied B Proton Diode with a Preformed Anode Plasma, Proc. Ninth International Conference on High-Power Particle Beams, (ed. D.Mosher, G.Cooperstein), May 25-30, 1992, Washington DC, USA, Vol.I. p.51.

[4] P. Hoppé et al. , this report

[5] K. Baumung et al., Light-ion Beam-Target Interaction Experiments on KALIF, Nuovo Cimento 106 A (1993) 1771 and this reportt

[6] A.V. Bushman, G.I. Kanel, A.L. Ni, V.E. Fortov, Thermal Physics and dynamics of Intense Pulse Action, Inst. of Chemical Physics, Chernogolovca (1988).

[7] G.D. Tsakiris, E. Eidman, JQSRT 38 (1987) 353.

[8] A.Ya. Polyshchuk, V.E. Fortov, V.S. Khloponin, Sov. J. Plasma Phys. 17 (1991) 523.

[9] S.K. Godunov, Finite Difference Method for Numerical Computation of Discontinuous Solution of Equations of Fluid Dynamics, Mat. Sbornik 47 (1959) 271.

[10] O.Yu. Vorobjev, A.L. Ni, B. Goel, Numerical Simulation of Foil Acceleration Experiments with Light Ion Beams, Report KfK 5299, April (1994).

[11] W. Ebeling, A. Föster, V.E. Fortov, V.K. Gryaznov, A.Ya. Polishchuk, Thermophysical Properties of Hot Dense Plasmas, Teubner-Texte zur Physik, Bd. 25, Teubner Verlag, Stuttgart-Leipzig 1991

[12] Lawrence Livermore National Laboratory, Report UCID-118574-82-2 (1982).

[13] A.V. Bushman,, V.E. Fortov, I.A. Lomonosov, Proc. Enrico Fermi School 1989, Elsevier Publ. 1989, p.249.

[14] B. Goel, H. Bluhm, Determination of Proton Stopping Power in Hot Plasma at KALIF, J. de Physique, C7-49 (1988)C7-169.

Numerical modeling of plasma shield formation and divertor plate erosion during ITER tokamak plasma disruptions

F. Kappler, I. Landman*, G. Piazza , H. Würz

* permanent address: Troitsk Institute for Innovation and Fusion Research, 142092 Troitsk Russia

The high divertor heat load during ITER tokamak plasma disruptions and ELMs results in sudden evaporation of a thin layer of divertor plate material, which acts as plasma shield and protects the divertor from further excessive evaporation. Formation and effectiveness of the plasma shield and material erosion are calculated in one-dimensional planar geometry with the radiation magnetohydrodynamics code FOREV-1. The FOREV-1 results are coming in satisfactory agreement with results from simulation experiments, thus demonstrating that theoretical tools are becoming available which allow to tackle the problem of material erosion under tokamak disruption conditions. For modeling the real and rather complicated tokamak situation with inclined magnetic field lines, with tilted target, finite width of the scrape off layer (SOL) and inhomogeneous power density across the SOL, the 2D radiation magnetohydrodynamics (MHD) code FOREV-2 is under development. Finally, for solving the radiative energy transfer problem in a nonhomogeneous plasma shield (with temperature and density gradients) a self consistent approach is developed and is going to be implemented into FOREV-1.

1. Introduction

During the thermal quench phase of a tokamak plasma disruption and during ELMs the divertor plates are hit by an intense plasma flow consisting of electrons and ions. In ITER this flow is estimated to have the following parameters: particle energy around 10 keV, pulse duration larger than 100 μs, energy density up to 150 MJ/m^2 for disruptions and up to 10 MJ/m^2 for ELMs [1]. This high divertor heat load causes sudden evaporation of a thin layer of divertor plate material which acts as plasma shield and protects the divertor from further excessive evaporation [2]. Once a protective target plasma layer is formed radiative energy transport becomes the most important energy transfer path from the impinging plasma flow to the target [3]. It is of vital interest to know the behavior of the divertor under such high pulsed heat loads and to estimate its lifetime against

During the thermal quench phase of a tokamak plasma disruption a rapid loss of most part of the thermal energy content of the plasma is occurring. Recently it was observed that this loss is accompanied by a very intense soft x-ray (SXR) flash and by a density wave caused by target material evaporation coming in from the plasma edge [4]. Recently obtained results from disruption simulation experiments with carbon targets at the two plasma gun facility 2 MK-200 [5] have shown that in less than 2 μs due to local heating of the vapor cloud by the intense plasma flow a hot plasma layer with temperatures up to 80 eV is formed [6]. In this non-LTE plasma corona the plasma flow energy efficiently is converted into SXR line and continuum radiation [7]. Thus the results from these simulation experiments support the observations made during tokamak plasma disruptions. Recently it was shown theoretically that also in front of a beryllium target hit by an intense plasma flow there is produced a plasma corona in which the plasma flow energy is converted into SXR radiation with an efficiency of more than 30 % [8]. For low Z materials it is of importance how effectively the intense flash of SXR radiation produced in the low dense plasma corona is transferred through rather dense cold plasma layers to the target [9]. In order to solve this radiative energy transfer problem adequately a self consistent approach is necessary.

In 1993 the numerical modeling work to be reported here was performed in the frame of the European Fusion Technology Program under subtask PPM3-2. In 1994 it became part of the ITER task T60 on plasma disruption simulation and in 1995 it is part of the ITER task T226b. In the frame of this ITER task modeling activities are also underway at IPP Garching [10], at ANL Argonne [11] and in Russia at Kurchatov Fusion Center together with Cheljabinsk [12].

2. Modeling of plasma flow target interaction

The 1D radiation magnetohydrodynamics code FOREV-1 [13] is used for modeling of the plasma flow target interaction. The modeling is based on the three classical conservation equations for mass, momentum and energy. The energy balance equation is coupled with the equation for the radiation transport and the momentum equation with the magnetic field diffusion equation. Heat conduction into the bulk target, erosion and melt front propagation into the target and beam energy deposition by ions and Maxwellian distributed electrons are modeled. Momentum deposition of the ion component of the incident plasma flow is taken into account. Spatial mesh and frequency group optimization are important features which result in improved accuracy of the modeling results.

In the case of 1D MHD it is assumed that the magnetic field lines are parallel to the target surface. The target plasma expands perpendicular to them. In this case the time and space dependent magnetic pressure $p_m = B_z^2(x,t)/2\,\mu_o$ enters as additional pressure term into the momentum equation with x perpendicular to the target and z the toroidal direction. Via $B_z(x,t)$ the momentum equation is coupled with the time and space dependent magnetic field diffusion equation for $B_z(x,t)$.

In reality the magnetic field lines are inclined as is schematically indicated in Fig. 1. This is described by a 1½ D MHD model. In this case there are two velocity components u_x and u_z and two components of the magnetic field, with $B_x = B_o \sin\alpha$ = const and B_o the unperturbed magnetic field [14].

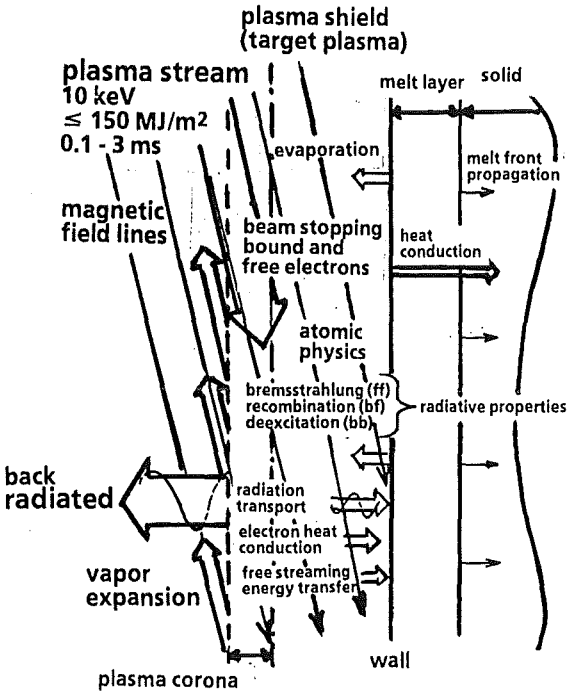

Fig. 1: Plasma stream target interaction schematically.

The radiative energy transfer is the most important source of heat load at the target [3]. Radiation transport therefore is the most sensitive part of the numerical modeling. In FOREV-1 radiation transport is treated in the forward reverse transport approximation [15]. The space dependent spectral radiation fluxes $E_i(\nu)$ with ν the frequency are calculated for the two directions forward (i = 1) and reverse (i = 2). For the stationary case the two equations for E_1 and E_2 are given in the multigroup description as

$$\frac{1}{2}\frac{dE_1^g}{dx} = \eta^g - \kappa_P^g E_1^g$$

$$-\frac{1}{2}\frac{dE_2^g}{dx} = \eta^g - \kappa_P^g E_2^g \qquad (1)$$

with g frequency group, $E_i^g = \int_{\Delta\nu} I_i(\nu)d\nu$,

$$\kappa_P^g \text{ Planck opacity for absorption } = \frac{\int_{\Delta V} \kappa_V E_P^V dv}{\int_{\Delta V} E_P^V dv} \quad (2)$$

E_P^V the Planckian spectral radiation

energy density and η^g the plasma emissivity.

η^g is obtained from the Planck opacity for emission $\beta^g{}_P$ (emission coefficient) according to

$$\eta^g = \beta_P^g E_P^g \quad \text{with} \quad \beta_P^g = \frac{\int \beta^V E_P^V dv}{\int E_P^V dv}$$

The coupling of the spectral radiation fluxes with the energy balance equation is via the photon energy exchange term E_r. E_r is given according to:

$$E_r = \sum_g \left(4\pi \eta^g - c \kappa_P^g E^g\right) = \pi \frac{d}{dx} \sum_g \left(E_1^g - E_2^g\right) \quad (3)$$

3. Calculation of plasma radiative properties

The radiative properties of a plasma are described by the frequency, temperature and density dependent absorption and emission coefficients $\kappa = \kappa$ (v,T,n) and $\beta = \beta$ (v,T,n). κ and β describe the probability of a photon of frequency v to be absorbed or emitted in a plasma of temperature T and density n. In the absorption process the photon energy hv is transferred to the interaction partner, either a bound or a free electron.

3.1 Optical properties of multicharge plasmas

The code TOPATOM (thermodynamic and optical properties of atoms and ions) from Lykov Institute of Heat and Mass Transfer, Minsk [16] and the code CRE from University of Wisconsin (UWM) [17] are used for calculating the optical properties

of multicharge plasmas. A recently performed comparison of absorption and emission coefficients for low Z materials calculated by TOPATOM and CRE has shown rather good agreement between both codes for optically thin plasma.

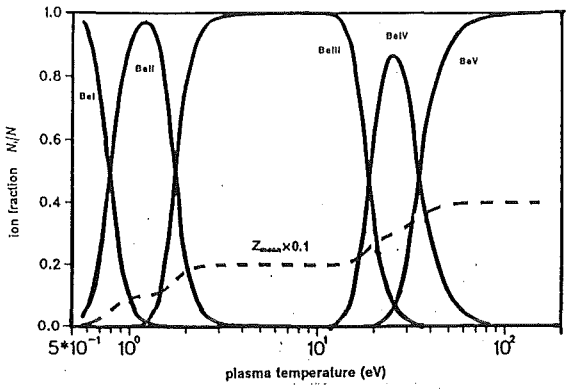

Fig. 2a: Ion concentrations and mean charge for beryllium plasma. Plasma density 10^{17} cm^{-3}.

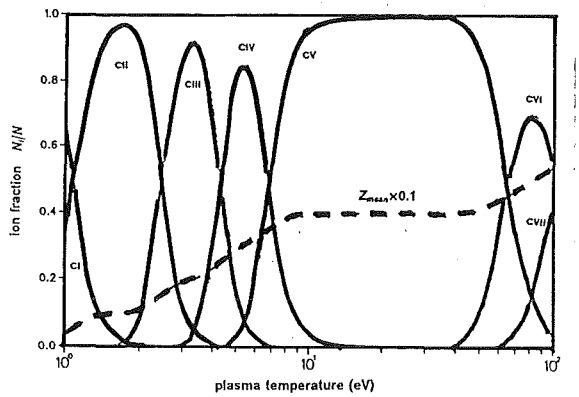

Fig. 2b: Ion concentrations and mean charge for carbon plasma. Plasma density 10^{17} cm^{-3}.

Ion concentrations are shown in Fig. 2a and b for a beryllium and a carbon plasma of density of 10^{17} cm^{-3}. In the plasma temperature range from 2.5 to 15 eV BeIII ions (He like ions) are the only species. Therefore the radiation properties of a Be plasma in this temperature range are rather poor. Fig. 3 shows absorption coefficients for beryllium for a plasma density of 10^{17} cm^{-3} for the two plasma temperatures 2.5 eV and 20 eV. For 2.5 eV there are many lines from Li like ions and lines from He like ions near the H like ion ionization edge.

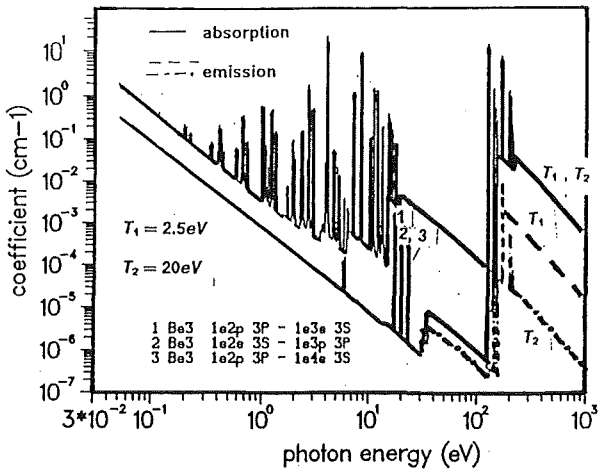

Fig. 3: Absorption and emission coefficient for Be for two plasma temperatures. Plasma density 10^{17} cm^{-3}.

The transitions for He like and H like ions $1\ s^2$ - 1snp and 1s-np are calculated up to $n = 7$. Due to the transition from Li like to He like ions the absorption coefficient in the photon energy region between 20 and 120 eV is considerably larger than for a plasma temperature of 20 eV. But in both cases the plasma is optically thin for the continuum radiation and for most lines except for the lines from He like ions near the H like ionization edge. At plasma temperatures above 10 eV the optical properties are determined by absorption and emission of He and H like ions and by recombination

radiation of H like ions. Most radiation is emitted as SXR radiation in the photon energy region from 120 eV up to 220 eV.

Fig. 4 shows absorption coefficients for carbon for a plasma density of 10^{17} cm^{-3} for the plasma temperatures 2.5 eV and 25 eV. For 2.5 eV the lines are from CII, CIII and CIV ions. Most lines and a part of the continuum recombination radiation is optically thick for plasma densities above 10^{17} cm^{-3}. For plasma temperatures above 10 eV the plasma of density of 10^{17} cm^{-3} is optically thick only for a few lines close to the H like ionization edge. Most radiation is emitted as SXR radiation in the photon energy region from 308 eV up to 400 eV.

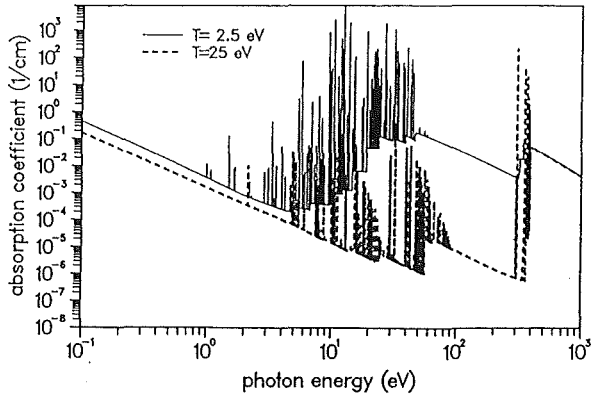

Fig. 4: Absorption coefficient for carbon plasma for two plasma temperatures. Plasma density 10^{17} cm^{-3}.

For high Z materials the assumption is made that the plasma is in local thermodynamic equilibrium (LTE). The concentrations of ion species are calculated using the Saha equations. Emission and absorption coefficients are identical (Kirchhoff law). For calculation of κ_ν it is assumed that for S and P electrons level splitting is small and thus negligible. For vacant D shells and especially if this shell is an inner one this condition is not fulfilled. For the configuration $5d^4\ 6s^2$ the electrostatic splitting is rather large. Transitions like $5d^4\ 6s^2$ - $5d^3\ 6s^2\ 6p$ can split up into 10^3 lines. As a result numerous lines with strong intersecting profiles are obtained instead of one line. Thus a quasicontinuum is established with a complicate frequency dependence of the absorption coefficient. A solution of the radiation transport problem by taking into account all separate lines is practically impossible. An averaging of the absorption coefficients has to be done.

3.2 Emission coefficients for low Z plasmas

Emission coefficients are calculated with the collisional radiative equilibrium model (CRE) for optically thin plasma [16]. Reabsorption of radiation in optically thick plasma is taken into account by escaping factors. In comparison with the CRE results for optically thin plasma escaping factor corrected emission coefficients of lines are larger as is shown in Fig. 5. Due to radiative ionization in non-

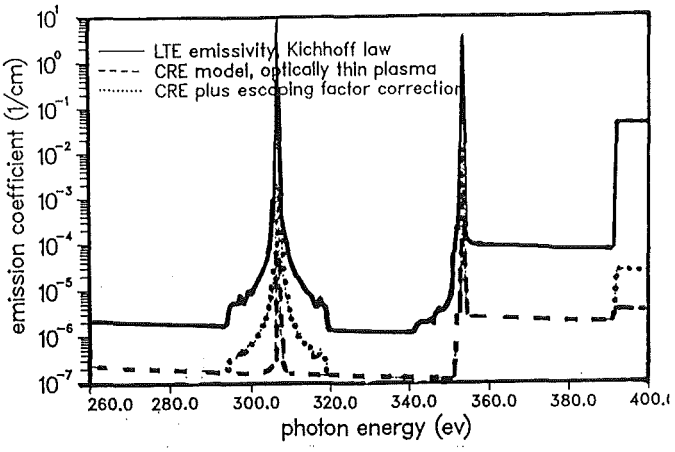

Fig. 5: Comparison of emission coefficients for carbon plasma. Plasma temperature 20 eV, plasma density 10^{17} cm^{-3}.

LTE plasma reabsorption can also result in changes of the ion population. In the example shown, H like ions are produced by reabsorption, resulting in increased emissivities for H like to He like ion recombination radiation (edge at hv = 394 eV).

3.3 Optical properties of molecules

The optical properties of a plasma at temperatures below 1 eV are determined to a large extend by molecular absorption. For carbon and carbon-hydrogen plasma the molecules H_2, CH, C_2 and C_3 contribute to the optical properties. The molecular spectra differ strongly from atom/ion spectra. Electronic vibrational and rotational transitions in the visible, nearest infrared and ultraviolett frequency range are important. In the plasma flow target interaction the plasma density near the target exceeds values of 5×10^{18} cm^{-3} at temperatures below 3 eV. Thus the plasma is in LTE and molecules have to be taken into account. The concentration of the molecular species was calculated using the law of mass action according to

$$\frac{p_A^X \, p_B^Y \, p_C^Z}{p_M} = K_p(T) \tag{4}$$

with M molecule in the form of $A_X B_Y C_Z$ consisting of atoms A, B, C, with X, Y, Z atom numbers. p_A, p_B, p_C partial pressure of the atoms A, B, C, $K_p(T)$ the equilibrium constant.

In the temperature range below 1.2 eV C atoms are the dominating species. For temperatures above 1.2 eV C^+ ions are dominating. The concentrations of the C_2 and C_3 molecules decrease sharply with increasing plasma temperature and become negligible for temperatures above 0.5 eV.

Photoabsorption from ground state and from inner shells essentially starts at photon energies above 10 eV. Below 10 eV the absorption is determined by photo processes from excited levels and by bremsstrahlung. At plasma temperatures below 1 eV the population of excited levels is small and bremsstrahlung is negligible because of small concentration of free electrons. Therefore the absorption coeffi-

cient for plasma temperatures below 1 eV is rather small (see Fig. 6). The presence of molecules with concentrations in the range of 1 - 10 % leads to a significant increase of the absorption coefficient (as is seen from Fig. 6).

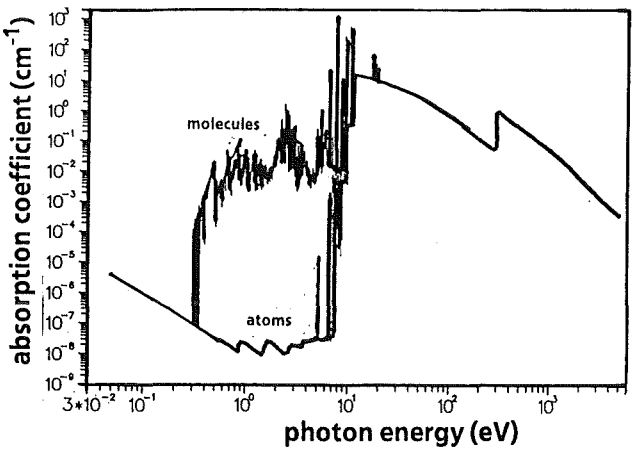

Fig. 6: Comparison of absorption coefficients for carbon plasma with and without C_2 molecules. Plasma temperature 0.5 eV, plasma density 10^{18} cm^{-3}.

With increasing plasma temperature the contribution of the photoabsorption from excited states increases simultaneously with a decrease of the number of molecules. Thus at temperatures above 1 eV the contribution of molecules to the absorption coefficient becomes negligible.

4. Code validation

Disruption simulation experiments are aimed to quantify the divertor damage under tokamak typical disruption conditions [18, 19]. However simulation experiments with lasers and high energetic electron beams are not tokamak typical and yield too high erosion because of absence of vapor shielding. Results from erosion experiments with monoenergetic electron beams at the SOM facility have been used for validation of the stopping power models used in FOREV-1 and of the program part dealing with heat conduction into the bulk target [20]. Experimentally it was found that for carbon erosion starts after reaching a threshold energy density value of 1 MJ/m^2. Onset of target plasma formation strongly depends on beam power density and for 2 MW/cm^2 starts only after 70 µs. Temperature and density of the target plasma remain low and the fraction of neutrals is high.The modeling results in terms of delay in target plasma formation, of target plasma temperature and erosion are in good agreement with the experimental results as is seen from Fig. 7. Vapor shield formation is negligible. The erosion is mainly determined by the power density of the unattenuated beam.

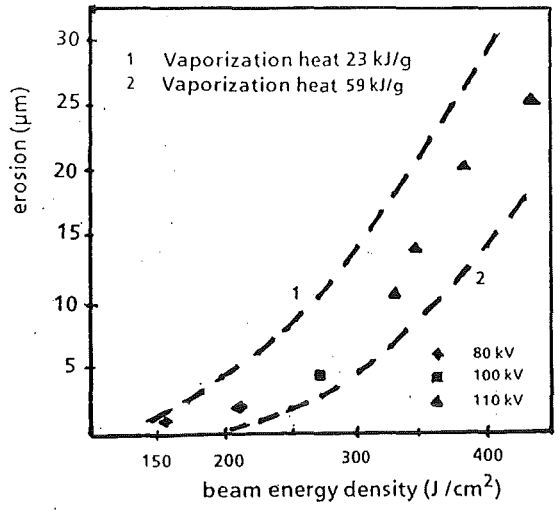

Fig. 7: Measured and calculated erosion for carbon. The average diode voltage is indicated.

The results from simulation experiments at the two plasma gun facility 2MK-200 [5] have been modeled with FOREV-1 too. For tungsten there was obtained good agreement [7]. For carbon the calculated plasma temperatures close to the target are still lower than the measured values. However the experimental situation is nonstationary. The heated plasma corona is continuously lost because of diverging magnetic field lines. As a consequence the impinging plasma stream penetrates closer to the target. The calculated and measured erosion is in agreement.

5. Vapor shield formation and erosion for ITER tokamak plasma disruptions

The disruptive plasma stream of ITER hits the divertor plates under an impact angle of 5°. It is assumed that the impact energy of the deuterium ions and the temperature of the Maxwellian electrons is 10 keV. Ions and electrons contribute equally to the energy deposition. As the stopping power of 10 keV deuterium ions in solids is rather large the energy deposition is treated as surface heat load. Electrons due to their larger range act as volumetric heat source. In solid targets stopping power and range are only weakly dependent on the impact angle α.

In a plasma the range $R(\alpha)$ and the stopping power $dE(\alpha)/dx$ of magnetized electrons and ions for impact angles $\alpha \ll 90°$ are obtained from the values for $\alpha = 90°$ by applying a $\sin\alpha$ correction according to $dE(\alpha)/dx = 1/\sin\alpha\, dE(90°)/dx$ and $R(\alpha) = R(90°)\sin\alpha$.

To check whether there are differences in vapor shield formation and erosion for electrons and ions calculations at first were performed for both species separately. Afterwards the impact of a plasma stream with equal contributions of electrons and ions was modeled.

5.1 High Z materials

Typical FOREV-1 results from 1D radiation MHD calculations with 512 group Planck opacities are shown in Fig. 8 for tungsten for a 10 keV Maxwellian electron beam of beam power density of 10 MW/cm^2.The target heat load due to the external beam dominates during the first 4 µs. Due to the volumetric heating and the heat sink of the bulk target this high heat load results in rather small erosion. However the erosion rate is sufficient to form a vapor layer which after 4 µs effectively shields the target and which after 40 µs stops completely the external beam and thus terminates direct heating of the target. Then radiative energy transfer becomes the dominating heat source. The spectral boundary radiation fluxes to the wall and backradiated essentially are Planckian. The temperature in the plasma corona remains below 3.5 eV. After an initial but rather short free expansion phase the plasma motion across the 5 T magnetic field lines becomes diffusive. After 100 µs the diffusive velocity is 2 x 10^4 cm/s. The plasma layer thickness after 1 ms is about 14 cm. The magnetic field penetrates the target plasma and produces a low β situation.

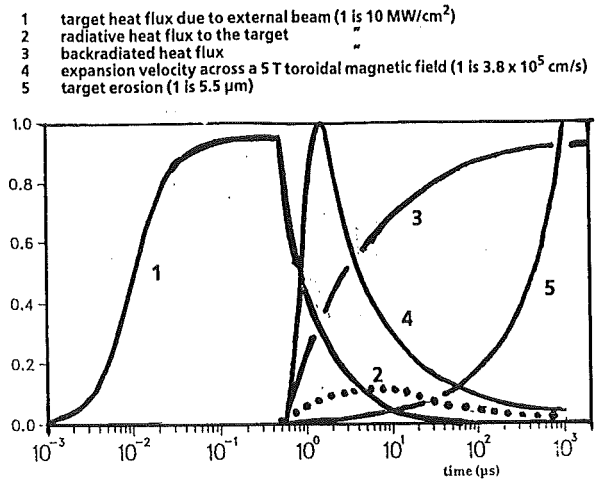

Fig. 8: Typical FOREV-1 modeling results for tungsten for 10 keV Maxwellian electron beam of power density of 10 MW/cm^2. Beam impact angle 5°, toroidal magnetic field 5 T.

The two quantities radiative heat load and heat load handled by the bulk target due to heat conduction are comparable in size. Erosion as determined by the difference remains rather small and heat conduction into the bulk target is important. Its neglection would result in an overestimation of erosion. After the target plasma is formed and upheated at least 85 % of the incoming beam energy is converted into radiation in the plasma corona and at least 90 % of this radiation is backradiated.

5.2 Low Z materials

FOREV-1 calculations were performed for carbon and beryllium target materials. Typical temperature and density profiles in a beryllium target plasma after 100 µs are shown in Fig. 9 for a 10 keV ion beam of power density of 10 MW/cm^2. In the corona the plasma temperature achieves a value of 20 eV. This is caused by the

rather low emissivity of beryllium for plasma temperatures between 3 and 10 eV (see Fig. 3).

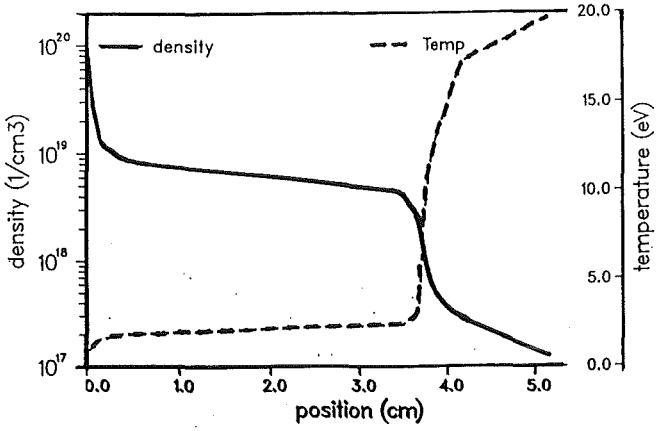

Fig. 9: Temperature and density profiles for Be target plasma at 100 µs for 10 keV ion beam of power density of 10 MW/cm^2.

Close to the target the density reaches 10^{20} cm^{-3}, the temperature drops below 1 eV. In this region molecular effects are becoming important. After 100 µs the diffusive expansion velocity across the magnetic field lines is 4 x 10^4 cm/s. The plasma layer thickness is 5.5 cm. The magnetic field decreases towards the target and a high β situation is achieved.

As a consequence of the rather high plasma temperature in the corona more than 50 % of the backradiated flux is due to soft x-ray (SXR) radiation in the photon energy region from 123 eV up to 300 eV. The contribution of different photon energies to the radiative target heat load is shown in Fig. 10.

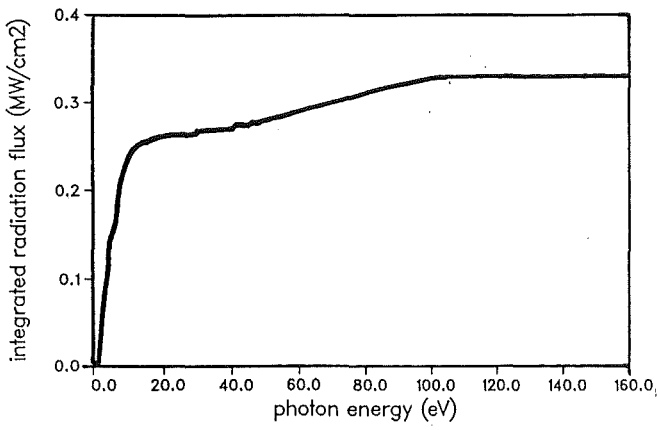

Fig. 10: Radiative target heat load for Be as function of photon energy after 100 µs for 10 keV ion beam of power density of 10 MW/cm^2.

Recombination radiation in the frequency range 50 - 100 eV contributes with about 20 % to the target heat load in the multigroup opacity calculations. The SXR radiation from the plasma corona is absorbed in the rather dense and cold plasma layer close to the target. For carbon and for a 10 keV ion beam of power density of 10 MW/cm^2 the temperature in the plasma corona is 41 eV.

5.3 Erosion

First estimations for 1D erosion and results of melt layer calculations are listed in Table 1 for beam power densities of 10 and 100 MW/cm^2 for beryllium, carbon and tungsten. Erosion for a 10 keV Maxwellian electron beam is typically a factor of 2.0 for low Z materials and a factor of 5 for high Z materials larger than for 10 keV ions. The radiative heat conduction approximation overestimates erosion for carbon up to a factor of 5, but gives fairly good results for beryllium. The melt layer thickness is larger than erosion. Therefore melt layer instability if occurring

during a disruptive event could become the most dangerous event for beryllium and tungsten targets.

Table 1

First results of 1D erosion and melt layer calculations in μm for beam power densities of 10 MW/cm² and 100 MW/cm². Emission coefficients from Kirchhoff law for tungsten, for carbon and beryllium from CRE model with escaping factor correction.

target	radiative properties	10 keV ions 10	100 (MJ/m²)		10 keV electrons[1] 10	100 (MJ/m²)	
carbon	512 group Planck opacities	2.1[3]	9.0	<15[2]	3.9	20	15[2]
	rad. heat cond.	8.2					
beryllium	512 group Planck opacities	2.2[3]		8.9[2][3]	4.3[3]		
	rad. heat cond.	1.4	5.0				
	melt layer	40	135				
tungsten	1024 group Planck opacities	0.2	1.2	1.4[2]	1.0	5.6	4.0[2]
	melt layer	35	118				

(1) Maxwellian distributed, impact angle $\alpha = 5°$

(2) power density 100 MW/cm², $\Delta t = 100$ μs

(3) rebuilding of mesh in region of gradients, but still insufficient number of meshes

6. Self consistent radiation transport

The transport of SXR photons from the plasma corona to the target requires a more detailed radiation transport modeling. The multigroup opacity concept is not appropriate because it doesn't allow to take into account the interaction of hot photons with a cold plasma. Preliminary results of self consistent radiation transport calculations with a simple plasma multilayer model indicate that for Be

hot photons can increase the target heat load due to an increase of the intensity of recombination radiation in the energy range 50 - 100 eV and due to an increase of excited level populations of Li like ions in the region of the dense cold plasma close to the target. Therefore the erosion values as given in Table 3 will increase for the low Z materials carbon and beryllium if radiation transport is treated self consistently in the radiation MHD calculations.

First important steps to accomplish this aim were completed. The frequency dependent absorption and emission coefficients κ_ν and β_ν are calculated using an atomic data base containing energy levels, ionization potentials, rate coefficients for all transitions, photoionization cross sections and oscillator strengths and spectral radiation fluxes as calculated in a previous time step. The new κ_ν and η_ν then are used in a certain number of next time steps of the radiation hydrodynamics calculation. The method is rather flexible and allows calculations at point frequencies using several frequencies per line for detailed line transfer calculations and calculations in multigroup approach. Fig. 11 gives a comparison of emission coefficients calculated by TOPATOM and by the self consistent approach.

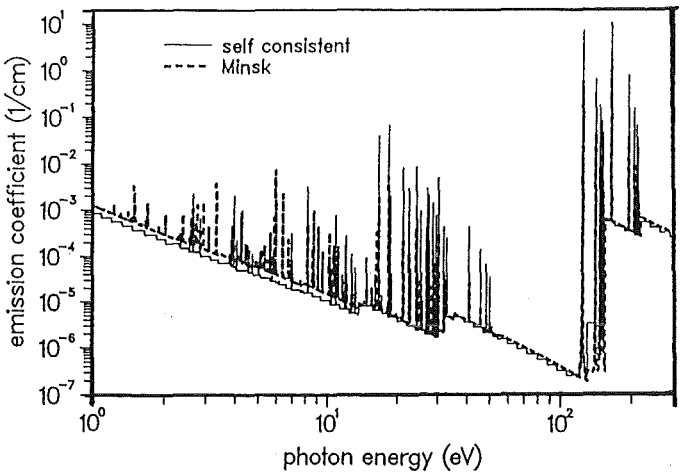

Fig. 11: Comparison of emission coefficients for Be plasma. Plasma density 10^{17} cm^{-3}, temperature 15.9 eV.

7. Conclusions

The 1D radiation MHD code FOREV-1 was applied to the analysis of ITER tokamak disruptive erosion. Typical for the plasma flow target interaction is that after plasma shield formation more than 85 % of the incoming beam power is converted into radiation and most of that is backradiated. This may cause problems to internal tokamak structures and thus needs careful checking. For high Z materials radiation transport with multigroup opacities is fully adequate. For low Z materials however a non-LTE plasma corona effectively converts a significant fraction of the beam energy into SXR radiation. To calculate the transfer of SXR radiation from this plasma corona through cold and dense plasma layers a self consistent approach to radiation transport is required. In case of inclined mag-

netic field lines moreover the 1½D MHD model is needed for obtaining a realistic expansion velocity of the plasma shield perpendicular to the target.

Another problem is the dense and rather cold plasma layer in front of the target. The influence of molecules on the optical properties leads to a decrease of the radiative heat transfer due to increased opacities. This was demonstrated in radiation transport calculations [21] but more detailed radiation hydrodynamics calculations are still needed for a quantification of this effect.

For modeling of the tokamak situation with finite SOL width and tilted target and for calculation of plasma expansion in case of inclined magnetic field lines the code FOREV-2 is developed. 2D radiation transport is done either by using a generalized forward reverse scheme with 4 angular directions or by using the discrete ordinate method (S_N). The magnetohydrodynamics of FOREV-2 is based on a 2½D MHD model. Three components of the expansion velocity and 2 components of the magnetic field are used to describe the time and spatial evolution of the plasma shield.

Acknowledgement

The authors would like to thank Dr. Boris Bazylev and Dr. Vladimir Tolkach from Lykov Institute of Heat and Mass Transfer Minsk for many illuminating discussions on radiation transport and self consistent approach and for making available atomic data bases and optical data for Be, C and W including the plasma emissivities with escaping factor correction for Be and C.

7. References

[1] G. Janeschitz et al., 11th Int. Conf. on Plasma Surface Interactions in Controlled Fusion Devices, Mito, May 23 - 27, 1994.

[2] A. Sestero, Protection of walls from hard disruptions in large tokamaks, Nucl. Fusion 17,1, 1977, p. 115.

[3] H. Würz et al., Numerical modeling and experimental simulation of vapor shield formation and divertor material erosion for ITER typical plasma disruptions, J. Nucl. Mat, 212 - 215, 1994, p. 1349.

[4] F.C. Schüller et al., 21st EPS Conf. on Controlled Fusion and Plasma Physics, Montpellier, June 27 - July 1, 1994, Vol 18B, Part I, p. 230.

[5] N.I. Arkhipov et al., Interaction of high temperature plasma with solid targets, Fusion Technology 1992, Vol, 1, p. 171.

[6] N.I. Arkhipov et al., 18th SOFT Karlsruhe, 1994.

[7] H. Würz et al., 11th Int. Conf. on Plasma Surface Interactions in Controlled Fusion Devices, Mito, May 23 - 27, 1994.

[8] B. Bazylev, I. Landman, H. Würz, 21st EPS Conf. on Controlled Fusion and Plasma Physics, Montpellier, June 27 - July 1, 1994, Vol. 18B, Part II, p. 742.

[9] I. Landman, H. Würz, Vapor shield formation and erosion of divertor plates during ITER tokamak plasma disruptions, 18th SOFT, August 22 - 26, 1994, Karlsruhe.

[10] L. Lengyel, P. Spathis, 21st EPS Conf. con Controlled Fusion and Plasma Physics Montpellier, June 27 - July 1, 1994, Vol. 18B, Part II, p. 778.

[11] A. Hassanein, J. Nucl. Mat., 212 - 215 (1994), p. 1272.

[12] Y. Martynenko, private communication

[13] I. Landman, H. Würz, Proc. Int. Conf. on Phenomena in Ionized Gases, ICPIG-21, Sept. 21 - 24, 1993, Bochum, Vol. II, p. 201.

[14] G. Piazza et al., The magnetic vapor shield effect of divertor plates during plasma disruption, 18th SOFT, August 22 - 26, 1994, Karlsruhe.

[15] Y.B. Zeldovich, Y.P. Raizer, Physics of Shock Waves and high temperature hydrodynamic phenomena, Academic Press NY 1966.

[16] B. Bazylev et al.,Phys. Engineering Journal Vol. 58, No. 6, 1990, p. 1012 (in russian).

[17] J.J. MacFarlane, P. Wang, Laser and particle beams, Vol. p. 10, 349, 1992.

[18] V.R. Barabasch et al., Proc. 2nd ISFNT Karlsruhe 1991. North Holland Amsterdam, 1991, p. 145.

[19] J. van der Laan et al., Proc. 2nd ISFNT Karlsruhe 1991, p. 135.

[20] V. Engelko et al., Test of divertor materials under simulated ITER plasma disruption conditions at the SOM electron beam facility, 11th PSI, Mito, May 23 - 27, 1994.

[21] B. Bazylev et al., First estimation of the influence of molecules on radiative heat transfer, Int. Workshop on divertor target behavior during ITER tokamak plasma disruptions, Aug. 29 - 30, 1994, Karlsruhe.

V Addendum

Possible industrial applications of high voltage pulsed power techniques

H. Bluhm

All scientific and industrial applications based on high voltage pulsed power technique use its capability to deposit in matter an appreciable amount of energy in a very short time interval. It is this pulsed energy release which opens a large field of new scientific and industrial applications.

The available electrical energy is either released directly in the form of an electrical discharge or through the intermediate step of electron- and ion-beam generation. Application paths thereby accessible are presented in the diagram of Fig. 1. The power level as well as the pulsed energy and the treated volume can be varied over many orders of magnitude and adapted to the respective requirements of the application.

The biggest potential for industrial applications of this technique will probably be found in the surface treatment of materials. High energy pulsed electron and ion beams can melt large areas (? 1000 cm^2) of material surfaces to a depth around 50 μm in a very short time. After termination of the pulse very high cooling rates of the molten layer reaching values as high as 10^9 °K/s occur through heat conduction into the bulk material. Through this rapid quenching amorphous structures and other phases can be frozen in sealing, hardening and polishing the material surface and thereby improving the corrosion and wear resistance. Such a kind of surface treatment can be carried out for metallic as well as for ceramic materials of nearly any shape. Since the range of electrons and ions depends on their energy it is possible to control the depths of the molten layer within certain limits.

Volume energy deposition is also the basis for the production of thin layers through ablation, conserving the stoichiometry of such complex compositions like hydroxyl-apatite (an inorganic component of bones and teeth) and teflon. This observation has led to the recent big success of ablation facilities based on the channel spark.

Nearly unexploited are applications that utilize the direct release of pulsed energy in a high voltage discharge. A cost effective process for the production of large quantities of nanopowder is e.g. the explosive electrical discharge through a thin wire. If we succeed to optimize the distribution of particles resulting from this discharge, i.e. to eliminate particles larger than 50 nm, this process may become superior to competing ones.

Pulsed discharges in solid materials lead to fragmentation. This energetically very favourable technique possesses a large variety of possible applications ranging from the fragmentation of concrete to the mining of minerals as well as the production of stable suspensions. Together with the Polytechnic Institute of the University of Tomsk we have very recently taken into operation a 250 kV, 50 kJ generator running at 5 Hz repetition rate. First experiments with concrete, glass, granite are very promissing.

Pulsed discharges in liquids create big shock amplitudes, which can be utilized to destroy micro organism. It has also been found that such a pulsed discharge can lead to antiseptic water whose

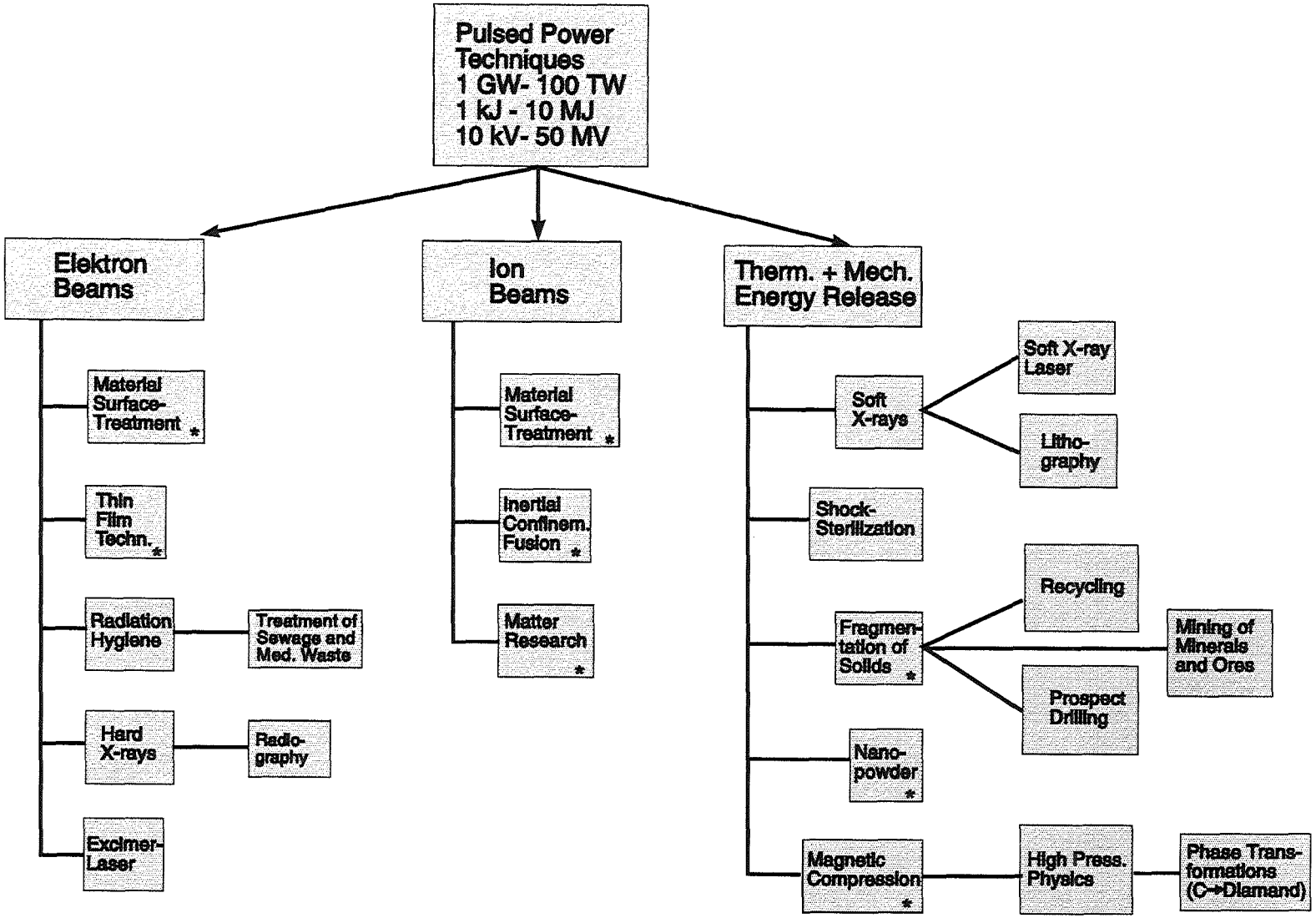

Fig. 1 Possible fields for industrial and scientific applications of pulsed power techniques.
** Present activities at INR*

sterilizing effect persists for several minutes. Thus it seems conceivable to replace large quantities of disinfecting organic liquids in hospitals.

A very important consideration of industrial applications are the specific costs of a facility. Presently they lie around 20 DM/J of usable energy for a high voltage pulse generator. Since this techniques is also based on simple robust components and since the efficiency of ion and electron beam production can be as high as 80 % it is also to be expected that the operational costs will stay low.

Until recently the repetition rate capability of pulsed power generators seemed questionable. However, through the advent of magnetic- and solid state switches this problem was solved.

More work needs to be done to develop reproducible pulsed high power electron and ion beam diodes with repetition rate capabilities. Since pulsed electron beam diodes are much easier to build than ion diodes we have decided to investigate the potential of pulsed electron beam treatment of material surfaces first. A 22 kJ, 200 kV, 22 μs pulsed electron beam generator using a current controlled multipoint cathode is presently under construction at the Efremov Institute in St. Petersburg and will be transferred to Karlsruhe in autumn 1995.

Publications:

Journals:

K. Baumung , H.U. Karow, D. Rusch, H.J. Bluhm, P. Hoppé, G.I. Kanel, A.V. Utkin, V. Licht

"High-power proton beam-matter interaction diagnostics by analysis of the hydrodynamic response of solid targets"
J. Appl. Phys. 75 (12), 7633 (1994).

G.I. Kanel, S.V. Razorenov, A.V. Utkin, V.E. Fortov, K. Baumung, H.U. Karow, D. Rusch

"Spall strength of molybdenum single crystals"
J. Appl. Phys. 74 (12), 7162 (1993)

H. Laqua, H. Bluhm, L. Buth, P. Hoppé

"Properties of the nonequilibrium plasma from a pulsed sliding discharge in a hydrogen gas layer desorbed from a metal hydride film"
J. Appl. Phys. accepted for publication

K. Baumung, H.J. Bluhm, H.U. Karow, D. Rusch, O. Stoltz, J. Singer, G.I. Kanel, A.V. Utkin, S.V. Razorenov, and V.E. Fortov

"Hypervelocity Launching and Impact Experiments on the Karlsruhe Light Ion Facility KALIF"
Hypervelocity Impact Symposium, Santa Fee, Oct. 16 - 19, 1995 & acc. for publ. in *J. Impact Engeneering*

H. Würz, N.I. Arkhipov, V.P. Bakhin, B. Goel, W. Höbel, I. Konkashbaev, I. Landman, G. Piazza, V. Safronov, V.M. Sherbakov, D.A. Toporkov, A.M. Zhitlukhin

"Numerical modeling and experimental simulation of vapor shield formation and divertor material erosion for ITER typical plasma disruptions"
Journ. of Nucl. Materials, 212 - 215, 1349 (1994).

C.-D. Munz

"A Tracking Method for gas flow into vacuum based on the vacuum Riemann problem"
Math. Meth. in Applied Science 17 (1994), 597 - 612

VI Publications

C.-D. Munz

"On Godunov-type schemes for Lagrangian gas dynamics"
SIAM J. Numer. Anal. 31 (1994), 17 - 42

M.F. Göz

"Unique Solvability of the Periodic Cauchy Problem for Wave-hierachy Problems with Dissipation"
Math. Meth. in Applied Sciences 17, 787 - 805 (1994)

Conference Contributions:

H. Bluhm, P. Hoppé, H. Bachmann, W. Bauer, K. Baumung, L. Buth, H. Laqua, A. Ludmirski, D. Rusch, O. Stoltz, S. Yoo

"Stability and Operating Characteristics of the Applied B Proton Extraction Diode on KALIF"
Proc. 10th Intern. Conf. on High Power Particle Beams, 1994, Vol. I, p. 77.

W. Bauer, W. Höbel, E. Stein, A. Ludmirsky, T. Westermann

"A Contribution to the Magnetic Focusing in an Applied B-Extractor Ion Diode by a Laser Pulse Driven Solenoid"
Proc. 10th Intern. Conf. on High Power Particle Beams, 1994, Vol. I, p. 83

K. Baumung, H. Bluhm, P. Hoppé, H.U. Karow, D. Rusch, O. Stoltz, J. Singer, G.I. Kanel, A.V. Utkin, S.V. Razorenov

"Hydrodynamic Beam-Target Interaction Experiments on the Karlsruhe Light Ion Facility KALIF"
Proc. 10th Intern. Conf. on High Power Particle Beams, 1994, Vol. I, p. 211

G.I. Kanel, A.V. Utkin, K. Baumung, H.U. Karow, D. Rusch

"Dynamics of the High-Power Ion Beam Interaction with Targets"
Proc. 10th Intern. Conf. on High Power Particle Beams, 1994, Vol. I, p. 236

A. Ludmirsky, K. Baumung, H. Bluhm, L. Buth, B. Goel, G. Meisel, D. Rusch, O. Stoltz, J.J. Mac Farlane, P. Wang

"Calculations for K_α-Spectroscopy of Hot Dense Plasmas Produced by the KALIF Ion Beam"

Proc. 10th Intern. Conf. on High Power Particle Beams, 1994, Vol. II, p. 723

V. Engelko, C. Schultheiß, H. Würz, S. Schalk
"Pulsed Intense Proton Beam Facility for ITER Disruptions Simulation"
Proc. 10th Intern. Conf. on High Power Particle Beams, 1994, Vol. II, p. 785

O.Yu. Vorobjev, B. Goel
"Application of Intense Ion Beams for Investigation of Matter Properties Under High Pressures and Temperatures"
Proc. 10th Intern. Conf. on High Power Particle Beams, 1994, Vol. II, p. 825

G. Müller, C. Schultheiß
"Deposition by Means of Pulsed Electron Beam Ablation"
Proc. 10th Intern. Conf. on High Power Particle Beams, 1994, Vol. II, p. 833

B.A. Knyazev, P.J. Melnikov, H. Bluhm
"'Catalytic Resonance Ionization'" - A Novel Universal Technique for the Formation of a Two-Component Anode Plasma"
Prof. 10th Intern. Conf. on High Power Particle Beams, 1994, Vol. I, p. 451

H. Bluhm, P. Hoppé, H. Bachmann, W. Bauer, K. Baumung, L. Buth, H. Laqua, A. Ludmirski, D. Rusch, O. Stoltz, S. Yoo
"Recent progress in ion diode development at KfK"
IAEA Technical Committee Meeting on Drivers for Inertial Confinement Fusion, Paris, Nov. 14 - 18, 1994

I. Landman, H. Würz
"Vapor shield formation and erosion of divertor plates during ITER tokamak plasma disruptions"
18th Symp. on Fusion Technology, Karlsruhe, Aug. 22 - 26, 1994

M.F. Göz, C.-D. Munz
"Lagrangian Gas Dynamics: Godunov-Typ Schemes and Discontinuous Flux Functions"
ZAMM, Z. angew. Math. Mech. 74 (1994) 5, T380 - T382

C.-D. Munz, R. Schneider, O. Gerlinger
"The numerical approximation of a free gas-vacuum surface"

Notes on Numerical Fluid Mechanics, Vol. 47, Vieweg Verlag, Braunschweig/Wiesbaden 1994, 181 - 190

E. Halter, J. Kündahl, M. Krauß, C.-D. Munz, R. Schneider, E. Stein, U. Voß, T. Westermann

"Interaktive Gittererzeugung im Rahmen eines offenen CAD-Systems"
G. DGLR/AG STAB-Symposium 1994, Erlangen 1994

R. Schneider, C.-D. Munz

"Die numerische Lösung der Maxwell-Lorentz-Gleichungen für technisch relevante Geometrien"
DMV-Tagung, Duisburg, 1994.

Reports:

H.P. Laqua

"Das Nicht-Gleichgewichts-Plasma einer Oberflächengleitentladung auf einem Metallhydridfilm als Ionenquelle" Dissertation
KfK - 5286 (1994)

O.Yu. Vorobiev, A.L.Ni, B. Goel

"Numerical simulation of foil acceleration experiments with light ion beams"
KfK - 5299 (1994)